

UNIVERSITÉ DE GENÈVE

Département de physique nucléaire et corpusculaire

FACULTÉ DES SCIENCES

Professeur Martin Pohl

Tests And Production Of The AMS-02 Silicon Tracker Detectors

THÈSE

présentée à la Faculté des sciences de l'Université de Genève
pour obtenir le grade de Docteur ès sciences, mention physique

par

Philipp AZZARELLO

de Genève (GE)

Thèse N° 3530

GENÈVE

Atelier de reproduction de la Section de physique

2004

La Faculté des sciences, sur le préavis de Messieurs M. POHL, professeur ordinaire et directeur de thèse (Département de physique nucléaire et corpusculaire), A. G. CLARK, professeur ordinaire (Département de physique nucléaire et corpusculaire), et J.-P. VIALLE, professeur (Laboratoire d'Annecy-le-Vieux de physique des particules – Annecy, France), autorise l'impression de la présente thèse, sans exprimer d'opinion sur les propositions qui y sont énoncées.

Genève, le 16 juin 2004

Thèse - 3530 -



Le Doyen, Jacques WEBER

Contents

Résumé	xi
1 Introduction	1
2 The AMS experiment	3
2.1 The Big Bang model	3
2.1.1 Baryogenesis	4
2.2 The Big Bang nucleosynthesis	5
2.3 Dark matter	6
2.4 Stellar nucleosynthesis	7
2.4.1 Hydrogen burning stars	7
2.4.2 Helium burning stars	9
2.4.3 Advanced burning stages	9
2.5 Cosmic rays	10
2.5.1 Isotopic composition	10
2.6 The AMS experiment	13
2.7 The AMS-01 mission	13
2.8 Results and performances of AMS-01	15
2.9 The AMS-02 mission	15
2.10 AMS-02 subdetector description	16
3 The silicon microstrip detectors	21
3.1 Introduction	21
3.2 The semiconductors	21
3.3 Intrinsic semiconductors	22
3.4 Extrinsic semiconductors	23
3.4.1 Energy levels induced by donors	23
3.4.2 Energy levels induced by acceptors	24
3.4.3 Impurity levels occupation	24
3.5 The p-n junction	26
3.5.1 Diode current	28
3.5.2 The p ⁺ -n junction	31
3.6 The p-n ₁ -n ₂ junction	32

3.6.1	The p ⁺ -n-n ⁺ junction	33
3.7	Breakdown	34
3.8	The silicon microstrip detectors	35
3.8.1	Single-sided microstrip detectors	35
3.8.2	Double-sided microstrip detectors	36
3.8.3	Detector operation	37
3.9	Silicon detector modules, ladders	41
3.10	Charge sharing and capacitive coupling	42
3.10.1	Capacitive coupling	42
3.10.2	Charge sharing	44
3.11	Calibration and signal detection	47
3.11.1	Signal detection	47
3.11.2	Calibration	48
3.12	Noise contributions	49
3.13	Qualification tests	50
3.14	Conclusions	52
4	The microstrip detectors in the AMS experiment	55
4.1	Introduction	55
4.2	The Silicon Tracker	55
4.3	The AMS ladder	58
4.4	The AMS silicon microstrip detectors	59
4.4.1	The AMS-01 microstrip detector	59
4.4.2	The AMS-02 silicon microstrip detector	59
4.4.3	Anti-reflective sensors	61
4.5	K5 and K7 Upilex cables (K-side)	64
4.6	K6 Upilex cable (S-side)	65
4.7	The Tracker Front End electronics: the hybrids	67
4.7.1	The RCAMS	67
4.7.2	The VA preamplifier	67
4.7.3	The Hybrid Control Circuit (HCC)	70
4.8	Ladder bias	73
4.8.1	AMS-01	73
4.8.2	AMS-02	74
4.9	Remarks	76
5	Ladder assembly	77
5.1	Introduction	77
5.2	The Geneva assembly line	77
5.3	Assembly phase 1	78
5.3.1	Preparation	78
5.3.2	Silicon positioning	78
5.4	Long Upilex (K5/K7) gluing	81

5.5	Reinforcement gluing	83
5.6	K-hybrid gluing	86
5.7	S-hybrid / K6 Upilex gluing	86
5.8	Bonding	88
5.9	Phase 2	88
5.10	Feet gluing	90
5.11	Spacer gluing and shielding wrapping	90
5.11.1	Spacer gluing	90
5.11.2	Shielding wrapping	90
5.12	Electrical tests	94
5.13	Remarks	94
6	Tests on silicon detectors	95
6.1	Introduction	95
6.2	Test equipment and procedures	96
6.2.1	Probe station measurements	96
6.2.2	Tests performed in probe station	97
6.2.3	Ladder calibrations	100
6.3	Tests on ladder H12 PI 015	101
6.3.1	Introduction	101
6.3.2	Procedure	101
6.3.3	Leakage current evolution	101
6.3.4	Noise evolution in step 1	106
6.3.5	Common mode noise in step 1	107
6.3.6	Noise evolution in step 2	107
6.3.7	Common noise of step 2	108
6.3.8	Comments	108
6.4	Conclusions	109
6.5	Test ladder H02 GT 030	110
6.5.1	Introduction	110
6.5.2	Selected sensors	110
6.5.3	K5 Upilex and reinforcement gluing	110
6.5.4	Ladder evolution	111
6.5.5	Measurements after bonding	112
6.5.6	Remarks	114
6.6	Study of assembly step effects	116
6.6.1	Introduction	116
6.6.2	Sensor 97_13/04 evolution	117
6.6.3	Sensor 97_13/10 evolution	117
6.6.4	Reinforcement sanding	117
6.6.5	Conclusions	117
6.7	Test ladder L12 GT 031	122

6.7.1	Introduction	122
6.7.2	Assembly	122
6.7.3	Noise dependence on voltage	123
6.7.4	Leakage current effects	123
6.7.5	Repair by bond removal	124
6.7.6	Remarks	128
6.8	Conclusions	130
7	AMS-02 production	131
7.1	Introduction	131
7.2	Pre-production	131
7.3	AMS-02 production	132
7.4	Extended electrical tests	132
7.4.1	Low resistance RCAMS channels	133
7.4.2	Bonding quality	133
7.5	AMS-01 ladder refurbishment	134
7.6	Silicon performances	136
8	Beam test analysis	141
8.1	Introduction	141
8.2	Configuration	141
8.3	Selected ladders	143
8.4	Analysis	144
8.4.1	Alignment	144
8.4.2	Cluster identification	145
8.4.3	Trigger to hold time	146
8.4.4	Signal charge study	146
8.4.5	Cluster integral corrections	152
8.5	Comments	168
9	Conclusions	175
A	AMS-02 TFE hybrid schematics and designs	177
A.1	S-hybrid schematics	178
A.2	K-hybrid schematics	179
A.3	Mechanical designs	180
B	K6 and K5/7 Upilex dimensions and positions	181
B.1	K6 Upilex	182
B.2	K5/7 Upilex	183
C	Reinforcement designs	185
D	Spacer designs	187

E Ladder Bonding Schemes	189
E.1 S-side bonding scheme	190
E.2 K-side bonding scheme	191
E.3 K7 bonding scheme	192
E.4 AMS-01 refurbished ladders K-side bonding scheme	193
F Assembly phase 2	195
F.1 Hybrids preparation and feet gluing	195
F.2 Airex spacer bonding	197
F.3 Shielding wrapping	198
G Ladder naming scheme	199
Bibliography	201

Remerciements

Je remercie le Prof. Maurice Bourquin, qui m'a reçu dans le groupe d'AMS Genève, pour mon travail de diplôme, puis pour le doctorat. Ma reconnaissance va également au Prof. Martin Pohl, directeur de thèse, qui m'a accordé sa confiance dans la phase de préparation de la production des échelles d'AMS-02. Je le remercie également pour ses conseils durant l'analyse ainsi que pour la rédaction de cette thèse.

Ma reconnaissance va également aux membres du jury, le Prof. Jean-Pierre Vialle et le Prof. Allan Clark, pour leurs commentaires pertinents au sujet de la thèse.

Je tiens à saluer les membres actuels ou précédents d'AMS Genève, avec qui j'ai collaboré de près ou de loin, Nicolas Produit, Giovanni Ambrosi, Davide Vité, Divic Rapin, la Prof. Catherine Leluc, Eduardo Cortina et Daniel Haas dont je garde un très bon souvenir lors du test faisceau en 2002; Mathieu Ribordy et Markus Cristinziani les précédents doctorants d'AMS-Genève. Les personnes qui se sont investi ou s'investissent dans la production des modules AMS-02, Sonia Natale, Mercedes Paniccia.

L'utilisation de l'appareillage de test des détecteurs au silicium était partagée entre AMS et le groupe ATLAS de Genève. A ce titre je souhaite également remercier Didier Ferrère, dont les conseils et discussions ont été fort utiles.

La phase de développement et de construction d'un détecteur est inconcevable sans une collaboration intense avec les groupes d'électronique et de mécanique.

J'aimerais saluer, pour le groupe d'électronique, Alain Christinet, Jean-Pierre Richeux et Pierre Béné, et pour le groupe de mécanique, Silvio Bergamaschi, pour les différents outils réalisés en CNC, notamment pour la préparation du test faisceau en octobre 2002, Jean Covillot, Maarten Weber pour ses cours de métrologie, Eric Perrin et Florian Masciocchi.

Je les ai côtoyés longtemps en salles blanches pour la (pré-)production d'AMS-02, mais aussi aux repas de midi, durant lesquels nous eûmes des conversations sur tout et rien, mais le plus souvent dans la bonne humeur, Philippe Bouvier et Manfred Willenbrock je vous apprécie beaucoup.

Pour l'atelier de mécanique de la section de physique, Roland Pellet, Wolfgang Hatt et Gabriel Andrey pour sa patience et sa disponibilité lors de la mise au point des gabarits de collage des pieds.

Les ordinateurs sont des entités parfois turbulentes, heureusement Yann Meunier sait les dompter, son aide a été précieuse.

L'aide de Peggy Argentin et Catherine Blanchard dans les diverses procédures administratives a été précieuse, je m'en rends compte de plus en plus et je vous en remercie.

La collaboration avec nos collègues de l'école polytechnique fédérale de Zürich (ETHZ), au CERN, fut fort intense lors de la production phase 1, je souhaite saluer Werner Lustermann, Viktor Aleksandrov et Georgi Petrov.

Résumé

Introduction

Nombre de questions concernant l'évolution de notre univers restent ouvertes. Il est acquis qu'aux premiers moments du big-bang, autant de matière que d'antimatière devaient co-exister. Néanmoins l'observation de notre propre environnement indique la non-existence d'antimatière en abondance, du moins dans le superamas de galaxies dans lequel nous nous trouvons. Plusieurs scénarios sont envisageables, soit en considérant des processus favorisant largement la matière, ou bien des évolutions permettant des domaines isolés d'antimatière. Dans les deux cas, des processus physiques à ce jour non-identifiés en seraient à l'origine. La question de l'antimatière est particulièrement intéressante: si les positrons et antiprotons existent dans notre galaxie, et leurs productions peuvent être correctement expliquées par des processus internes à celle-ci, il n'en va pas de même pour les antinoyaux. Ainsi, la détection d'antihélium serait un indice de l'existence de zones d'antimatière d'origine primordiale. La nucléosynthèse primordiale ne permettant pas la création d'atomes de carbone, la détection d'anticarbone signalerait l'existence d'antiétoiles.

La nature de la matière sombre est aussi pour l'heure inconnue. La particule supersymétrique la moins massive, le neutralino $\tilde{\chi}^0$, pourrait la composer. L'annihilation de cette particule pourrait entraîner une signature caractéristique, dans le spectre des positrons, protons ou photons.

Les rayons cosmiques désignent les particules chargées qui se propagent dans l'espace, et sont produits par les phénomènes astrophysiques se déroulant dans notre galaxie. Leur étude permet ainsi de sonder ces phénomènes. Les rayons cosmiques ont été découverts par V. Hess en 1912, au cours d'une mesure en ballon. Les vols en ballons furent par la suite couramment utilisés pour étudier ces rayons, en particulier leur composition, ce qui contribua au développement de la physique des particules.

Les rayons cosmiques interagissant avec l'atmosphère, il est crucial de réaliser les mesures aux altitudes les plus élevées, du moment que l'origine galactique de ceux-ci est étudiée. Une autre solution consiste à installer l'appareillage de mesure dans l'espace, ce qui présente un avantage supplémentaire, le temps d'acquisition plus long permet la détection d'événements rares.

L'expérience AMS

AMS signifie «Alpha Magnetic Spectrometer» (spectromètre magnétique de Alpha, Alpha étant l'ancien nom de la station spatiale internationale ISS): il s'agit d'un détecteur de rayons cosmiques et de photons, dont le but est d'acquérir les spectres des particules dans un domaine de rigidité allant jusqu'à quelques TV (la rigidité R correspond au quotient de la quantité de mouvement et de la charge électrique de la particule: $R = p/(e \cdot Z)$).

Le déroulement de cette expérience est constitué de deux étapes. La première consiste en un vol de test et de qualification, qui eut lieu entre les 2 et 12 juin 1998: le détecteur était installé dans la soute de la navette spatiale Discovery, et la prise de données eut lieu durant les dix jours de la mission. Les buts de ce vol étaient de valider les technologies et les performances du détecteurs, ainsi que d'obtenir une vision claire de la nature des rayons cosmique sur une orbite similaire à celle que suivrait la station spatiale internationale. Cette mission, réalisée avec succès, permit à la collaboration AMS de s'engager dans la seconde étape: la finalisation et/ou amélioration du détecteur, pour un séjour minimum de trois ans sur ISS. L'installation d'AMS sur ISS n'aura pas lieu avant octobre 2007, les vols de navettes spatiales étant suspendus jusqu'en avril 2005 au plus tôt.

AMS-01

C'est sous la dénomination AMS-01 que l'on désigne la première étape de l'expérience AMS. Le détecteur AMS-01 était composé de (voir figure 2.5):

- Un aimant permanent, composé de 64 sections de 100 blocs de Nd-Fe-B produisant un champ magnétique dipolaire de 0.15 T, pour un pouvoir de courbure de 0.15 T·m². Le moment magnétique est réduit, afin de minimiser les interactions avec le champ magnétique terrestre.
- Quatre plans de scintillateurs, deux au-dessus et deux en-dessous de l'aimant. Le temps de vol de la particule traversante, ainsi que sa position, sa direction de passage et la perte d'énergie étaient mesurés.
- Des scintillateurs disposés sur la paroi interne de l'aimant servaient à sélectionner les particules circulant dans l'ouverture de l'aimant, mais aussi à exclure des particules secondaires produites dans l'aimant.
- Un détecteur de traces au silicium, composé de six plans de détecteurs au silicium à micropistes (implantées sur les deux faces). Les 56 modules de silicium totalisaient une surface de détection de 2.04 m². Ils étaient fixés sur des plans composés d'aluminium en nids d'abeille. La couche externe des plans est composée de fibre de carbone. Quatre plans d'un diamètre de 1.0 m et de 12 mm d'épaisseur étaient situés à l'intérieur de l'aimant, tandis que deux plans (1.4 m de diamètre, 40 mm d'épaisseur) se trouvaient à l'extérieur, l'un au-dessus, l'autre en-dessous de l'aimant. Le détecteur de trajectoires était conçu pour avoir une résolution en quantité de mouvement de 7% dans un domaine compris entre 1 et 10 GeV/c/A.

- Un détecteur Čerenkov à seuil, avec un radiateur en aérogel ($n = 1.035$). Structuré sous la forme de deux couches de cinq et six modules respectifs, ce détecteur avait pour but de séparer les e^\pm des \bar{p}/p .
- La face supérieure d'AMS était recouverte d'un écran protecteur contre les particules de basse énergie, inférieure à 5 MeV.

Les résultats produits par AMS furent fructueux et au-dessus de toute attente. Le détecteur se comporta comme prévu, et l'acquisition de données se déroula sans problèmes. Un tableau clair de la population en rayons cosmiques les plus abondants fut établi. De plus, une recherche d'antimatière fut réalisée, sans succès, établissant une limite à la population en antihélium ($1.1 \cdot 10^{-6}$) inférieure aux valeurs trouvées jusqu'alors par des détecteurs embarqués sur ballons, et ce avec seulement dix jours de prise de données.

Une étude se focalisa sur les antinoyaux avec $Z < -2$, fixant une limite au rapport antimatière/matière à $2.00 \cdot 10^{-5}$. Cette étude permit également de révéler les capacités du détecteur au silicium à identifier clairement les ions jusqu'à l'oxygène (fig. 2.6).

AMS-02

Avant d'installer AMS sur la station spatiale, il était prévu de compléter le détecteur. Dans certains cas, l'expérience acquise durant AMS-01 a permis d'envisager l'amélioration de sous-détecteurs comme l'aimant ou le détecteur de traces. Voici les sous-détecteurs qui composeront AMS-02 (fig. 2.7):

- Un aimant supraconducteur, dont le pouvoir de courbure s'élèvera à $0.78 \text{ T}\cdot\text{m}$ et le champ magnétique central à 0.87 T , soit six fois plus intense que pour AMS-01. Le champ, principalement créé par deux bobines, est de type dipolaire. Des bobines périphériques permettent d'améliorer le champ, et de minimiser le moment magnétique pour limiter les interactions indésirables avec le champ magnétique terrestre. Le système de refroidissement utilise les avantages de l'hélium liquide de type II, superfluide. Le réservoir aura une contenance de 2500 l. La température de l'hélium sera de 1.8 K.
- Un détecteur à radiation de transition (TRD), composé de 20 couches d'un radiateur en polyéthylène/polypropylène. Entre chaque couche sont disposés des tubes proportionnels d'un diamètre de 6 mm, remplis d'un mélange de gaz (80% Xe et 20% CO_2). Le TRD sera utile pour distinguer les p/\bar{p} des e^\pm , afin de réduire le bruit de fond dû aux e^-/p , avec un facteur de rejection de $10^{-3} - 10^{-2}$ dans le domaine d'énergie 10-300 GeV.
- Quatre plans scintillateurs (TOF), qui rempliront le même rôle que dans AMS-01. La technologie a quelque peu évolué cependant, en raison notamment du champ magnétique plus intense. La résolution temporelle attendue sera de 140 ps pour les protons, et devrait s'améliorer pour des noyaux plus lourds.
- Un détecteur de traces au silicium. Il s'agit de la version complétée et améliorée de celle d'AMS-01. La surface de détection s'élèvera à 6.39 m^2 . Un changement d'envergure

concerne l'installation de modules sur les deux faces des plans intérieurs (au nombre de trois), la quantité de couches de détection s'élève désormais à huit.

- Des plans de scintillateurs disposés sur la paroi interne de l'aimant, comme dans AMS-01.
- Un détecteur Čerenkov à imagerie annulaire (RICH) permettra de mesurer la charge et la vitesse de la particule traversante. Aidé du détecteur de trace, le RICH pourra identifier les isotopes jusqu'à $A \lesssim 15 - 20$ dans le domaine $1 \text{ GeV}/c < p/A \lesssim 12 \text{ GeV}/c$. Une identification de la charge sera possible jusqu'à $Z \lesssim 26$ (Fe). Le domaine de quantité de mouvement sera couvert jusqu'à env. $p/A \sim 1 \text{ TeV}$. Deux types de radiateurs seront employés, du NaF et de l'aérogel.
- Un calorimètre électromagnétique (ECAL) placé à l'extrémité inférieure d'AMS, permettra de mesurer l'énergie des e^\pm et des photons. Combiné au TRD, le rejet des p^+ atteindra un facteur 10^6 avec efficacité de détection des e^+ de 90%. L'ECAL est composé de neuf couches, chacune orientée de 90° par rapport à la précédente, afin d'obtenir une mesure de la gerbe en trois dimensions.
- Un localisateur d'étoiles, composé de deux caméras CCD, permettra de connaître la position du détecteur de traces avec une précision de l'ordre de la seconde d'arc.

Tous ces sous-détecteurs permettent de récolter une information complète, voire redondante sur la nature de la particule traversante et en terme de vitesse, charge, énergie et direction.

AMS présente plusieurs avantages par rapport aux expériences embarquées sur ballon. Premièrement, son acceptance et la durée d'acquisition permettent une grande statistique ainsi que la détection d'événements rares. Deuxièmement, AMS s'affranchit des inconvénients liés à l'atmosphère (particules secondaires, durée d'acquisition). Cet avantage indéniable a cependant un prix: AMS est soumis aux mêmes contraintes que tout satellite spatial. La puissance électrique est limitée à 2 kW, le poids à 14'809 livres. Le détecteur, soumis aux vibrations produites lors des vols de navette, doit rester intact afin de permettre des mesures de précision. L'impossibilité d'intervenir sur le détecteur en cas de défaillance nécessite des tests de fiabilité sur les composants, ainsi qu'une certaine redondance.

Les détecteurs de silicium à micropistes

Le détecteur de traces est composé de détecteurs au silicium, avec des implantations de micropistes. Le principe de base de ces détecteurs repose sur les propriétés des jonctions $p - n$, les diodes.

Schématiquement, une diode (fig. 3.7) est formée de deux semi-conducteurs en contact, l'un étant composé d'impuretés de type *donneur* (par exemple le phosphore), l'autre d'impuretés de type *accepteur* (comme le bore). Le semi-conducteur du premier type est dit n , celui du second type est dit p . Ceci a pour effet, à température ambiante, de produire

dans la zone n un excès d'électrons dans la bande de conduction, tandis que dans la zone p , on observe un déficit d'électrons dans la bande de valence (formulé autrement, on parle d'un excès de trous).

Entre les deux semi-conducteurs, un transfert de charge s'opère pour établir un équilibre, entraînant autour de la jonction une zone dépourvue de porteurs de charge libres (électrons pour n , trous pour p). Cette région, non-conductrice, est nommée *zone de déplétion*. Une diode, dans cet état, ressemble à un condensateur, avec deux bornes conductrices, et une zone isolante entre les bornes, ayant le semi-conducteur pour diélectrique. La différence avec un condensateur réside dans le fait que la zone déplétion s'étend ou se réduit selon la différence de potentiel appliquée sur les bornes. Si la borne p est mise à la masse, une tension négative appliquée sur la borne n induira une diminution, puis la suppression de la zone déplétion: la diode devient conductrice avec une résistance négligeable. On parle de polarisation directe.

Si, au contraire, une tension positive est appliquée sur la borne n , la zone de déplétion s'étend: la capacité de la diode diminue, et la diode demeure isolante. Il s'agit de la polarisation inverse. Lorsque la zone de déplétion atteint les limites géométriques de la diode, la capacité se stabilise, et la tension de seuil se nomme *tension de déplétion*. Il faut aussi noter que contrairement à l'image simplifiée donnée ci-dessus, l'énergie thermique permet, en polarisation inverse, le passage d'un courant infime, appelé *courant de fuite*. L'intensité de ce courant dépend de la température ambiante.

Un détecteur au silicium avec implantations de micropistes consiste en un monocristal de silicium de type n , en général d'une épaisseur de $300 \mu\text{m}$, avec des pistes implantées p^+ (fort dopage p) sur sa surface (fig. 3.13). Ces pistes, qui font de l'ordre de $15 \mu\text{m}$ de largeur et qui sont implantées en surface, ne sont rien d'autre que des jonctions $p - n$. Le principe de fonctionnement est donc le suivant: la face munie des pistes p connectées à la masse, on applique une tension positive sur la face opposée. Dans ces conditions, les zones de déplétion occupant le volume autour des pistes (qui sont des jonctions $p - n$) s'étendent au fur et à mesure que la tension positive augmente, jusqu'à ce que la tension de déplétion soit atteinte. Tout le monocristal est alors vidé des ses porteurs de charge libres.

L'énergie déposée par une particule chargée traversant le détecteur dans une telle configuration va induire la création de paires électron-trou. Le champ électrique au sein du détecteur permettra la récupération des trous au niveau des pistes: une localisation de la particule traversante est alors possible.

Des modèles plus évolués de détecteurs micropistes incorporent l'implantation de pistes n^+ (fort dopage n) sur le côté inverse (dit côté n , fig. 3.15). Dans ce cas, si les pistes n^+ sont orientés à 90° par rapport aux pistes p^+ , la collecte des trous (côté p) et des électrons (côté n) permet, avec un seul détecteur, la localisation de la particule dans deux coordonnées. Cette technologie présente l'avantage de minimiser la quantité de matière traversée par la particule à détecter. A noter cependant que la collecte de charges côté n présente quelques difficultés techniques, étant donné que sur cette face la résistance entre les pistes et le substrat est plutôt faible. La solution retenue est de placer entre les pistes n^+ des pistes p^+ (p-stop, p-box) qui permettent une isolation des pistes n^+ . A titre d'exemple, une particule (de charge $Z = 1$) dans un régime de minimum d'ionisation, produit 22'000 paires électron-trou dans

un détecteur de $300 \mu\text{m}$ d'épaisseur.

Les principales caractéristiques des détecteurs micropistes sont la tension de déplétion, le courant de fuite des pistes, ainsi que les capacités entre pistes. La tension de déplétion permet d'identifier à partir de quelle tension le détecteur fonctionne correctement sur ses deux faces. Dans le cas d'AMS, une tension maximale de 50 V a été choisie. Une marge de sécurité est adoptée, de sorte que la tension de fonctionnement est de 80 V. Le courant de fuite des pistes, ainsi que la capacité entre les pistes définissent les caractéristiques du bruit de fond du détecteur. A ce stade, il nous faut mentionner le rôle de l'électronique d'amplification. Une charge de 22'000 électrons est très faible, une amplification est donc nécessaire. Le bruit global, exprimé en électrons, a pour origine:

- le courant de fuite du canal de lecture;
- la résistance de polarisation (la résistance entre la piste et la ligne d'alimentation);
- la résistance de la métallisation recouvrant la piste de détection;
- la capacité totale du canal de détection.

Ainsi, minimiser le bruit revient à: minimiser le courant de fuite, maximiser la résistance de polarisation, minimiser la résistance de la métallisation et minimiser la capacité totale de la piste lue. Ces paramètres se définissent en partie lors de la conception du dessin du détecteur, mais les processus de fabrication peuvent y prendre une part non-négligeable. De plus, le bruit dépend de la longueur de la piste.

Le but premier du détecteur à micropistes est la localisation spatiale, ce qui revient à dire que plus les pistes sont rapprochées, plus la résolution spatiale sera petite. Cependant, pour mener ce raisonnement jusqu'au bout, il est nécessaire de lire chaque piste pour récupérer le signal de détection. Cette solution est très coûteuse. Si nous considérons le cas d'AMS, nous aurions besoin de 2568 préamplificateurs sur une distance de 7 cm, ce qui pose des problèmes géométriques d'une part, et un excès de consommation électrique d'autre part. Une astuce permet de réduire fortement la quantité de canaux de lecture, sans pour autant porter un grave préjudice à la résolution spatiale: le couplage capacitif entre les pistes permet de transmettre à des pistes de lecture les charges déposées à proximité de pistes qui ne sont pas lues. Ce point par ailleurs soulève un paradoxe: pour optimiser le couplage capacitif, la capacité entre pistes doit être élevée, alors que pour limiter le bruit, ce même couplage doit être réduit. Il convient donc, selon les applications, de définir le meilleur compromis.

Le silicium dans AMS-02

Un module au silicium d'AMS (appelé *échelle*, fig. 4.2) est composé d'un alignement de sept à quinze détecteurs à micropistes double-face ($72.045 \times 41.36 \times 0.3 \text{ mm}^3$). Les pistes sont connectées les unes à la suite des autres côté *p*, tandis qu'un câble flexible en Upilex permet la transmission des signaux côté *n*. Pour AMS-02, 192 échelles seront produites. Ces modules seront répartis sur huit couches, totalisant une surface de détection de 6.39 m^2 . Une structure (appelée «renfort») faite de mousse en Airex et d'une couche en fibre de carbone permet de

donner une rigidité à l'ensemble. Des pieds en aluminium, collés sur la fibre en carbone du renfort permettent de fixer les échelles sur l'une des huit couches de détection.

Les cartes de l'électronique d'amplification (appelées *hybrides*, fig. 4.13) sont connectées dans le prolongement du silicium, via des câbles en Upilex, pour chaque côté de détection de l'échelle (le côté supérieur est appelé «S», le côté inférieur «K»). Au total, 1024 canaux de lecture sont associés à une échelle. Les préamplificateurs, nommés VA, accomplissent la mise en forme du signal de façon continue. Le signal mémorisé par le VA doit correspondre au maximum du pulse détecté: la mémorisation est donc effectuée un délai après le signal de déclenchement. Dans l'acquisition, le délai écoulé entre le déclenchement de l'acquisition (la détection par le TOF) et la mémorisation du signal est appelée «trigger to hold time» (TTH). Ce temps n'est pas à confondre avec le temps de mise en forme du signal, propre à l'électronique et au silicium qui lui est connecté, le «shaping time» (ST). Une acquisition optimisée vise à faire coïncider le TTH avec le ST.

L'assemblage des échelles nécessite un équipement particulier, ainsi qu'un environnement adéquat. Un système d'application de colle CAM/ALOT avec un microdoseur volumétrique sont utilisés pour le collage de l'Upilex K. Les micropistes sont connectées les unes aux autres par microsoudure, tandis que l'alignement des détecteurs est contrôlé par une machine de métrologie Mitutoyo. La fragilité des détecteurs au silicium vis-à-vis des manipulations et des poussières nécessitent également un environnement d'une propreté extrême, d'où la nécessité de travailler dans une salle blanche.

La production est partagée par trois sites: G&A Engineering, une industrie italienne, l'Université de Perugia (Italie) et l'Université de Genève. Chacun des sites est, ou a été, impliqué dans l'assemblage des modules, mais à des périodes différentes. Ce processus consiste en l'alignement des senseurs sur un gabarit de précision, le collage de l'Upilex K, le collage du renfort, le collage des hybrides côtés K et S, et la réalisation des micro-soudures. L'Université de Perugia, secondée par G&A se spécialise dans les tests de validation des senseurs au silicium avant assemblage, tandis que Genève est le site par lequel tous les modules transitent, pour subir les dernières étapes d'assemblage: installation des hybrides dans une boîte en aluminium, collage des pieds qui permettront la fixation sur les plans. L'installation des échelles sur les plans s'opère en outre à Genève.

Tout au long du processus d'assemblage, les échelles subissent des tests électriques: mesure du courant de fuite à 80 V et 90 V, ainsi que des calibrages, pour notamment identifier les canaux bruyants ou inactifs. Une échelle présentant des défaillances durant le processus d'assemblage est écartée et si possible ultérieurement réparée.

Tests sur la qualité des détecteurs au silicium

Le détecteur de traces d'AMS-01 fonctionna parfaitement, cependant certains aspects de la production indiquaient que quelques modules se dégradaient au cours de l'assemblage. Dans le but de requalifier les équipements de la salle blanche de Genève, ainsi que les procédures observées par les opérateurs, une série de tests a été lancée au cours de l'année 1999. Globalement, ces tests indiquent que des senseurs passivés (c.-à-d. munis d'une couche protectrice

de 1 μm de SiO_2) étaient souhaitables: cette couche permet de grandement minimiser les dommages causés par des rayures dues aux poussières résiduelles pendant les frottements parfois difficilement évitables entre la surface du silicium et des gabarits d'assemblage. Déjà très importante, la surveillance de la propreté des outils et des senseurs devait être accrue. Il apparut également que la procédure de déglaçage de la fibre en carbone des renforts (pour permettre un bon collage des pieds) avait des conséquences parfois néfastes sur la qualité des modules durant la production AMS-01: pour AMS-02, cette opération se réalise au moment de la fabrication du renfort.

Des tests supplémentaires sur une échelle prototype montrent clairement l'impact de pistes détériorées par microsoudure, effet difficilement maîtrisable: un seul défaut peut induire un canal drainant un courant jusqu'à 1000 fois supérieur à la valeur nominale, induisant par couplage capacitif un bruit non-négligeable sur les canaux voisins. Une solution pour limiter cet effet existe, toutefois, elle peut dans certains cas provoquer des dégradations de la qualité des préamplificateurs. Un lien est aussi clairement établi entre les canaux bruyants et les pistes de silicium à grand courant, du moins sur le côté S, le côté K ne pouvant être testé aisément. Un autre aspect intéressant concerne les condensateurs de découplage entre les préamplificateurs et les pistes des détecteurs au silicium: lorsqu'un condensateur est défaillant, il présente une résistance de l'ordre du $\text{k}\Omega$, et le courant de la piste connectée peut circuler par le préamplificateur. Cela n'endommage pas le préamplificateur, mais le sature, et le rend insensible aux charges recueillies par la piste.

Test faisceau avec des ions lourds

En septembre 2002, six échelles AMS-02 (comptant parmi les premières produites) furent testées au CERN. Les produits de fragmentation issus de noyaux de plomb de 20 $\text{GeV}/c/A$ projetés sur une cible de beryllium furent sélectionnés selon leur rigidité ($R = p/Z$). Trois modes de sélection étaient possibles: $A/Z = 2$, $A/Z = 3/2$, $A/Z = 7/4$. Une analyse cumulant les événements de ces trois types de noyaux fut alors conduite.

Un test préliminaire examina le «trigger to hold time» (TTH) afin de vérifier son accord avec de précédentes mesures utilisant des particules de charge 1. Le résultat qui en découle est que si le côté K présente une très bonne stabilité, il n'en est pas de même pour le côté S, où le «shaping time» (ST) optimal est inférieur à celui du côté K (fig. 8.4). Ce résultat confirme un comportement différent de l'électronique pour les deux côtés K et S. Des test supplémentaires avec une diode laser ont conduit à adopter un TTH de 3 μs pour le côté S, et de 4 μs pour le côté K, dans la version finale de AMS-02.

Une étude concernant la réponse des échelles en fonction des ions traversants a été conduite. Les résultats indiquent que cinq des échelles testées présentent des facteurs d'amplification inférieurs à ceux attendus, ce qui permit la mise au point de tests systématiques pour le reste de la production.

Une dépendance en fonction du centre de gravité du signal est observée (figs. 8.16 à 8.19). Cet effet est présent sur les deux faces du détecteur, néanmoins il est plus net sur le côté K. Une étude, conduite pour chaque Z et chaque échelle, a permis de maîtriser cet effet.

Un autre effet, sur le côté S, n'a pu être complètement levé: il s'agit d'une saturation du gain pour les éléments compris entre le bore et le fluor, qui a pour effet de mélanger les distributions du signal pour ces éléments (fig. 8.5).

La procédure de correction se déroule en plusieurs étapes. Dans un premier temps, les signaux correspondant aux différents Z sont isolés, ce grâce à une représentation en deux dimensions de la charge brute calculée pour les deux côtés des détecteurs (fig. 8.7). Une fois les domaines correctement identifiés pour chaque Z , une étude pour un élément particulier est faite, pour déterminer la distribution du signal en fonction de son centre de gravité. Il apparaît en effet que la magnitude du signal dépend de la proximité de la particule traversante avec une piste de lecture (dont le pas est $110 \mu\text{m}$ sur le côté S, et de $208 \mu\text{m}$ sur le côté K). Les fonctions d'interpolation qui expriment le signal en fonction du centre de gravité sont le plus souvent de forme trigonométrique, en raison de la périodicité du détecteur. Cette première approche permet en outre de déterminer une relation entre le signal moyen (débarrassé de la dépendance du centre de gravité) et le Z^2 de l'échantillon observé (figs. 8.24 à 8.27). Cette approche est assimilable à un calibrage de gain pour chaque échelle et chaque VA. L'application de cette simple relation sur les résultats bruts nous permet de constater une linéarisation de la charge mesurée (figs. 8.28 et 8.29). Reste cependant encore à appliquer les corrections liées au centre de gravité du signal. Pour cette étape, on se limite encore une fois à des échantillons présélectionnés: on étudie la distribution de la charge corrigée du gain et du centre de gravité, en ajustant une loi normale (figs. 8.31 et 8.32). Les paramètres ainsi obtenus permettront d'appliquer des tests de sélection dans la dernière étape de l'analyse: tous les événements sont alors pris en compte. Pour chaque événement, une valeur de Z est choisie en fonction de la charge brute côté K ou S selon la grandeur de ces charges. En même temps, une correction pour $Z - 1$ et $Z + 1$ est appliquée. Une étude des rapports de vraisemblance, basés sur les ajustements de la loi normale (mentionnés plus haut) permet de décider si le choix initial de Z est bon. Dans le cas contraire, le test est à nouveau amorcé pour $Z - 1$ ou $Z + 1$, selon les rapports de vraisemblance. Une fois la valeur de Z la plus adaptée identifiée, la charge corrigée est sauvegardée. Les événements douteux sont stockés à part. Les figures 8.35 et 8.36 représentent les distributions de charge corrigée sur un graphique à deux dimensions, l'abscisse représentant la charge K, l'ordonnée la charge S.

On constate que la méthode de correction est surtout efficace côté K, où l'éparpillement du signal est le plus marqué. Aussi, le gain présente côté S deux régimes distincts, et la région de transition entre les deux régimes a pour effet de noyer les signaux propres aux éléments compris entre le bore et le fluor. La correction en fonction du centre de gravité améliore le résultat, mais ne peut rien contre le mélange dû au gain. La comparaison du facteur de corrélation entre les charges K et S, avant et après correction mettent bien en évidence cette situation (fig. 8.37). Il est à noter que grâce à cette méthode de «calibrage», il est possible de détecter des éléments jusqu'au titane. Avec des échelles de qualité finale, il est envisageable d'atteindre le fer. A ce stade de la discussion, il n'est pas inutile de rappeler qu'AMS sera constitué de huit couches de détecteurs au silicium, ainsi la statistique nous permettra probablement d'accroître la performance de la mesure de charge. En tout état de cause, si il était attendu que le détecteur de trace puisse distinguer des signaux

jusqu'à l'oxygène (cette performance ayant été observée dans AMS-01), il n'était pas prévu de pouvoir atteindre $Z = 22$. Ainsi, même si le RICH sera certainement le sous-détecteur le plus optimisé pour ce genre d'identification, il est plutôt réjouissant de constater qu'un autre sous-détecteur puisse confronter ses observations avec celles du RICH.

Conclusions

Les détecteurs à micropistes au silicium sont des détecteurs coûteux, dont les manipulations nécessitent un environnement spécifique et des instruments particuliers. Les détecteurs de physique des particules en sont tous équipés, nous pouvons même noter que la surface couverte par ces composants augmente avec le temps, augmentant d'autant le coût de l'instrument final. La raison qui pousse à utiliser un tel détecteur est la résolution spatiale qu'il procure, de l'ordre de quelques microns (dans le cas d'AMS, $7 \mu\text{m}$ côté S, $30 \mu\text{m}$ côté K). Pour ce qui concerne le détecteur de traces d'AMS, si la fonction principale est, bien justement, la reconstruction de la trajectoire, l'amplitude du signal permet aussi de déterminer la charge de la particule traversante. Une étude suite à un test faisceau réalisé au CERN en octobre 2002 nous permet d'envisager une mesure de la charge jusqu'à $Z = 22$, voire plus. Ce résultat est par ailleurs confirmé par un test faisceau réalisé en 2003, les données ont même pu être comparées avec les mesures d'un prototype du RICH, avec un excellent accord.

AMS est en cours d'assemblage, et devra encore passer par nombre d'étapes avant l'installation sur la station spatiale internationale. Néanmoins, la mise en route du détecteur représente une perspective passionnante, tant les champs d'exploration d'AMS sont multiples, dans les domaines de l'antimatière, la matière sombre, les photons à haute énergie ou encore les processus de propagation des rayons cosmiques.

Chapter 1

Introduction

The AMS (Alpha Magnetic Spectrometer) experiment, installed on the International Space Station (ISS), will determine the charge (sign and magnitude), momentum and nature of traversing cosmic rays. The subdetectors composing AMS are typical particle physics detectors, like the ones used at CERN for example at the LEP experiments. Those subdetectors are assembled in particle physics institutes by technicians and physicists used to the particle physics technology. Nevertheless, this experiment is exceptional as the AMS detector is to be sent into space. All the constraints proper to space experiments apply: vacuum, power consumption and weight limitations, and thermal controls. Furthermore, the strong vibrations endured by the detector during the shuttle transportation must not alter the components, as well as their precise alignment. Last but not least, as human intervention is hardly possible once the detector is installed on the ISS, the system will need to be autonomous during at least three years.

Thus AMS uses the particle physics technical knowledge and experience, under the constraints of a space experiment.

The next chapter will present the motivations of the AMS experiment and describe the detector. After a description of the silicon microstrip detectors and of the AMS silicon tracker, a description of my activites at the University of Geneva follows. Tests on silicon sensors and silicon modules, as well as the assembly of the AMS silicon modules are presented. Finally an analysis based on a beam test performed in October 2002 at CERN will be described, presenting the performance of the silicon modules regarding nuclei detection from helium up to the highest detectable charges.

Chapter 2

The AMS experiment

2.1 The Big Bang model

The expansion of the universe was observed by E. Hubble in 1920's [1]. Friedmann and Lemaître developed independently a model including the expansion and the cosmological principle, i.e. the universe, at a large scale, is isotropic and homogeneous. This model presents a primordial singularity at $t = 0$ i.e. the density $\rho \rightarrow \infty$ when $t \rightarrow 0$. An interesting aspect of this theory is the prediction of an isotropic relict radiation at about 3 K, which was discovered in 1965 by Penzias and Wilson [2]. The COsmic Background Explorer satellite measured this radiation, with a temperature of 2.725 ± 0.002 K [3] and the isotropy was measured with an accuracy better than 10^{-4} .

Based on these observations, the evolution of the early universe can be summarized as follows:

- At 10^{-43} s, the fundamental interactions (gravitation, weak, electromagnetic and strong) are unified. This period corresponds to the Planck era. Here quantum mechanics is needed to describe gravitation.
- At 10^{-39} s, i.e. $T = 10^{17}$ GeV the gravitation differentiates from the Grand Unified interaction (which unifies the electroweak and strong interactions).
- At 10^{-34} s, $T = 10^{16}$ GeV, the strong interaction differentiates from the electroweak interaction, the quarks and leptons are created.
- At 10^{-9} s, $T = 100$ GeV, the electroweak transition occurs, W and Z bosons become massive through the Higgs mechanism.
- At $T = 1$ GeV, the quarks and antiquarks annihilate, with a slight excess of quarks. At $T = 200$ MeV, the quarks become confined into mesons and baryons.
- At $T = 1$ MeV, neutrinos stop interacting with electrons and positrons, and decouple from the electromagnetic plasma.
- when the temperature goes below the rest mass of the electron, the number of photons increases through $e^+ e^-$ annihilations.

- At $T = 0.1$ MeV the formation of nuclei starts. The abundance of light nuclei is determined by the conditions at that time.
- At about $1.5 \cdot 10^5$ years, the electrons compound with nuclei to form neutral atoms.
- At about $4 \cdot 10^5$ years, the photons can propagate freely, and are at the origin of the now observed Cosmic Microwave Background (CMB).

As noted earlier, the Big Bang theory makes important predictions, such as the existence of the CMB, or the relative abundance of the light nuclei. The latter depends on only one parameter, namely the baryon to photon ratio:

$$\eta = \frac{n_B}{n_\gamma} = \frac{n_b - n_{\bar{b}}}{n_\gamma} \quad (2.1)$$

where n_b corresponds to the number of baryons, $n_{\bar{b}}$ to the number of antibaryons.

The isotropy of the CMB was not directly described by the Big Bang model. This aspect is solved by introducing the inflation process, an exponentially rapid expansion, such that the universe starting with a size of $\sim 10^{-33}$ cm (Planck size), had a size of $\sim 10^{120}$ cm after $\sim 10^{-35}$ s. This dimension is many orders of magnitude larger than the now observable part of the universe. As a consequence the initial inhomogeneities have been diluted. This is also why the universe looks flat, as only a fraction of it is observable.

2.1.1 Baryogenesis

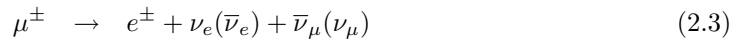
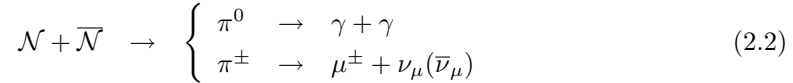
One more important question remains the apparent baryon asymmetry we observe. If we rely on the particle physics observations, particles and antiparticles are created by pairs from neutral states. Thus we would expect our universe to contain equal amounts of matter and antimatter that should have completely annihilated during its history. The direct observations of antimatter are as of now unsuccessful.

From a theoretical point of view, two approaches are possible: the universe is baryon symmetric at very large scales, in which case, one has to understand how and why both types of matter separated. The alternative approach consists in introducing a process which dynamically favours matter, to the detriment of antimatter. Such a process is called baryogenesis. For such a baryogenesis to happen, three conditions are necessary, as stated by Sakharov [4]:

- The baryon charge is not conserved.
- The C and CP symmetries are violated.
- A period out of thermal equilibrium is needed.

In the grand unification theory, the gauge bosons involved in the unified interactions can decay into quark-antiquark or quark-lepton. Thus a baryon asymmetry is provided. Nevertheless, CP violation must be introduced into the model but its observed strength is not sufficient. Another theoretical solution is to generate the baryon asymmetry at the electro-weak scale [5].

For a direct observation, the best candidates are $Z < -1$ antinuclei, as antiprotons can be produced during the interaction of cosmic rays with the interstellar medium, and the cross section to produce $Z < -1$ nuclei in such processes is negligible. For indirect measurements, the observation of the annihilation photons due to the interaction between the matter and antimatter areas should be observable. In particular, following reactions would take place:



The signature of those reactions have not been observed, up to 10 Mpc ($1 \text{ pc} \cong 3.09 \cdot 10^{16} \text{ m}$), from diffuse X-rays studies, thus excluding large zones of antimatter in our super cluster of galaxies¹ [6]. This on the other hand does not exclude small local zones, and a direct search for antimatter, in particular, detecting antihelium would be the evidence for cosmologically significant amounts of antimatter (of primordial origin). The detection of anticarbon would signal the existence of anti-stars as the carbon nucleus cannot be produced during the primordial nucleosynthesis (see next section).

In the case of annihilation, it should be noted that the signal to measure strongly depends on the model chosen to describe the separation between the matter and antimatter zones and the interactions between them.

2.2 The Big Bang nucleosynthesis

The primordial nucleosynthesis is an important topic, as it describes the formation and abundance of the light element nuclei D, ${}^3\text{He}$, ${}^4\text{He}$ and ${}^7\text{Li}$ based on only one parameter, the baryon to photon ratio η . The predicted abundances are in correct agreement with the observational data.

The light element synthesis depends on the conditions corresponding to an age $\gtrsim 1 \text{ s}$ and temperatures $\lesssim 1 \text{ MeV}$. For higher temperatures, the weak interactions are at equilibrium, and the neutron to proton ratio is:

$$\frac{n}{p} = e^{-Q/T} \quad (2.5)$$

with $Q = m_n - m_p = 1.293 \text{ MeV}$. With the temperature decrease, the proton-neutron interconversion rate decreases faster than the expansion rate, and the equilibrium is broken. At that time ($T \sim 1 \text{ MeV}$), the neutron to proton ratio is 1/6. After freeze-out, the neutrons can β -decay, leading to $n/p = 1/7$. At that time nuclear reactions start.

The nucleosynthesis starts with the reaction



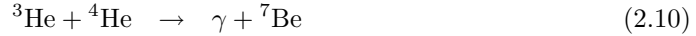
But the photon density is high, and thus the reaction is delayed due to photodissociation, even when the temperature is well below the binding energy of deuterium. Below $T \simeq 0.1 \text{ MeV}$

¹Galaxies are grouped in clusters, with a size of some Mpc. Galaxy clusters are grouped in super clusters with a size of some tens of Mpc.

the nuclei can be formed without being dissociated by photons. Two reactions take place, involving D:



Nearly all neutrons present at the beginning of the nucleosynthesis end up in a 4He nucleus. As there is no stable nucleus for $A = 5$ or $A = 8$, and because of the large Coulomb barriers for the reactions 2.9 and 2.10, nuclei heavier than 4He are present in a small amount:



It is then possible to estimate the primordial 4He mass fraction Y_p :

$$Y_p = \frac{4n_{He}}{n_{tot}} = \frac{4(n/2)}{n + p} = \frac{2(n/p)}{1 + n/p} \simeq 0.25 \quad (2.11)$$

Figure 2.1 shows the calculated abundances for D, 3He , 4He and 7Li as a function of $\eta_{10} = \eta \cdot 10^{10}$. Figure 2.1 shows that a comparisons between the large box for each abundance measurement indicate an overall concordance. In particular, if we take into account the theoretical uncertainties, as well as the observation errors, an agreement between the abundances is possible for:

$$2.6 \leq \eta_{10} \leq 6.2 \quad (2.12)$$

An interesting probe for η is the D/H ratio, as it steeply decrease with η . It seems that D cannot be produced in any other way than the Big Bang nucleosynthesis. The stellar reactions convert D into more tightly bound nuclei. Due to its charge ($Z = 1$), reactions with protons destroy D, even in relatively low temperature stars. Thus the stellar matter will be deprived of D nuclei.

The nuclei 6Li , 9Be , ${}^{10}B$ and ${}^{11}B$ are not created during the Big Bang nucleosynthesis. They are probably produced via spallation: their production cross sections have close values with a difference less than an order of magnitude above 200 MeV, furthermore, the ordering of the cross sections are similar to the ordering of the solar system abundances [8].

2.3 Dark matter

The value of η indicated in section 2.2 has an important consequence, as it allows to determine the baryon density. In particular, it is observed that most baryons are optically dark. Moreover, most of the matter in the universe is not only dark, but also of a non-baryonic nature. Furthermore, the measurements of rotational speed of galaxies indicate a constant value independent of the distance r from the galaxy center, while if the galaxies were only constituted by luminous matter, the rotational speed should evolve like $\frac{1}{\sqrt{r}}$. Both observations lead to the conclusion that a major part of the galactic matter is non-luminous and non-baryonic.

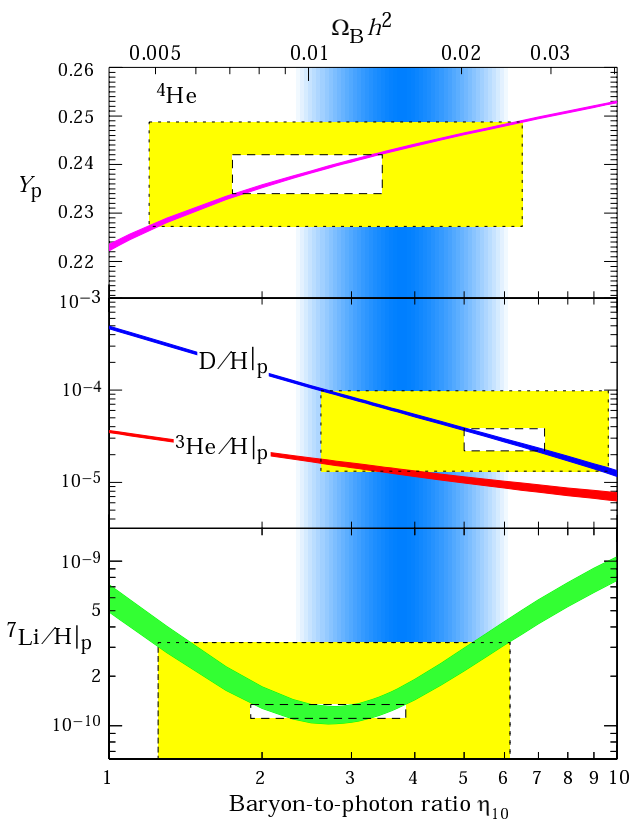


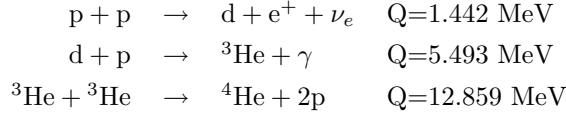
Figure 2.1: The primordial abundances of D, ${}^3\text{He}$, ${}^4\text{He}$ and ${}^7\text{Li}$. Predicted by the standard model of Big Bang nucleosynthesis, the abundances are compared with the observed values (represented by boxes: the small boxes correspond to the 2σ statistical error, the large boxes to the 2σ statistical and systematic errors added in quadrature) [7].

We can distinguish the hot relativistic dark matter, like neutrinos, and the cold, non relativistic dark matter, like brown dwarfs, gas clouds. The latter candidates seem not to be sufficient to account for all the dark matter and cannot be responsible for its large non-baryonic component. The lightest supersymmetric particle, the neutralino $\tilde{\chi}^0$ seems to be a good candidate. It is a stable neutral scalar fermion, which is its own antiparticle. The neutralino annihilations could be identified via e^+ , \bar{p} or photon signals.

2.4 Stellar nucleosynthesis

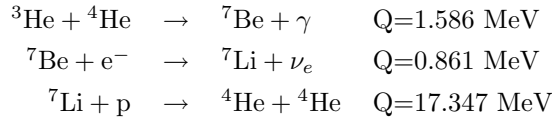
2.4.1 Hydrogen burning stars

At low temperatures, the hydrogen burning is realized via the so-called PP chains. The PPI chain occurs at the lowest temperatures:



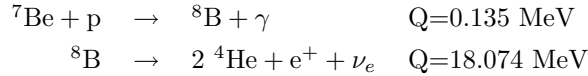
The first reaction is slow, as it involves the weak interaction and the number of close proton pairs is small. The probability of finding such a pair depends on the temperature and the density, taking into account the Coulomb repulsion. The next reaction involves the strong interaction and releases about four times more energy than the first reaction. For the last reaction of the PPI chain a larger Coulomb barrier must be penetrated. Note that there may exist stars for which the temperature is not high enough to proceed with the last reaction. Schematically, the net effect of the PPI chain is $4p \rightarrow {}^4\text{He} + 2e^+ + 2\nu_e$. The neutrinos have an average energy of 265 keV.

For higher temperatures, the PPII chain occurs, in which the ${}^3\text{He}$ is fused with ${}^4\text{He}$:



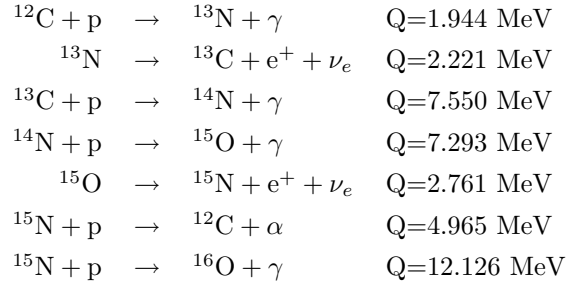
The neutrino average energy is small. As more and more ${}^4\text{He}$ is produced, the PPII chain is favoured.

For even higher temperatures, the PPIII chain occurs:



The ${}^7\text{Be}$ is destroyed by proton capture rather than by electron capture. Because of the Coulomb barrier, this reaction needs a higher temperature. The neutrino energy is large with an average of 7.2 MeV.

In higher temperature configurations, the slow $p + p$ reaction can be replaced by faster weakly interacting reactions. The first cycle will be:



Actually, all the C and N isotopes act as catalysts, which result in the so-called equilibrium CNO abundance. At higher temperatures, the NO and the OF cycles occur, producing heavier isotopes up to ${}^{19}\text{F}$. A threshold temperature indicating whether the $p - p$ process or the CNO cycle dominate can be computed [8]:

$$T \approx 1.7 \cdot 10^7 \left(\frac{X_H}{50X_{CN}} \right)^{1/12.1} \quad (2.13)$$

where X_H is the nucleon fraction of hydrogen, X_{CN} is the nucleon fraction of C and N. As temperature increases, heavier nuclei can be produced.

While the hydrogen nuclei decrease, the star contracts and the surface temperature increases. Two cases are then possible: either the star is massive enough to start helium burning, or the hydrogen surrounding the depleted core starts burning (shell burning phase).

2.4.2 Helium burning stars

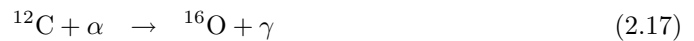
The triple-alpha reaction:



is an important reaction. It is a three-body interaction and its rate is proportional to the square of the density. The stars have a lower entropy than found in Big Bang cosmology, thus they are denser for the same temperature. This is why no $A > 7$ nuclei were produced during the Big Bang nucleosynthesis. The reaction is composed of two steps:



The ^8Be very unstable, with a lifetime $\tau \approx 2.6 \cdot 10^{-16}$ s. The next reactions to take place are:



During the helium burning stage, the s-process takes place, in which neutron capture on a slow timescale happens. Thus the nuclei can beta-decay before the next neutron capture. This process produces nuclei up to $N = 50$ (neutron number). Stars which present a double-shell burning stage (i.e. H and He burning) favour the s-process reactions. Note also that in helium burning stars, the larger the mass, the larger the production of O relative to C. Thus the abundances of the C and O nuclei in the universe strongly depend on a subtle balance between the carbon produced by the triple-alpha reaction and its destruction via the $^{12}\text{C} + \alpha \rightarrow ^{16}\text{O} + \gamma$ reaction.

2.4.3 Advanced burning stages

The next processes to take place are carbon, then oxygen burning. Those processes involve the ^{12}C , ^{16}O fusion, and many other reactions, as among the fusion products, protons, neutrons and alpha particles are released. Those particles can then react with other nuclei, and much faster than the basic $^{12}\text{C}+^{12}\text{C}$ fusion. A detailed description of the processes is found in [8]. The dominant nuclei after carbon and oxygen burning are ^{28}Si and ^{32}S , with ^{24}Mg . Due to the Coulomb barrier, very high temperatures would be needed to start the fusion of such nuclei. Before such temperature levels are reached, photodisintegration starts: a photon is captured and a proton or neutron or alpha particle is released. The photodisintegration rate depends on the binding energy of the ejected particle [9]. The reverse reaction is also possible,

due to the small Coulomb barrier. Many of the ejected particles will be captured by nuclei in which they will be more tightly bound than in the previous nucleus. Thus the nucleons will be redistributed to be in more tightly bound states. Alpha nuclei ($A = 2 \cdot Z$ with Z even) can be thus produced with the successive capture of alpha particles. In particular, ^{56}Ni decays into ^{56}Fe , the most tightly bound nucleus.

Heavier nuclei are produced in supernovae, in particular via the r-process, in which neutrons are added rapidly to a nucleus. In such case, an unstable nucleus does not have the time to disintegrate before the next neutron capture. As the nucleus becomes more and more unstable with the successive neutron increase, the decay time decreases, and an equilibrium is established, until the neutron flux diminishes. The nucleus beta-decays to a more stable isotope, thus increasing Z .

2.5 Cosmic rays

The charged particles travelling in our galaxy are called cosmic rays. The cosmic rays were discovered by V. Hess in 1912, during a balloon flight experiment. This discovery opened a new era in the physics studies, which would later lead to the discovery of new particles, like the positron identified by C. Anderson in 1933 [10]. Anderson and Hess share the 1936 Nobel prize in Physics for their respective discoveries.

The cosmic rays are mainly composed of protons ($\sim 80\%$), ^4He ($\sim 15\%$), e^- $O(1\%)$, e^+ $O(0.01\%)$ [11]. Figure 2.2 shows the CR composition in the rigidity ($R = p/Z$) range 1 GV to 1 TV. In addition, the baryonic component also includes heavier nuclei, for a few % of the total cosmic rays flux.

2.5.1 Isotopic composition

The Big Bang theory correctly predicts the abundances of the light nuclei: the fundamental reactions which took place during the primordial nucleosynthesis describe the production of nuclei up to ^7Be , though this element is unstable and disintegrates into ^7Li .

Except ^7Li , the Li, Be and B elements are consumed during the stellar processes. Nevertheless, the cosmic ray abundances evidence a difference with the solar system abundance (fig. 2.3). The excess of Li, Be and B are due to spallation reactions from energetic p and α fragmenting C, N, O and heavier nuclei. Similar processes are at the origin of the excess of Sc, Ti, V, Cr and Mn, as well as the odd- Z elements from F to K [8].

The cosmic rays near Earth are composed of galactic cosmic rays (GCR), solar energetic particles (mostly protons correlated with the solar activity), and anomalous cosmic rays (singly charged particles, with energy < 100 MeV/n).

AMS will be able to detect cosmic rays in a kinetic energy range from 0.1 to 200 GeV/n, which concerns only the GCR. Nevertheless, the solar activity influences the GCR flux, as the lower energy galactic particles interact with the solar wind. An anticorrelation with the solar activity is thus observed.

The GCR can have energies up to 10^{15} eV. Their acceleration process is related to su-

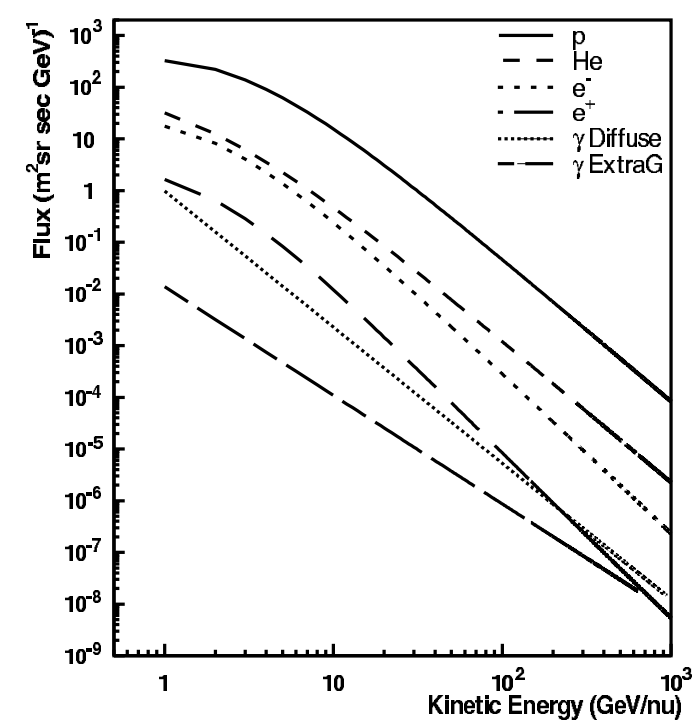


Figure 2.2: Cosmic rays composition in the rigidity range from 1 GV to 1 TV [12]

pernovae (SN) explosions, the accelerated particles may be produced during the SN, or be part of the interstellar medium. In the diffusive shock acceleration process, particles interact repeatedly with the shock waves. The energy the particles acquire while interacting with a SN shock is limited to $10^{13} - 10^{14}$ eV, thus other processes still not identified are necessary to describe the CR with higher energies. Possible sources could be the stellar winds in the presupernova phase, or rotational energy of young pulsars or binary stars.

With an energy $< 10^{15}$ eV, the nuclear radiation has its origin in, and is confined to propagate in our galaxy. For example, nuclei with 10^{10} eV have gyroradii less than 10^{-5} pc in the interstellar magnetic fields while the galactic disk thickness ranges between 200 and 400 pc. The particle motions are governed by the irregular magnetic fields, thus the cosmic rays appear isotropic in the solar neighbourhood [13].

As the cosmic rays propagate they interact with the interstellar medium. Some components of the cosmic rays are products of these interactions, like the Li, Be and B isotopes. In particular, the ^{10}Be radioactive isotope ($\tau_{\frac{1}{2}} = 1.5 \cdot 10^6$ years) is of great interest. The abundance of ^{10}Be relative to ^{9}Be allows to estimate the containment lifetime of primary cosmic nuclei in the galaxy.

As the CR propagate in the galaxy, they interact with the galactic magnetic field ($B_{gal} = 1 - 3 \mu\text{G}$), with the interstellar medium or decay.

We can describe the cosmic rays propagation with the variable x , the amount of matter traversed by the particles. The matter distance x_0 traversed in a time T is $x_0 = \rho\beta cT$, with

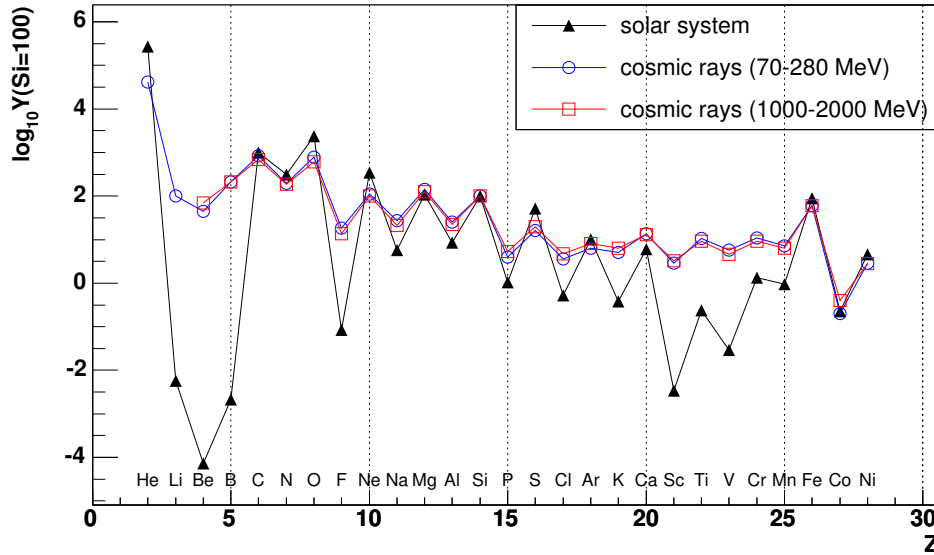


Figure 2.3: Cosmic ray abundances compared with solar system abundance [8, 13].

ρ the density of matter and β is the velocity in units of the speed of light. The propagation of cosmic rays can be described as [13]:

$$\frac{\partial J_i}{\partial x} = \frac{\partial}{\partial E} \left(\frac{dE}{dx} J_i \right) - \frac{N_a \sigma_i^t J_i}{\bar{A}} - \frac{J_i}{\gamma \beta \rho c T_i} + \sum_{j \neq i} \frac{N_a \sigma_{ij} J_j}{\bar{A}} + \sum_{j \neq i} \frac{J_j}{\gamma \beta \rho c T_{ij}} \quad (2.19)$$

$J_i(x)$ is the flux of species i after propagating through an amount of matter x ($J_i(0)$ is the source flux), dE/dx is the rate of ionization energy loss, σ_i^t is the total inelastic cross section for species i , T_i the mean life time at rest of the radioactive species i , σ_{ij} the cross section for production of species i from fragmentation of species j , T_{ij} is the mean lifetime at rest of species j decaying into species i , N_a is the Avogadro's number and \bar{A} is the mean atomic weight of the interstellar gas. Thus the second term of equation 2.19 describes the energy loss, the third term the nuclear interactions, the fourth term the radioactive decay, the fifth term the spallation production and the last term the production by radioactive decay.

There are indications from the secondary to primary nuclei ratio that only a fraction of the primary cosmic rays interact with the interstellar medium. Thus, a part of the cosmic radiation escapes from the confinement region. It seems that the cosmic rays are in a steady state in which the source products are balanced by the escape from the galaxy, the nuclear spallation and the energy loss by ionization at low energy.

The leaky box model describes the confinement in a homogeneous volume where the surface is frequently encountered by particles with a small constant probability of escaping the volume. A simplified model for cosmic rays propagation can be introduced using this model: the loss by escape and spallation are balanced by fragmentation production and the source term. If we neglect the ionization energy loss and the radioactive decay, the

propagation equation takes a simple form:

$$\frac{dJ_i}{dx} = Q_i - \frac{j_i}{\lambda_e} - \frac{j_i \sigma_i^t N_a}{\bar{A}} + \sum_{j \neq i} \frac{j_i \sigma_{ij} N_a}{\bar{A}} = 0 \quad (2.20)$$

Q_i is the source term, λ_e is the mean free path for escape from the confinement region.

It is necessary to have a good knowledge (value and energy dependence) on the parameters σ_i^t , σ_{ij} , dE/dx , but also the pathlength distributions and the radioactive decay and branching ratios for each species.

Cosmic rays with energies larger than 10^{15} eV are believed to have an extragalactic origin. An interesting question remains the possibility of extragalactic CR to reach our own galaxy. Various studies lead to contradicting results, nevertheless the probability of detecting such a particle certainly increases with energy.

2.6 The AMS experiment

AMS is an astroparticle physics detector, to be installed on the International Space Station, for a three year data taking mission. The large acceptance of $0.5 \text{ sr}\cdot\text{m}^2$ and the long duration acquisition will allow large statistics. The scientific goals of AMS are multiple. It will determine the fluxes of individual elements up to $Z \lesssim 26$, in the energy range $0.1\text{GeV}/n \lesssim E \lesssim 1\text{TeV}/n$. AMS will be able to distinguish D from H, and ${}^3\text{He}$ from ${}^4\text{He}$ in the energy range $0.1 \lesssim E \lesssim 10 \text{ GeV}/n$, and ${}^9\text{Be}$ from ${}^{10}\text{Be}$ in the range $0.15 \lesssim E \lesssim 10 \text{ GeV}/n$ [14]. Thus it will be possible to test various cosmic rays propagation models, in examining for example the D/H or the ${}^{10}\text{Be}/{}^9\text{Be}$ ratios. The charge sign identification will determine whether the particle was a nucleus or an antinucleus. AMS will also examine the presence of dark matter in examining the $e^+/(e^+ + e^-)$ fraction as well as the \bar{p} spectrum to identify a possible signature from the lightest supersymmetric particle $\tilde{\chi}^0$ [15]. Finally, high energy photons (between few GeV and few hundred GeV) will be detected, for dark matter study, as well as high energy galactic and extragalactic photon sources [16].

The AMS realization is achieved in two stages. The first step, completed in 1998 consisted in qualifying the detector design and performance, but also to understand the background environment in which the detector will be immersed during the three year mission on the ISS. The second step is the realization of the final AMS detector, which will be installed on the ISS. The final date is for now unknown, as the space shuttle activities are suspended until at least April 2005. In its actual state, the ISS is not ready for the installation of AMS, the port truss segment on which AMS will be installed is not assembled yet (see figure 2.4). As of now, the shuttle mission (assembly flight UF-4.1) is foreseen to transport AMS in October 2007.

2.7 The AMS-01 mission

The first version of AMS, later named AMS-01, was a qualification process. The detector, only partially equipped, was flown aboard the space shuttle Discovery during June 2 to 12, 1998. The detector was composed of (fig. 2.5) [17]:



Figure 2.4: Artist view of AMS-02 (on the left) on the International Space Station (ISS).

- A permanent magnet, composed of 64 Nd-Fe-B sections, each made of 100 blocks, producing a magnetic field of 0.15 T and a bending power of 0.15 Tm². The magnet weight, including the support structure was 2.2 tons. The magnet generated a dipole field, with a reduced dipole moment, thus limiting interaction with the Earth magnetic field.
- Four scintillator planes, two above and two below the magnet. The particle time of flight, energy loss, coordinate and direction were measured. The scintillators triggered the acquisition.
- Scintillators placed on the magnet interior (veto counters) were used to select particles traversing through the magnet, and to exclude secondary particles produced in the magnet.
- A silicon tracker, composed of six planes equipped with 56 silicon microstrip detector modules. The planes were partially equipped, with a total detection area of 2.04 m². The tracker was designed to have a momentum resolution of 7% in the range of 1 to 10 GeV/c/A. The planes are made of an aluminium honeycomb structure, with a carbon fiber external layer. Four planes (1.0 m diameter, 12 mm thick) were located inside the magnet, two planes (1.4 m diameter, 40 mm thick) were outside the magnet [18].
- An aerogel threshold Čerenkov counter ($n = 1.035$), composed of two layers of 5 and 6 modules respectively. The aim of the Čerenkov counter was to separate the e^\pm from the \bar{p}/p .
- The upper side of AMS was covered by a low energy particle shield, protecting the detector from particles with energy below 5 MeV.

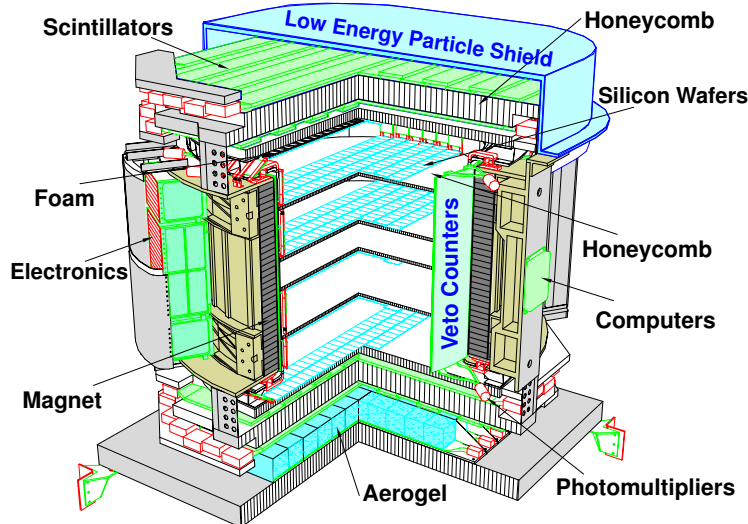


Figure 2.5: The AMS-01 detector.

2.8 Results and performances of AMS-01

The AMS detector was flown aboard the space shuttle Discovery (flight STS-91) from 2nd to 12th June 1998. With an orbital inclination of 51.7° , the shuttle geodetic altitude varied between 320 and 390 km.

Studies about the cosmic ray spectrum, the e^+ , e^- , p , \bar{p} composition and spectra characteristics were done [19, 20, 21, 17], giving a clear picture of the CR environment at ISS. Moreover, no antihelium nuclei were found at any rigidity [22]. An upper limit at the 95% confidence level of on the relative flux of $\overline{\text{He}}$ to He of $1.1 \cdot 10^{-6}$ was found, in the rigidity range $1 < R < 140$ GV. This result assumes that rigidity spectra have the same shape for He and $\overline{\text{He}}$.

A study on particles with $|Z| > 2$ was done [23]. No antimatter candidate was found, setting a limit to the antimatter-to-matter flux ratio to $2.00 \cdot 10^{-5}$, in the rigidity range $1 < R < 100$ GV. Moreover, this analysis characterize the AMS-01 silicon tracker performance. In particular, fig. 2.6 shows that the silicon detectors enabled to identify elements up to oxygen.

2.9 The AMS-02 mission

For the AMS-01 mission, the AMS detector was not fully equipped, additional detectors had to be installed or completed for AMS-02. In some cases, detector configurations were modified, based on the AMS-01 results. In particular, a more intense magnetic field was needed. To achieve larger magnetic fields, the only possible solution was to replace the permanent magnet by a superconducting one.

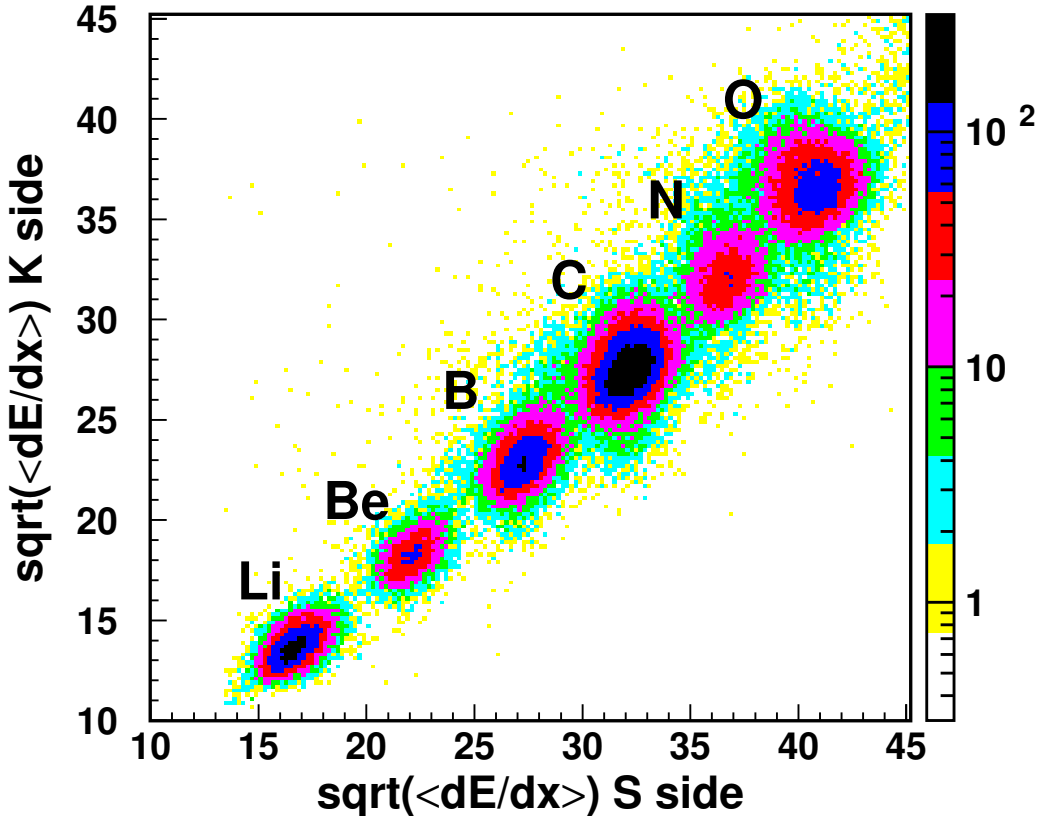


Figure 2.6: Element identification with the silicon tracker of AMS-01 [23]. Elements up to oxygen are clearly separated.

2.10 AMS-02 subdetector description

AMS-02 is composed of (figure 2.7):

- A **superconducting magnet** [24, 25], with a bending power of $0.78 \text{ T}\cdot\text{m}^2$ and a central transverse (perpendicular to AMS vertical axis) magnetic field of 0.87 T, six times stronger than for AMS-01. The magnet is composed of two large dipole coils (similar to a Helmholtz pair configuration), generating most of the transverse magnetic field. One pair of six smaller racetrack coils are also present, to increase the magnitude of the dipole field, limit the stray field outside the magnet, and to minimize the magnetic dipole moment, thus avoiding the undesirable interactions with the Earth magnetic field. The magnet is cooled by indirect conduction with superfluid helium at a temperature of 1.8 K. The coils are placed in a vacuum tank. Four concentric radiation shields are cooled with the He vapour, moreover the outermost shield is cooled by four cryocoolers. The magnet is designed to recover from a quench (i.e. to be cooled and operational again) in an estimated time of three days. Superfluid helium presents some advantages. The density of liquid He II is higher than for liquid He I, this allows to transport

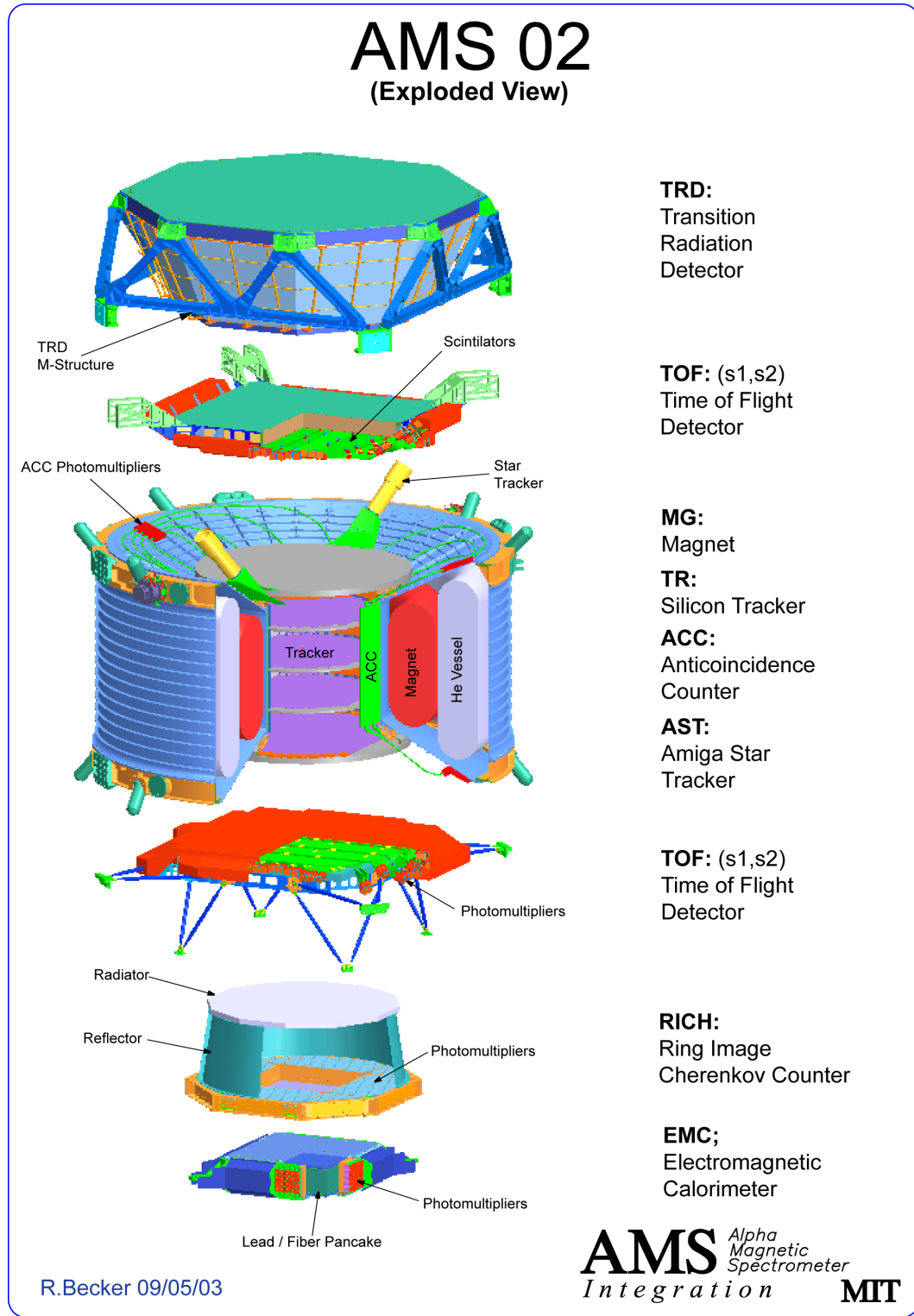


Figure 2.7: Exploded view of the AMS-02 detector.

more Helium for a given volume (2500 l). Also, the He II considerable high thermal conductivity avoids thermal stratification. Such a large magnet has never been operated in space until now.

- A **transition radiation detector (TRD)** [26, 27], composed of 20 layers made of a 22 mm fleece of 10 μm polyethylene/polypropylene radiator. Between each layer, 6 mm diameter proportional-mode straw-tubes chambers filled with a gas mixture of 80% Xe and 20% CO₂ are implemented. In total, 5248 straws will be readout. The TRD will help distinguish p/ \bar{p} from e⁺/e⁻, to reduce the e⁻/p background to a rejection factor $10^{-3} - 10^{-2}$ in the energy range 1.5-300 GeV. The 4 upper and 4 lower layers are oriented along the x-axis (parallel to the magnetic field), while the intermediate layers are oriented along the y-axis.
- **Four plastic scintillator planes** [28, 29] (two above and two below the magnet) composed of 34 paddles, with 2 or 3 photomultipliers at each extremity, will enable to determine the particle time of flight (TOF). Furthermore, it will provide the particle crossing position, travel direction, as well as energy loss. Finally, the TOF will originate the trigger signal for the acquisition. The expected time resolution will be 140 ps for protons, and should be smaller for particles with $Z > 1$. An important difference with the AMS-01 design is due to strong magnetic field to which are exposed the photomultiplier tubes, thus imposing a particular geometry to the light guides. New readout electronics will allow a better charge resolution.
- A **silicon tracker**, composed of eight layers of double-sided microstrip sensors, for a 6.39 m² total detection surface. The tracker will measure the particle rigidity ($R = p/Z$) up to ~ 3 TV. Section 4.2 details the tracker characteristics.
- **Anticoincidence counters**, to reject particles not travelling through the magnet aperture.
- A **ring imaging Čerenkov counter (RICH)** [30, 31] will measure the particle charge and velocity. Thanks to the tracker momentum measurement, the RICH will enable an isotope identification for $A < \sim 15 - 20$ in the range 1 GeV/c < $p/A < \sim 12$ GeV/c. Moreover, a charge identification will be possible for $Z < \sim 26$ (i.e. Fe). At this level, the charge resolution will be of the order of one unit. The momentum range will be covered up to $p/A \sim 1$ TeV/c. Two types of radiator were chosen: NaF for the $p/A = 1$ GeV/c - ~ 5 GeV/c range, and silica aerogel for the $p/A = 4$ GeV/C - ~ 12 GeV/c range. The dynamic range of the electronics is designed to be linear up to the maximum signal expected for Fe. The particle velocity will be determined from the cone reconstruction, based on the trajectory detected by the tracker. The detection area, composed of 680 16-anode photomultipliers, is located between the ECAL (see below) detection area and the conical reflector borders.
- A **3-D sampling electromagnetic calorimeter (ECAL)** [32, 33] located at the bottom of the detector will measure the energy of e⁺, e⁻ and γ . In the range 1.5 GeV

- 1 TeV the hadron rejection will be of 10^4 . Combined with the TRD measurements, the p^+ rejection is increased to a factor of 10^6 at 90% e^+ efficiency. The ECAL is 16.5 cm thick and measures 65.8 cm x 65.8 cm. It is made of 9 18.5 mm superlayers each composed of 11 layers of scintillating fibers (1 mm diameter) embedded in lead foils. The radiation length is about 10 mm, thus the ECAL thickness is about $16 X_0$. The superlayers are alternatively rotated by 90° , and a 3D measurement of the shower is possible. The photomultipliers are composed of four $9 \times 9 \text{ mm}^2$ cells. Thus the shower is sampled at 18 depth levels. The ECAL electronics need a wide dynamic range (60000): one minimum ionizing particle will induce about 8 photoelectrons for a readout cell, while the maximum energy released by a 1 TeV shower in a cell will correspond to 7000 MIPs.

- A **star tracker**, to determine the position of the silicon tracker with an arcsecond precision. Composed of two CCD cameras pointing to different directions, it will compare the star positions with an onboard catalogue.

The particle velocity is determined by the RICH and the TOF systems. The particle absolute charge is measured by the tracker, TOF and RICH, independently. The charge sign is determined by the direction measured by the TOF, and the particle trajectory measured by the tracker. The ECAL and TRD separate hadrons from e^+ and e^- .

The interest of AMS is its large acceptance combined with a long term acquisition, outside of the atmosphere. The drawback is that the detector has to comply with constraints inherent to spatial experiments:

- The power consumption is limited to 2 kW.
- The total weight (detector and fixation structure) must be limited to 14809 lbs.
- The detector must endure the strong vibrations during the shuttle taking off and landing, with no damage or mechanical precision loss.
- The detector is operated in vacuum. As a consequence, the materials must be chosen depending on their outgassing properties. This also has implication on the detector thermal cooling.
- AMS will be installed during at least three years on the ISS. No maintenance will be possible, thus the subdetectors must have reliable components and present redundancy in case of failure.
- The detector must be adapted to allow a depressurization completed in 2 minutes.
- The electronics components must withstand the ionizing radiation ($\sim 1 \text{ kRad/year}$) and the heavy ions at the origin of single event effects (latch up, bit flip).

The next chapters focus on the silicon microstrip detectors and the AMS-02 silicon tracker. In particular a beam test analysis presents the silicon module performance with nuclei.

Chapter 3

The silicon microstrip detectors

3.1 Introduction

Silicon microstrip detectors can be used to obtain a spatial resolution of as low as a few microns. At the same time they can also measure the ionization energy loss (dE/dx) of a traversing charged particle, thus measuring the charge ($dE/dx \propto Z^2$). Since the 1980's the technology allowed the development of such detectors, as well as the appropriate readout electronics.

As silicon microstrip detectors are mainly arrays of diodes, this chapter begins with a description of the p-n junction, before presenting the detectors main properties. General remarks regarding the readout electronics and the detector noise are also discussed.

3.2 The semiconductors

The crystal structure infers the energy band properties. Depending on the Fermi energy level E_f , a material will be a conductor, an insulator or a semi-conductor as schematically shown in figure 3.1.

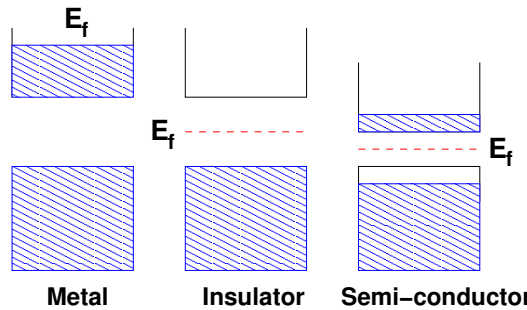


Figure 3.1: A schematic view of the energy band structure for a metal, an insulator and a semiconductor. The hatched area indicates the filled energy levels, E_f is the Fermi energy level.

The conductivity of a material depends on the presence of electrons in the highest energy band. If the band is not full, electrons are free to move from one site to another, and thus allow for conductivity. The band is then called the conduction band.

Thermal energy may allow the transfer of an electron from a full band to the conduction band, if it is close enough in energy. This is basically the difference between an insulator and a semiconductor: a semiconductor is a material for which the energy gap is of the order of 1 eV, or less. Insulators usually have a gap 5 to 10 times larger.

3.3 Intrinsic semiconductors

An ideal intrinsic semiconductor is defined as being perfect and with no impurities. The temperature gives some electrons of the valence band sufficient energy to travel to the conduction band. A thermal equilibrium is established between the electron density $n(T)$ and the hole density $p(T)$.

For the majority of the semiconductors (in particular silicon), it is reasonable to suppose that the bandgap energy $E_g \gg k_b T$, where k_b is the Boltzmann constant. Thus, the density of conduction electron energy states is:

$$f_e(E) = \frac{1}{\exp\left(\frac{E-\mu}{k_b T}\right) + 1} \approx \exp\left(-\frac{E-\mu}{k_b T}\right) \quad (3.1)$$

where μ is the chemical potential. For the hole energy density:

$$f_h(E_e) = 1 - f_e(E_e) = \frac{1}{\exp\left(-\frac{E_e-\mu}{k_b T}\right) + 1} \approx \exp\left(\frac{E_e-\mu}{k_b T}\right) \quad (3.2)$$

In terms of hole energy, we have:

$$f_h(E_h) \approx \exp\left(-\frac{E_h+\mu}{k_b T}\right) \quad (3.3)$$

Thus the electron density in the conduction band is given by:

$$n(T) = \int_{E_g}^{\infty} 2f_e(E)N_e(E)dE \quad (3.4)$$

where the factor 2 is due to the electron spin and the energy state density N_e is expressed as:

$$N_e(E) = \frac{1}{4\pi^2} \left(\frac{2m_e^*}{\hbar^2}\right)^{3/2} \sqrt{E - E_g} \quad (3.5)$$

and m_e^* is the electron effective mass. Finally, we find:

$$n(T) = 2 \left(\frac{m_e^* k_b T}{2\pi \hbar^2}\right)^{3/2} \exp\left(\frac{\mu - E_g}{k_b T}\right) \equiv n_0 \exp\left(\frac{\mu - E_g}{k_b T}\right) \quad (3.6)$$

For holes, a similar calculation leads us to:

$$p(T) = 2 \left(\frac{m_h^* k_b T}{2\pi \hbar^2}\right)^{3/2} \exp\left(-\frac{\mu}{k_b T}\right) \equiv p_0 \exp\left(-\frac{\mu}{k_b T}\right) \quad (3.7)$$

Multiplying $n(T)$ and $p(T)$, we find an expression independent of the chemical potential μ :

$$n_i^2 = n(T)p(T) = 4 \left(\frac{k_b T}{2\pi\hbar^2} \right)^3 (m_h^* m_e^*)^{3/2} \exp\left(-\frac{E_g}{k_b T}\right) \quad (3.8)$$

where n_i is called intrinsic density. Equation (3.8) is called the *mass action law*, and it will be still correct for extrinsic semiconductors.

3.4 Extrinsic semiconductors

Semiconductors containing impurities are called extrinsic. Their behaviour strongly depends on the nature and amount of impurities. The presence of impurities in semiconductors is known as *doping*. There are two kinds of doping, depending on the nature of the impurity (the *dopant*):

- n-doping, due to pentavalent elements like phosphorus, arsenic or antimony. These elements introduce locally an additional electron in the semiconductor crystal structure. These dopants are called *donors*;
- p-doping, due to trivalent elements like boron, aluminium, gallium or indium, which introduce an additional hole and are thus called *acceptors*.

3.4.1 Energy levels induced by donors

Let us consider a silicon crystal with phosphorus dopant (figure 3.2). A silicon atom has four nearest neighbours. Phosphorus, which is pentavalent, will have four neighbours (the silicon atoms) and there will remain an electron with no possible chemical bond. Locally there is approximately a hydrogen atom situation: an electron is bound to a positive centre of charge $+e$, the phosphorus atom. So, we can use the hydrogen atom energy levels, with two corrections: the first is to replace the electron mass m_0 with the effective mass m_e^* to take into account the crystal periodic potential. The second correction is to introduce the silicon dielectric constant, as the interaction between the electron and the ion takes place in silicon. Thus, from the ionisation energy E_0 of the hydrogen atom, we find the electron binding energy to the ion:

$$E_d - E_g = -\frac{q^4 m_e^*}{2(4\pi\epsilon\epsilon_0\hbar)^2} = -E_0 \frac{m_e^*}{m_0} \frac{1}{\epsilon^2} \quad (3.9)$$

where q is the electron charge, E_d is the donor energy level, and E_g is the gap energy. It results that the donor impurities introduce an additional level located in the energy gap, at a distance $E_d - E_g$ from the conduction band. For phosphorus, $m_e^* = 0.45 \cdot m_0$. Thus $E_d - E_g = -44$ meV.

These impurities strongly modify the semiconductor conductivity, as the electron bound to the ion may be thermally excited. At room temperature $E_d - E_g$ is of the order of $k_b T$ (about 26 meV), which is much smaller than E_g (1.1 eV for silicon as schematically shown in figure 3.3). As a consequence, the majority of the donor electrons will be located in the conduction band.

3.4.2 Energy levels induced by acceptors

When the impurity is of the acceptor family, that atom will only have three valence electrons, but still four silicon neighbours (figure 3.4). Thus, to complete the last bond, a supplemental electron from the silicon valence band is used: there will be a hole in the valence band and a negative ion to which the hole is bound. Again, we have a hydrogen-like situation, and the hole has a binding energy $-E_a$:

$$-E_a = -E_0 \frac{m_h^*}{m_0} \frac{1}{\epsilon^2} \quad (3.10)$$

For a boron acceptor, $m_h^* = 0.44 \cdot m_0$, and, as for the donor case, nearly all the acceptors are ionised at room temperature (figure 3.5).

3.4.3 Impurity levels occupation

The mean number of electrons occupying the donor level is:

$$n_d = \frac{N_d}{\frac{1}{2} \exp\left(\frac{E_d - \mu}{k_b T}\right) + 1} \quad , \quad (3.11)$$

where N_d represents the amount of donors impurities. For the acceptor level, we have:

$$p_a = \frac{N_a}{\frac{1}{2} \exp\left(\frac{\mu - E_a}{k_b T}\right) + 1} \quad (3.12)$$

Let us find the corresponding equation to the intrinsic case $n(T) = p(T)$. Consider a semiconductor such that $N_d \geq N_a$. At $T = 0$, N_a of the N_d donor electrons can occupy the acceptor levels. The fundamental level is characterised by the occupation of the whole valence band and of all the acceptor levels (figure 3.6). Also, $N_d - N_a$ of the donor levels are occupied and the conduction band levels are empty. At temperature T (and thermal equilibrium), as the total number of electrons remains the same, we have $n_d + n > N_d - N_a$. Additional $p(T)$ electrons come from the valence band, and $p_a(T)$ from the acceptor levels. Thus we get:

$$n(T) + n_d(T) = p(T) + p_a(T) + N_d - N_a \quad (3.13)$$

To summarize, at room temperature the semiconductor charge densities are expressed as:

$$n(T) = n_0 \exp\left(\frac{\mu - E_g}{k_b T}\right) \quad (3.14)$$

$$p(T) = p_0 \exp\left(-\frac{\mu}{k_b T}\right) \quad (3.15)$$

$$n_d(T) = \frac{N_d}{\frac{1}{2} \exp\left(\frac{E_d - \mu}{k_b T}\right) + 1} \quad (3.16)$$

$$p_a(T) = \frac{N_a}{\frac{1}{2} \exp\left(\frac{\mu - E_a}{k_b T}\right) + 1} \quad (3.17)$$

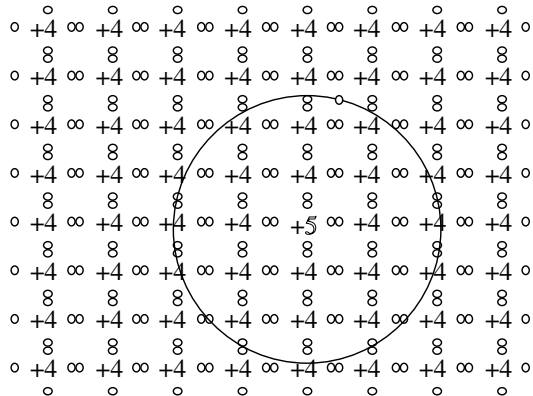


Figure 3.2: n-doped silicon [34].

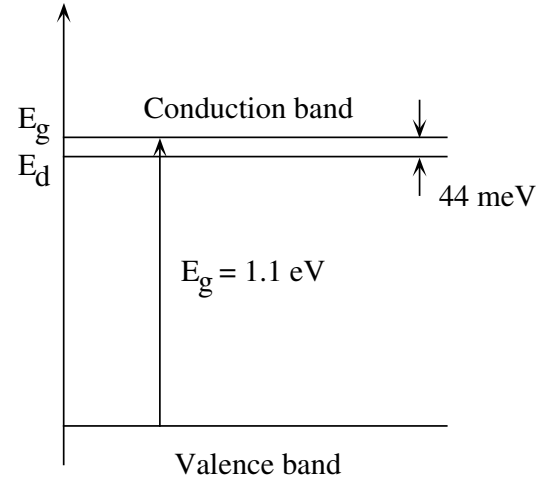


Figure 3.3: n-silicon energy levels.

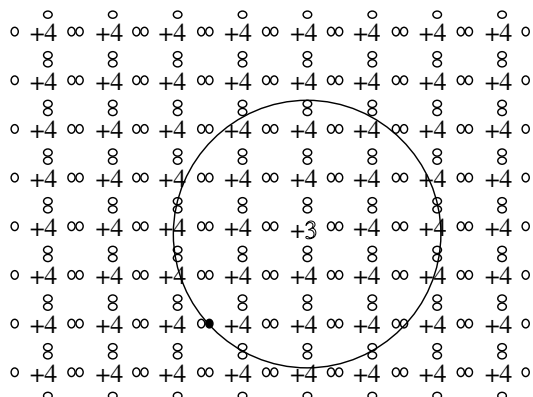


Figure 3.4: p-silicon [34].

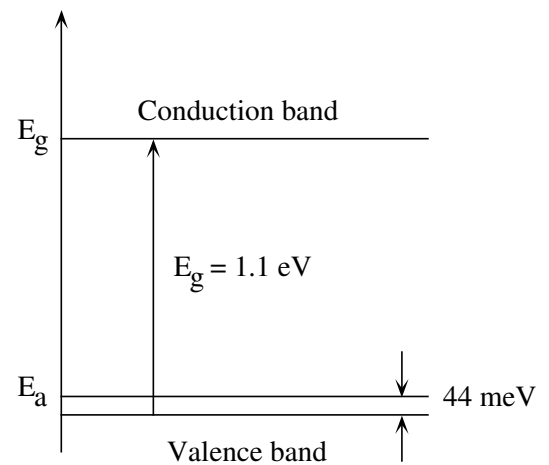


Figure 3.5: p-silicon energy levels.

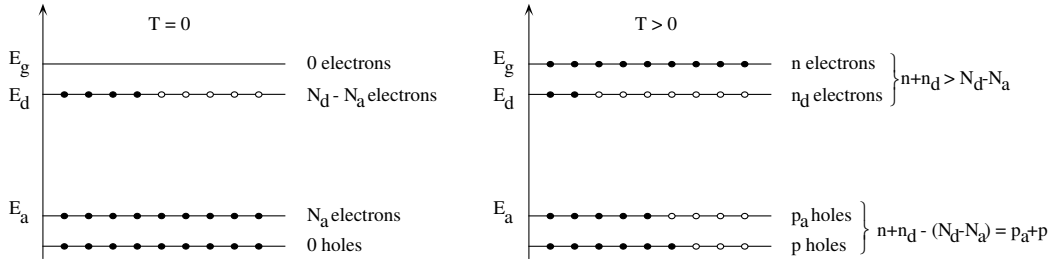
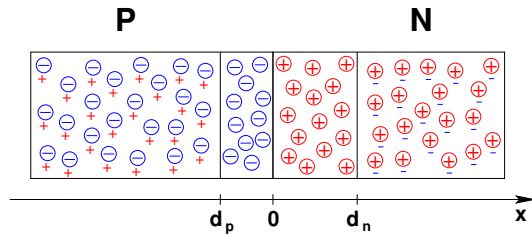


Figure 3.6: Impurity occupation.

Figure 3.7: An ideal simplified p-n junction: \oplus depict acceptor sites, \ominus the donor sites, $+$ the holes and $-$ the electrons.

3.5 The p-n junction

A schematic view of a one-dimensional p-n junction consists in making a contact between a p-type and an n-type semiconductor (figure 3.7). The properties of such a junction will depend on the position along the dimension x considered. We will suppose that the chemical potential μ is much greater than the p-type semiconductor acceptor level, and that it is much lower than the n-type semiconductor donor level, i.e.:

$$E_d - \mu \gg k_b T \quad \mu - E_a \gg k_b T \quad (3.18)$$

In such a case, $n_d \ll N_d$ and $p_a \ll N_a$. As a consequence $n \cong N_d$ and $p \cong N_a$ when far away from the junction.

When the two different semiconductors are put in contact, at the junction there is a strong imbalance in the conduction band and in the valence band: the electrons in the conduction band of the n-side will migrate to the conduction band of the p-side, while the holes in the valence band will travel from the p-side to the n-side. Of course, before the junction is ideally realized, both pieces are electrically neutral, and the charge migration creates a local polarisation in the vicinity of the junction: there will be a potential $\phi(x)$ across the junction. Because of this potential, the amount of electrons and holes change, and expressions (3.14) and (3.15) will become:

$$n = n_0 \exp \left(\frac{\mu - E_g + q \cdot \phi(x)}{k_b T} \right) \quad (3.19)$$

$$p = p_0 \exp \left(-\frac{\mu + q \cdot \phi(x)}{k_b T} \right) \quad (3.20)$$

where q is the elementary charge. Far away from the junction, the semiconductor has the same properties as before, thus $N_d \cong n(\infty)$ and $N_a \cong p(-\infty)$. As at thermal equilibrium the chemical potential is the same in the whole semiconductor, we deduce:

$$q \cdot (\phi(\infty) - \phi(-\infty)) = E_g + k_b T \ln \left(\frac{N_d N_a}{n_0 p_0} \right) \quad (3.21)$$

which is of the order of E_g . Moreover:

$$n = N_d \exp \left(-\frac{q \cdot (\phi(\infty) - \phi(x))}{k_b T} \right) \quad (3.22)$$

$$p = N_a \exp \left(-\frac{q \cdot (\phi(x) - \phi(-\infty))}{k_b T} \right) \quad (3.23)$$

This means that in an area near the junction the density of mobile charge carriers is reduced (at room temperature, for silicon, $\frac{E_g}{k_b T} \cong 44$). This region is called the *depletion zone*.

Now we can find the potential behaviour, using Poisson's equation and the charge density $\rho(x)$:

$$-\nabla^2 \phi = \frac{\rho(x)}{\epsilon \epsilon_0} \quad (3.24)$$

$$\rho(x) = q \cdot (N_d(x) - N_a(x) - n(x) + p(x)) \quad (3.25)$$

As $n \ll N_d$ and $p \ll N_a$ in the depletion area, we derive an approximate expression for the charge density:

$$\frac{\rho(x)}{q} = \begin{cases} 0 & x \geq d_n \\ N_d & x \in [0; d_n[\\ -N_a & x \in [-d_p; 0[\\ 0 & x < -d_p \end{cases} \quad (3.26)$$

Where d_p and d_n represent the depletion zone limits in the p- and n-side respectively. The solution of equation (3.25) is:

$$\phi(x) = \begin{cases} \phi(\infty) & x \geq d_n \\ \phi(\infty) - \frac{q N_d d_n^2}{2 \epsilon \epsilon_0} \cdot \left(1 - \frac{x}{d_n} \right)^2 & x \in [0; d_n[\\ \phi(-\infty) + \frac{q N_a d_p^2}{2 \epsilon \epsilon_0} \cdot \left(1 + \frac{x}{d_p} \right)^2 & x \in [-d_p; 0[\\ \phi(-\infty) & x < -d_p \end{cases} \quad (3.27)$$

To find the expressions of the depletion zone limits, we need to apply the boundary conditions:

$$\lim_{\substack{x \rightarrow 0 \\ x < 0}} \phi(x) = \lim_{\substack{x \rightarrow 0 \\ x > 0}} \phi(x) \quad (3.28)$$

$$\lim_{\substack{x \rightarrow 0 \\ x < 0}} \phi'(x) = \lim_{\substack{x \rightarrow 0 \\ x > 0}} \phi'(x) \quad (3.29)$$

The depletion zone is limited by:

$$d_n = \sqrt{\frac{2 \epsilon \epsilon_0 (\phi(\infty) - \phi(-\infty))}{q N_d \left(1 + \frac{N_d}{N_a} \right)}} \quad (3.30)$$

$$d_p = \sqrt{\frac{2 \epsilon \epsilon_0 (\phi(\infty) - \phi(-\infty))}{q N_a \left(1 + \frac{N_a}{N_d} \right)}} \quad (3.31)$$

Finally, the electric field inside the diode is:

$$E(x) = \begin{cases} 0 & x \geq d_n \\ -\frac{eN_a d_n}{\epsilon \epsilon_0} \cdot \left(1 - \frac{x}{d_n}\right) & x \in [0; d_n[\\ -\frac{eN_a d_p}{\epsilon \epsilon_0} \cdot \left(1 + \frac{x}{d_p}\right) & x \in [-d_p; 0[\\ 0 & x < -d_p \end{cases} \quad (3.32)$$

Figure 3.5 summarizes the evolution of dopant concentration, space charge density, free carrier density, potential and electric field along the junction.

3.5.1 Diode current

The electronic device constituted by a p-n junction is called “diode”. We examine the current flowing through a diode when a voltage is applied across the junction. We have seen that a potential was already established when two differently doped semiconductors were put together. Let us now consider a voltage V applied to the n-side of the junction, while the p-side is grounded. The potential difference at the junction is increased by a value V :

$$\Delta\phi = (\phi(\infty) - \phi(-\infty)) + V = (\Delta\phi)_0 + V \quad (3.33)$$

The depletion zone size depends on the applied voltage:

$$d_{n,p}(V) = d_{n,p}(0) \sqrt{1 + \frac{V}{(\Delta\phi)_0}} \quad (3.34)$$

Therefore, the depletion area increases with the voltage. We would like to describe the phenomena which happen in the junction. First we have to distinguish two kinds of current densities:

- the charged particle current density J ;
- the electric charge current density j .

Charge currents due to electrons and holes are expressed respectively as:

$$j_e = -qJ_e \quad j_h = qJ_h \quad (3.35)$$

When $V = 0$, the charge carriers cross the junction from one direction to the other in the same amount, which implies that the total current is zero. When $V \neq 0$, this equilibrium disappears. Let us consider the hole current across the junction: it has two components in the depletion zone:

- in the n-side, holes may be created thanks to thermal excitation. Because of the electric field due to the depletion, the holes will move to the p-side, whatever the potential. This hole current is called the *generation current* and is independent of the potential barrier.

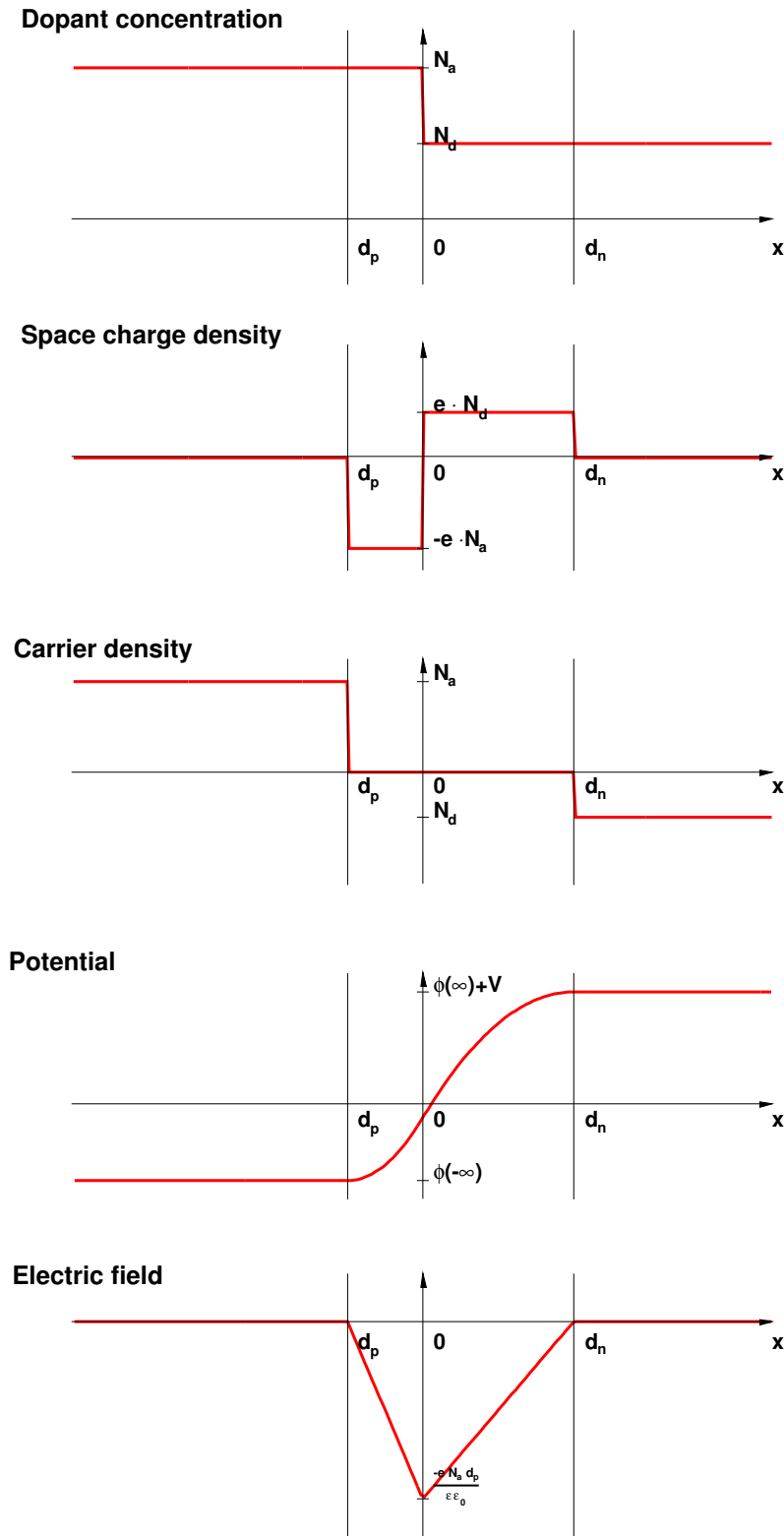


Figure 3.8: Characteristics of a p-n junction, with a positive voltage V applied on the n-side terminal.

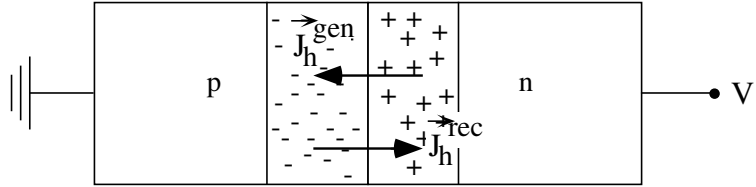


Figure 3.9: Generation and recombination hole currents.

- in the p-side, holes can only cross the junction if the thermal energy is greater than the potential barrier. Holes which reach the n-side have a high probability to recombine with an electron: this current is called the *recombination current*. The number of holes passing through the junction is proportional to $\exp(-q(\Delta\phi)/k_bT)$. Thus,

$$J_h^{rec} \propto \exp\left(-\frac{q((\Delta\phi)_0 + V)}{k_bT}\right) \quad (3.36)$$

At $V = 0$ the total hole current is zero, and we have $J_h^{rec}(V = 0) = J_h^{gen}$. Hence:

$$J_h^{rec}(V) = J_h^{gen} \exp\left(-\frac{qV}{k_bT}\right) \quad (3.37)$$

The total hole current across the junction is:

$$J_h = J_h^{gen} - J_h^{rec} = J_h^{gen} \left(1 - \exp\left(-\frac{qV}{k_bT}\right)\right) \quad (3.38)$$

The same arguments with electrons lead us to the expression of the total *charge* current:

$$j = qJ_h - (-q)J_e = q(J_h^{gen} + J_e^{gen}) \left(1 - \exp\left(-\frac{qV}{k_bT}\right)\right) \quad (3.39)$$

This describes the rectifying effect: when the voltage applied to the n-side is positive, the current is small, and it is called *leakage current*. If the voltage is negative, the current grows exponentially. In the first case, the diode is said to be reverse biased, in the second case we talk of a directly biased diode.

For a fully depleted diode, the explicit form of $J_{h/e}^{gen}$ is:

$$J_{h/e}^{gen} = l \frac{n_i}{\tau_{h/e}} \quad (3.40)$$

where $l = d_p + d_n$ is the depletion zone width, n_i the intrinsic density and $\tau_{h/e}$ is the hole (h) or electron (e) lifetime in the depletion area. Thus (3.39) is expressed as:

$$j = q \cdot l \cdot n_i \left(\frac{1}{\tau_e} + \frac{1}{\tau_h}\right) \left(1 - \exp\left(-\frac{qV}{k_bT}\right)\right) \quad (3.41)$$

This equation holds if the diode is fully depleted. When this is not the case, we have also to consider charge carriers coming from the non-depleted regions.

At room temperature the exponential term, for silicon, is negligible: the temperature dependence in (3.41) is only due to n_i . From (3.8) we find the following relation to normalise measured currents to a temperature T_0 :

$$\frac{j(T)}{j(T_0)} = \left(\frac{T}{T_0}\right)^{3/2} \exp\left(-\frac{E_g}{2k_b} \left(\frac{1}{T} - \frac{1}{T_0}\right)\right) \quad (3.42)$$

As an example, figure 3.10 shows $\frac{j(273.2+\theta)}{j(273.2+\theta_0)}$ where θ is the temperature in $^{\circ}\text{C}$ and $\theta_0 = 20^{\circ}\text{C}$ the reference temperature.

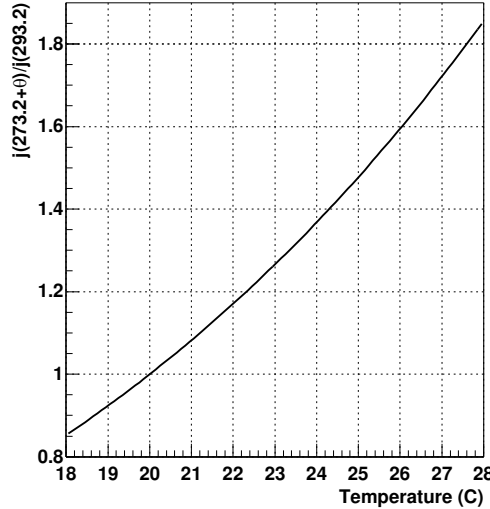


Figure 3.10: Diode leakage current as a function of the temperature (equation 3.42), normalized to 20°C .

3.5.2 The p⁺-n junction

A p-n junction where the acceptor doping is much greater than the donor doping is called a p⁺-n junction. In such a case, $N_a \gg N_d$ and the depletion widths become:

$$d_n = \sqrt{\frac{2\epsilon\epsilon_0(\Delta\phi)}{qN_d}} \quad (3.43)$$

$$d_p = \sqrt{\frac{2\epsilon\epsilon_0(\Delta\phi)N_d}{qN_a^2}} \ll d_n \quad (3.44)$$

We note that d_n depends on the n-side dopant concentration only.

Full depletion - The depletion voltage

We know from equation 3.34 that the width over which the silicon is depleted depends on the applied voltage. It may be interesting to know above what voltage the full p⁺-n junction is depleted. This voltage is known as the *depletion voltage*. It may be easily determined if we measure the reverse biased diode capacitance. To evaluate the diode capacitance, consider an increase dV in the reverse bias. As we examine a p⁺-n diode, with area S , the depletion area will mainly grow in the n-side, to a distance $d(d_n)$. Therefore the additional charge due to dV is:

$$dQ = q\rho(x) \cdot S \cdot d(d_n) = \frac{qN_dS}{2\sqrt{(\Delta\phi)}} \sqrt{\frac{2\epsilon\epsilon_0}{qN_d}} dV \quad (3.45)$$

Thus the capacitance is:

$$C = \frac{dQ}{dV} = \frac{S\epsilon\epsilon_0}{d_n} \quad (3.46)$$

As a consequence, the p⁺-n junction acts like a capacitor with variable capacitance. When the junction is totally depleted (at a voltage V_{depl}), the depletion width ℓ is equal to the diode thickness L :

$$C = \epsilon\epsilon_0 \frac{S}{\ell} = \begin{cases} \sqrt{\frac{qN_d\epsilon\epsilon_0 S^2}{2(\Delta\phi)}} & V < V_{depl} \\ \epsilon\epsilon_0 \frac{S}{L} & V \geq V_{depl} \end{cases} \quad (3.47)$$

When $V \gg (\Delta\phi)_0$, the depletion voltage is:

$$V_{depl} = \frac{qN_d L^2}{2\epsilon\epsilon_0} \quad (3.48)$$

If the thickness is known, one can compute the impurity density N_d , and hence the bulk resistivity:

$$\rho = \frac{1}{q\mu_e N_d} = \frac{L^2}{2\epsilon\epsilon_0 V_{depl} \mu_e} \quad (3.49)$$

where μ_e is the electron mobility (1350 cm²/V·s for silicon). In the case e.g. of a 300 μm-thick n-type silicon substrate with 50 V measured depletion voltage, $N_d \cong 7.2 \cdot 10^{11} \text{ cm}^{-3}$ and the resistivity is $\rho \cong 6.4 \text{ k}\Omega\cdot\text{cm}$.

3.6 The p-n₁-n₂ junction

We consider now the case where the n-side presents two different dopings, i.e. the charge density is:

$$\frac{\rho(x)}{q} = \begin{cases} 0 & x \geq d_n \\ N_e & x \in [\ell; d_n[\\ N_d & x \in [0; \ell[\\ -N_a & x \in [-d_p; 0[\\ 0 & x < -d_p \end{cases} \quad (3.50)$$

Where ℓ represents the n₁-area thickness. Obviously, as long as the applied voltage is such that $d_n < \ell$, the diode behavior is the same as the standard p-n junction. We will thus focus on the case $d_n \geq \ell$. Solving Poisson's equation (3.25) leads to following expression of the potential $\phi(x)$:

$$\phi(x) = \begin{cases} \phi(\infty) + V & x \geq d_n \\ \phi(\infty) + V - \frac{qN_e d_n^2}{2\epsilon\epsilon_0} \cdot \left(1 - \frac{x}{d_n}\right)^2 & x \in [\ell; d_n[\\ \phi(\infty) + V - \frac{qN_d \ell^2}{2\epsilon\epsilon_0} \cdot \left(1 - \frac{x}{\ell}\right)^2 + \frac{qN_e}{2\epsilon\epsilon_0} \cdot (d_n - \ell)(2x - d_n - \ell) & x \in [0; \ell[\\ \phi(-\infty) + \frac{qN_a d_p^2}{2\epsilon\epsilon_0} \cdot \left(1 + \frac{x}{d_p}\right)^2 & x \in [-d_p; 0[\\ \phi(-\infty) & x < -d_p \end{cases} \quad (3.51)$$

Applying the standard boundary conditions at $x = 0$ (3.28, 3.29) leads to following relation:

$$N_d\ell + N_e(d_n - \ell) = N_a d_p \quad (3.52)$$

and the depletion widths are expressed as:

$$d_n = \frac{-\ell \frac{N_e}{N_a} (N_d - N_e) + \sqrt{\Delta}}{N_e \left(1 + \frac{N_e}{N_a}\right)} \quad (3.53)$$

$$d_p = \frac{\ell(N_d - N_e) + \sqrt{\Delta}}{N_a \left(1 + \frac{N_e}{N_a}\right)} \quad (3.54)$$

where

$$\Delta = N_e \ell^2 (N_e - N_d) \left(1 + \frac{N_d}{N_a}\right) + N_e \left(1 + \frac{N_e}{N_a}\right) (\Delta\phi) \frac{2\epsilon\epsilon_0}{q} \quad (3.55)$$

and $(\Delta\phi) = V + \phi(\infty) - \phi(-\infty)$. To check the consistency of the result, we can determine the voltage $(\Delta\phi)_{depl}$ such that $d_n = \ell$:

$$d_n = \ell \Leftrightarrow \ell N_e \left(1 + \frac{N_d}{N_a}\right) = \sqrt{\Delta} \quad (3.56)$$

$$\Leftrightarrow \ell = \sqrt{\frac{2\epsilon\epsilon_0(\Delta\phi)_{depl}}{q N_d \left(1 + \frac{N_d}{N_a}\right)}} \quad (3.57)$$

which corresponds to the expression of d_n for the p-n junction (3.30).

The electric field is:

$$E(x) = \begin{cases} 0 & x \geq d_n \\ \frac{qN_e}{\epsilon\epsilon_0} \cdot (x - d_n) & x \in [\ell; d_n[\\ \frac{qN_d}{\epsilon\epsilon_0} \cdot (x - \ell) - \frac{qN_e}{\epsilon\epsilon_0} \cdot (d_n - l) & x \in [0; \ell[\\ -\frac{qN_a}{\epsilon\epsilon_0} \cdot (x + d_p) & x \in [-d_p; 0[\\ 0 & x < -d_p \end{cases} \quad (3.58)$$

3.6.1 The p⁺-n-n⁺ junction

As it will be mentioned in section 3.8.1, the microstrip detectors are composed of p⁺-n junctions, while the surface of the n-side is heavily doped, thus presenting a p⁺-n-n⁺ structure. Considering the results of section 3.6, with $d_n \geq \ell$, we assume that $N_d \ll N_e$ and $N_d \ll N_a$. As a consequence, the expression of $\sqrt{\Delta}$ can be approximated, leading to the following simple results:

$$d_n - \ell \cong \frac{\ell N_d}{2 N_e} \left(\frac{(\Delta\phi)}{(\Delta\phi)_{depl}} - 1 \right) \quad (3.59)$$

$$d_p \cong \frac{\ell N_d}{2 N_a} \left(\frac{(\Delta\phi)}{(\Delta\phi)_{depl}} + 1 \right) \quad (3.60)$$

In particular, the electric field inside the n-area only depends on N_d and becomes:

$$E(x) = \frac{2(\Delta\phi)_{depl}}{\ell^2} - \frac{1}{\ell} ((\Delta\phi) - (\Delta\phi)_{depl}) \quad (x \in [0; \ell] \quad (\Delta\phi) \geq (\Delta\phi)_{depl}) \quad (3.61)$$

which means that

$$E(0) = -\frac{1}{\ell}((\Delta\phi) + (\Delta\phi)_{depl}) \quad (3.62)$$

$$E(\ell) = -\frac{1}{\ell}((\Delta\phi) - (\Delta\phi)_{depl}) \quad (3.63)$$

The field is the most intense at the junction level. Before the depletion voltage is reached, the field at the junction level is expressed as:

$$E(0) = -\frac{2}{\ell}\sqrt{(\Delta\phi) \cdot (\Delta\phi)_{depl}} \quad (3.64)$$

which only depends on N_d .

As an example, figure 3.11 illustrates the field evolution as a function of the applied voltage. Here we suppose $N_d = 7.2 \cdot 10^{11} \text{ cm}^{-3}$, $N_a = 10^3 \cdot N_d$ and $\ell = 300 \mu\text{m}$ (i.e. $V_{depl} = 50 \text{ V}$). Clearly, in such a configuration, the depletion area expansion rate drastically decreases as soon as the n^+ area is reached, while the electric field still increases.

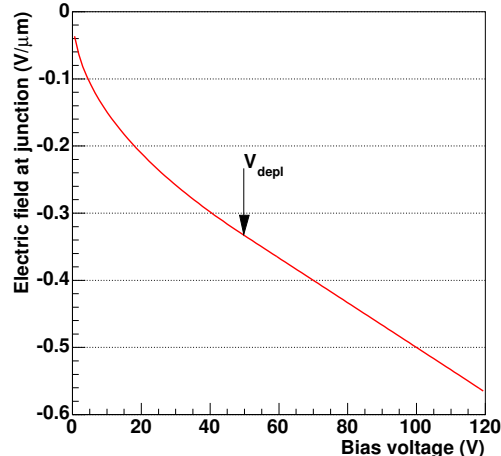


Figure 3.11: Electric field at the junction level, for a p^+ -n-n $^+$ configuration, as a function of the bias voltage, with $N_d = 7.2 \cdot 10^{11} \text{ cm}^{-3}$ and $\ell=300\mu\text{m}$.

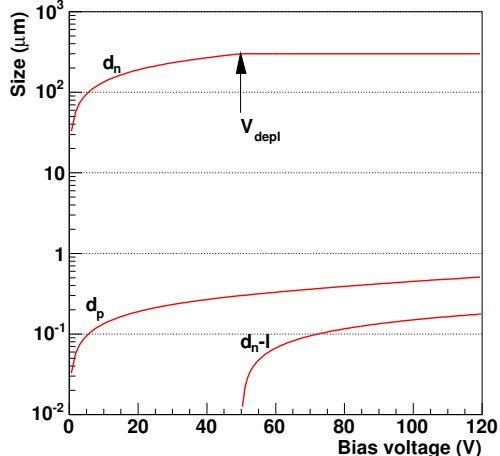


Figure 3.12: Depletion widths of a p^+ -n-n $^+$ configuration, as a function of the bias voltage, with $N_d/N_a = N_d/N_e = 10^{-3}$, $N_d = 7.2 \cdot 10^{11} \text{ cm}^{-3}$ and $\ell=300\mu\text{m}$.

3.7 Breakdown

In the reverse bias mode, a junction cannot indefinitely withstand an arbitrary voltage: when the electric field is too high, the current will steeply increase. This situation is called the breakdown; three different phenomena may originate a breakdown:

- Thermal instability: at high voltages, the heat produced by the current makes the latter increase, which in turn implies an increase of the dissipated heat. This situation will at the end cause the junction break down. This effect appears for semiconductors with small band gap widths like germanium.

- Tunneling effect: a tunnelling current may appear in silicon if the field is around 10^6 V/cm. Such a situation is possible when both the p and n sides are highly doped. In such a case, the depletion region width is at most of the order of 500 Å. The tunnelling effect is known to appear at voltages under about $4E_g/q$, i.e. 4.4 V for p⁺-n⁺ silicon junctions. The tunnelling breakdown voltage decreases when the temperature increases.
- Avalanche multiplication: this phenomenon appears with electric fields of about 10^5 V/cm (10 V/ μ m). The principle is similar to gas discharges: minority carriers of thermal origin acquire an energy high enough to ionise crystal atoms. An electron-hole pair is thus created and accelerated by the electric field, and it may ionise an atom. Breakdown effects above $6E_g/q$ (i.e. 6.6 V for silicon) are due to avalanche effects. The breakdown voltage due to avalanche multiplication increases with temperatures.

3.8 The silicon microstrip detectors

3.8.1 Single-sided microstrip detectors

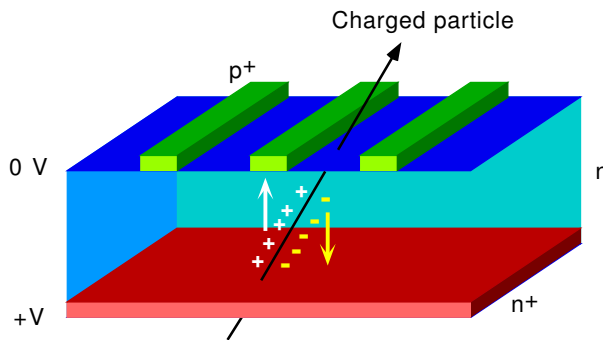


Figure 3.13: Schematic view a single-sided microstrip detector.

A single-sided microstrip detector is composed of an n-doped silicon bulk, covered with longitudinal heavily p-doped silicon strips (fig. 3.13). The detector is thus composed of an array of p⁺-n diodes. On the other side of the silicon bulk, commonly called backplane, there is a heavily n-doped layer, which allows a better ohmic contact with an aluminium deposit. In addition, this n⁺ layer prevents the depletion zone from reaching the aluminium layer [35].

A thin silicon oxide (SiO₂) layer is deposited on the bulk surface between each strip, allowing the silicon surface atoms to perform all their possible bonds [36]. The surface state density, which plays a role in the surface leakage currents and breakdown, is thus under control. Figure 3.14 is a schematic view of such a detector.

The microstrip detector is operated at full depletion, or even at over-depletion. When a charged particle passes through the depleted detector, electron-hole pairs are created along the particle trajectory, inducing an electric signal at the nearest p⁺ strips with respect to the backplane. Because of the electric field in the depleted area, the holes travel to the p⁺

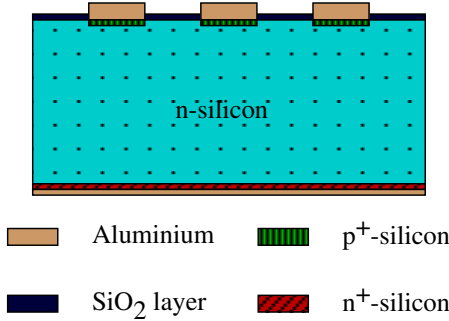


Figure 3.14: Cross section of a single-sided microstrip detector.

strips, whereas the electrons travel to the n⁺ side. The signals are then amplified and sent to appropriate front-end electronics.

All around the strips there is a p⁺ implant named guard ring. Its role is to limit edge and surface currents [37, 38].

The detector thickness is a compromise between two constraints:

- It must not be excessive, else secondary particles may be created, also multiple scattering may occur;
- It must be sufficiently large to allow the creation of enough electron-hole pairs, ensuring a proper amplitude value.

An adequate value seems to be around 300 μm [36]. The most probable energy loss in silicon for a minimum ionizing particle is 262 eV/ μm [7]. As 3.6 eV are needed to create an electron-hole pair [35], a minimum ionizing particle will produce a most probable value of ~ 22000 pairs in a 300 μm thick detector.

The presence of the oxide layer on the silicon bulk has some drawbacks: to compensate the unavoidable presence of positively charged impurities in the oxide, a negatively charged layer at the SiO₂-Si interface will accumulate in the silicon bulk [36]. The following phenomena result from its presence [39]:

- The interstrip capacitance between the p⁺ strips will be larger, increasing the signal noise;
- In the proximity of the p⁺ strips, the electric field is increased, inducing higher leakage current or breakdowns at lower voltages.

In order to have a good resolution, the charge division over the strips must be limited thus requiring high bulk resistivity [35], i.e. of the order of 10 k $\Omega\cdot\text{cm}$ implying low doping (about 10¹¹ cm⁻³).

3.8.2 Double-sided microstrip detectors

In order to measure the particle position in a plane, two measurements are needed, one for each dimension. It is possible to use two single-sided microstrip detectors in a back-

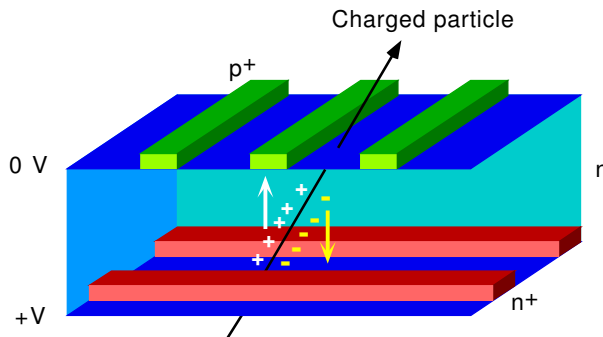


Figure 3.15: Schematic view of a double-sided microstrip detector.

to-back configuration, but this would inevitably increase the overall material budget for multiple scattering. Double-sided microstrip detectors have been developed, replacing the n^+ homogeneous layer with n^+ strips, orthogonal to the p^+ strips or slightly tilted with respect to the p^+ strips. However, just adding n^+ strips is not sufficient. As negative charges are present in the bulk near the SiO_2 layer, the resistance between neighbouring n^+ strips is reduced to some $k\Omega$, whereas it is of the order of $100 \text{ M}\Omega$ on the p-side [40]. One solution to this problem is to insert between each n^+ strip a p^+ strip (called “p-stop”), which will ensure proper strip insulation (figure 3.16).

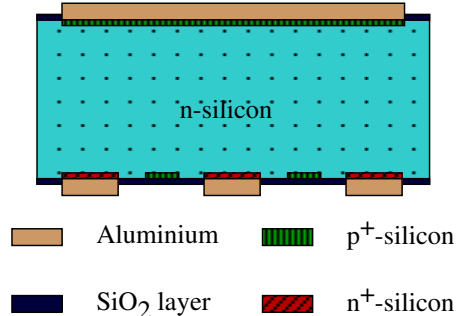


Figure 3.16: Double-sided microstrip detectors: p-stop strips are inserted between n^+ strips.

The functioning of the n-side is slightly different from the p-side, as the charges collected are carried by electrons. The consequences are multiple. As electrons have a greater mobility than holes, the former are more sensitive to magnetic fields; also charge collection is faster for electrons than for holes. Moreover, the electric field in the silicon bulk increases from the n- to the p-side. Therefore the electrons are collected in the low field area, and are more subject to diffusion, implying a possible loss of resolution [41].

3.8.3 Detector operation

As mentioned earlier, the detector is operated at least at full depletion. To this purpose, one solution is to ground all strips and positively bias the n-side. The biasing may be realized

through the preamplifier readout channels (DC coupling configuration). This solution has drawbacks: only the strips connected to the readout electronics are biased, forbidding the use of intermediate strips. Furthermore channels with too high a leakage current may saturate the amplifier [42].

Instead of making a direct contact to each strip, solutions to bias all the strips via a reduced number of contacts on the detector exist. In such a case, an AC coupling can be envisaged: a capacitor is connected between the strips and the amplifiers. The capacitor is either implemented on the electronics board, or directly on the silicon detector strips (AC-detectors). We now enumerate the different strategies to bias a detector.

Punch-through

The punch-through technique allows to resistively connect each strip to the guard ring [36, 42, 37] through the bulk n-silicon. Figure 3.17 shows a schematic: The guard ring is grounded

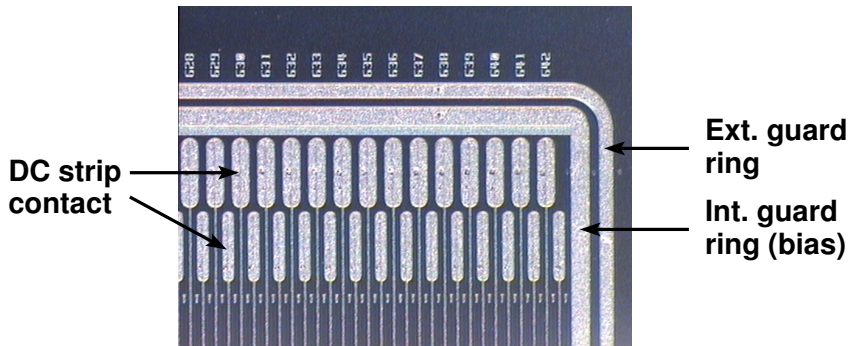


Figure 3.17: A microstrip detector with the punch-through method.

and the strips are “floating” i.e. biased, but not directly connected. When the voltage applied to the backplane increases, the guard ring depletion zone extends and eventually merges with the strip depletion zones (figures 3.18 and 3.19). As the strips are floating, they are nearly at the same potential as the bulk silicon. After the depletion areas have merged, the strips will be forward biased with respect to the bulk, and the guard ring reverse biased. As a consequence, a hole current from the strips to the guard ring appears as there is no barrier against holes at the reverse junction. This *punch through* current charges the strips, spreading the strip depletion volume (figure 3.20).

The punch-through current stops as soon as the strips are charged enough to establish a potential barrier to retain holes. Subsequent voltage increases will extend the depletion zone, while the potential difference between the guard ring and the strips will remain practically constant. With this method all the strips are at the same voltage, though not directly connected: this is necessary to ensure correct functioning of the charge division process. Besides, as the guard ring is biased, the depletion zone will extend beyond the outermost strips.

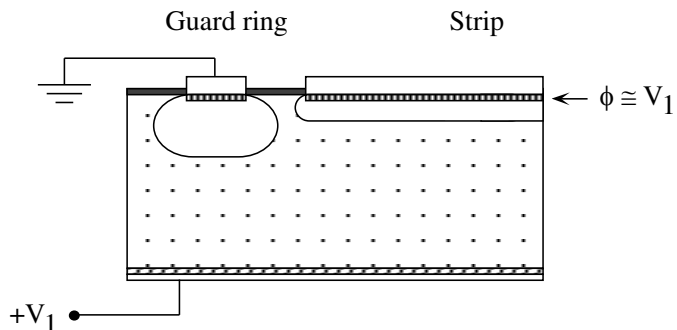


Figure 3.18: Depletion zones before merging.

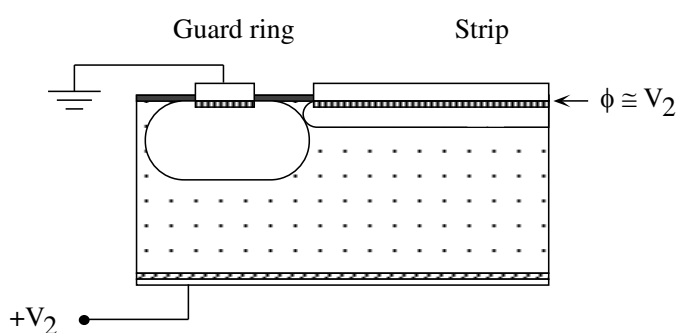
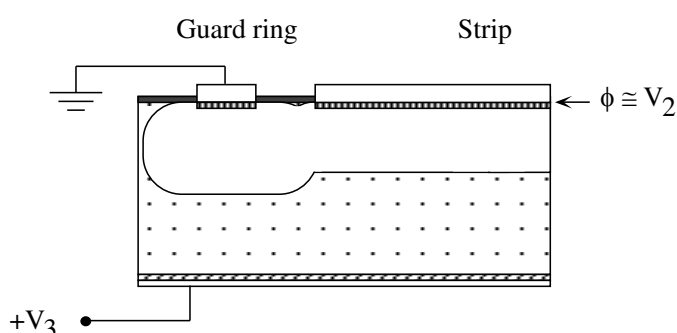
Figure 3.19: Reach through voltage V_2 : Depletion zones merge.

Figure 3.20: Depletion zones after merging (full depletion not yet reached).

FOXFET detectors

To improve the polarization resistance control, a metallization layer, the gate, can be deposited between the guard ring and the strips [43], as schematically shown in figure 3.22. This structure corresponds to a MOSFET (figure 3.21): a negative voltage applied to the gate induces a depletion of the free charge carriers, thus creating a voltage controlled resistance between the two p⁺ implants (source and drain). On the p-side of a microstrip detector, the source is the bias, while each strip is a drain. The function of the gate is to have a good and uniform control on the strip polarization resistances: with a negative gate voltage, the electrons accumulated at the Si-SiO₂ interface will be repelled.

For double-sided detectors, a similar principle is possible for the n-side, between the n⁺ guard ring and the n⁺ strips.

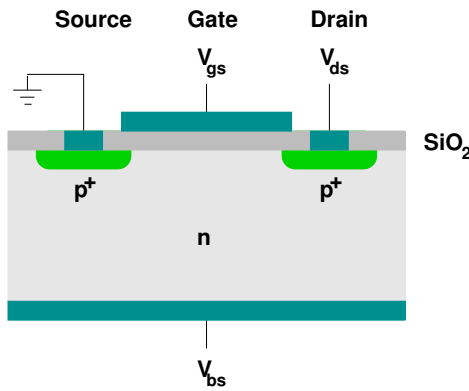


Figure 3.21: Cross section of a MOSFET. To induce a charge carrier depletion, a negative voltage is applied.

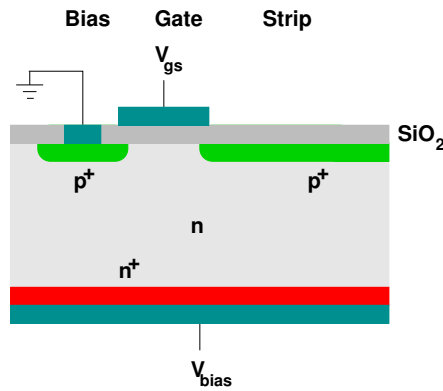


Figure 3.22: Cross section of a FOXFET detector. The gate voltage is negative, the bias voltage is positive.

Polysilicon resistors

Polysilicon resistors may be implemented between the strips and a metallized ring (bias or bus) onto which the bias voltage will be applied [36]. Figure 3.23 shows a BaBar detector, which presents this operating method. Note that this detector is a double-sided detector (see section 3.8.2).

N-side connection

For single-sided detectors, a positive voltage is applied on the n⁺ backplane. If the detector is double-sided, the voltage is applied on an n⁺ bias ring. The biasing methods on the n-side are similar to the p-side. One option is to connect the n⁺ strips to a biased ring through polysilicon resistors. Another solution is to implement an n⁺ guard ring as for the p-side. Nevertheless, the resistance between strip and the guard ring is low, because of the doping and of the negative charges at the SiO₂-Si interface. This induces a greater leakage current between strips and guard ring.

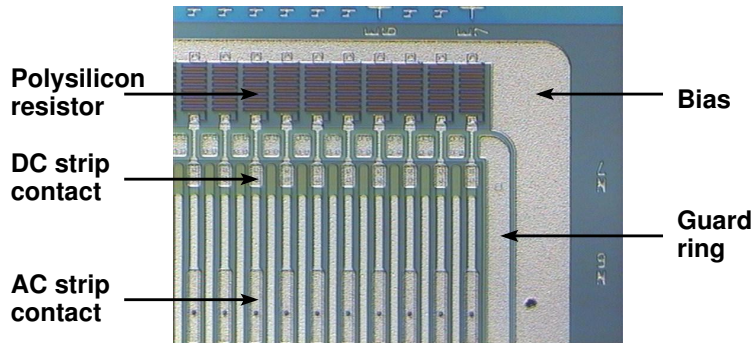


Figure 3.23: p-side view of a BaBar detector, note that this is a double-sided detector.

To obtain a higher resistance many solutions are available. First the distance between the guard ring and strips is widened, in order to increase the resistance. In addition, the p^+ implants are designed to reduce the guard-strip currents. As an example, figure 3.24 presents the solution retained for the ALEPH silicon detector [42, 41].

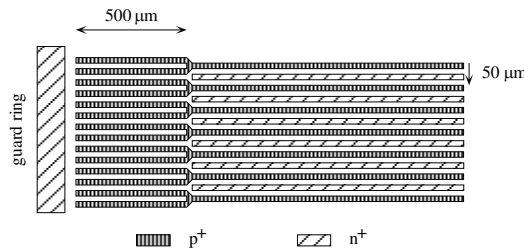


Figure 3.24: p-stop design of the ALEPH silicon microstrip detector.

Finally, a FOXFET type connection is also possible.

3.9 Silicon detector modules, ladders

A silicon microstrip detector alone is not enough to detect a particle: once the charge has been released, front-end electronics are necessary to read out the signals. Usually, the electronics board consists of decoupling capacitors (if the sensors are of DC-type) and preamplifiers. Thus a module will be composed of the silicon detectors, the readout electronics and the appropriate mechanics.

Arrays of silicon detectors with daisy chained strips (i.e. the strips of neighbour sensors are connected together, as schematically shown in figure 3.25) are called *ladders*. This configuration allows for a larger detection surface while limiting the number of readout channels, provided the occupancy is low. (see fig. 3.25). In the case of AMS ladders, the length varies in a range from 7 to 15 sensors.

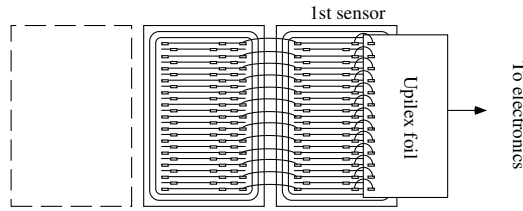


Figure 3.25: On a ladder the strips are daisy chained, increasing the detection surface while limiting the number of readout channels

3.10 Charge sharing and capacitive coupling

This topic is closely related with spatial resolution and signal collection efficiency. To illustrate the discussion we consider a microstrip detector with a strip pitch p , crossed by a minimum ionizing particles impinging perpendicular to the detector surface. We consider also that only one strip collects the charge released by the particle passage. For a homogeneous energy deposit, the spatial resolution is expressed as:

$$\sigma^2 = \frac{1}{p} \int_{-\frac{p}{2}}^{\frac{p}{2}} x^2 \cdot dx = \frac{p^2}{12} \quad (3.65)$$

In this case, the resolution does not depend on the readout method (digital or analogies). The resolution is improved if the readout pitch decreases to the order of the charge diffusion width, which in case of a MIP is about $20 \mu\text{m}$. In such a case, the charge is shared between two strips, and calculating the center of gravity of the total signal will allow to improve the spatial resolution.

Nonetheless this solution is only possible in case the readout pitch corresponds to the implantation pitch, which in addition is considerably small. Such a configuration imposes important mechanical constraints, as well as high density of readout electronics. With large scale experiments, where power consumption and volume occupation are a concern, such a high readout density is unacceptable and other solutions have to be envisaged to reconcile spatial resolution with reasonable readout channel numbers.

The limitation of readout electronics imposes an increase of the readout pitch. Nevertheless, this does not necessarily imply a degradation of the spatial resolution, if the capacitive coupling between adjacent strips is taken into account. Indeed this method enables to get a very good resolution with a readout pitch larger than the implant pitch. In the best cases, it has been shown that a resolution of $10 \mu\text{m}$ could be achieved with up to $200 \mu\text{m}$ readout pitch (but electronics with a high S/N is also needed) [44, 45].

3.10.1 Capacitive coupling

Figure 3.26 illustrates a detector where half of the strips are read out. A simplistic approach describes the process: a charge Q is released at strip n and via the interstrip capacitance C_i a charge $Q/2$ is transmitted to the neighbouring readout strips. As the capacitance C_c to

the electronics is much larger than the interstrip coupling, nearly no charge is transmitted to the second neighbouring strip. Thus, the total signal received by electronics corresponds to a charge Q . It is important to note that the intermediate strips are also biased. In the opposite case, the capacitive charge sharing would be inefficient [46].

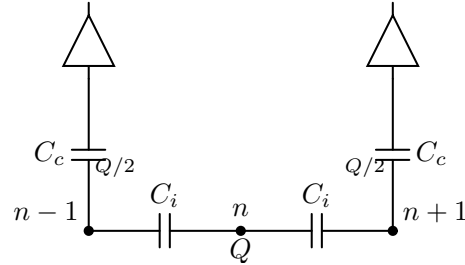


Figure 3.26: A charge released at the intermediate strip n is transferred to the neighbouring strips connected to readout electronics ($n - 1$ and $n + 1$).

This model can be generalized to more intermediate strips. In the case of the AMS detector, on the p-side, the implant pitch is $27.5 \mu\text{m}$, while the readout pitch is $110 \mu\text{m}$, i.e. three intermediate strips separate the readout strips. In such a case (fig. 3.27), we realize that the coupling of the center strip with the closest readout strip $C_l = C_r \approx \frac{C_i}{2}$ while for strips 2 and 4, the couplings are $C_l \approx C_i$ and $C_r \approx \frac{C_i}{3}$. Under the condition of an analogue readout, it is then possible, by interpolation, to more precisely locate the passage of the crossing particle.

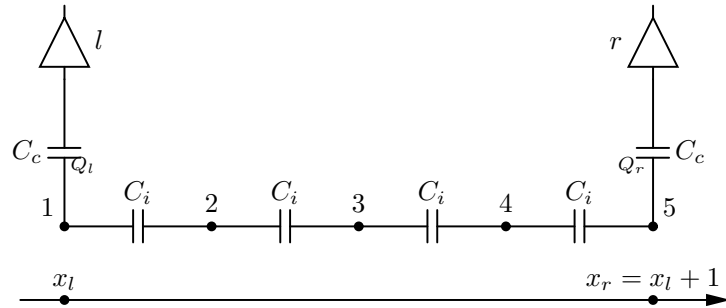


Figure 3.27: A configuration with three intermediate strips.

Taking into account the signals collected by the two amplifiers, it is thus possible to evaluate the original signal position, by computation of the center of gravity: If Q is the charge deposited on strip n , we define as Q_l and Q_r the charges transmitted to the left and right readout channels, respectively. Using the relation

$$\frac{Q_l}{C_l} = \frac{Q_r}{C_r} \quad (3.66)$$

where C_l and C_r correspond to the capacitance between the intermediate strip n and the left

(right) readout strip respectively. The center of gravity is then expressed as:

$$cog = \frac{Q_l x_l + Q_r x_r}{Q_l + Q_r} = \frac{Q_l x_l + Q_r(x_l + 1)}{Q} \quad (3.67)$$

where x is the position expressed in readout pitch units. If the charge is released on the central strip then

$$\left. \begin{array}{l} C_l = C_r \\ Q_l = Q_r \end{array} \right\} \Rightarrow cog = x_l + 0.5 \quad (3.68)$$

If Q was collected by a non-center intermediate strip, e.g. strip 2, then

$$\frac{Q_l}{C_i} = \frac{Q_r}{\frac{1}{3}C_i} \Rightarrow Q_l = 3Q_r \quad (3.69)$$

thus

$$cog = \frac{Q_l x_l + Q_r x_r}{Q_l + Q_r} = \frac{3Q_r x_l + Q_r(x_l + 1)}{4Q_r} = x_l + \frac{1}{4} \quad (3.70)$$

which is the correct position.

3.10.2 Charge sharing

The center of gravity is expressed as

$$cog = \frac{Q_l x_l + Q_r(x_l + 1)}{Q_l + Q_r} = \frac{Q x_l + Q_r}{Q} = x_l + \frac{Q_r}{Q} \quad (3.71)$$

Now let us include to this simplified model the charge sharing between two adjacent strips. We assume that the diffusion process spreads the released charges to a width of $\sim 20 \mu\text{m}$ [44], and that the implant pitch is of the same order, e.g. $25 \mu\text{m}$. We suppose that there are N intermediate strips, with an implant pitch p . In most of the cases, the charge released by the traversing particle will be shared between the neighbouring strips m and $m + 1$: $Q_{tot} = Q_m + Q_{m+1}$. If x denotes the particle impact position, we define:

$$\alpha(x) = \frac{Q_{m+1}(x)}{Q_{tot}} \quad (3.72)$$

$$\Rightarrow cog = x_l + \alpha(x) \cdot \frac{Q_r}{Q_{m+1}} \quad (3.73)$$

The charges collected by strips m and $m + 1$ induce charges on the strips connected to the readout electronics. The charge collected on the left and right readout channels are thus the sum of the contributions of strips m and $m + 1$:

$$Q_l = Q_{m,l} + Q_{m+1,l} \quad (3.74)$$

$$Q_r = Q_{m,r} + Q_{m+1,r} \quad (3.75)$$

Using relation 3.66 we get

$$Q_{j,r} = Q \cdot \left(1 + \frac{C_l}{C_r}\right)^{-1} \text{ with } j = m, m + 1 \quad (3.76)$$

The expression of the center of gravity (3.67) becomes:

$$cog = x_l + \frac{1}{Q} \cdot \sum_{j=m}^{m+1} Q_j \left(1 + \frac{C_{j,l}}{C_{j,r}}\right)^{-1} \quad (3.77)$$

For a strip j , the couplings $C_{j,l}$ and $C_{j,r}$ can be expressed as:

$$C_{j,l} = \frac{C_i}{j-1} \quad (3.78)$$

$$C_{j,r} = \frac{C_i}{N+2-j} \quad (3.79)$$

Thus

$$cog = x_l + \frac{1}{Q \cdot (N+1)} \sum_{j=m}^{m+1} Q_j(j-1) \quad (3.80)$$

$$= x_l + \frac{m-1+\alpha(x)}{N+1} \quad (3.81)$$

As $x_m = x_l + p \cdot (m-1)$, and $p \cdot (N+1) = 1$,

$$cog = x_m + p \cdot \alpha(x) \quad (3.82)$$

We now define an expression for $\alpha(x)$. A particle impacting the detector at position x will produce a detected charge tube with a width δ (see figure 3.28). The charge carriers

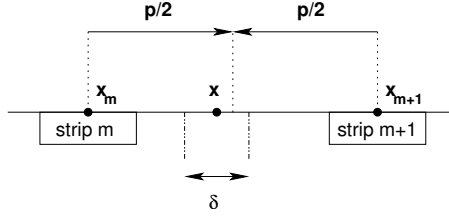


Figure 3.28: Simple model of charge sharing. x is particle impact coordinate.

located at a position $x < x_m + p/2$ will accumulate on strip m , else they will be collected by strip x_{m+1} . Thus following expression of $\alpha(x)$:

$$\alpha(x) = \begin{cases} 1 & x > x_m + \frac{1}{2}(p+\delta) \\ \frac{1}{\delta}(x-x_m) + \frac{1}{2\delta}(\delta-p) & x \in [x_m + \frac{1}{2}(p-\delta); x_m + \frac{1}{2}(p+\delta)] \\ 0 & x < x_m + \frac{1}{2}(p-\delta) \end{cases} \quad (3.83)$$

As a consequence, the center of gravity expression becomes:

$$cog = \begin{cases} x_{m+1} & x > x_m + \frac{1}{2}(p+\delta) \\ x_m + \frac{p}{\delta}(x-x_m) + \frac{p}{2\delta}(\delta-p) & x \in [x_m + \frac{1}{2}(p-\delta); x_m + \frac{1}{2}(p+\delta)] \\ x_m & x < x_m + \frac{1}{2}(p-\delta) \end{cases} \quad (3.84)$$

Figure 3.29 shows the correspondence between the impact coordinate x and the center of gravity for a detector with 3 intermediate strips, and various tube widths with respect to the pitch, for $x \in [0, 1]$. In particular, the center of gravity corresponds to the impact position if $\delta = p$.

Those examples rely on three simplifications:

1. the only relevant couplings are the interstrip capacitance C_i , thus no charge loss is considered,

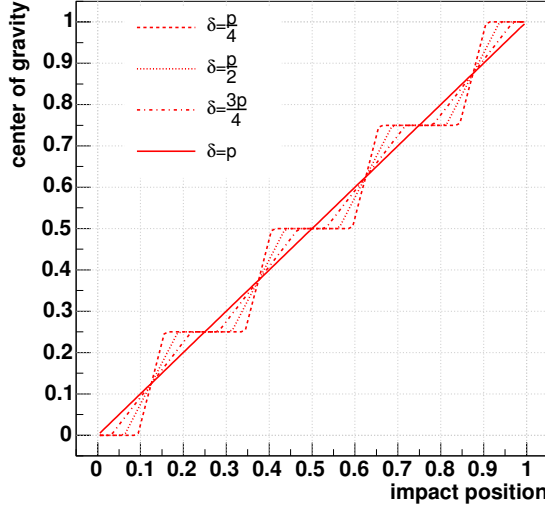


Figure 3.29: Center of gravity as a function of the impact position x . There is identity for $\delta = p$.

2. the charge sharing due to diffusion is linear with the particle crossing position,
3. the readout electronics transmit a signal linear with the input charge.

Nevertheless, the previous approach shows us that under ideal conditions, the capacitive coupling of strips conjugated with the charge sharing between two neighbouring strips allow to obtain a better spatial resolution than $p/\sqrt{12}$. A better spatial resolution will be reached if the implant pitch has dimensions close to the charge tube dimensions.

This model is too simplistic, though, and needs to be described in more details. In addition to the direct interstrip capacitance, the coupling with the second neighbouring strips should also be taken into account. Also, the coupling to the backplane C_b is an important parameter, as this capacitance should be kept as low as possible compared to C_i : a too high C_b degrades the charge collection efficiency, and thus the signal to noise ratio (S/N). Figure 3.30 shows a better description of all couplings which should be taken into account. Determining the correct capacitive network of a microstrip detector is also important to understand the total input capacitance of a readout channel, as this parameter plays a determining role in the quality of the signal over noise ratio.

It has been observed that C_b does not depend on the strip width, but on the strip pitch. Also, C_i is proportional to the strip width w . As mentioned earlier, the electronics noise depends on the load capacitance, thus increasing C_i too much will decrease the S/N. Thus an optimization study has to be performed during the detector development to identify the best compromise in noise and performance.

The previous discussion points out the importance of the terminology: a microstrip detector is composed of strips. The readout electronics is connected to readout strips, while the signal is most of the time collected by intermediate strips, which are biased like the readout

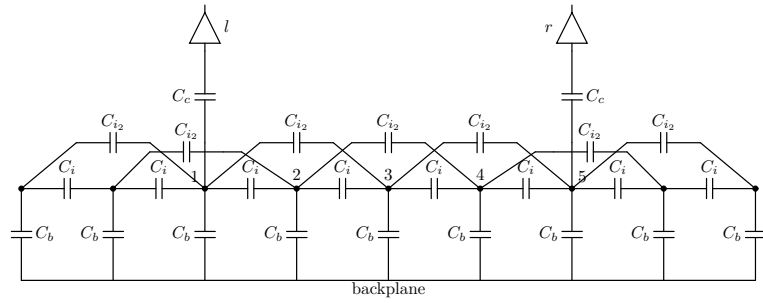


Figure 3.30: A better model of a detector with three intermediate strips. Coupling to backplane and to second neighbours have been added.

strips, while not directly read out. This subtle distinction may lead sometimes to confusion, where some authors mix the concepts of readout channels, readout strips and implant strips. It should be then emphasized that for AMS, there are 640 readout channels on the S-side, one channel corresponding to n strips daisy chained. Nevertheless, each sensor has 2568 p^+ implants. The K-side readout scheme depends on the tracker plane, but for what concerns the internal planes, one intermediate strips is located between two readout strips.

3.11 Calibration and signal detection

The signal collected by a readout strip is amplified and digitized. The digital values corresponding to each readout channel need then to be correctly interpreted to extract the relevant information. Usually, a readout front end is composed of N_a preamplifier chips with N_c readout channels.

3.11.1 Signal detection

We denote by x_k^{ij} the value issued by channel i located on preamplifier chip j for event k :

$$x_k^{ij} = p^{ij} + cn_k^j + s_k^{ij} + q_k^{ij} \quad (3.85)$$

where:

- p^{ij} , the *pedestal*, is the channel mean value, a constant proper to each readout channel.
- cn_k^j follows the preamplifier chip *common mode noise* distribution.
- s_k^{ij} , the channel fluctuation, follows a Gaussian distribution $N(0, \sigma^{ij})$. σ^{ij} is commonly named the channel *noise*.
- q_k^{ij} , the real signal, follows the Landau distribution around dE/dx .

The residual r_k^{ij} is defined as:

$$r_k^{ij} = x_k^{ij} - p^{ij} - cn_k^j \quad (3.86)$$

Note that the mean value of r^{ij} is 0 as the common mode noise is random.

A cluster is defined as a group of contiguous channels such that r_k^{ij} is larger than a given threshold. The cluster selection criteria are the following:

$$\frac{r_k^{ij}}{\sigma^{ij}} > C, \text{ where } C = \begin{cases} c_1 & \text{for the maximum signal channel} \\ c_2 & \text{boundary channels} \end{cases} \quad (3.87)$$

with $c_1 > c_2$.

The cluster integral, proportional to the deposited energy, is defined as:

$$int_k = \sum_{i=i_0}^{i_0+\ell-1} r_k^{ij} \quad (3.88)$$

where ℓ is the cluster length, i.e. the number of channels composing the cluster, and i_0 the first channel index.

3.11.2 Calibration

To evaluate the residual r_k^{ij} , the parameters p^{ij} and σ^{ij} must be computed from a calibration procedure. The channel pedestal p^{ij} is calculated with N_{ev} events:

$$p^{ij} = \frac{1}{N_{ev}} \sum_{k=1}^{N_{ev}} x_k^{ij} \quad (3.89)$$

Another important issue is the channel fluctuation. To characterize the channel stability, the width of the distribution of $x_k^{ij} - p^{ij}$ for N_{σ_0} events is calculated:

$$\sigma_0^{ij} = \sqrt{\frac{1}{N_{\sigma_0}} \sum_{k=1}^{N_{\sigma_0}} (x_k^{ij} - p^{ij})^2} \quad (3.90)$$

σ_0^{ij} is called the channel *raw noise*. It is possible to separate the fluctuation into two components: a common mode fluctuation of a whole preamplifier chip, and an individual channel fluctuation. The common mode noise cn_k^j is calculated for each readout event k and each preamplifier j :

$$cn_k^j = \frac{1}{N_{CN}} \sum_i (x_k^{ij} - p^{ij}) \cdot s^{ij} \quad (3.91)$$

with

$$N_{CN} = \sum_{i=(j-1)N_a+1}^{jN_a} s^{ij} \quad (3.92)$$

where $s^{ij} \in \{0; 1\}$ is channel status.

The channel noise σ^{ij} is defined as the width of the distribution of r_k^{ij} for N_σ events:

$$\sigma^{ij} = \sqrt{\frac{1}{N_\sigma} \sum_{k=1}^{N_\sigma} (r_k^{ij})^2} \quad (3.93)$$

The noise parameters allow to interpret the channel status. Furthermore, the width of the distribution of cn_k^j informs the operators on the electromagnetic insulation of the setup.

3.12 Noise contributions

The noise has two origins, the preamplifier and the silicon detector itself. The noise contribution is expressed in equivalent noise charge (*ENC*), i.e. the corresponding charge if it were a real signal. The various contributions due to the silicon detector are [47]:

$$\text{Strip current: } ENC_{lc} = \frac{e}{q} \sqrt{\frac{t_p q I}{4}} \quad (3.94)$$

$$\text{Polarization resistance: } ENC_{br} = \frac{e}{q} \sqrt{\frac{t_p k_b T}{2 R_{pol}}} \quad (3.95)$$

$$\text{Strip metallization: } ENC_{met} = \frac{e C_t}{q} \sqrt{\frac{k_b T R_{ms}}{6 t_p}} \quad (3.96)$$

where I corresponds to the channel total current, t_p is the preamplifier shaping time, R_{pol} the polarization resistance (i.e. the strip-bias resistance), R_{ms} is the channel metallization resistance, C_t is the channel input capacitance, T the temperature in $^{\circ}\text{K}$, q is the elementary charge, $e = \exp(1)$, k_b the Boltzmann constant.

For a preamplifier of the Viking family, the noise contribution is expressed as

$$ENC_{preamp} = \frac{1}{\sqrt{t_p}} (K_1 + K_2 C_t) \quad (3.97)$$

where C_t is the channel total input capacitance, K_1 and K_2 are two constants. For the VA HDR (see section 4.7.2), $K_1 = 857(\mu\text{s})^{0.5} e^-$ and $K_2 = 9.8(\mu\text{s})^{0.5} e^- p\text{F}^{-1}$ [48]. The channel total input capacitance is defined as:

$$C_t = \left(\frac{1}{C_c} + \frac{1}{C_{strip}} \right)^{-1} \quad (3.98)$$

with C_c the coupling capacitance between the amplifier and the strip and C_{strip} the total strip capacitance, which results from the contributions of the intermediate strips and their own couplings with the backplane. Using figure 3.30 (p.47), and neglecting C_{i_2} we express an approximation of C_{strip} :

$$C_{strip} \cong C_b + 2 \cdot f^3(C_i) \quad \text{with} \quad f(c) = \left(\frac{1}{C_i} + \frac{1}{C_b + c} \right)^{-1} \quad (3.99)$$

if we assume $C_i \gg C_b$, then

$$C_{strip} \cong C_b + \frac{C_i}{2} \quad (3.100)$$

The total equivalent noise charge is expressed as:

$$ENC_{total} = ENC_{preamp} \oplus ENC_{lc} \oplus ENC_{br} \oplus ENC_{met} \quad (3.101)$$

The noise depends on the channel length, i.e. on the number daisy chained strips. For a

channel composed of n strips, we define:

$$\text{total channel leakage current: } I(n) = n \cdot I(1) \quad (3.102)$$

$$\text{total metallization resistance: } R_{ms}(n) = n \cdot R_{ms}(1) \quad (3.103)$$

$$\text{total polarization resistance: } R_{pol}(n) = \frac{1}{n} \cdot R_{pol}(1) \quad (3.104)$$

$$\text{total input capacitance: } C_t(n) = n \cdot \left(\frac{1}{C_t(1)} + \frac{n-1}{C_c} \right)^{-1} \quad (3.105)$$

where $I(k)$, $R_{ms}(k)$, $R_{pol}(k)$, $C_t(k)$ are the values for a detector with k strips daisy chained.

Note that if $C_c \gg C_i$ then

$$C_t(n) \cong n \cdot C_t(1) \quad (3.106)$$

Thus the equivalent noise charges become:

$$ENC_{lc}(n) = \sqrt{n} \cdot ENC_{lc}(1) \quad (3.107)$$

$$ENC_{br}(n) = \sqrt{n} \cdot ENC_{br}(1) \quad (3.108)$$

$$ENC_{ms}(n) \cong n^{\frac{3}{2}} \cdot ENC_{ms}(1) \quad (3.109)$$

The latter expression relies on the approximation (3.106). Figures 3.31 and 3.32 show the equivalent noise charges as a function of the number of daisy chained strips. In particular, the contribution due to the strip metallization resistance increases faster than the other noise sources.

Moreover, the noise contributions depend either on $\sqrt{t_p}$ or on $1/\sqrt{t_p}$. Thus an optimal shaping time which minimizes the total noise exists, as depicted in figure 3.33. The electronics design is then chosen to achieve this optimal shaping time. In the case of long ladders, as it is the case for AMS, limiting the noise means acting on the silicon properties: high polarization resistances, low metallization resistances, strip current as low as possible. Those properties directly rely on the design and the production process. The module assembly, on the other hand, must limit the sensor degradation to a minimum.

3.13 Qualification tests

Various tests are performed on the microstrip detectors before integrating them into a module. The depletion voltage (section 3.5.2) is an important parameter, as it determines at which minimum voltage the sensor can be biased. The depletion voltage directly depends on the bulk doping (equ. 3.48), normally controlled from the very beginning, during the raw material procurement. The depletion voltage is determined by measuring the capacitance as a function of the bias voltage. In ideal cases, the threshold voltage at which the capacitance stabilizes is normally the depletion voltage. Usually the detectors are operated in “overdepletion”, i.e. the operating voltage is higher than the depletion voltage. This ensures that the n-side strips are correctly resistively isolated, thus suppressing the resistive charge sharing between the strips, which would reduce the spacial resolution and increase the channel noise.

In real cases, the capacitance measurements may reveal more complex behaviours, as a microstrip detector is not a simple diode, but an array of diodes, with various capacitive and

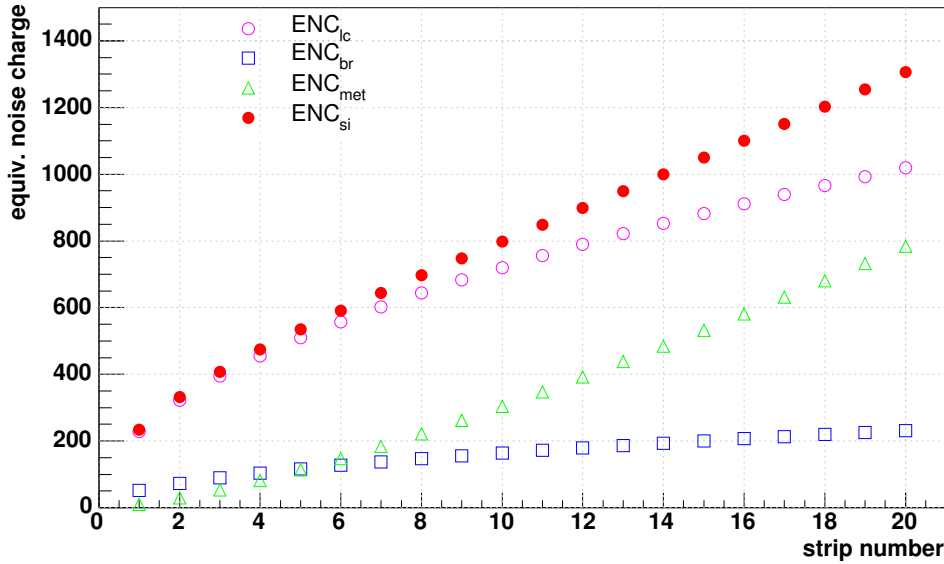


Figure 3.31: Noise contributions from the AMS-02 silicon detector as a function of the number of daisy chained strips with a shaping time of $4.5 \mu\text{s}$: $ENC_{si} = ENC_{lc} \oplus ENC_{br} \oplus ENC_{met}$ corresponds to the total silicon noise.

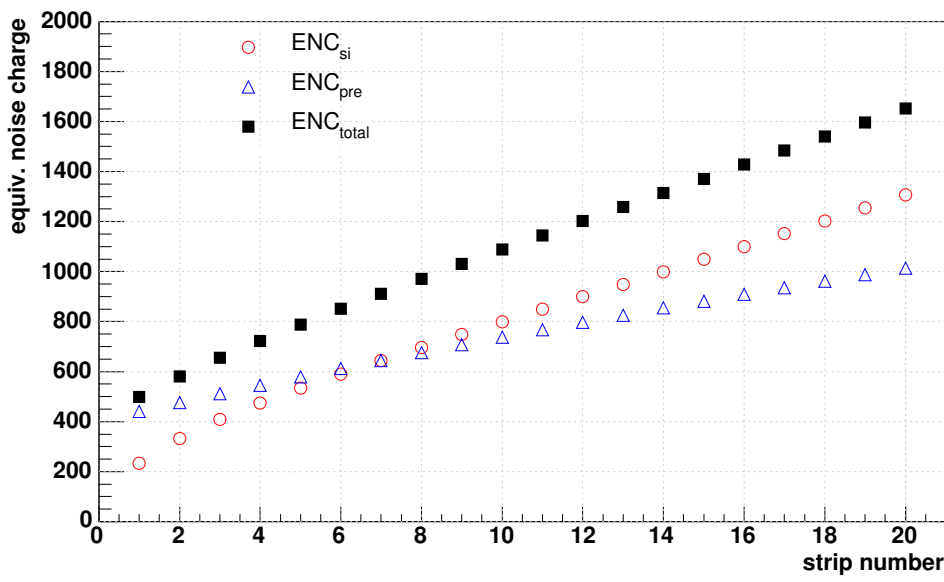


Figure 3.32: Noise contributions from the AMS-02 silicon detector and the preamplifier as a function of the number of daisy chained strips $ENC_{total} = ENC_{preamp} \oplus ENC_{si}$ with a shaping time of $4.5 \mu\text{s}$.

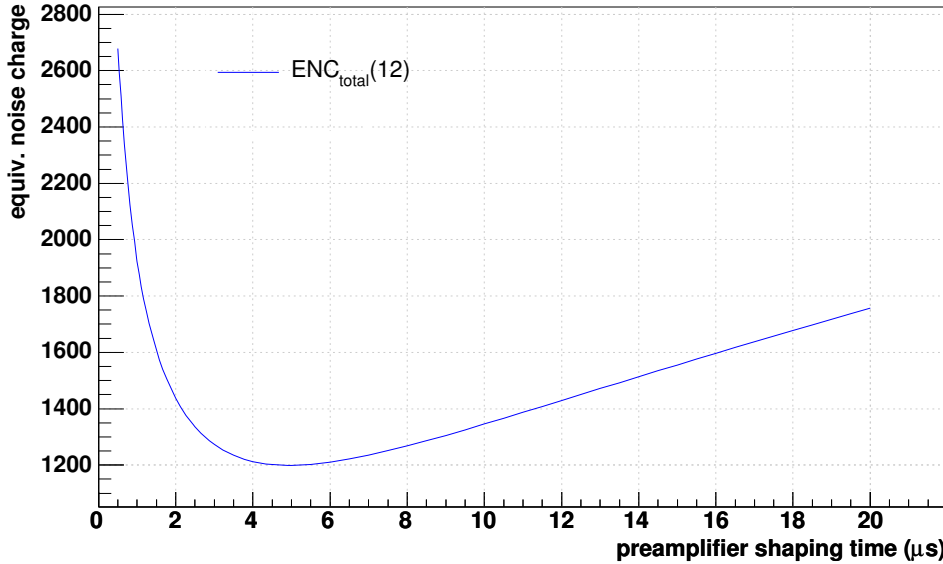


Figure 3.33: Total noise dependence with the shaping time t_p for a readout channel composed of 12 daisy chained strips.

resistive couplings and the capacitance measurement may depend on the frequency of the test signal.

Clearly, the noise parameters described in section 3.12 are measured, as they provide information on the detector quality, which will determine the future module overall performance.

The individual strip leakage currents as well as the detector total current are measured at the operating voltage. Usually selection criteria accept a limited amount of high current strips (named “hot” strips) and a maximum total current is defined too. The total current corresponds ideally to the sum of the individual strip currents, but can also have contributions from surface currents. Strips seriously damaged will induce a large total current increase, thus excluding the detector from the assembly line.

On a regular basis, the interstrip capacitance, the interstrip resistance, as well as the polarization resistance are measured. As an example, table 3.1 summarizes the criteria applied to the AMS-02 microstrip detector.

3.14 Conclusions

The characteristics of the silicon microstrip detectors and the related readout issues have been presented. The use of intermediate readout strips allows to keep a good spatial resolution (thanks to the capacitive coupling) while limiting the number of readout channels, thus the cost and power consumption. A good knowledge of the sensor properties are necessary to design a readout electronics limiting the total noise. In addition to the detector intrinsic

Max. depletion voltage	50 V
Max. total leakage current	$2 \mu\text{A}$
p-side hot strip definition	$I_{strip} > 2 \text{ nA}$
n-side hot strip definition	$I_{strip} > 20 \text{ nA}$
Max. number of p-side hot strips	6
Max. number of n-side hot strips	4

Table 3.1: Selection criteria applied to the AMS-02 silicon microstrip detectors [49].

properties (bulk doping, implantation designs), the detector handling during assembly is a critical issue, as damaged strips will induce noisy readout channels. Chapter 4 details the AMS microstrip detector and module properties, chapter 5 describes the module (ladder) assembly and chapter 6 presents tests to evidence the potential influence of the assembly steps on the sensor quality.

Chapter 4

The microstrip detectors in the AMS experiment

4.1 Introduction

This chapter explains how the silicon microstrip detectors are used in AMS. The silicon tracker of AMS-02 is briefly presented, then the silicon modules, named ladders, are described. After discussing the AMS microstrip detectors, other ladder components are examined, in particular the front-end electronics.

4.2 The Silicon Tracker

The silicon tracker (fig. 4.1) is composed of eight layers of double-sided silicon microstrip detectors. The mechanical structure is made of five aluminium honeycomb support structures (called planes) produced by Contraves AG, previously used in the AMS-01 tracker. The AMS-01 tracker had two outer planes (located outside the magnet) of 1.4 m diameter, and four inner planes (placed inside the magnet) of 1.0 m diameter, each equipped with silicon modules on one side only.

The physics goals of AMS-02, regarding the rigidity resolution, induce important design changes. First, the AMS-01 permanent magnet is replaced by a superconducting magnet. Second, two more silicon layers have been added, and the silicon layer positions have been optimized. Compared to AMS-01, one inner plane is suppressed, but the three remaining planes are equipped on both sides, thus eight layers of silicon detectors will compose the tracker. As the planes were originally not equipped to accept modules on both sides, machining and installation of a new fixation system needed to be implemented on the sides not used in AMS-01. The new configuration enables a better track reconstruction, introducing redundancy for each internal plane. The number of measurements in the magnetic field volume is increased to better evaluate the track sagitta. Finally, this configuration allows to better compare tracks separately reconstructed with the upper and lower layers. The silicon modules, the ladders, composed of 7 to 15 (except 8) microstrip detectors, have a length

ranging from 29 cm up to 62 cm. Each ladder provides 1024 readout channels. The tracker, composed of 192 ladders (see table 4.1) provides 196'608 channels for total detection surface of 6.39 m². The module mechanical concept is based on the Silicon Microvertex Detector (SMD) of the L3 experiment at CERN [50]. Table 4.1 describes the ladder types per layer, and Appendix G describes the ladder naming scheme. The spatial resolution is 10 μm on the bending plane (p-side) and 30 μm on the non-bending plane (n-side) [23].

The magnet change also has important implications in the cooling design. While the AMS-01 permanent magnet played the role of heat exchanger, the new magnet must be isolated from the heat produced by the ladder front-end electronics. For this purpose, a cooling system composed of mechanically pumped two-phased CO₂ loop will be assembled. The tracker power consumption is foreseen to be of the order 640 W. The tracker will weigh 186 kg.

The ladder front-end electronics is connected, via flat cables, to the Tracker Data Reduction boards (TDR). The TDR design is based on the Common Digital Part, a circuit structure common to each AMS-02 subdetector readout. The CDP (Common Digital Part) is connected to the analog circuit, reading out the sub-detector. The CDP is composed of a gate array, a DSP, a buffer memory and a flash memory which contains the code for the DSP and the gate array.

In the TDR, the CDP is composed of three 12-bits ADCs and a 3-bit DAC. The ADCs are used to read out the signals coming from the ladders: 2 ADCs are dedicated to the S-side, the remaining ADC to the K-side. As AMS is a space experiment, with no possibility to recover a defunct part, it is necessary to implement redundancy. Nevertheless, the TDRs present no redundancy, in contrast to other CDPs in AMS. The redundancy is materialized by the silicon modules themselves, with 8 silicon layers, each having two detection sides.

The data are transmitted from the ISS to Earth via two connections. The High Rate Data Link enables a peak transmission rate of 10 Mbps, with a mean orbit rate of 2 Mbps. The Low Rate Data Link, offers a constant 10 kbps (out) and 1 kbps (in) transmission and is used to transmit the status information and also the control signals.

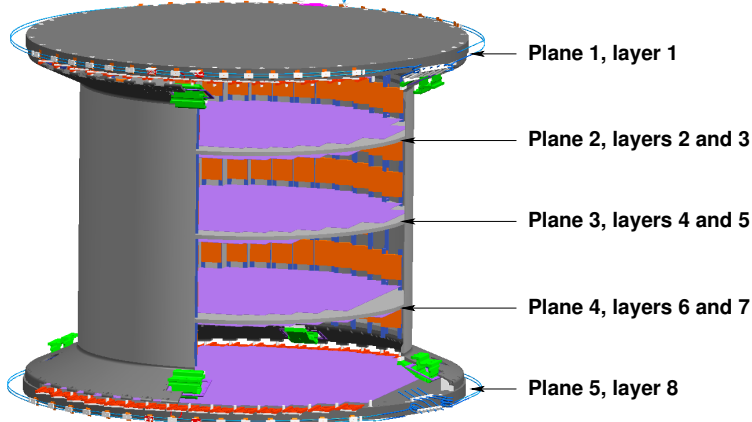


Figure 4.1: The silicon tracker of AMS-02. The internal planes (2 to 4) are equipped with silicon microstrip detectors on both sides, while the external planes (1 and 5) are equipped on one side only. The total detection surface is close to 6.39 m^2 .

Ladder Length	Type	Layer								Total	
		L1	L2	L3	L4	L5	L6	L7	L8	Ladders	Sensors
7	I (K5)		2						2	4	28
9	I (K5)		4	4	4	4	4	4		24	216
10	I (K5)		2	2	2	2	2	2		12	120
10	O (K7)	4							4	8	80
11	I (K5)		4	4	4	4	4	4		24	264
11	O (K7)	2							2	4	44
12	I (K5)		5	5	5	5	5	5		30	360
12	H (K5l)		3	2	3	2	3	2		15	180
12	J (K5u)		2	3	2	3	2	3		15	180
12	O (K7)	2							2	4	48
13	O (K7)	4							4	8	104
14	I (K5)		2	2			2	2		8	112
14	O (K7)	6							6	12	168
15	N (K7l)	3							2	5	75
15	P (K7u)	2							3	5	75
15	O	7							7	14	210
Total:		30	24	22	20	20	22	24	30	192	2264

Table 4.1: Ladders composing the AMS-02 tracker. There is a total of 192 modules, corresponding to a total of 2264 silicon detectors, i.e. a total detection surface of 6.39 m^2 .

4.3 The AMS ladder

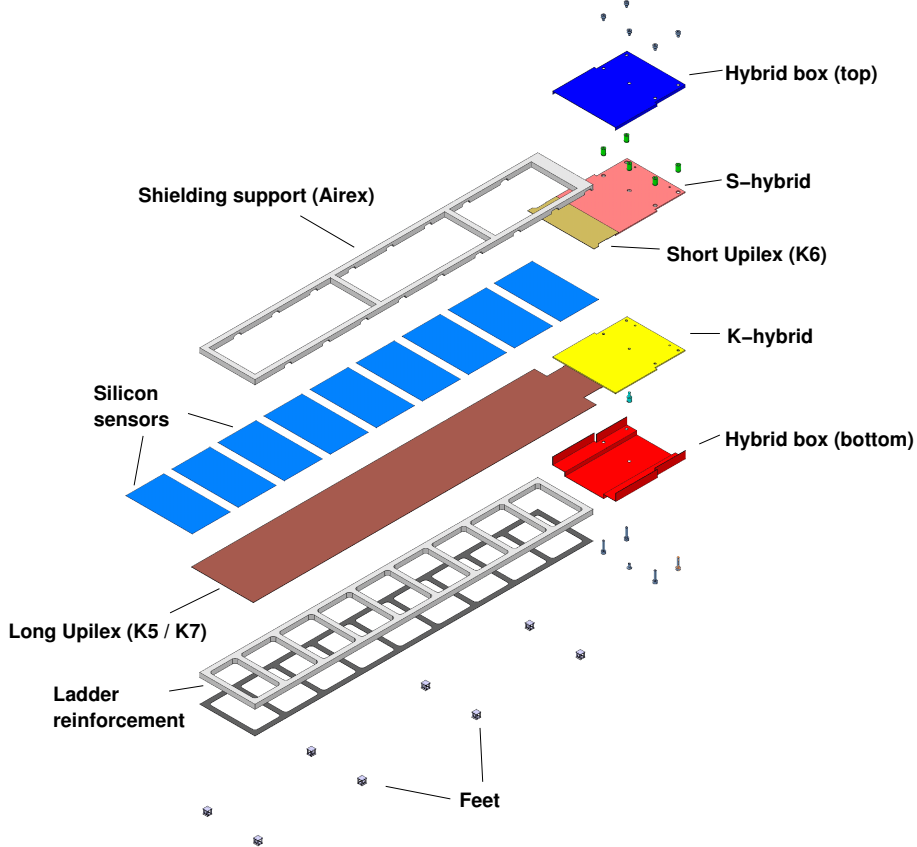


Figure 4.2: Structure of an AMS ladder, the electromagnetic shield is not shown here.

A ladder (see fig. 4.2) is composed of an array of 7 to 15 silicon microstrip detectors. The p-side is facing up and is known as the ladder S-side. The reverse side, corresponding to the silicon n-side, is called K-side. On the S-side, the strips are daisy chained with micro-wire bonds, to redirect the signals to the electronics. The final routing is achieved through a short Upilex cable, connecting the first sensor strips to the S-readout electronics (“S-hybrid”). On the K-side, a long Upilex cable is glued to redirect the signals to the K-readout electronics (“K-hybrid”), as the strips are transverse. In total, a ladder provides 1024 readout channels, 640 for the S-side, 384 for the K-side. A reinforcement (see appendix C) made of Airex foam and carbon fiber is glued on the K-side Upilex: this “spinal column” ensures sufficient flexibility to sustain the strong vibrations during the shuttle flights, yet maintaining sensor positions to the required accuracy. The front-end electronics (called *hybrids*) are protected by a grounded aluminium box. Aluminium feet to allow fixation of the ladder on the tracker plane are glued on the reinforcement. An Airex foam spacer (see appendix D) is glued on the S-side to protect the silicon surface from a metallized Upilex foil wrapped around the ladder. The role of this foil is twofold: first, connected to the hybrid box it acts as an

electromagnetic shield. Second it mechanically protects most of the silicon surface. As a side-effect, this electromagnetic shield also limits the amount of ambient light reaching the silicon surface.

4.4 The AMS silicon microstrip detectors

The AMS microstrip detector results from the research and development realized from the 1980's until the 1990's to create first the ALEPH [37] detector design, then the L3 SMD [50] detector.

4.4.1 The AMS-01 microstrip detector

Figure 4.3 shows corners of the AMS-01 and AMS-02 microstrip detectors, p- and n-sides, while table 4.2 summarizes the detector geometries. On the p-side, there are two guard rings: the innermost (bias) is connected, while the outer (guard) is left floating. The guard ring metallization extends over the p^+ strips, as schematically shown in figure 4.4: this structure is similar to a FOXFET detector with 0 V gate voltage. Figure 4.5 shows a schematics of the AMS-01 sensor p-stop design. The detector is operated in applying a positive voltage on the n-side guard ring, and in connecting the p-side inner guard ring to ground. Due to a change in substrate procurement (i.e. in the substrate n-doping), two operating voltages (50 V and 100 V) were needed.

4.4.2 The AMS-02 silicon microstrip detector

For AMS-02, the silicon design was upgraded to decrease as much as possible the noise transmitted to the readout channel. It is important to note that long silicon modules (up to 15 double-sided silicon sensors) are not common in particle physics experiments, due to noise limitations (see section 3.12) and to occupancy limitations e.g. in a high multiplicity collider environment. This kind of configuration introduces effects usually neglected for smaller modules modules. As mentioned in section 3.12 , the noise issued from a silicon ladder is due to:

- the strip leakage current;
- the polarization resistance, i.e. the resistance between the strips and the guard ring to which is applied the biasing voltage;
- the strip metallization resistance;
- the preamplifier noise, which depends on the input capacitance.

All these parameters actually depend on the channel length, i.e. the number of sensors in a ladder. An intense collaboration between the tracker group and the manufacturer (CSEM, now Colibrys [51]) resulted in the modification of the sensor design and fabrication, to:

- Decrease the silicon dark current ('Lowleak' process).

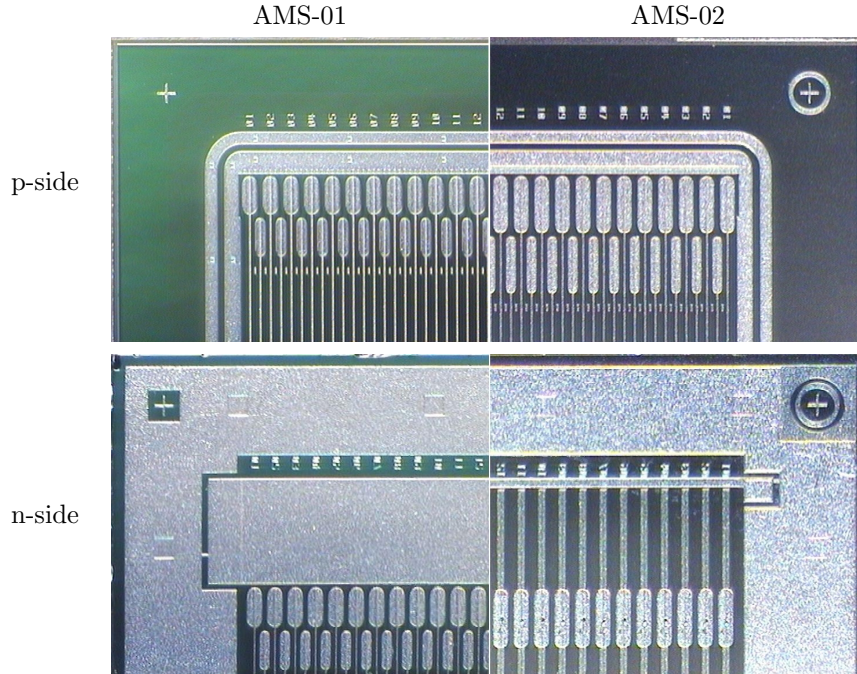


Figure 4.3: AMS-01 (left) and AMS-02 (right) sensor metallizations, for p- and n-sides.

	AMS-01	AMS-02
Dimensions	$72.045 \times 41.360 \text{ mm}^2$	
Thickness	$\sim 300 \mu\text{m}$	
Active width, p side	70.595 mm	
Strip pitch, p side	27.5 μm	
no. of p-strips	2568	
no. of metal strips, p-side	1284	
no. of p-side readout strips	640	
Readout pitch, p side	110 μm	
Active width, n side	39.832 mm	
Strip pitch, n side	52 μm	104 μm
no. of n-strips	767	384
no. of metal strips, n-side	767	384
no. of n-side readout strips	192	
Readout pitch, n side	208 μm	

Table 4.2: AMS microstrip detectors geometries.

- Decrease the strip metallization resistance, in increasing the metallization thickness.
- Increase, on the n-side, the polarisation resistance, using the surface through method.

In addition to these points, other modifications are:

- The n-strips are wider and their number is reduced by half, to increase the K-side charge collection [23].
- The sensors have a $1 \mu\text{m}$ SiO_2 passivation layer to protect the silicon surface against surface degradation during manipulations and surface contacts. This enables safer assembly procedures.
- New metrology patterns have been designed (see fig. 4.3), to take a better advantage of the optical pattern recognition system of the metrology machine.
- The cutting line has dashed metallised lines, to make the cutting procedure easier.
- The bonding pad length has been increased to $300 \mu\text{m}$.

The maximum allowed depletion voltage is 50 V (thus corresponding to a bulk resistivity of minimum $6 \text{ k}\Omega \cdot \text{cm}$, and the chosen operating voltage is 80 V).

The n-side strip insulation is different from the solution retained in AMS-01. The strips are surrounded by n-boxes, themselves separated with n-stops, as depicted in figure 4.6. We also recognize a FOXFET-like structure, with a 0 V gate voltage, as the gate metallization is connected to the guard ring metallization.

4.4.3 Anti-reflective sensors

In the tracker, an infrared laser alignment system will be implemented to survey the tracker layer alignment. For this purpose, openings are designed on the corresponding K-side Upilex cables and on the Upilex shielding. Moreover, the silicon surface has to be treated and the strip metallization is narrowed (from 12μ to 10μ for the p-side, from 36μ to 10μ for the n-side) to improve the infrared beam passage through the detectors. Figure 4.7 shows the silicon anti-reflective circle design. Note that thanks to the anti-reflective treatment, the strip implantations are optically observable as shown on figure 4.8.

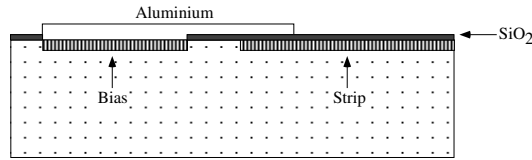


Figure 4.4: Schematics of the p-side guard ring metallisation.

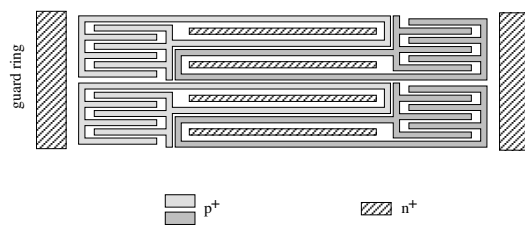


Figure 4.5: Schematics of the n-side p-stop design (not to scale; in particular, the n⁺ strips have been shortened).

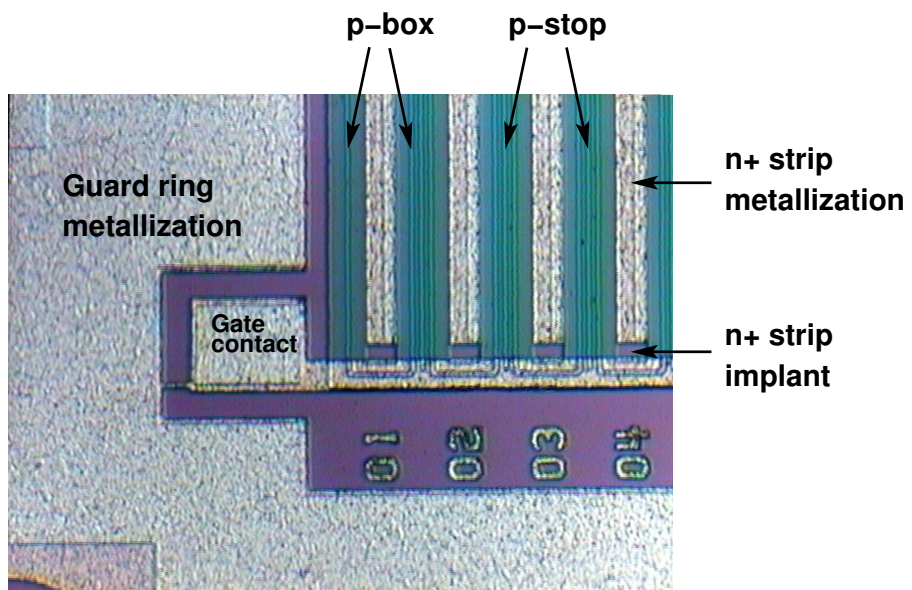


Figure 4.6: n-side of the AMS-02 detector: closeup view.

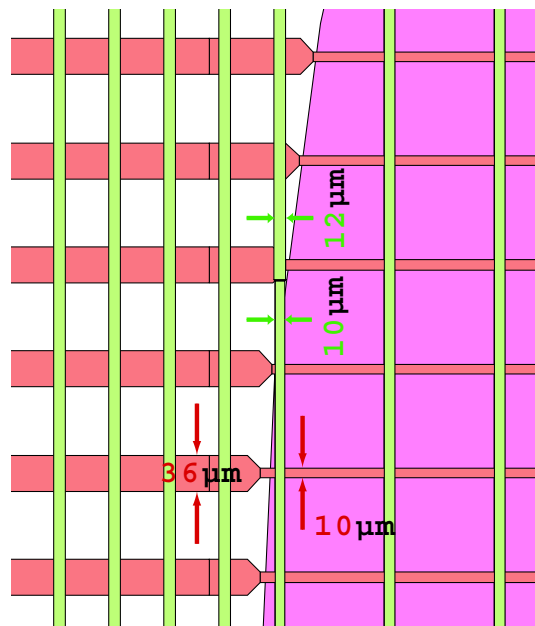


Figure 4.7: Anti-reflective circle design, detail.

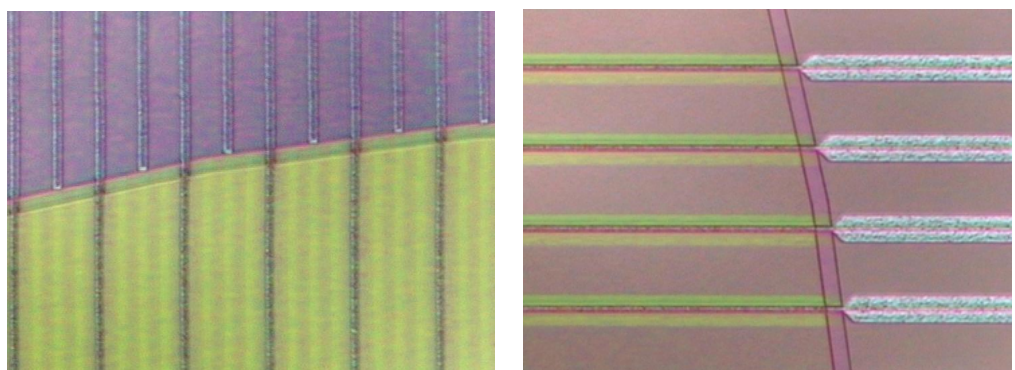


Figure 4.8: Anti-reflective circle, p-side (on the left) and n-side (on the right). Note that thanks to the special surface treatment, the strip implantations are optically observable.

4.5 K5 and K7 Upilex cables (K-side)

The cables are made of a $50\mu\text{m}$ thick Upilex foil. The strips used to transmit the signals are composed of a $1.5\ \mu\text{m}$ thick gold layer covered by a $5\ \mu\text{m}$ thick copper layer. The standard cable version (K5), used for internal layer ladders, is schematically shown in figure 4.11, a simplified representation is shown in figure 4.9. The 192 readout strips of sensors 1, 3, 5, 7, ... are daisy chained, and correspond to the VA preamplifiers (see section 4.7.2) 1 to 3 (channels 1 to 192). The 192 readout strips of sensors 2, 4, 6, 8, ... are daisy chained and correspond to VA preamplifiers 4 to 6 (channels 193 to 384). The cable thus reduces the $n \cdot 384$ strips to $2 \cdot 192$ readout channels. Table 4.3 describes the relation between the readout channels and the silicon readout strips.

Channel	Strip
1 and 193	384
2 and 194	382
3 and 195	380
\vdots	\vdots
191 and 383	4
192 and 384	1

Table 4.3: K-side strip and channel classification. Channels 1 to 192 correspond to odd position sensors, channels 193 to 384 correspond to even position sensors.

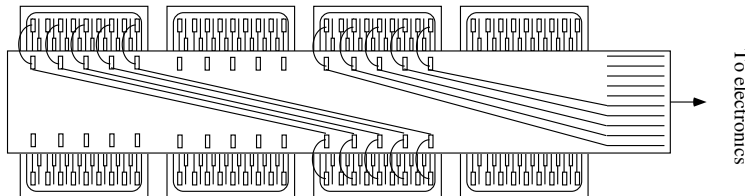


Figure 4.9: The way K5 Upilex chains the silicon strips on the K-side; for clarity, only one group is shown bonded.

The n-strip signal routing is more elaborate for the outer layer ladders: the K7 design (figure 4.12) mixes strips of neighbouring sensors using two different Upilex strip pitches. The 384 readout channels are divided in 12 groups of 32 channels. As shown in figure 4.12, the sensor n-strips are divided in 7 groups of 32 strips. As an example, consider sensors 1 and 2. With such a bonding scheme, to readout the detection surface of both sensors, the strip groups 6 and 7 of sensor 2 are connected to channel groups 1 and 2. K5/7 Upilex dimensions are described in appendix B.2. The bonding scheme of the K7 Upilex is described in appendix E.3.

4.6 K6 Upilex cable (S-side)

This cable allows the connection between the first sensor p-side strips and the capacitor channels on the hybrid. The K6 Upilex is directly glued on the silicon surface. On the silicon detector, a second bonding pad raw is implanted, 5.15 mm distant from the standard bonding pad row as shown in fig. 4.10, to allow the strip connection to the cable. See appendix B.1 for more information.

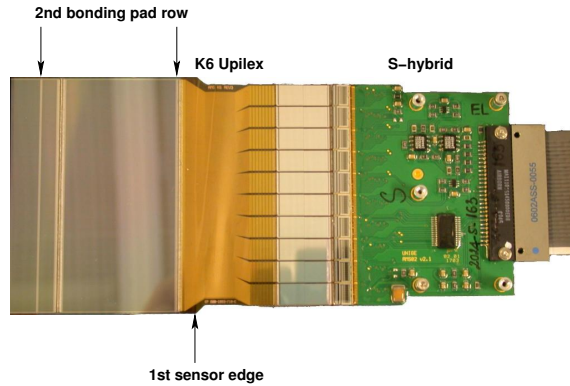


Figure 4.10: The K6 Upilex cable connects the p-side daisy-chained strips to the electronics (on the right).

On the S-side, there are 640 readout channels, while the silicon detectors provide 1284 metallized strips, 642 with large bonding pads, 642 with small bonding pads (fig. 4.3). The readout channels correspond to the silicon strips with large bonding pads, but strips 2 and 641 are not connected, as shown in appendix E.1. Thus, we have the following conversion table:

Channel	Strip
1	1
2	3
3	4
⋮	⋮
639	640
640	642

Table 4.4: S-side strip and channel conversion table. Strips 2 and 641 are not connected.

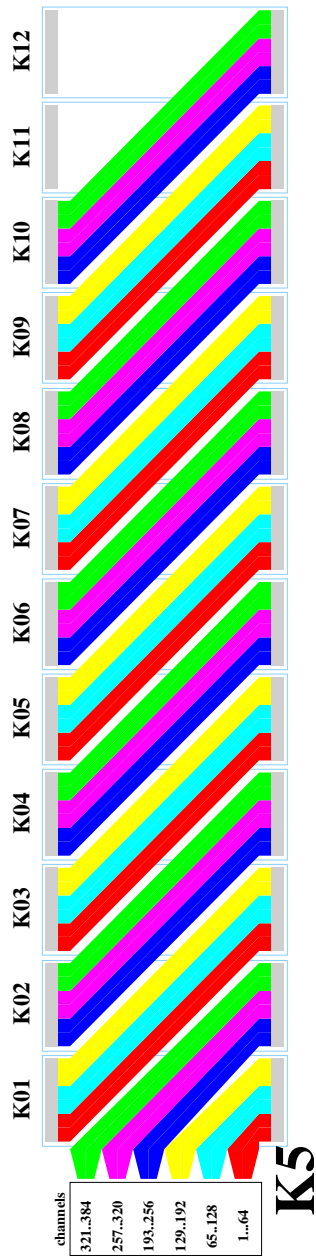


Figure 4.11: Signal routing for the K5 design (inner layers) based on [52].

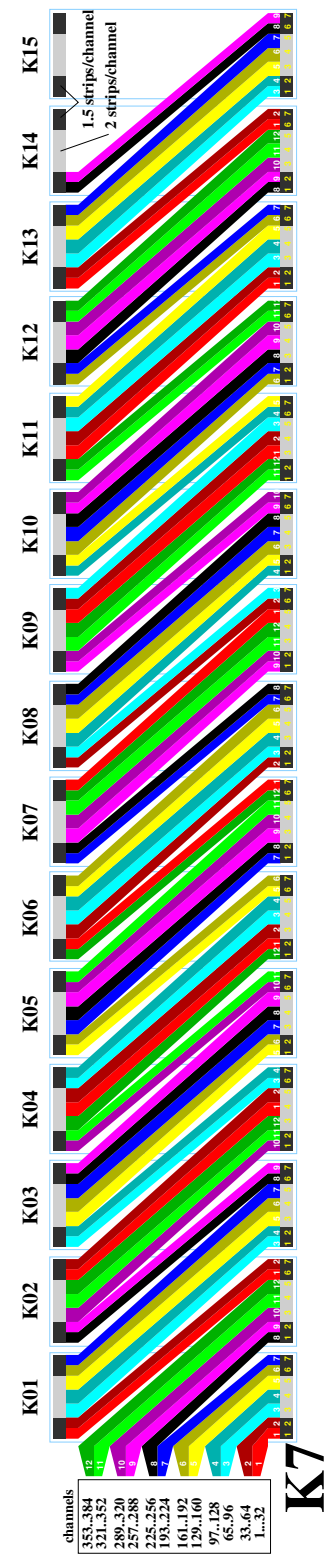


Figure 4.12: Signal routing for the K7 design (outer layers) based on [52].

4.7 The Tracker Front End electronics: the hybrids

Two separate boards are used to read out the ladder, one for each side. The S-side board reads 640 channels, while the K-side reads out 384 channels. The main hybrid structure is the same on both sides: the first stage is composed of decoupling capacitor chips (RCAMS), the second stage is composed of the preamplifier/shapers, the VA64_hdr9a. The VA control sequences are driven by the HCC chip, and the output signals are amplified by AD8052 operational amplifiers. Additionally, the K-hybrid is equipped with a DS1820 temperature sensor, with a unique serial number, which identifies the ladder. Further components involved in the ladder bias are described in section 4.8. See appendix A for more information about the hybrids.



Figure 4.13: AMS-02 hybrids: K-side on the left, S-side on the right.

4.7.1 The RCAMS

The RCAMS, produced by Colibrys, is composed of 64 capacitors, each with a typical capacitance of 725 pF. An additional line, the bias, is available to transmit the bias voltage to the silicon detectors. The designs for AMS-01 and AMS-02 present differences. The AMS-01 capacitors chip was based on the models used for the ALEPH [37] and L3 [50] experiments at LEP. The schematic design is presented in figure 4.14. The double Zener diodes protect the capacitor from heavy charge release which may occur in case of beam loss [50]. The diodes become conductive, thus avoiding that the charge accumulates on the capacitors and eventually damages them.

In AMS-02, the RCAMS design has been simplified: as the detector is not exposed to an intense particle beam, it was decided to suppress the protection diodes. The motivation to simplify the design was to decrease the risk of having defective capacitor channels, due to a too low diode conductive threshold voltage, thus hindering the signal to reach the VA input.

4.7.2 The VA preamplifier

The VA, produced by IDEAS, a Norwegian company, exists in versions with different number of input channels and various gains. The VA design is originally based on the VIKING design

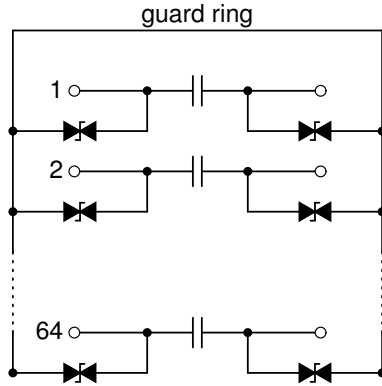


Figure 4.14: Schematics of RCAMS-01 capacitor chip.

[53, 54]. The motivation for developing such a device was the necessity to have a low noise amplifier, particularly adapted to silicon microstrip detectors. Indeed, the signal produced by a minimum ionizing particle (about 22000 electron-hole pairs) needs to be amplified and thus all noise sources need to be reduced. The VIKING design is based on the AMPLEX chip, described in detail in [55].

The AMPLEX processor

This chip was used for the readout of the UA2 silicon detectors ([56]). It had to respect two main constraints: a low power consumption (less than 1 mW per channel), and a signal processing time between 600 ns and 800 ns. An important aspect of the AMPLEX design is that it allows for a DC coupling with the detector: the readout channel is biased through the amplifier. Also, it is constantly sensitive to the input signal: no trigger is needed to start the readout. The AMPLEX design relies on two operating transconductance amplifiers (OTA). Figure 4.15 shows the schematic of one AMPLEX channel.

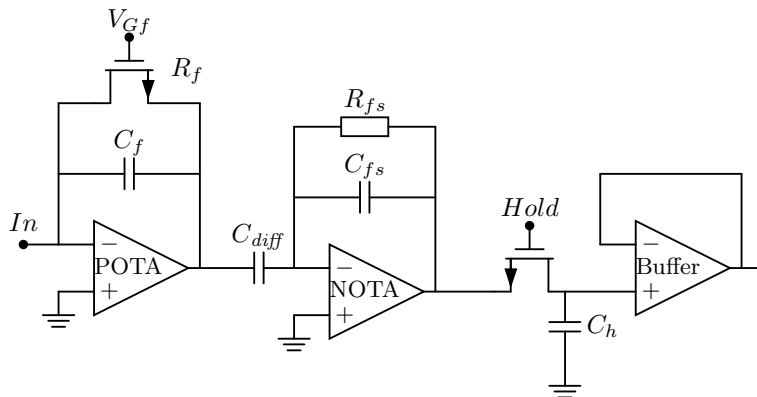


Figure 4.15: Amplifier and shaper stages of one AMPLEX channel.

The first stage, built around the POTA amplifier, is used to bias the detector, and works

as a charge amplifier, thanks to the capacitor C_f . A MOSFET, connected in parallel with the capacitor is used to bias the detector, and to avoid pile-up effects, i.e. to allow the discharge of C_f . The MOSFET gate voltage V_{Gf} controls the polarization resistance R_f while the OTA transconductance is externally controlled. The shaping stage has a CR-RC structure and is composed of a NOTA amplifier and the C_{diff} capacitor (differentiation stage), C_{fs} and R_{fs} (integrator stage). C_{diff} also isolates the shaper from the DC fluctuations due to the leakage current.

The POTA bias current controls the transconductance g_m , which influences the rise time:

$$T_{rise} \cong \frac{C_{in}}{C_f} (C_{load} + C_f) \frac{1}{g_m} \quad (4.1)$$

where $C_{in} = C_{gsi} + C_{det}$ and C_{gsi} is the capacitance from source to gate of the input FET, C_{det} the detector capacitance, $C_{load} \cong C_{diff}$. The feedback FET behaves as a variable resistor, dependant on the traversing current, which is the detector leakage current. In particular, when the current becomes very small, the equivalent resistance exponentially increases (the feedback FET is in weak inversion mode) to the order of $G\Omega$, inducing a limited noise to the amplifier. Furthermore, the feedback capacitance C_f must be the lowest possible to reduce the noise.

The previous description considers a detector bias through the preamplifier stage. It is nevertheless also possible to use an AC coupling between the detector and the preamplifier. In such a case, the feedback MOSFET function is to avoid the pile-up effects.

Consider C_{diff} , C_{fs} the shaper feedback MOSFET resistance, C_h the hold capacitance, C_{is} the shaper OTA input capacitance: we define $C_{ts} = C_{diff} + C_{is} + C_{fs}$ and $C_{os} = C_h + C_{fs} +$ associated parasitic capacitances. The peak time is then expressed as:

$$T_p = 2 \cdot C_{ts} \cdot \left(\frac{g_{ms} \cdot C_{fs}}{C_{os}} + \frac{1}{R_{fs}} \right)^{-1} \quad (4.2)$$

Finally, the voltage gain is expressed as follows:

$$A_{V_s} = \omega_c \cdot C_{diff} \cdot R_{fs} \quad (4.3)$$

where $\omega_c = 1/T_p$. The charge to voltage gain of the whole amplification line is then:

$$A_c = \frac{A_{V_s}}{q \cdot C_f} \quad (4.4)$$

where C_f is the preamplifier feedback capacitance.

Note that to get the best amplifier performance, R_{fs} and g_{ms} need to be adjusted according to relation 4.2.

In the Viking chip, R_{fs} is also controlled via a MOSFET, thus increasing the chip parameterization. As a conclusion, four parameters allow to control the Viking behaviour:

- The preamplifier OTA bias current acts on the rise time. Also, the bias current changes the POTA input voltage thus altering R_f .
- The preamplifier MOSFET gate voltage controls the pile-up suppression, and in the case of a DC connection, the detector bias.

- The shaper bias current (via g_{ms}) and the shaper MOSFET gate voltage control the peak time and the voltage gain.

Depending on the applications, the optimal control parameters may vary, and if not set by the manufacturer, need to be determined by the user himself.

The VA64_hdr

The VA64_hdr is a high dynamic range charge sensitive preamplifier-shaper circuit, with simultaneous sample and hold. It has a multiplexed analog readout and has a gain calibration mode. The VA parameters are controlled via the `vfs`, `vfp`, `pre_bias` and `sha_bias` inputs. The AMS-02 version, the VA64_hdr9 offers in addition preset parameters, thus reducing the component number on the PCB. Initially, for AMS-02, three versions of this VA were developed, 'a' and 'b' versions had different fixed gains, while the 'c' version offered 4 different gains, controlled via the `g0` and `g1` pads. The VA architecture is presented in figure 4.16 . The VA is operated with 3 voltage levels: -2 V (V_{ss} and back contact), 0 V (gnd) and +2 V (V_{dd}). The analog input pads are at -1 V.

The VA reset, readout and test mode sequences are described in figure 4.5. Before a readout sequence can be initiated, a reset must be performed.

As mentioned earlier, a calibration mode is available. It is controlled through the `test_on` input. In this mode, the clock is used to select the channel to be examined and the output signal of the selected channel can be constantly observed. Consequently, the behaviour of a particular channel can be studied, with i.e. a triggered physical signal (e.g. from the `cal` input, or from an infrared laser beam on the silicon detector). By way of the test mode, the preamplifier gain of a specific channel can be surveyed: a 2 pF capacitor integrated in the VA enables to create the calibration pulse with a square signal. The test pulse thus generated is then added to the input pad signal.

4.7.3 The Hybrid Control Circuit (HCC)

In AMS-01, the TDR boards controlled the generation of the `holdb`, `dreset`, `ckb`, `shift_in_b`, `test_on` and `cal` signals. `shift_in_b` was necessary to enable the readout of the first VA. The remaining VAs were triggered by the `shift_out_b` issued by their preceding neighbour. This connection scheme presents a severe drawback: if an intermediate VA fails, the next chips never receive the `shift_out_b` signal i.e. the readout of the remaining VAs is inhibited.

Designed for the AMS-02 hybrid, the HCC completely pilots the VAs with four control signals (`S`, `SB`, `H`, `HB`). The `cal` signal is still produced by the TDR and sent through the cable to the hybrid. In addition, the HCC directly controls the shift-in input of each VA. Thus, if a VA stops working correctly, it does not inhibit the readout of the other VAs. The HCC provides:

- 6 shift-in signals (`Shinb`)
- 6 digital reset signals (`Dreset`)
- 4 clock signals (`C1k`)

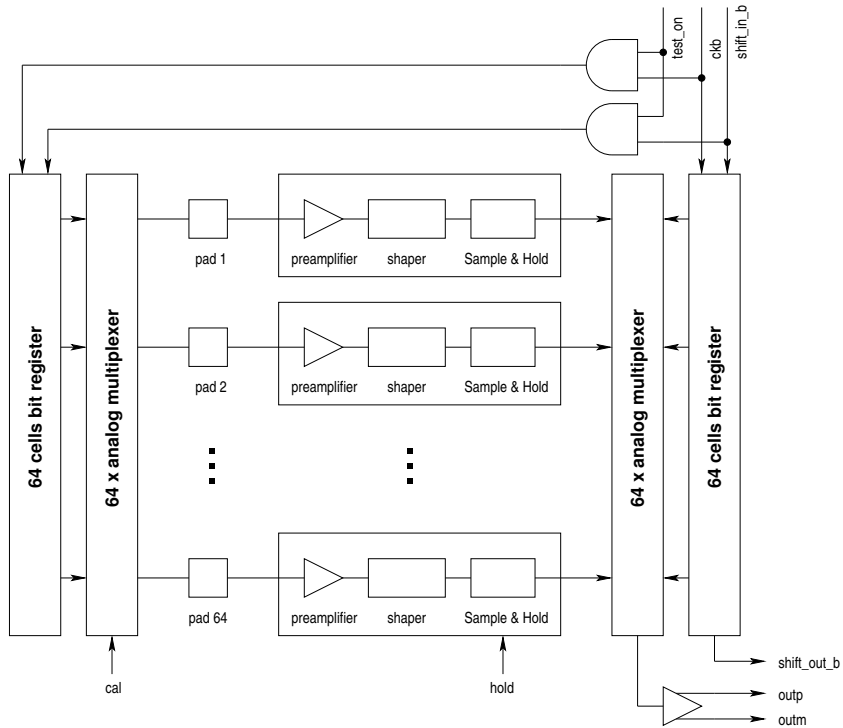


Figure 4.16: VA64_hrd9a architecture [57].

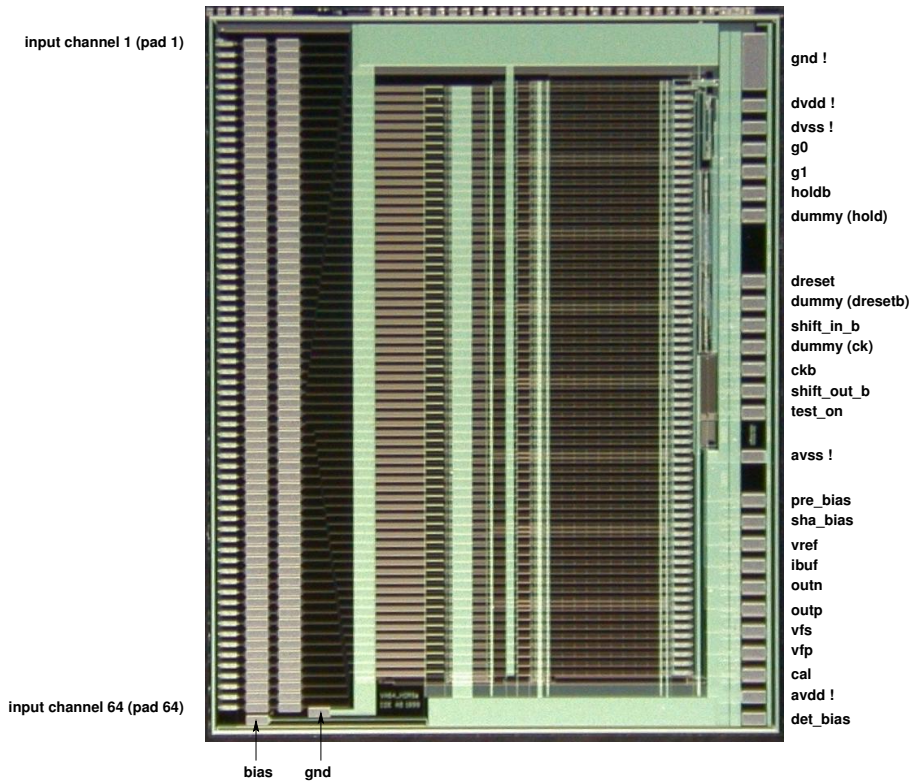


Figure 4.17: VA64_hrd9 pinout.

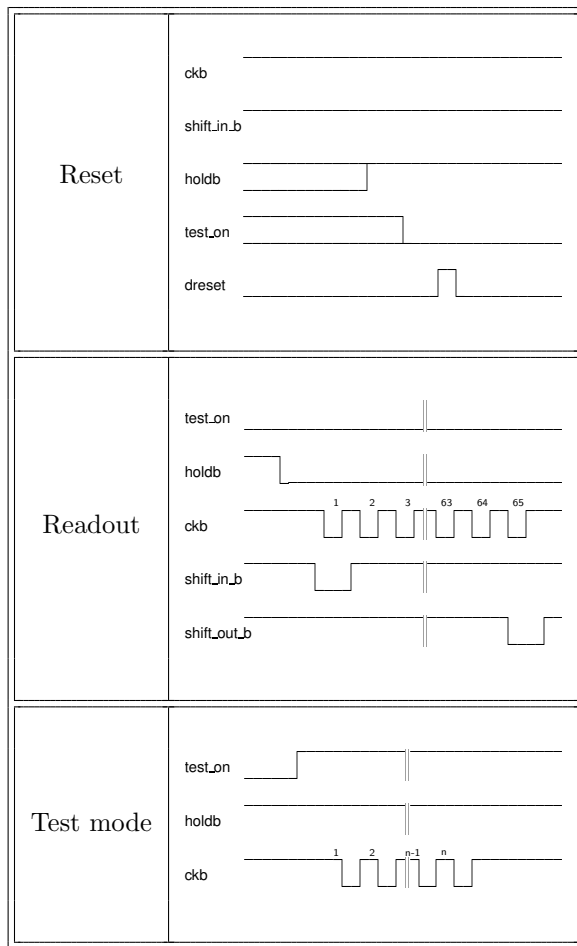


Table 4.5: VA control sequences.

- 1 hold signal (HoldVA)
- 1 teston signal (Teston)

The four clock signals result from the combination of S and SB: $CLK_{i=1..4} = \text{NOT}(S \text{ AND NOT}(SB))$. As an example, figure 4.18 describes the VA readout sequence.

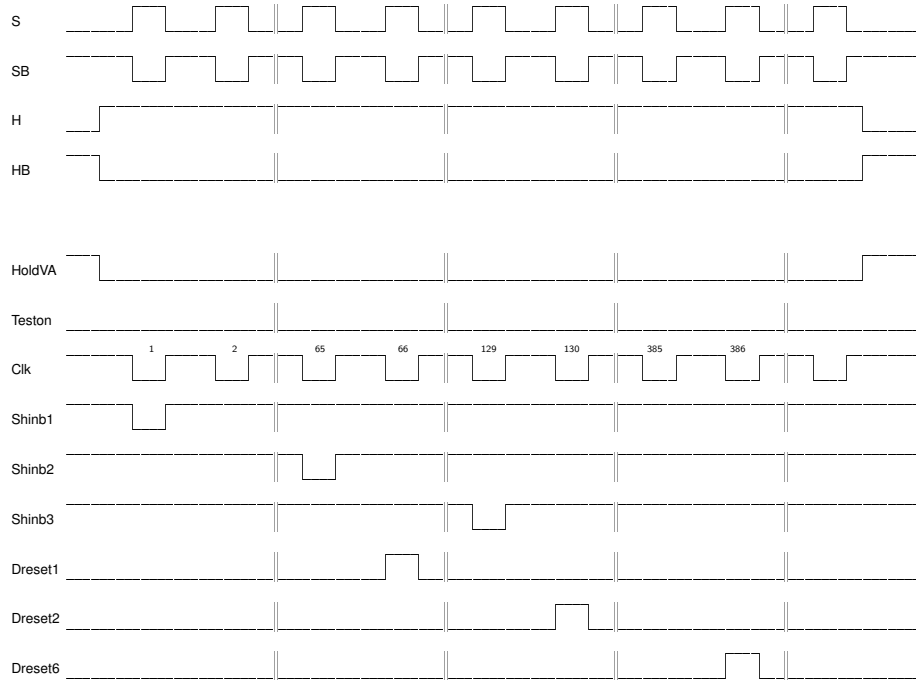


Figure 4.18: HCC control sequence: VA readout.

4.8 Ladder bias

To better control the strip voltages with respect to the VA input channel voltage, the bias voltage is split into three stages, as shown in figures 4.19 and 4.20. The voltage between the S and K local grounds (noted $lgnd_S$ and $lgnd_K$) is (improperly) called *bias voltage*. To adjust as best as possible the readout strip with the VA input voltage ($lgnd - 1$ V), it is possible to correct the voltage between the local ground and the guard ring. Knowing the mean voltage drop between the strips and the guard ring allows to choose a value minimizing the voltage difference between the capacitor terminals: if a decoupling capacitor is damaged, the current flowing into the amplifier will be minimized to limit the amplifier saturation [43]. Due to the design evolution between AMS-01 and AMS-02 both cases will be treated.

4.8.1 AMS-01

Figure 4.19 describes the bias scheme:

- V_{bias} is the voltage between the local ground S ($lgnd_S$) and the local ground K ($lgnd_K$);
- The local ground S corresponds to the system ground;
- V_{guardS} is the voltage applied between the guard ring S and $lgnd_S$;
- V_{guardK} is the voltage applied between the guard ring K and $lgnd_K$;
- R_{polS} is the mean polarization resistance between the guard ring S and a p-strip;

- R_{polK} is the mean polarization resistance between the guard ring K and an n-strip;
- p_{strip} symbolizes a p-n junction, an individual strip on the p-side.

The schematic of figure 4.19 is symbolic: a p-strip is not individually connected to the n-guard ring. Actually, it is resistively and capacitively connected to all the n-strips. The schematic allows a simplified representation of the biasing. As indicated earlier, the silicon is operated at reverse bias. Thus a positive voltage is applied on the n-side, i.e. the K-side, while the negative voltage is applied on the p-side, i.e. the S-side. In the case of AMS-01 detectors, the voltage drop U_{pol} between guard ring and strips was of some hundreds millivolts for the K-side, and around 3 V for the S-side at operating bias voltage. Neglecting the voltage drop at R_{polK} leads to $V_{guardK} = -1V$. For the S-side, we need

$$-V_{guardS} + lgndS = -U_{polS} + lgndS - 1$$

i.e. $V_{guards} = U_{polS} + 1$. Finally, if we consider to apply a voltage V_0 between guard ring S and guard ring K, the voltage applied between both local grounds will be:

$$V_{bias} = V_0 - V_{guardK} - V_{guardS}$$

For example, if $V_0 = 50V$ then $V_{bias} \cong 50 - 3 - (-1) = 48V$. To achieve better comparisons between single sensor current measurements and ladder measurements, one should take into account this difference. Note the confusing terminology: when measuring single detectors, V_{bias} is the voltage between n- and p- guard rings, while on a ladder V_{bias} usually corresponds to the voltage difference between the local grounds.

Two $6.8 \mu F$ capacitors, located on the K-hybrid, are connected in series between the two local grounds. They ensure a bias voltage stability in case of load fluctuation. Moreover, they act as a filter from the power supply. The capacitors are in series for redundancy: if one capacitor is damaged, a short between the local grounds is avoided thanks to the second capacitor.

4.8.2 AMS-02

The biasing method (fig. 4.20) is similar to the one described in section 4.8.1. An addition to the AMS-01 design is the low-pass filters (the $10 k\Omega$ resistors and the $470 nF$ capacitors) between the guard ring and the local grounds. The average voltage drop between n-strips and n-guard is of the order of 4 V, much larger than for AMS-01. This means that $lgnd_K - 1 + 4 = lgnd_K + V_{guardK}$ leads to $V_{guardK} = 3V$. In the case of AMS-02, $V_0 = 80V$. Thus $V_{bias} = V_0 - V_{guardK} - V_{guardS}$ and the difference between V_0 and V_{bias} is larger than for AMS-01. Note also the simplification of the schematics due to the absence of the protection diodes. This design points out a weakness of the hybrid design: if a bias line (S or K) is broken, the ladder will be biased through the VA channels, once at least one capacitor channel is shorted due to an overvoltage on the terminals. In such a case, the corresponding amplifier may be saturated, hindering then signal transmission. The protection diodes would have prevented the hybrids from this circumstance, even though they were initially not designed for this purpose.

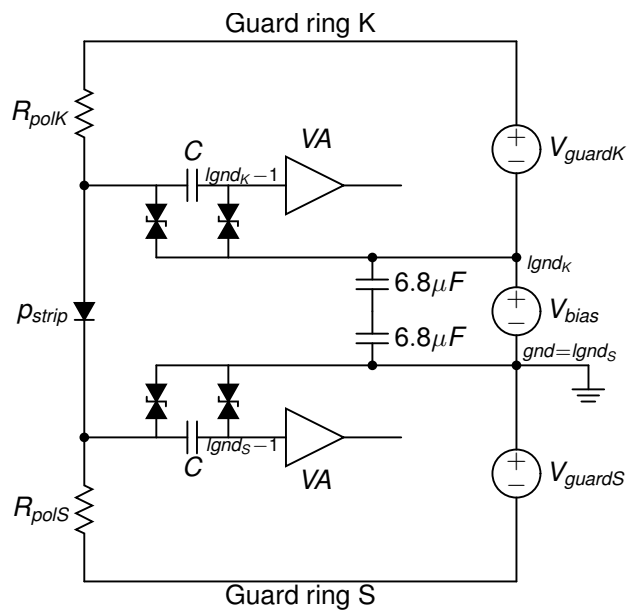


Figure 4.19: Biasing of an AMS-01 ladder.

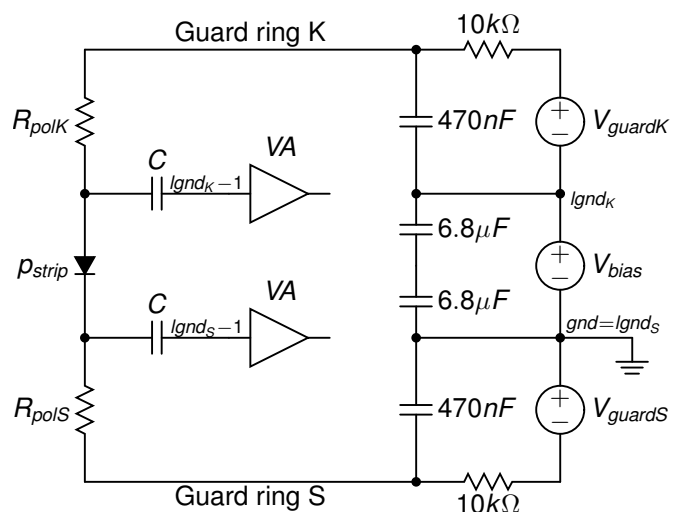


Figure 4.20: Biasing of an AMS-02 ladder.

4.9 Remarks

The silicon tracker is composed of 192 ladders. The ladder length ranges from 7 to 15 sensors. The silicon sensor properties, as well as the front-end electronics were presented. More details regarding the ladder structure are described with the ladder assembly, in the next chapter.

Chapter 5

Ladder assembly

5.1 Introduction

The ladder assembly involves three sites: the University of Geneva (in collaboration with an ETHZ team at CERN), the University of Perugia, and an Italian industry: G&A Engineering. The assembly sequence and quality control criteria are identical for the three sites. We distinguish three assembly steps: silicon detectors final qualification, assembly phase 1, and assembly phase 2. The phase 1 corresponds to the silicon sensor gluing, the hybrid gluing and the micro-wire bonding. Assembly phase 2 corresponds to the hybrid final operation, feet gluing and metallized foil wrapping. Once the assembly phase 2 is completed, the ladder is ready to be installed on a tracker plane (integration). G&A has in charge most of the phase 1 production, while Geneva is the only site performing phase 2. Furthermore the plane installation is realized in Geneva. Table 5.1 sums up the production activities of the three assembly lines.

Site	Silicon tests	Phase 1	Phase 2	Integration
Geneva/ETHZ		■	■	■
Perugia	■		■	
G&A	■	■		

Table 5.1: The three production lines and their activities.

The next sections present the ladder assembly sequences, from the silicon sensor gluing to the metallized foil wrapping.

5.2 The Geneva assembly line

Silicon microstrip detectors are sensitive devices: producing ladders is thus not an easy task and cannot be performed in a standard laboratory. It is mandatory to work in a clean room environment to avoid dust particle contamination, which presence could degrade the silicon quality (mechanically or electrically). As the detector spatial resolution is of the order of

some microns, precise alignment and survey tools are needed. The assembly conditions must minimize the impacts on the silicon sensor qualities. Furthermore, the reproducibility of the ladder properties, in terms of mechanical and electrical parameters is mandatory. Those conditions impose the use of typical industrial equipments, as well as strictly controlled environments, such as clean rooms.

Clean rooms are needed to perform the ladder assembly. Working in such an environment imposes constraints on the operators: special clothes, gloves, masks, caps must be worn.

To check the precise alignment, a Mitutoyo metrology machine (equipped with a touch probe and an optical pattern recognition system) is used. To perform efficient, precise and yet fast gluing procedures, a CAM/ALOT gluing machine with a volumetric glue dispenser is used. Two binocular microscopes are also available for all precise handling or inspections. Finally, a vacuum network is needed, to ensure the stability of the silicon detectors once they are precisely aligned.

A grey room is available to perform electrical verifications on the ladders during the multiple assembly tests. Also, visual inspections are realized with a binocular microscope equipped with a video camera connected to a computer. In the same room, the last assembly steps are fulfilled, before the ladders are installed on the tracker plane.

Although the Geneva clean rooms are equipped with a wire bonding machine, the AMS group collaborates with an ETHZ group working at CERN to perform this task. The reason for this choice was to avoid a bonding work overloading due to the global needs of the particle physics department in Geneva. Given the considerable involvement of the ETHZ group in the AMS-01 ladder production, transferring the bonding activities to CERN was a good solution.

5.3 Assembly phase 1

The assembly phase 1 defines the operations starting from silicon positioning, and ending with wire bonding. Geneva university discontinued this task in March 2003, to allow a full involvement in the phase 2 activities. The following sections detail the phase 1 assembly steps.

5.3.1 Preparation

Before starting the ladder assembly, the total current of each sensor is measured a last time, to check the quality before assembly. If a sensor presents an unsatisfactory behavior, it is replaced. The detectors are then visually inspected on both sides with a microscope and all dust particles are removed using vacuum. The assembly jig surface is then cleaned with isopropyl alcohol and the jig is connected to ground.

5.3.2 Silicon positioning

Figure 5.1 shows how to differentiate the p- and n- sides of the AMS microstrip detector. The p-side is easily recognizable thanks to the second bonding pad raw. On the n-side, a

pattern, corresponding to a lack of metallization, is located at the same edge of the second p-side bonding pad raw.

To avoid electrical discharge, the operator should be connected to ground. This is usually the case as the clean room floor is grounded and the overshoes used are conductive.

A metrology program assists the operator during the detector positioning procedure.

1. The pins are inserted into the holes corresponding to the leftmost detector. The pins have to be placed as shown in figure 5.2. The pins have a flat edge which must be turned by about 90° with respect to the silicon edge.
2. The silicon detector is laid n-side up, writing to the right (figure 5.2). First, the right side is put on the Teflon surface, near the pins, but without touching them. Then the silicon is gently slid against the right-side pins, lowered until all the detector lies on the Teflon surface. Finally, the sensor is slid until it touches the upper pin. Still maintaining the detector against the pins, the vacuum is switched on under its position. Only then, the detector is released from the manipulating tool.
3. Once the detector is placed, the metrology program moves the camera above the silicon alignment pins to check if the silicon edges actually touch the alignment pins.
4. If there is no contact with one pin, the detector is removed and the procedure is started again.
5. Once the detector is correctly aligned, the pins are removed: each pin is turned so that the flat edge is facing the silicon edge, to avoid mechanical contact with the sensor. The pin can now be removed. It must always be held with the thumb and the index, both fingers permanently remaining on the Teflon surface: this helps avoiding collisions between the pin and silicon when the pin comes out of the hole.
6. As a first check, the corner metrology circles are measured.
7. The procedures 1 to 6 are repeated for the next detector.
8. Once all sensors are positioned the final metrology program is executed.
9. The metrology data are stored in a data base.

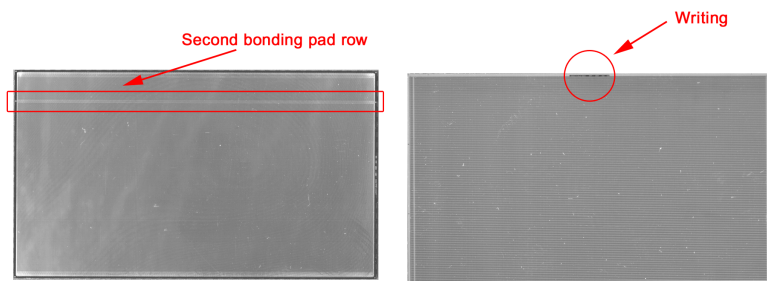


Figure 5.1: On the left: p-side of the AMS microstrip detector, on right: the n-side.

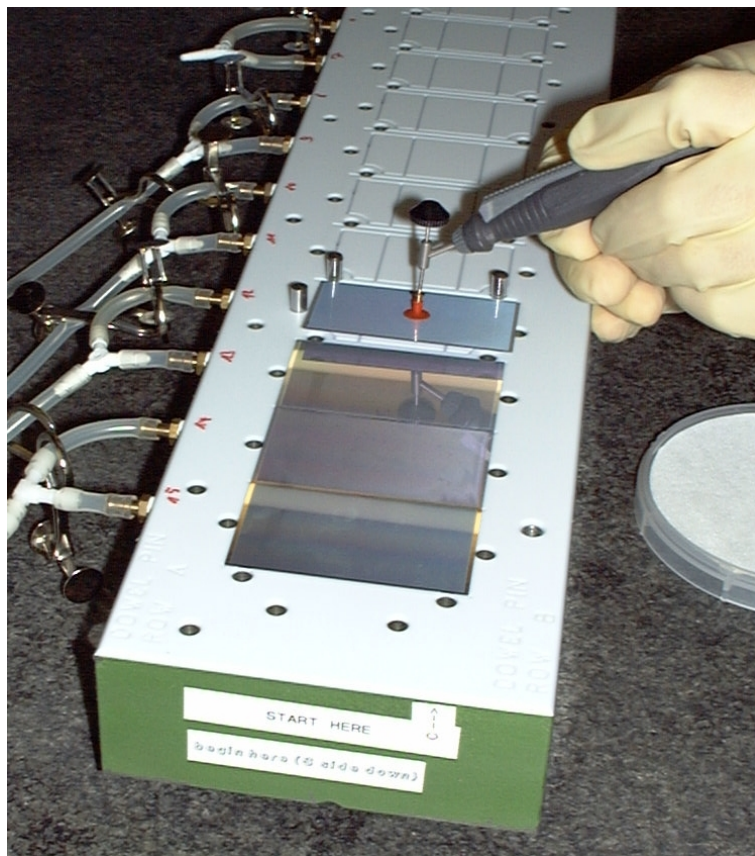


Figure 5.2: Sensor positioning. The detectors are longitudinally aligned with two pins, and transversely with one pin.

5.4 Long Upilex (K5/K7) gluing

For this manipulation, two jigs are needed: the Upilex alignment jig is used to prepare the Upilex cable for the transfer to the Upilex transfer jig, used for the glue deposition on the Upilex surface and for the Upilex gluing on the silicon detectors (figure 5.4).

1. Before gluing, the Upilex length and quality need to be checked. If necessary, the Upilex and jig surfaces are cleaned. The Upilex end has to be examined with care: in the corner, three crosses, two half cut, and one complete should be visible, as shown in figure 5.3.

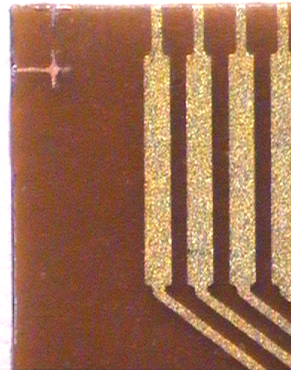


Figure 5.3: The crosses in the upper left corner show how the long Upilex should be cut

2. Alignment pins are inserted on the Upilex alignment jig.
3. The Upilex is delicately placed (gold strips up) to touch the pins.
4. To ensure that the Upilex lies flat on the jig, glass plates are deposited on the surface (figure 5.5).
5. Once the vacuum is switched on, the pins and plates are removed.
6. The jig positioning pins are put in the upper left and lower right holes (visible in figure 5.4, they will help positioning the transfer jig).
7. When the transfer jig is placed, vacuum is switched on. Then vacuum of the alignment jig is switched off.
8. The transfer jig is removed (fig. 5.6). The Upilex position is then checked a last time under the microscope.
9. Araldit 2011 is deposited with a volumetric dispenser.
10. When the glue deposition is completed, the Upilex transfer jig is placed on the ladder assembly jig (fig. 5.7).

The polymerization time is about 8 hours.

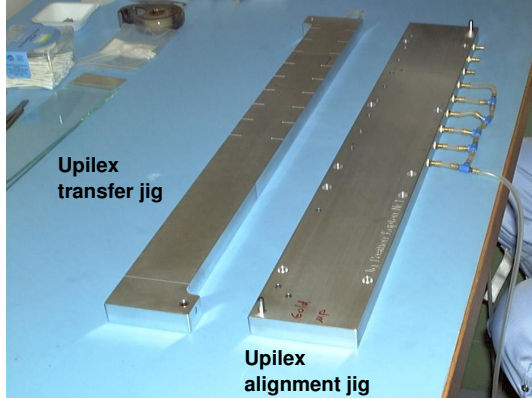


Figure 5.4: Jigs used to glue the long Upilex.



Figure 5.5: Upilex on jig. The alignment pins and the glass plates used to flatten the Upilex are visible.

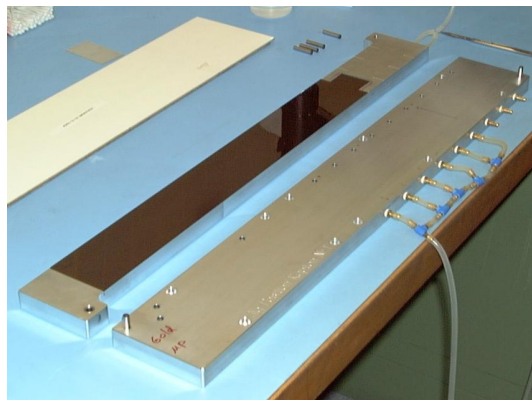


Figure 5.6: Upilex ready for glue deposition.



Figure 5.7: After glue deposition, the transfer jig is placed on the silicon jig.

5.5 Reinforcement gluing

1. First of all, the reinforcement is inspected, in particular, possible foam burrs are removed.
2. A large glass plate is prepared as shown on figure 5.8: 80 μm thick adhesive films are put on the plate, separated by about 10 cm.
3. The glue is dispensed on the glass and expanded with a spatula to obtain an uniform surface between both films (figure 5.9).
4. When the glue layer is ready, the reinforcement is laid on it, carbon fiber up (figure 5.10). After a few minutes, the reinforcement is removed and put on the table, Airex up. This allows the glue to expand on all the Airex surface.
5. The last step is repeated a few minutes later.

Meanwhile, the Upilex gluing jig is removed:

1. The vacuum of the Upilex transfer jig is switched off.
2. The transfer jig is delicately (in the improbable case that the glue expanded to the Upilex transfer jig) removed.
3. The reinforcement alignment bars (upper and left) are inserted as shown on figure 5.11.
4. The reinforcement is disposed on the Upilex, slightly pushed against the bars.
5. The last bar is screwed, as shown in figure 5.12.
6. Finally, to apply pressure on the reinforcement, glass plates with lead blocks are placed on the carbon surface (figure 5.13).

After 2-3 hours, the lead blocks and glass plates are removed.



Figure 5.8: Reinforcement gluing: Araldit 2011 is dispensed on a large glass plate.



Figure 5.9: The glue is spread with a spatula, the glue thickness will be close to 80 μm .

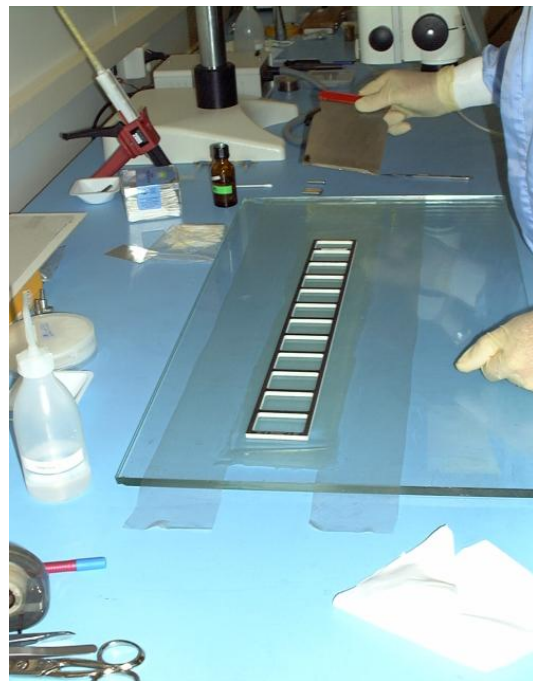


Figure 5.10: The Airex surface of the reinforcement is laid on the glue film.

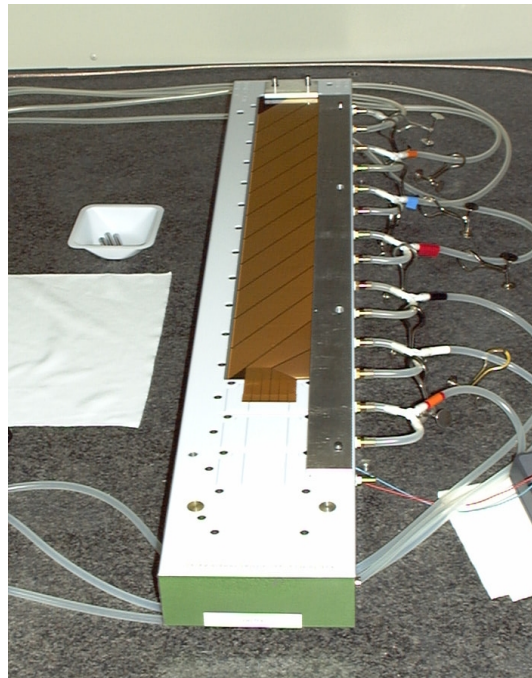


Figure 5.11: Alignment bars are inserted, to guide the reinforcement application.

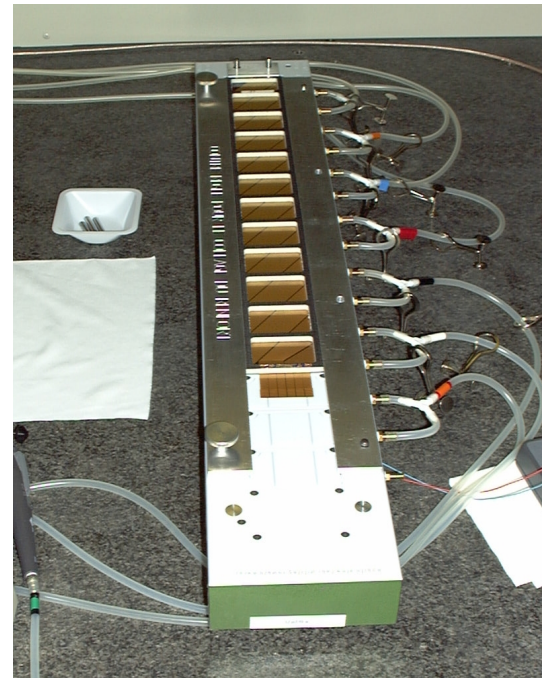


Figure 5.12: The last bar is fixed with screws.



Figure 5.13: Lead blocks on glass plates are placed on the reinforcement.

5.6 K-hybrid gluing

The K-side bonding jig and K-side extension are the tools needed during there operations. A black alignment tool is placed on the position corresponding to the ladder length. The alignment pins are screwed, round edge facing silicon position. The ladder is delicately put first against the alignment tool then against the pins (fig. 5.14).

Once the ladder is positioned, vacuum is set and clamps are screwed, then vacuum is switched off. The hybrid is screwed on the extension, using an alignment pin and the extension positioners. The extension is screwed to the K-side bonding jig. The Upilex position with respect to the hybrid must be checked: if not correctly aligned, the hybrid is re-aligned. A protective blue tape is applied on the Upilex bonding pads as shown on figure 5.15 . The extension is then removed, and Araldit 2011 glue is dispensed on the hybrid (non-volumetric dispensing). A presser is screwed on the extension as shown on figure 5.16. The glue expansion out of the Upilex is checked under microscope: an absence of glue usually denotes a locally bad surface contact between the Upilex and the silicon or the hybrid. In such exceptional cases, the operator must apply some pressure on this spot, with appropriate tools. After a few hours, the gluing jig is removed.

5.7 S-hybrid / K6 Upilex gluing

1. The ladder is transferred to the S-side bonding jig.
2. The S-hybrid is placed using the pin and extension positioners. The hybrid is fixed with the central screw.
3. Blue tape is placed on the Upilex bonding pads as shown on figure 5.17.
4. The K6 Upilex is aligned on the gluing jig (see figure 5.18).
5. If the hybrid is not flat, a presser is screwed as shown on figure 5.19.
6. The gluing jig is screwed on the extension.
7. The correct position of the Upilex with respect to the hybrid is checked.
8. The correct position of the Upilex with respect to the silicon is checked. If necessary, the silicon is realigned.
9. The K6 gluing jig is removed, and Araldit 2011 glue is deposited on the Upilex surface, with a non-volumetric dispenser.
10. The jig is placed back on the S-side extension (see figure 5.20).
11. The glue spread is surveyed under microscope.



Figure 5.14: Ladder on the K-side bonding jig. The ladder is aligned with help of pins and an alignment tool (on the left). The ladder is fixed with clamps, and the hybrid is screwed on the extension (on the right).

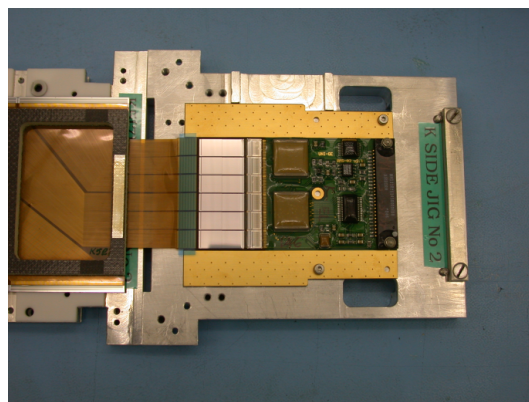


Figure 5.15: Blue tape is used to protect the bonding pads, in case the glue flows over them.

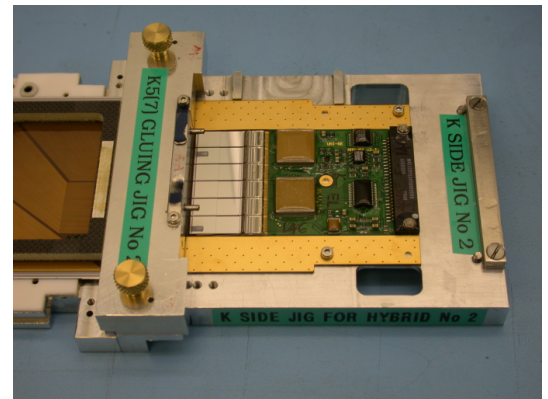


Figure 5.16: Last step of K-hybrid gluing: the presser is screwed.

5.8 Bonding

The Bonding schemes are described in appendix E. A ladder composed of n sensors needs $(n+1) \cdot 640$ bonds on the S-side, and $n \cdot 384$ bonds on the K-side, for a total of $1024 \cdot 1024 + 640$ bonds. The need of automatic bonding procedures is obvious.

5.9 Phase 2

After a careful ladder visual inspection, and electrical test, the hybrids need some additional manipulations before the feet are glued. A detailed procedure helps the operator to check the numerous control and assembly steps. The complete procedure is presented in appendix F. Here the main steps are summed up:

- The bias bonds between silicon and Upilex, and between Upilex and RCAMS #10 (S-side) or RCAMS #6 (K-side) are secured with Araldit 2011 glue.
- An Airex spacer, used to protect the bonds between RCAMS and Upilex from an accidental box contact is glued. The glue is only deposited on the RCAMS side, in case the hybrid is to be removed due to a later malfunction.
- Thermal grease is dispensed on the K-side box, and between both hybrids (at the VA locations, see fig. 5.23).
- A central column, used to fix together both hybrids is screwed and secured with Vibratite glue.
- The K- and S-side boxes are screwed. The final screws are installed and secured later, before the plane installation.

Once the hybrid boxes are installed, the ladder surface is cleaned, and the feet are glued.

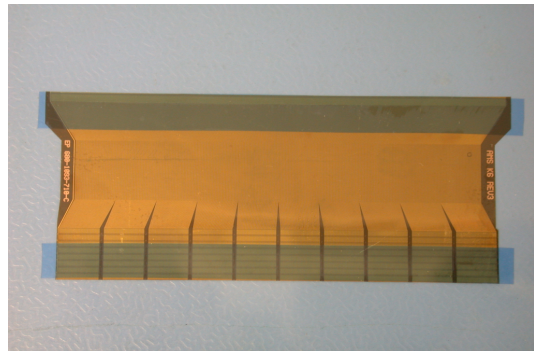


Figure 5.17: K6 Upilex with protection tape on the bonding pads

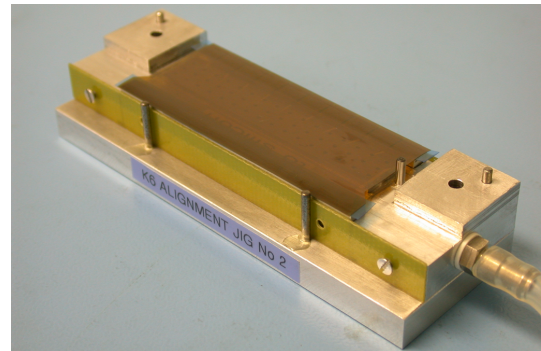


Figure 5.18: K6 Upilex on gluing jig. The metallized surface is facing down.

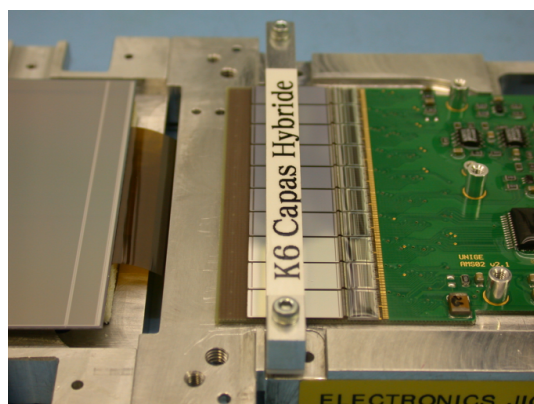


Figure 5.19: Presser used to flatten hybrid.



Figure 5.20: Gluing jig screwed on the S-extension.

5.10 Feet gluing

For this manipulation, two jigs are needed: the base, on which the ladder is fixed (S-side lying on the Teflon surface) and the feet gluing jig, on which the feet are screwed. There are four bases and at least one feet gluing jig for each ladder length.

Once the silicon surface is cleaned, the operator lays the ladder onto the base jig, the ladder being aligned thanks to Delrin pins (fig. 5.24). Once the ladder is immobilized with vacuum aspiration, the Delrin pins are removed.

The feet gluing jig is placed into the CAM/ALOT, and Araldit 138 is deposited with a standard dispenser, on the feet. The feet gluing jig is then inserted onto the base jig. After a few hours, the feet are unscrewed, and the feet gluing jig is removed.

Once the feet are glued, all the clean room operations have been performed, further manipulations will be realized in the grey room. The ladder is placed back into the transportation box, for an electrical test. If the ladder has not degraded, it is ready for the shielding wrapping operations.

5.11 Spacer gluing and shielding wrapping

5.11.1 Spacer gluing

As mentioned earlier, a metallized Upilex foil is wrapped around the ladder, connected to the electronics ground. For this purpose, an Airex spacer is glued with Araldit 2011 on the silicon surface. The gluing procedure is similar to the one for the reinforcement gluing on the long Upilex foil (see section 5.4). Figure 5.27 shows a ladder on the spacer bonding jig. The Airex spacer is placed on the silicon surface and aligned with a guiding jig made of plexiglas. A plexiglas lid, to apply pressure on the Airex spacer, is placed. Finally, brass loading blocks are laid on the lid. The curing time is around 8 hours.

5.11.2 Shielding wrapping

The metallized Upilex foil is placed on a wrapping table. The ladder is then laid on the table, guided with the feet. The feet are then screwed to immobilize the ladder on the table. Pushers are then fixed: they will help pushing and bending the foil, which present a rigidity due to the metal layer. Figure 5.28 depicts one side of the Upilex foil bent and positioned on the Airex surface. On the other side, the Upilex is not bent yet. To close the shielding, solder junctions are done with a rosin-free solder (tin-lead silver Sn62 type X39). Finally, the Upilex foils are soldered to the hybrid boxes. This constrains the ladder overall mechanics: for the inner plane ladders, the hybrids have an angle of 90° with respect to the ladder axis. For the outer plane ladders, the hybrids will lie flat. It should be emphasized that despite these operations seem simple, they actually are composed of numerous steps, needing care and precision. The operator follows a procedure (see appendix F) to ensure every step is successfully completed.



Figure 5.21: Airex spacer glued on S-hybrid. The left and right edges are machined to be compatible with the S-box.

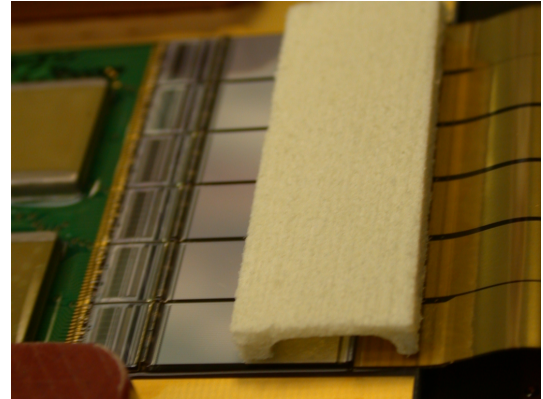


Figure 5.22: Airex spacer glued on the K-hybrid.

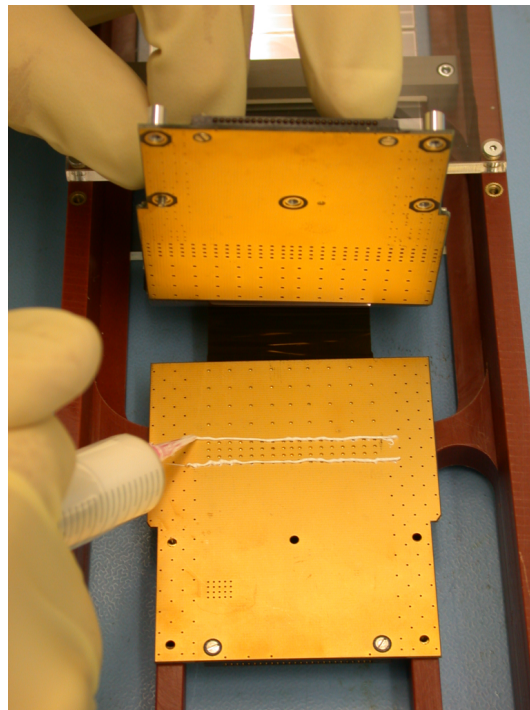


Figure 5.23: Thermal grease is dispensed between both hybrids, at the VAs location. The aim is to exhaust the heat produced by the VAs to the thermal bars to which is connected the K-hybrid box.

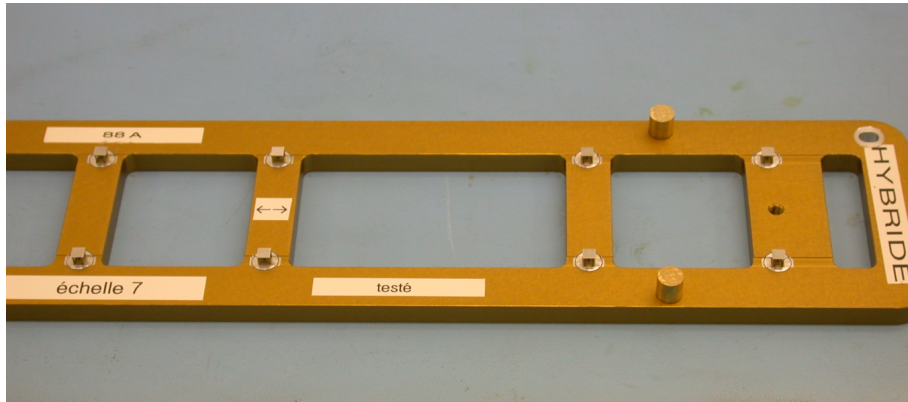


Figure 5.24: Feet gluing jig: the feet are screwed on the jig. Feet at the \leftrightarrow position are rotated by 90°. The jig is then laid into the glue dispensing machine.

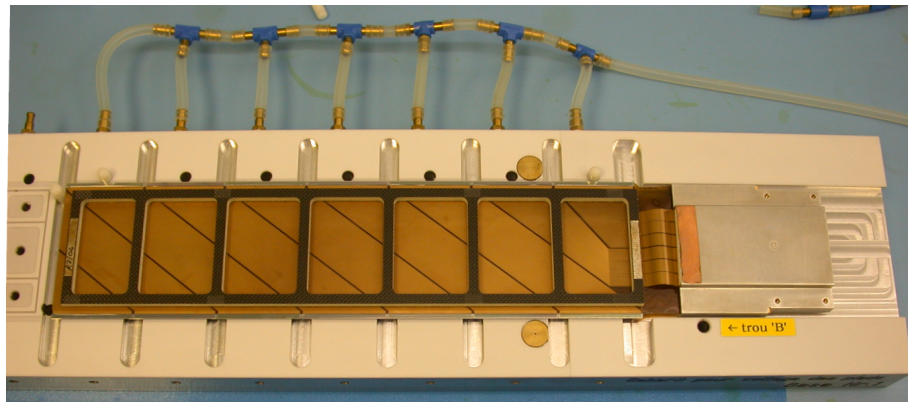


Figure 5.25: Base jig: the ladder is aligned with Delrin pins and fixed with vacuum.

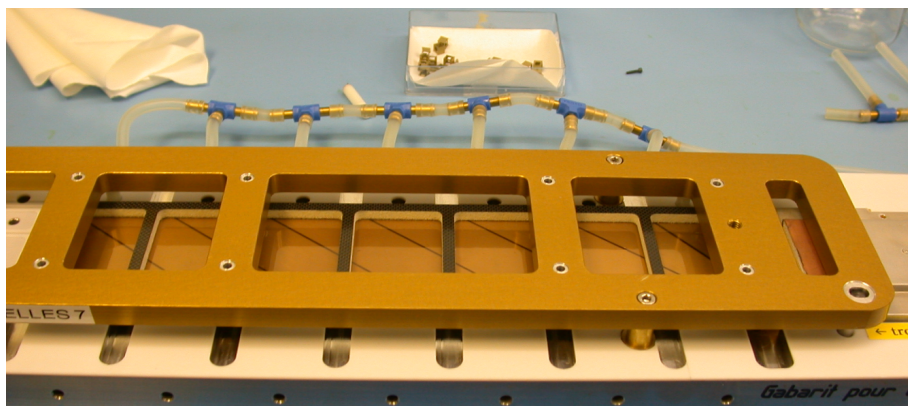


Figure 5.26: Once the glue is dispensed on the feet, the feet gluing jig is inserted onto the base jig.

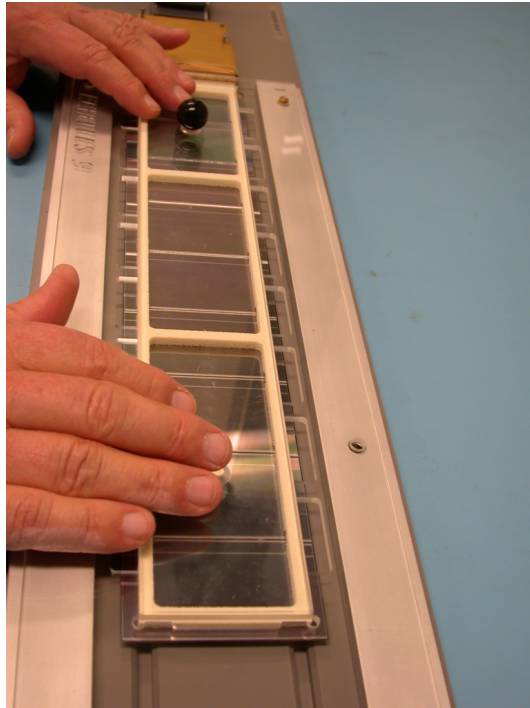


Figure 5.27: Airex spacer gluing. Once Araldit 2011 glue is dispensed on the spacer surface, in similar way as for the ladder reinforcement, the spacer is aligned with a plexiglas guide. A plexiglas lid is then laid on the spacer surface.

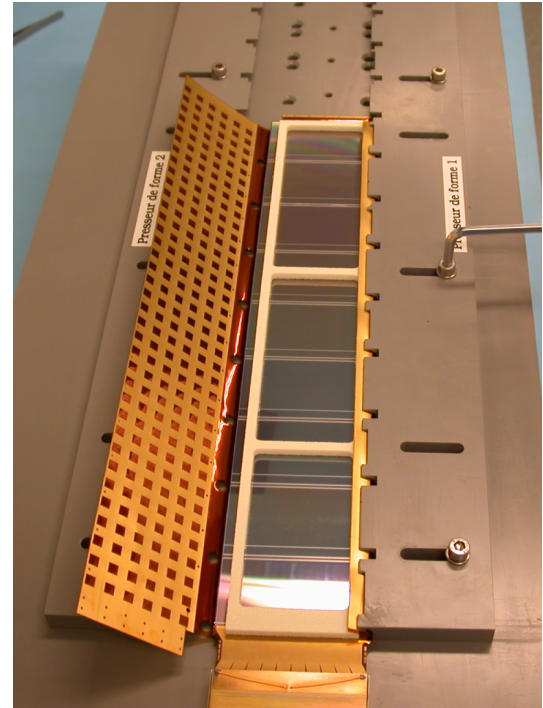


Figure 5.28: Upilex wrapping. The Upilex foil, then the ladder are placed on a table. The foil is bent over the ladder with pushers. The shielding is closed with rosin-free solder.

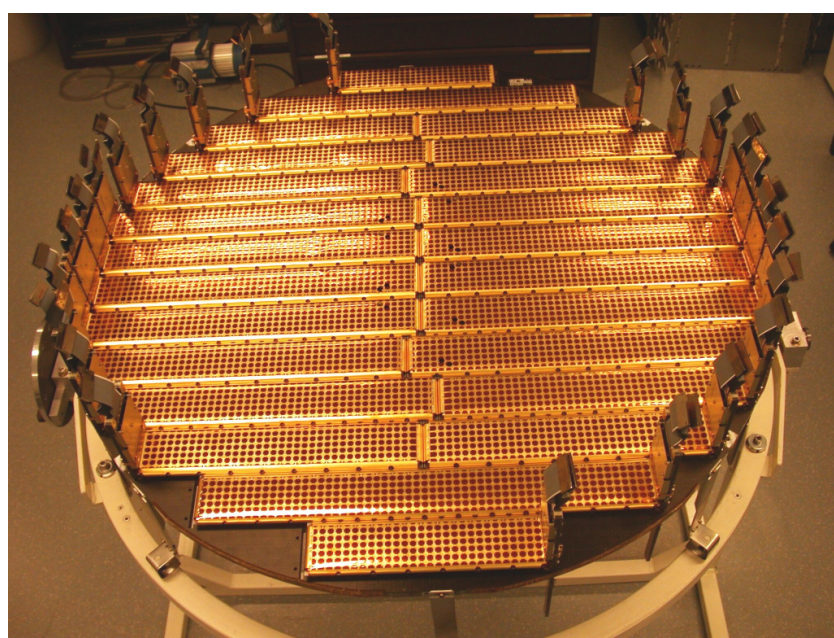


Figure 5.29: Tracker layer 2 equipped with its 24 ladders.

The ladder is ready to be installed on its assigned tracker layer. Figure 5.29 shows a picture of layer 2, with its 24 ladders installed.

5.12 Electrical tests

As soon as the bonding is completed, the ladder is regularly tested, to identify possible quality degradations. During such tests, the total silicon leakage current is measured at 80 V bias, and a standard calibration is performed. Also, a ^{90}Sr radioactive source is used to verify the VA gain performances. The electrical verifications are done:

- After bonding;
- For the ladders assembled in Italy, after reception in Geneva;
- After the feet gluing;
- After Upilex wrapping;
- After plane installation.

A ladder presenting a anomaly after an assembly step can be removed from the assembly sequence for further studies and eventually repair. The repair scenarios range from bond removal to hybrid replacement or even single sensor replacement, the latter operation being the most delicate.

5.13 Remarks

The sensor alignment is realized with only mechanical means. More elaborated systems with automatic alignment corrections for 7 up to 15 sensors would have considerably increased the costs.

The ladder assembly needs precise tools and a particular environment. Clean rooms offer the optimal conditions to limit the damage risks occurring during assembly (see chapter 6). The operations are most of the time delicate and need skillful operators. A paradox proper to these assembly conditions lies in the relative high number of modules to be produced: a routine may appear during the production, reducing the operator attention. It is the operator duty to constantly monitor his own behaviour, a not so easy task.

Chapter 6

Tests on silicon detectors

6.1 Introduction

Before restarting the ladder production for AMS-02, various tests to recommission the Geneva assembly line and the assembly procedures were made. A particular care was taken on the possible silicon quality decrease, as an important noise contribution comes from the silicon leakage current (see section 3.12).

The AMS-01 experiment was a success, and the tracker behaved perfectly. However the AMS-01 ladder production showed that the overall electrical quality decreased with the assembly steps. The Geneva recommission was the good opportunity to examine all the possible sources of degradation, and to perfect our assembly manipulations to reduce the possible accident sources. All these tests were done in a one-year period, starting in Spring 1999. Depending on the cases, direct measurements on the silicon sensors were done, or acquisition with assembled ladders were done, with a dedicated AMS-01 test system.

The observations lead to some clear conclusions. First, a passivation of the silicon sensors was necessary, as it protects the sensor from surface defects occurred during contacts with the assembly jig. The assembly steps had to minimize the surface contacts between the junction side and jig surfaces. In particular, this need implied to glue the hybrids at the place where the bonding was done. For the same reason, the silicon surface needed to be cleaned to avoid a single dust particle to remain when the junction side had to lie on the jig surfaces. A particular step of the AMS-01 assembly was also adapted. Before gluing the feet, the reinforcement surface was sanded to improve the glue adhesion between the carbon fiber surface and the feet. This procedure was done while the ladder was lying on the base jig. For AMS-02, it has been decided to sand the reinforcement carbon fiber surface before the ladder assembly.

Finally, the tests described in this chapter also helped us to better understand the calibration results, and to relate some noise properties with particular strip or hybrid damages.

6.2 Test equipment and procedures

To evaluate the silicon detector properties, two main methods are available. Either we measure the silicon sensor intrinsic properties on a probe station, or we test the full ladder properties, via a data acquisition system.

6.2.1 Probe station measurements

As the sensors need the best possible cleanliness, all measurements were performed in a clean room at the Department of Nuclear and Particle Physics (DPNC) at the University of Geneva. People entering the clean room wear special antistatic clothes and shoe protections to prevent dust pollution. Also, when manipulating silicon sensors, gloves are worn, as well as a mask and a special cap. The devices are tested on a probe station (Dr. G. Maehlum Electronic Test

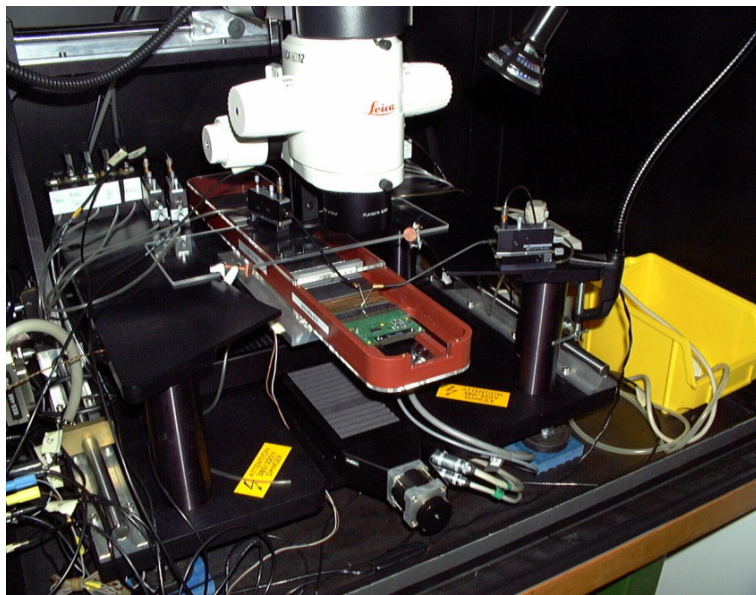


Figure 6.1: An AMS-02 ladder under test on the probe station table. The probe station is also equipped with micropositioners and a microscope.

Equipment, fig 6.1) shielded from light, as visible light would have enough energy to produce electron-hole pairs, increasing the leakage current. The probe station box is closed with a front panel, held by four screws. A positive voltage is normally applied on the probe station table (chuck), the electric contact with the device under test being performed by means of a conductive rubber sheet (Parker-Hannifin CHO-SEAL 1350). A good electric contact and mechanical tightness is ensured by vacuum applied through the chuck. On the upper side of the device, needles held in micropositioners (Karl Suss PH100) allow electric connections with particular elements. We performed measurements with the following instruments, all controlled by computer programs developed in LabView:

- Keithley electrometer 617

- Keithley electrometer 6512
 - HP LCR-meter 4263A
 - Keithley voltage source 6517
 - Keithley voltage source 230

As the LCR-meter cannot internally apply voltages greater than 2 V, an external electric circuit allowing higher bias must be used: figure 6.2 shows the schematics of the circuit, which accepts an external bias up to 1000 V. Figure 6.3 shows the measurement connections to the circuit and to the device under test.

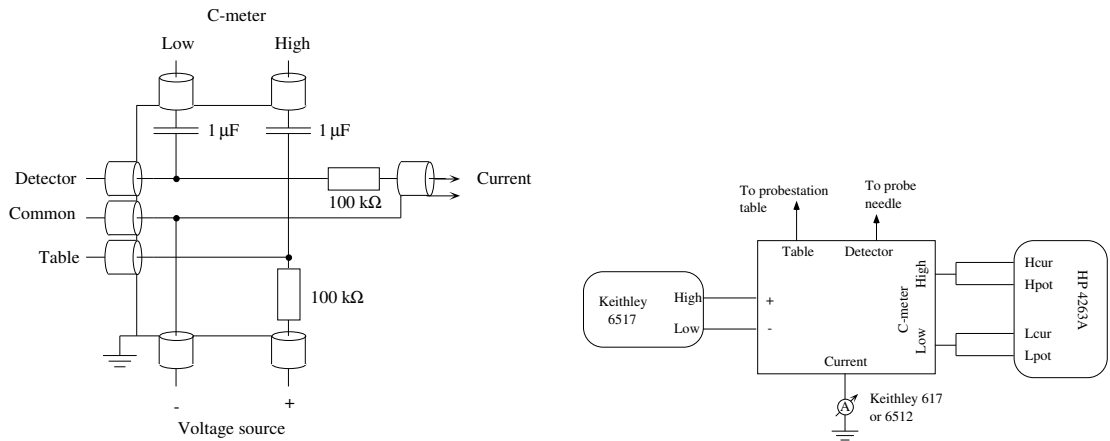


Figure 6.2: External circuit enabling voltages greater than 2 V for HP 4263A measurements.

Figure 6.3: C-V measurement setup.

6.2.2 Tests performed in probe station

The probe station equipment is most of the time used to test the silicon sensor properties: total dark current, individual strip current and depletion voltage. It is also used to characterize RCAMS chips: capacitance, parallel resistance and occasionally breakdown voltage of each RCAMS channel are measured.

Various configurations have been used to measure the total leakage current. The simplest one is to lay the detector on the conductive rubber, p-side up: the positive voltage is applied on the table (on which the n-side lies), the bias is then grounded through an electrometer, thus measuring the total current. This configuration, though, does not reflect the actual sensor operation, as n-strips are directly biased. Dedicated jigs to allow single connection to the n-side guard ring and to the p-side bias, by way of a micro bond were developed. This configuration improves the measurement conditions, this biasing connection avoiding the use of needles. Indeed, the table movements may infer a contact loss of the bias needle during the measurements.

Ladder total and strip current measurements have also been made. The ladder, in the transportation box, is fixed on the probe station table. The bias, when possible, is accomplished via the hybrid connector. If the ladder is not equipped with hybrids, then connection is realized by contact with the K5 Upilex cable and a needle on the p-side bias. In the case of a strip current measurement, and the S-side hybrid is absent, the bias micropositioner is placed on the transportation box. Operations involving measurements of ladders are delicate and need special care.

C-V measurement - Depletion voltage

A typical C-V measurement is shown in figure 6.5. The behaviour described in paragraph 3.5.2 is recognisable. Nevertheless, the capacitance measurement is highly frequency-dependent as shown in figure 6.4 for an AMS-01 detector. The lowest frequency (100 Hz) gives in our case the most realistic results. A simple calculation allows to estimate the expected capacitance. When the sensor is fully depleted, its capacitance stays constant to a value of (see equation 3.47):

$$C_{det} = \epsilon\epsilon_0 \frac{S}{L} = 11.7 \cdot 8.854 \text{pF} \cdot \frac{70.565 \text{mm} \cdot 39.832 \text{mm}}{300 \mu\text{m}} = 971 \text{pF} \quad (6.1)$$

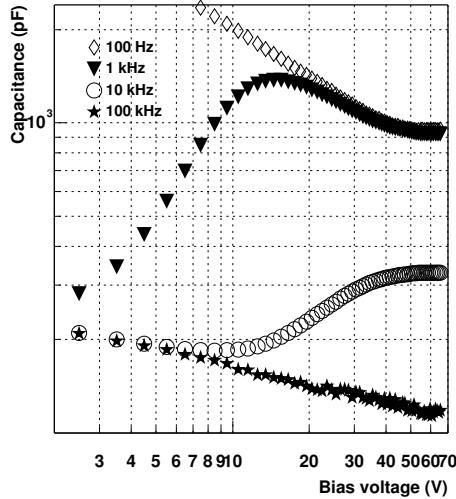


Figure 6.4: C-V measurement of an AMS-01 sensor, for different frequencies. 100 Hz gives the most realistic result.

The aim of the C-V measurements is to determine the sensor depletion voltage. Two methods were used: the first consisted in fitting the curve to an αV^β function both before and after full depletion. The second method was to plot $\frac{1}{C^2}$ as a function of V and to fit to linear functions. In both cases, the intersection of the two curves determines the depletion voltage, as shown in figure 6.5.

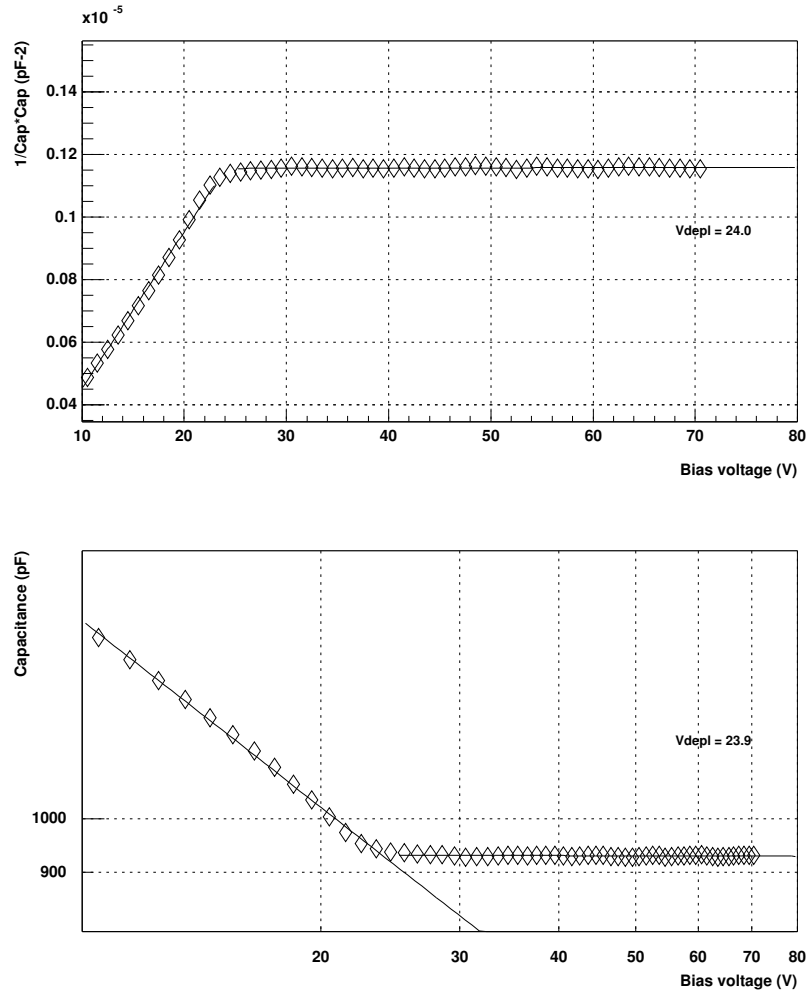


Figure 6.5: Two fit methods to determine the depletion voltage of a sensor (here an AMS-01 detector). The depletion voltage corresponds to the voltage at which the capacitance remains constant.

6.2.3 Ladder calibrations

The ladder test hardware is composed of a light tight metal box, a readout board, a computer and power supplies for the hybrid electronics, the test board and the ladder bias.

AMS-01

The AMS-01 test hardware was composed of power supplies for the hybrid electronics and silicon bias, and an ISA PC-board, to which were connected the ladder cables. A description of the acquisition board is found in [58]. The test box is connected to the computer, to reduce the electronics noise. The AMS-01 test software, written in Turbo-Pascal and run under MS-DOS, is composed of following programs:

- **calib** calculates the channel pedestal, noise and gain, and determines the channel conformity, and stores those information on disk..
- **cluster** is used to find out cluster signals when the ladder is used with a ^{90}Sr radioactive source.
- **dump** allows to store raw data, i.e. the 1024 channel ADC values per event, for a later analysis.
- **scope** displays the ladder response for each readout event. In particular, it helps isolating noisy channels, as well as the position of a radioactive source, or laser diode. Also, **scope** is an useful tool to individually test each VA channel, in calibration mode, looking at the channel response as a function of time for an input signal of preset amplitude.

AMS-02

The AMS-02 test system differs from the AMS-01 version in many aspects. First, to suppress the electronics noise generated by the computer, the acquisition board is located in a separate test box, connected to the computer via the parallel port. The AMS-02 hybrid schematics significantly differs from the AMS-01 version, and the acquisition board schematics needed to be adapted.

The acquisition software, run under linux, presents many improvements. It has been written in C++, using the ROOT [59] libraries. All AMS-01 programs have been merged into one integrated software, named **TDR**. The calibration procedure, in addition to the parameters saved in AMS-01, also stores the raw noise (see equ. 3.90), which presents interesting information about the sensitivity of a particular channel to the VA common noise. Also, the calibration process allows to directly save the raw data, thus allowing further comparisons between various calibration parameters. The source tests also produce two separate files, one with the ADC raw data, one with the reduced data (i.e. the cluster information).

6.3 Tests on ladder H12 PI 015

6.3.1 Introduction

The ladder H12 PI 015 has been built in 1997 to be placed in the AMS-01 silicon tracker. In Geneva a test before feet gluing was performed, and the ladder had a leakage current of $60 \mu\text{A}$ at 100 V bias. After feet gluing the leakage current increased drastically and the ladder was rejected. Before assembly, the total leakage current at 100 V of the sensors composing the ladder was $40 \mu\text{A}$. H12 PI 015 was regularly tested and its leakage current never was below $160 \mu\text{A}$ for a 92 V bias voltage. The aim of the tests described in further sections was to find the origins of the high ladder current, i.e. whether one or more sensors were involved, and possibly identify the origins of the defects.

Some noise characteristics were also studied, in particular the noise as a function of the number of connected sensors.

The main conclusion we got from these tests was that sensors close to the feet positions presented leakage current values larger than before assembly.

6.3.2 Procedure

Every time the ladder was modified, the leakage current was measured and a calibration was performed for various bias voltages, usually from 80 V to 100 V with a step of 5 V. We call “modification” the removal of bonds between strips, or bias lines, on the S- or the K-side. When the twelve sensors were connected, measuring above 85 V was not possible, because of the too high leakage current and the insufficient capabilities of the power supply. The calibrations were performed with an AMS-01 PC-card system, using the `calib` program.

The disassembly tests have been split into four steps:

1. First, bias bonds as well as strip bonds have been sequentially removed (step 1).
2. When only two fully connected sensors remained, we reconnected the biases of all the sensors and removed sequentially the bias lines (step 2). The initial S-side configuration is schematically depicted in figure 6.6.
3. Then, with only two fully connected sensors, we bonded again the K-side biases, and measured the individual leakage current of sensors 3 to 12 (step 3). The S-side configuration is shown in figure 6.7.
4. Finally we removed the S-side bonds between sensors one and two (step 4).

6.3.3 Leakage current evolution

Figure 6.8 shows the ladder leakage current measured during steps 1, 2 and 4 as a function of the number of sensors connected. These measurements are compared with the individual sensor leakage current values before ladder assembly, and during step 3. For steps 1 and 2, the values are obtained indirectly, in comparing the ladder leakage current before and after disconnecting a sensor.

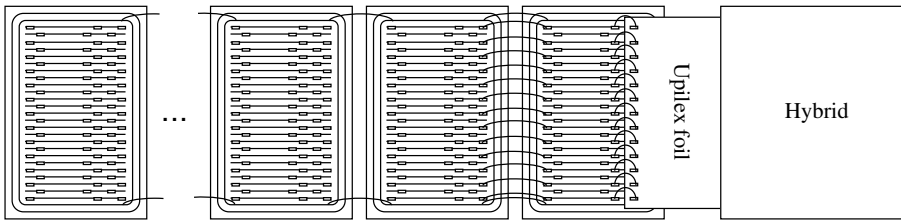


Figure 6.6: H12PI015 initial S-side configuration for step 2.

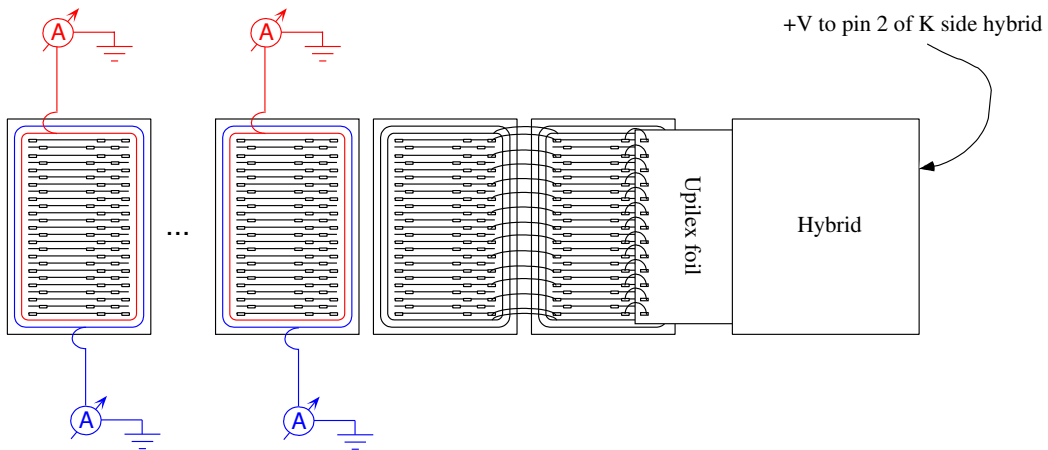


Figure 6.7: H12PI015 S-side configuration for step 3.

Clearly, the ladder leakage current remains higher than expected whatever the number of connected sensors is. The high ladder leakage current is due to the contribution of many sensors, and the leakage current increased for all of them.

Results from step 3 (direct measurements)

The ladder has been placed on an ‘S-side bonding jig’. All S-biases from sensors 3 to 12 were disconnected, while the K-side biases were bonded again. The S-side bias and guard rings were bonded to the jig. This allowed us to bias each sensor individually, connecting the positive bias voltage to pin 2 of the K-hybrid, and connecting the S-bias (and S-guard) to ground, through an electrometer (figure 6.7). A similar procedure was followed in step 4 for sensors 1 and 2. Three measurements have been performed:

- Leakage current from bias and guard rings as a function of the bias voltage;
- Capacitance as a function of the bias voltage (allowing us to estimate the depletion voltage);
- Leakage current evolution at 100 V during many hours (long term leakage current measurement).

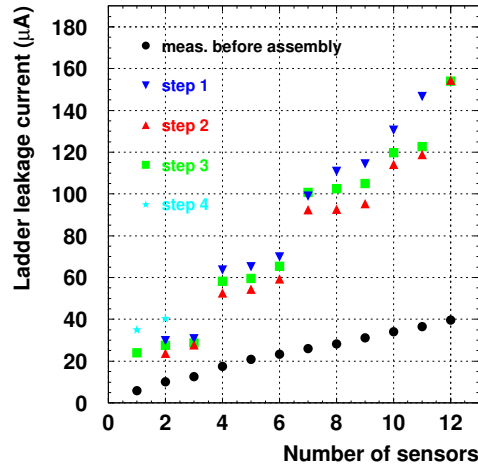


Figure 6.8: Ladder leakage current as a function of the number of sensors at 90 V bias, compared with the measurements at 100 V of the individual sensors.

In table 6.1 the sensor leakage currents at 100 V are shown before assembly in H12PI015 compared with the mean leakage current values from the long term measurements. Clearly, six of the twelve measured sensors present worse leakage currents. Some sensors seem to show an improvement: this is probably due to a temperature difference between the measurements.

Sensor	Position	Leakage current at 100 V (μA)	
		before assembly	after disconnection (20°C)
36_07	12	3.2	31.4
45_07	11	2.4	2.9
45_04	10	2.9	14.6
45_06	9	3.0	2.6
44_18	8	2.3	1.8
44_15	7	2.5	35.4
41_23	6	2.6	5.7
42_06	5	3.2	1.3
37_09	4	5.0	29.5
46_15	3	2.4	1.2
38_20	2	4.3	3.5
38_22	1	5.9	24.1

Table 6.1: Leakage current of each sensor before assembly and after disconnection.

In figure 6.9 the individual leakage currents at a bias of 0 to 130 V are shown. All guard currents remained low.

Table 6.2 compares the depletion voltages measured from the test diodes with the estimated values from the sensors. Usually, the value obtained from the sensor measurement is

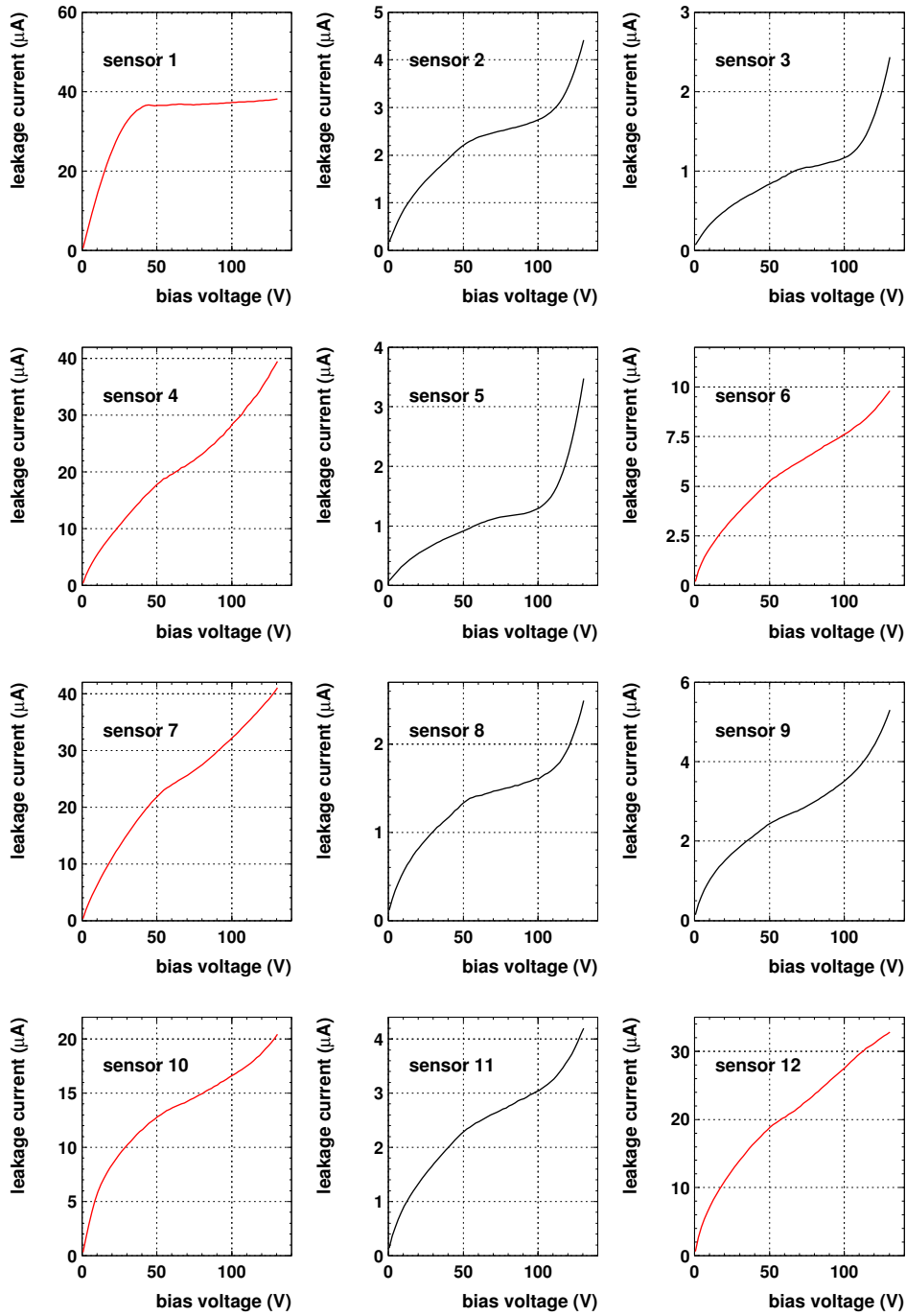


Figure 6.9: IV measurements of sensor 1 to 12, sensors. Sensor 1, 4, 6, 7, 10 and 12 present a higher than expected leakage current.

larger than the diode depletion voltage. For sensor 38_22 the difference is the largest, with a close to 20 V difference..

Sensor	Position	Depletion voltage (V) test diode	Depletion voltage (V) sensor
36_07	12	40.0	53.4
45_07	11	48.0	57.7
45_04	10	51.0	58.6
45_06	9	44.1	57.4
44_18	8	46.6	56.7
44_15	7	44.3	57.2
41_23	6	48.7	58.6
42_06	5	59.8	69.0
37_09	4	48.2	67.8
46_15	3	70.3	71.1
38_20	2	42.9	59.4
38_22	1	46.0	61.2

Table 6.2: Estimated depletion voltage of each sensor, compared with the test diode depletion voltage.

Leakage current variations

It has often been observed during steps 1 and 2 that the leakage current of the ladder was not exactly the same, even if the number of biased sensors had not changed. During the long term measurement some sensors showed leakage current variations in the first hours of biasing. Also, sensor 12 has a leakage current instability (figure 6.10).

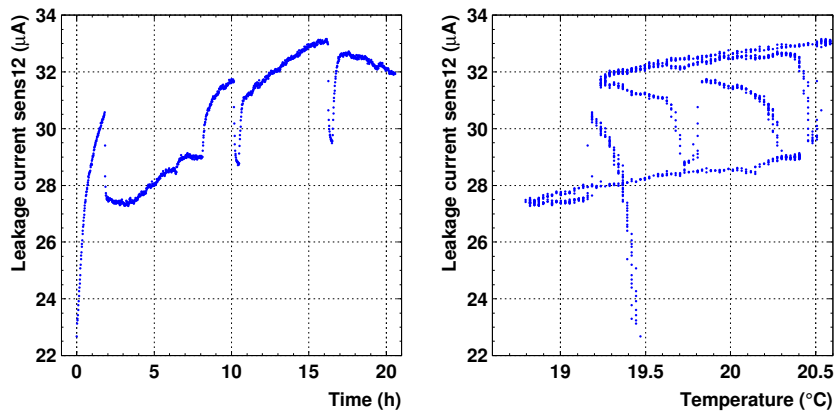


Figure 6.10: Long term leakage current measurement of sensor 12 at 100 V.

6.3.4 Noise evolution in step 1

As mentioned earlier, at each disconnection step, H12 PI 015 has been tested at various biasing voltages, and a calibration was performed for each biasing condition. Figure 6.11 shows the mean noise at 90 V bias for each side of the ladder. We clearly see that the mean channel noise depends on the number of connected sensors. If we consider a similar ratio of noisy strips for each sensor, the mean noise will linearly increase with the number of connected sensors. When only one sensor is connected, the mean K-side noise increases again: no sensor is connected to half of the K-side electronics: this is confirmed when even and odd sensors are examined separately (figure 6.11). In addition, we see that the odd sensor group is noisier than the even sensor group.

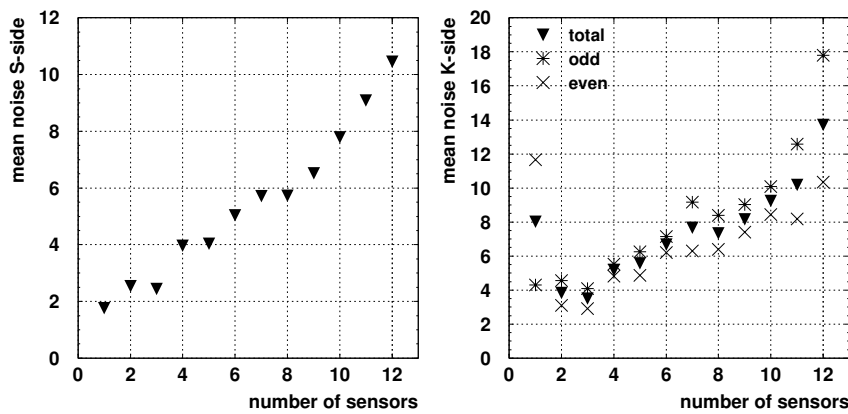


Figure 6.11: Step 1: mean ladder noise (in ADC counts) as a function of the number of sensors at 90 V bias.

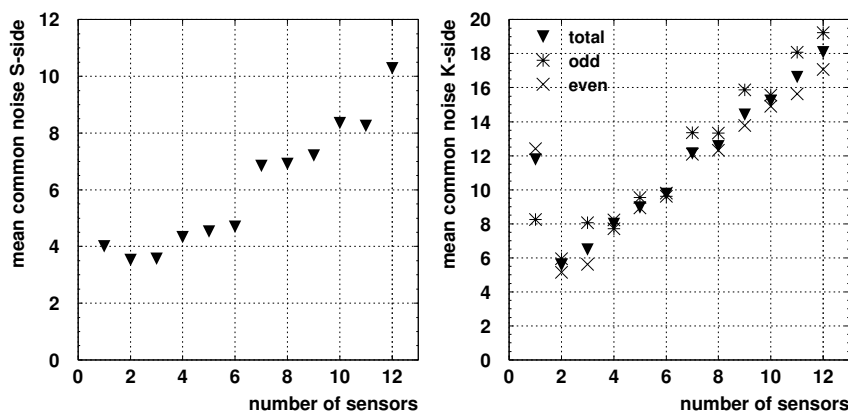


Figure 6.12: Step 1: mean common noise (in ADC counts) as a function of the number of sensors at 90 V bias.

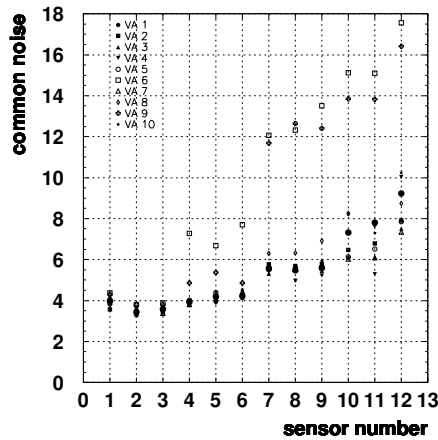


Figure 6.13: Step 1: S-side individual VA common noise as a function of the number of sensors at 90 V bias.

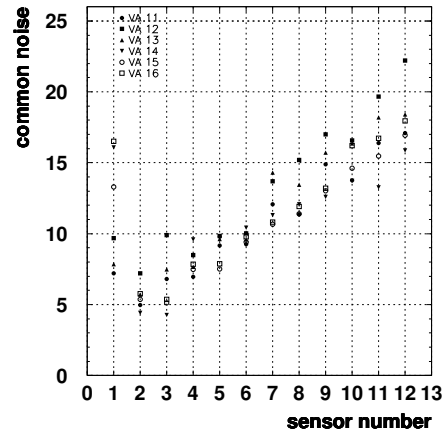


Figure 6.14: Step 1: K-side individual VA common noise as a function of the number of sensors at 90 V bias.

6.3.5 Common mode noise in step 1

The evolution of the mean common noise at 90 V as a function of the sensor number is shown in figure 6.12. We clearly see a dependence of the common noise on the number of sensors. The origins of this dependence could be an antenna effect. The longer the ladder is, the larger is the common mode. Nevertheless, this effect is less clear on the S-side. When only one sensor is connected, the common noise increases slightly though.

6.3.6 Noise evolution in step 2

In this section the noise dependence on the number of biased sensors is presented, in the following ladder configuration (figure 6.6):

- only the S-channels composed of the strips of sensors 1 and 2, daisy chained, are read out;
- only the K-channels of sensors 1 and 2 are read out.

Figure 6.15 shows the noise dependence on the number of connected sensors. We observe that the S-side noise slightly decreases when the number of biased sensors decreases. It remains relatively stable, though, and close to the noise value of two fully connected sensors (see figure 6.11).

This is not the case for the K-side noise. When all sensors are biased, the noise is even higher than for the step 1 configuration. It decreases to remain rather stable as soon as less than 7 sensors are connected. The value then reached is close the two fully connected sensor configuration. We observe a different behaviour on both sides. As the sensors on the K-side are not all connected together, we also checked separately the noise evolution for even and odd sensors: the results are similar, as shown in figure 6.15.

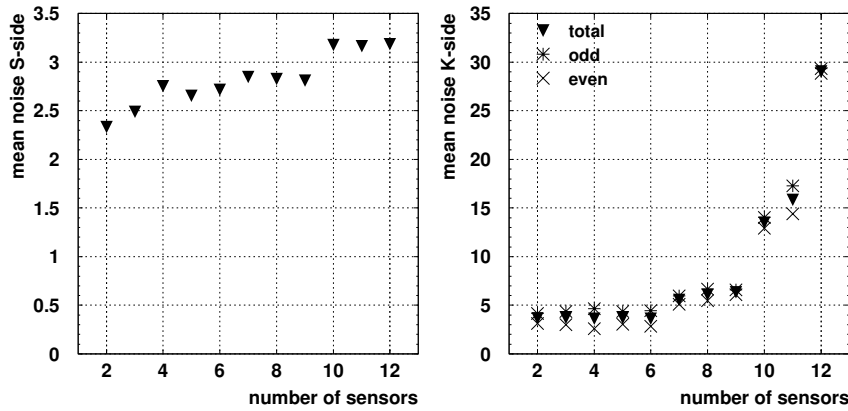


Figure 6.15: Step 2: noise evolution as a function of the connected sensors.

6.3.7 Common noise of step 2

The mean common noise remains stable and is thus independent of the total ladder leakage current. Nevertheless, VA 6 has a much larger common noise, which depends on the number of sensors connected (figure 6.17).

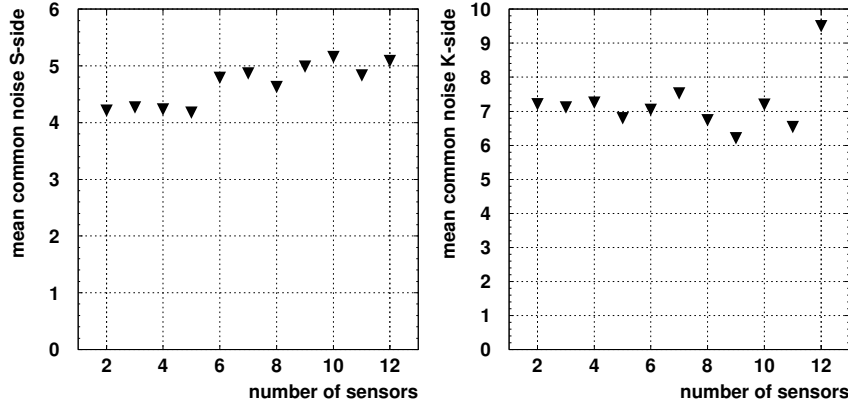


Figure 6.16: Step 2: mean common noise as a function of the number of sensors at 90 V bias.

6.3.8 Comments

The various tests performed with H12 PI 015 allowed us to learn many aspects of the ladder properties.

The leakage current problems are due to 6 out of the 12 sensors composing the ladder. As stated in the introduction, a strong leakage current increase was observed after feet gluing. Figure 6.19 shows the feet position on the ladder: where feet are located, at least one sensor presents a higher leakage current. This suggests a negative impact of the feet gluing proce-

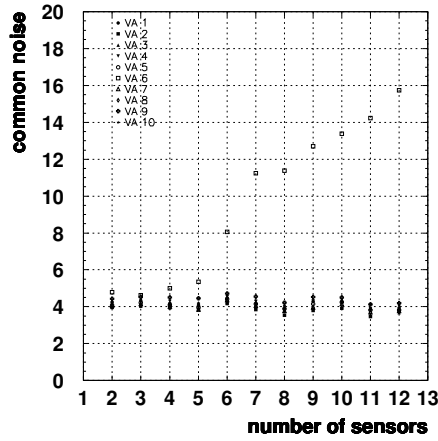


Figure 6.17: Step 2: S-side individual VA common noise as a function of the number of sensors at 90 V bias.

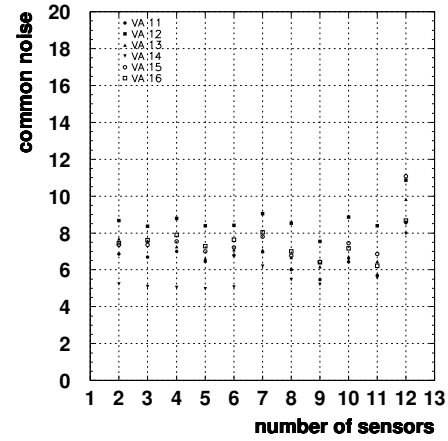


Figure 6.18: Step 2: K-side individual VA common noise as a function of the number of sensors at 90 V bias.

dure, consisting in sanding the carbon fiber surface of the reinforcement, while the ladder is lying on the feet gluing base.

Nevertheless, we note that on the K-side, even if the readout channels are only constituted of the two first sensors, the mean channel noise depends on the total leakage current. This may be understood if we consider each sensor as a current source, thus inducing small voltage variations. It is nevertheless interesting to note that the influence of such variations is not observable on the S-side. The noise on the K-side, with all bias lines connected, is even higher than when all the strips are connected together. It is also interesting to note that the K-side noise sensitivity is not due to one group (even or odd), as we found the same kind of behaviour when observing only the even or the odd sensors.

Finally, the common noise seems to depend on the channel length, and not on the total leakage current value.

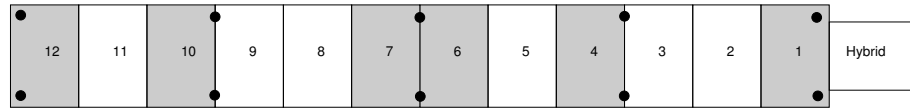


Figure 6.19: Feet positions compared with bad sensors (in gray).

6.4 Conclusions

The clearest information from the tests on H12 PI 015 is the correlation between feet location and degraded quality sensor. An additional test examining each assembly step (section 6.6)

confirms this interpretation. It was later decided to sand the reinforcement carbon fiber right after the reinforcement production, i.e. before it is glued to on the ladder.

6.5 Test ladder H02 GT 030

6.5.1 Introduction

In August 1999, it was decided to assemble a test ladder composed of two AMS-01 sensors. The chosen procedure was to first thoroughly examine the sensor properties with the probe station, then assemble the sensors and glue the hybrids. A comparison between strip current and channel noise was then possible.

The ladder evolution during assembly, i.e. a total current increase after the first assembly steps (K5 Upilex and reinforcement gluing) suspended the ladder assembly, and the sensor strip currents were measured. One strip was the main origin of the current increase. After bonding, more strips presented high currents.

Hybrids were never glued to this ladder, because of the ladder high leakage current. However the operations indicated that the first assembly steps could infer damages on the silicon sensors. Later examination enabled to relate the high strip current with a scratch on the sensor surface, a damage probably avoided with a passivated surface.

6.5.2 Selected sensors

Those sensors were part of batch never used for the assembly of AMS-01 ladders, and kept for a relatively long time on the original cutting support, made of a special adhesive tape. The first leakage current measurements evidenced that some surface contamination occurred during the storage period. The sensors were placed in an ultrasound machine for 6 minutes in a 50% acetone, 50% methanol mixture, then for 6 minutes in 100% methanol. The sensors were then dried with an N₂ flow. Over 20 sensors, 10 could be recovered, while two more were of marginal quality. Two sensors were then chosen to assemble the test ladder:

- #2218 , 2.0 μ A at 100 V (20 °C), $V_{depl}=66$ V, glued at position 1
- #2220 , 2.0 μ A at 100 V (20 °C), $V_{depl}=64$ V, glued at position 2

Figure 6.20 shows both sensors total current before assembly. The currents before cleaning are also plotted. In addition, the strip currents have been measured.

6.5.3 K5 Upilex and reinforcement gluing

Once the K5 Upilex and reinforcement were glued, the bias connections on K- and S-sides were realized: the ladder quality could be immediately monitored. The ladder leakage current was measured with the setup used to test ladders, in our clean room. The results indicated a quality decrease: the assembly was suspended to perform more precise and reliable measurements in a probe station.

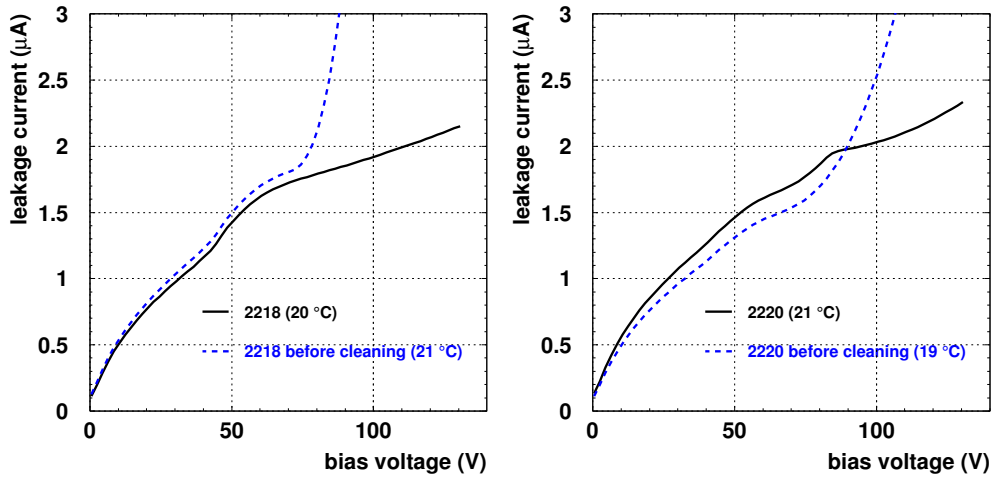


Figure 6.20: Individual leakage current measurements of sensors 2218 (left) and 2220 (right) composing ladder H02 GT 030. Current prior to cleaning are also plotted.

The increased leakage current indicates that the sensor quality clearly decreased during the assembly. Instead of an expected total current of about $4 \mu\text{A}$ at 100 V, we measured about $7.5 \mu\text{A}$ at 100.5 V (figure 6.21). Moreover, at least one sensor clearly presented a breakdown. This was confirmed by the individual sensor leakage current measurements (the S-side bias bond between both sensors had been removed):

- Sensor 2218 had a breakdown above 95 V. When both bias and guard rings were connected to ground, the breakdown occurred on the guard ring (fig. 6.22). This situation had already been observed on that sensor, before chemical cleaning. This could indicate that some pollution had altered the sensor quality.
- The leakage current of sensor 2220 was larger than before the assembly, while the guard current remained very small (fig. 6.23).

6.5.4 Ladder evolution

The ladder has been regularly measured. A few weeks after assembly, sensor 2218 showed no more breakdown, and the leakage current was again compatible with the values before assembly. Also, a strip current measurement on the p-side of each sensor was performed. No noticeable modification was observed on sensor 2218. Two of the measurable strips of sensor 2220 had a strong leakage current increase (table 6.3). These two strips induced a total leakage current variation of $1.1 \mu\text{A}$. The neighbouring strips presented a slight current increase (when compared to the local average value). The intermediate readout strips (half integer indices) were not measured before assembly: the initial aim was to know the readout strip currents to locate the noisy channels once the hybrids would be glued. As it is not possible to measure half of the p-strips, it is conceivable that at least one of those strips also

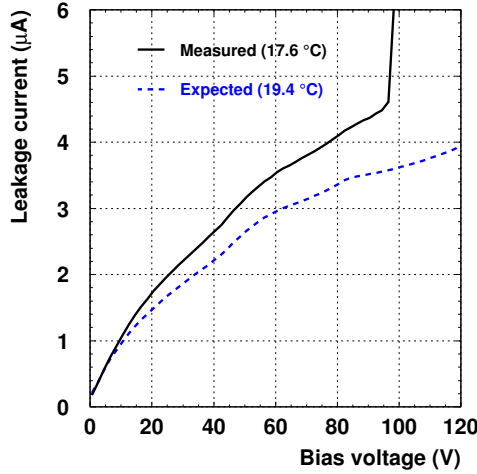


Figure 6.21: Ladder leakage current measurement after Upilex and reinforcement gluing, compared with the total current of sensors 2218 and 2220 before assembly.

has a high leakage current. Since the current increase of sensor 2220 was understood, and

Strip (p)	Current before assembly (nA)	Current after assembly (nA)
210.5	—	2.6
211	1.0	3.9
211.5	—	2.1
212	1.0	0.9
212.5	—	41
213	0.9	274
636.5	—	19
637	0.2	849

Table 6.3: Strips of sensor 2220 with current increase after assembly. Intermediate readout strips were not measured prior to assembly.

since 2218 recovered it was decided to resume H02 GT 030 assembly.

6.5.5 Measurements after bonding

A standard assembly would have combined the microstrip bonding with the hybrid gluing. Since the difficulties encountered in the first assembly step, it was decided to first bond the strips and glue the hybrids later. After the K- and S-side strips were bonded, the total current was measured again (fig. 6.24). Clearly the sensors suffered from additional damages. The first total current revealed a very high value ($40 \mu\text{A}$). After two long term measurements (the first one of 14 hours, the second one of 7 hours) the current stabilized to $10 \mu\text{A}$. Figure 6.25 compares the ladder readout strip currents with the individual sensor measurements. Additional strips have been damaged. The intermediate readout strip currents for each sensor show no modification. Table 6.4 shows the strips for which a change after bonding

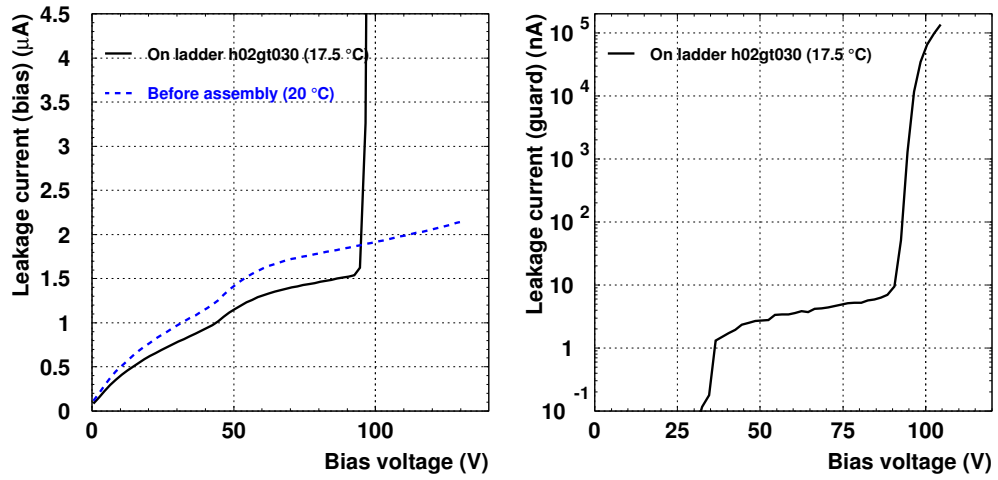


Figure 6.22: Sensor 2218 leakage current measurements. In the left-hand plot, the guard ring remained floating.

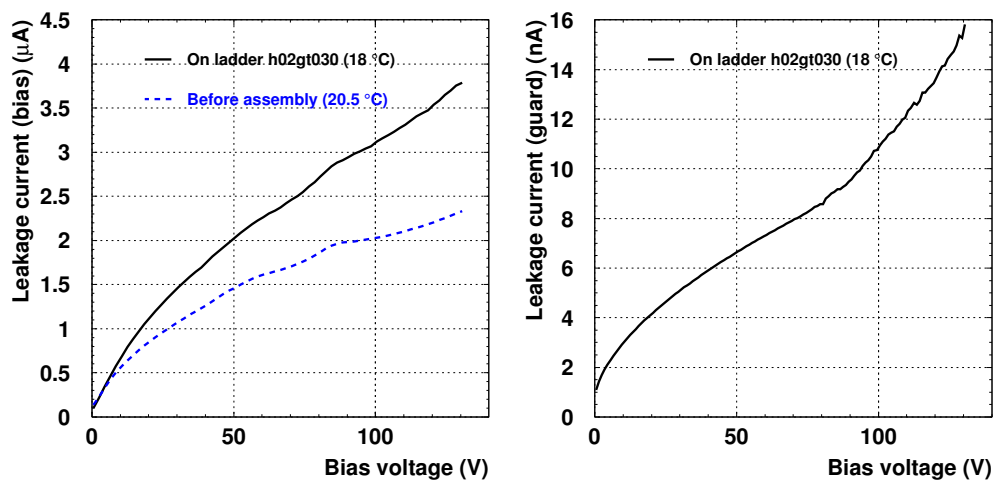


Figure 6.23: Sensor 2220 leakage current measurements. In the left-hand plot, the guard ring remained floating.

has been clearly noticed.

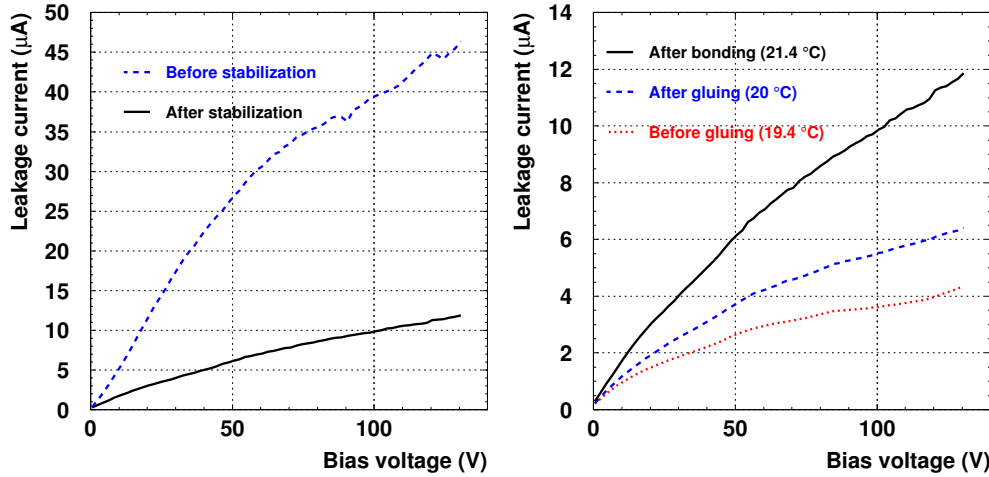


Figure 6.24: Total current measurement after strip bonding. The current measurement after bonding has been performed after long term stabilization.

6.5.6 Remarks

Clearly, the assembly operations induced a quality degradation of the p-side strips thus increasing the total leakage current. The Upilex and reinforcement gluing, as well as the K-side bonding operations need the p-side silicon surface to be in contact with the jig surface. A mechanical deterioration can occur during those manipulations. A visual inspection around strip 213 reveals a scratch (fig. 6.26). Besides, we see that strip 212 is undamaged, in agreement with the current measurements in table 6.3. The p-strip damages observed after the last assembly step may have two origins: mechanical (abrasive) or from bonding. A scratch usually involves more than one strip, thus isolated damaged strips most probably indicate a bonding problem. We can also note on figure 6.25 that the strip current after bonding seems less regular.

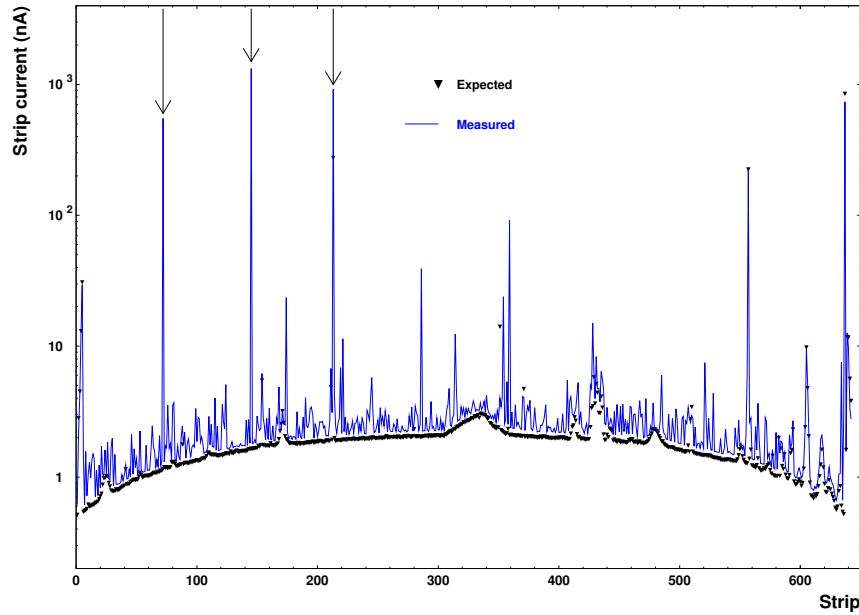


Figure 6.25: Readout strip current measurement on H02 GT 030. The strip current changes after bonding. The arrows locate the most damaged strips.

Strip	Before bonding (nA)	After bonding	
		1st meas. (nA)	2nd meas. (nA)
72	1.15	552.17	255.40
145	1.64	1327.11	2527.00
174	1.95	23.49	11.06
213	274.54	922.38	687.83
221	1.93	11.40	13.64
286	2.03	39.02	30.81
314	2.33	12.39	10.97
354	2.20	23.82	25.37
359	2.09	91.12	77.28
428	3.47	15.05	20.40
Total	1367	3981	4714

Table 6.4: Readout strips of H02 GT 030 for which the current changed after the bonding operations and is > 10 nA.

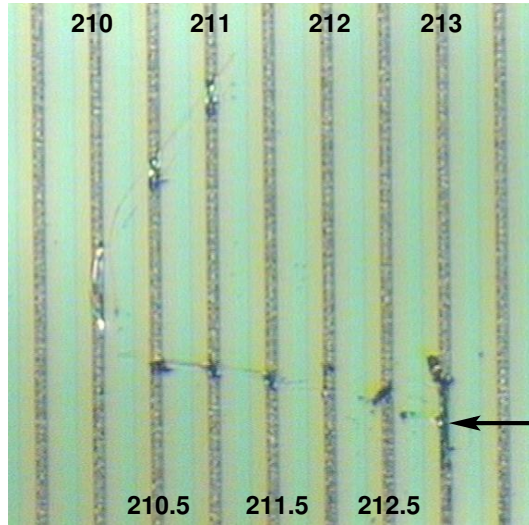


Figure 6.26: Scratch on sensor 2220. Strip 213 is the most damaged. Strips 210.5 to 211.5 are probably in short circuit.

6.6 Study of assembly step effects

6.6.1 Introduction

As mentioned earlier, the AMS-01 ladder quality decreased during the various assembly steps. Two main contributions seem to be at the origin of the degradation: bonding and p-side deterioration due to abrasive forces during the contact with jig surfaces. In particular, after the H12 PI 015 results (see section 6.3), the feet gluing operations were looked at. We decided to examine the effects of the assembly steps on single sensors.

Two medium quality sensors from an AMS-01 post-production batch were selected:

1. sensor 97_13/10: $3.2 \mu\text{A}$ at 50 V, $V_{depl}=24 \text{ V}$
2. sensor 97_13/04: $2.4 \mu\text{A}$ at 50 V, $V_{depl}=25 \text{ V}$

The assembly steps were as follows:

- Upilex gluing;
- Reinforcement gluing;
- Feet gluing.

Figure 6.27 shows a sensor once the feet are glued. After each gluing step, the total and strip currents were measured in the probe station. The sensor preparation needed special care: it was placed on a special jig which allowed to replace the needle contacts with micro-bonds, for optimized biasing conditions. Nevertheless, using this jig induced contacts between the jig and detector surfaces.

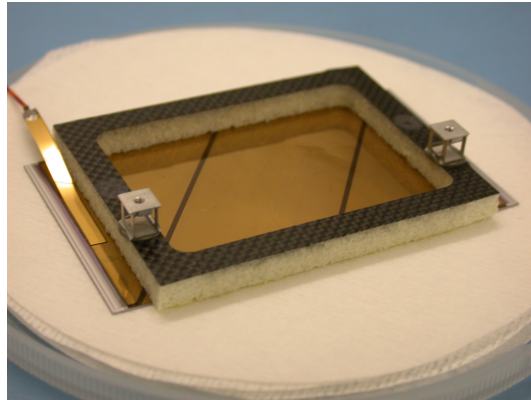


Figure 6.27: AMS-01 sensor 97_13/10 with Upilex, reinforcement and feet.

6.6.2 Sensor 97_13/04 evolution

No particular change was observed, until feet were glued. The I-V measurement performed then showed a soft breakdown, but after a long term test (fig. 6.28), the current decreased to go back to standard values (fig.6.29).

6.6.3 Sensor 97_13/10 evolution

No degradation was noticed until the sensor was scratched (fig. 6.30) due to a wrong manipulation during the installation on the measurement jig. The total leakage current increased and all the readout p-strips were measured (fig.6.31). Strip 66 had a higher leakage current, while it could not account for the total current increase: the neighbour (non-readout) strip 65.75 was then measured via its contact pad, with a current of $\sim 5 \mu\text{A}$.

6.6.4 Reinforcement sanding

During the AMS-01 production, the reinforcement carbon fibre surface was sanded, to improve the foot glue adhesion on the reinforcement surface. As the reinforcement was already glued, the sanding needed to be done on the assembled ladder. This was done while the ladder was lying on the feet gluing jig, using a sanding machine. After cleaning the feet were finally glued.

This procedure was performed on both sensors 97_13/04 and 97_13/10, to observe the possible effects of this process. Both sensors present degradations, evidenced by strip current increases. 97_13/10 has one more high current strip (figs. 6.32 and 6.33), while sensor 97_13/04 seems to be more damaged: many strips show a slight current increase, while three strips present a current larger than 100 nA.

6.6.5 Conclusions

After a sequence of manipulations involving multiple contacts between the sensor and jig Teflon surfaces, the strip quality clearly decreases. In particular, after the reinforcement

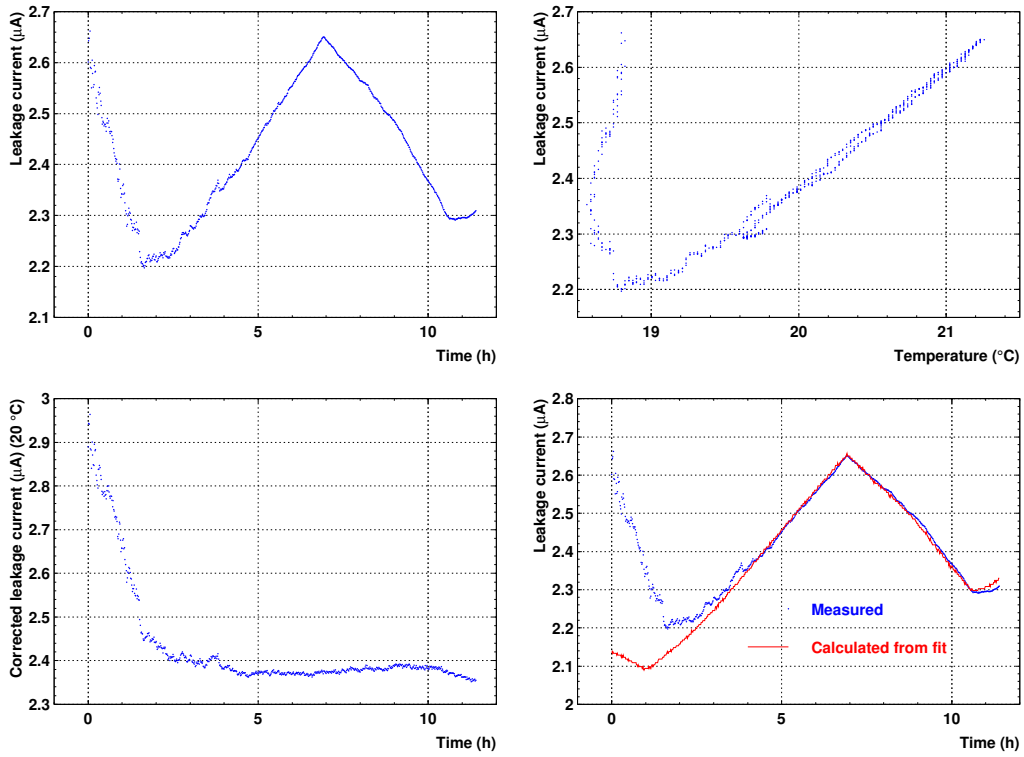


Figure 6.28: Long term measurement on sensor 97_13/04. The current goes back to a normal value after four hours.

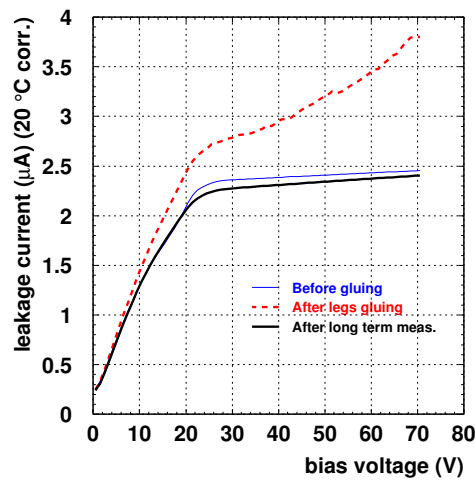


Figure 6.29: Total current measurement of sensor 97_13/04. After the leg gluing, the sensor presents a soft breakdown. After a long term biasing, the soft breakdown disappears.

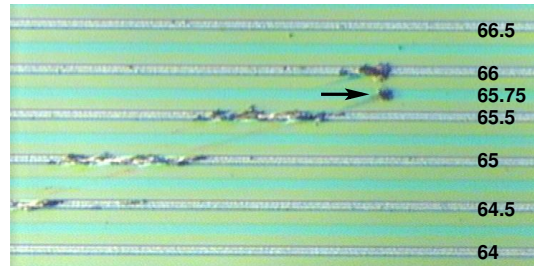


Figure 6.30: Scratch on sensor 97_13/10. The damaged strip is at position 65.75 .

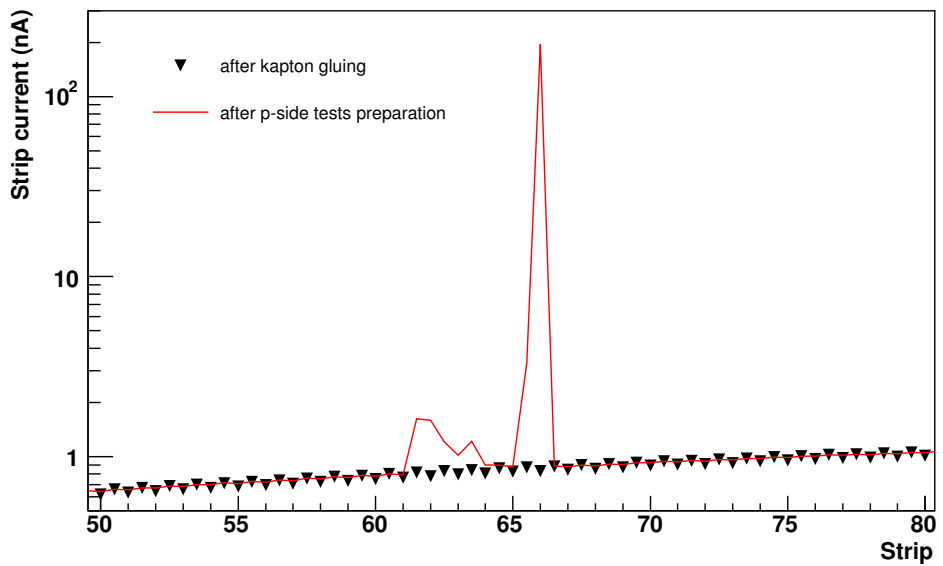


Figure 6.31: Strip current measurement on sensor 97_13/10. Readout and intermediate readout strip currents are plotted.

sanding, an obvious degradation is observable on the sensor 97_13/04. The AMS-01 sensors present a clear weakness, probably due to the absence of passivation. Also, the tests show the extreme importance of working in the cleanest possible environment. We decided from that moment to strictly enforce clean room discipline. Also, the sensors used for subsequent assemblies were individually cleaned, with a vacuum method, to remove all dust particles. The jigs are also examined under a microscope to check the jig surface imperfection.

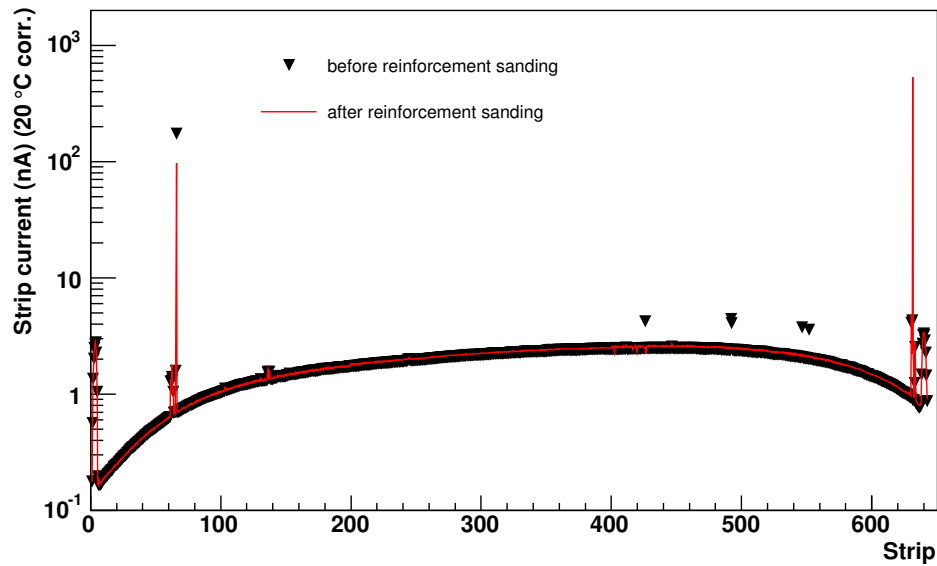


Figure 6.32: Strip current on sensor 97_13/10 before and after reinforcement sanding.

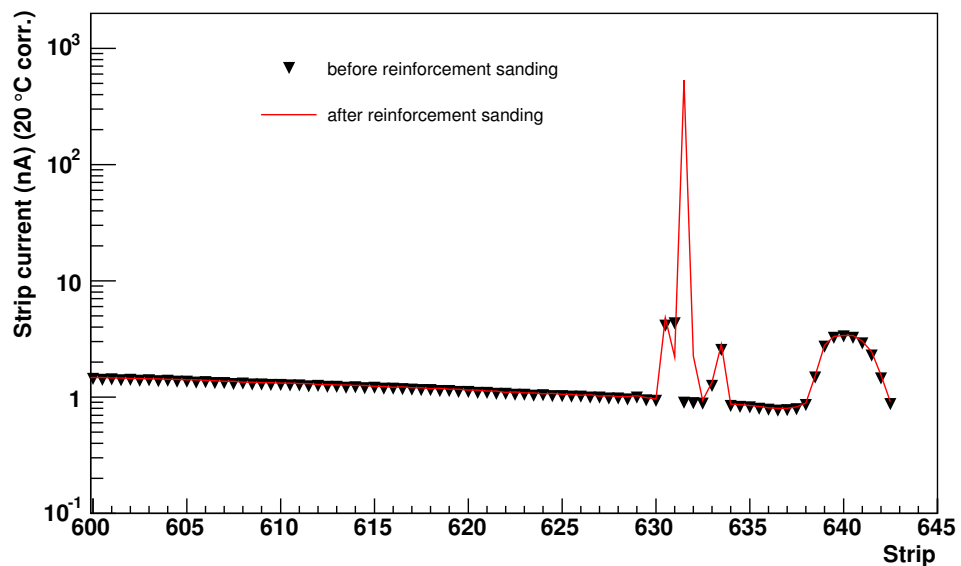


Figure 6.33: Strip current on sensor 97_13/10 before and after reinforcement sanding.

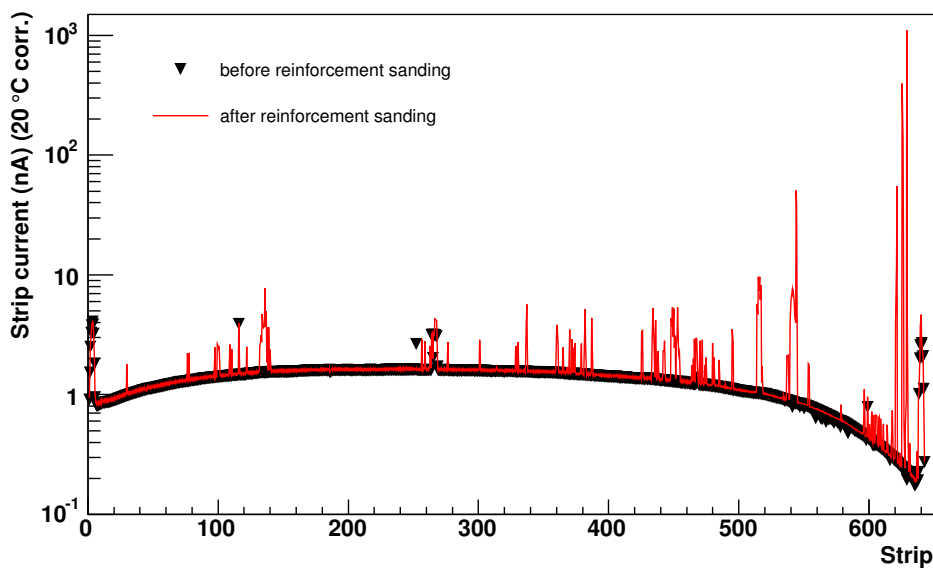


Figure 6.34: Strip current on sensor 97_13/04 before and after reinforcement sanding.

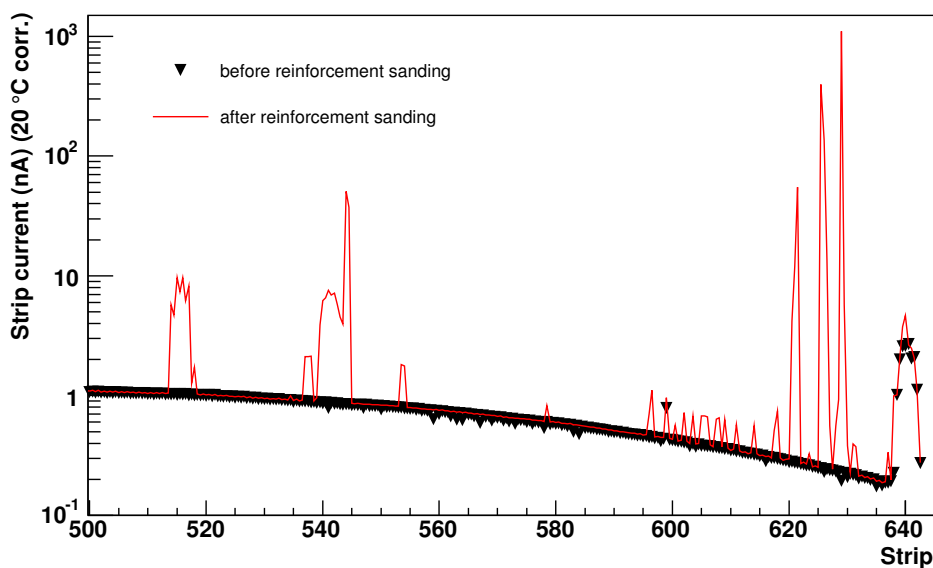


Figure 6.35: Strip current on sensor 97_13/04 before and after reinforcement sanding.

6.7 Test ladder L12 GT 031

6.7.1 Introduction

After the tests performed during 1999, our understanding of the risks proper to the ladder assembly, increased with manipulation of long modules (length from 29 cm to 62 cm), was considered good enough to decide the assembly of a 12-sensor test ladder. The sensors, part of the AMS-01 post-production 97_13 batch, were thoroughly tested from July 1998 to December 1999.

The Upilex cables were produced at CERN, and tested in our probe station: strip continuity and short circuit between strips were checked. The identified shorts were then repaired, and the cables were cut to their final dimension.

6.7.2 Assembly

Before assembly, the alignment jig surface was thoroughly examined and cleaned. Also, before placing the detectors on the jig, all dust particles were removed from the surface, with vacuum aspiration.

To check the silicon quality after gluing, the bias line was bonded on K- and S- sides. Before placing the ladder on the K-side bonding jig, the S-side surface was examined and cleaned. The total current was measured through the hybrid connectors. The total current measurement (fig. 6.36) was in agreement with the sum of the individual currents before assembly (normalized to 20 °C). The K-side was then totally bonded. On the S-side, all biases were connected, while only strips of sensors 1 to 7 were connected. A total current measurement shows that the ladder quality decreased, as shown in figure 6.37.

The p-side biases of sensors 8 to 12 were disconnected to determine their individual current: the sensor performances were similar to those before assembly. The currents of the 640 bonded channels were then measured, as shown in figure 6.39. Many strips present a current larger than before assembly, specifically strips 184, 610 and 630 draw a very high current. When those strips are grounded, the total ladder current is compatible again with the seven sensors individual currents before assembly (fig. 6.38).

The last sensors were reconnected and the bonding of the remaining strips was completed. Figure 6.40 shows the strip current measurement: three more strips are damaged. Due to a missing bond between sensors 9 and 10, channel 221 presents a smaller leakage current.

When only sensors 1 to 7 were bonded, the five last sensors were working correctly, while the ladder had a leakage current higher than expected. After bonding sensors 8 to 12, more strips present a high leakage current. Thus those defects involve sensors 7 to 12. As no mechanical action was performed on the sensors, the bonding is responsible for those defects. Strips 18, 63 and 536 are the additional damaged strips.

With an initial total current of 14 μ A at 40 V, the current evolved to 16.5 μ A and finally to 24 μ A after the two bonding steps. Since no other operation but bonding was executed between the two last steps, we consider that bonding is at the origin of at least four damages, and probably three more.

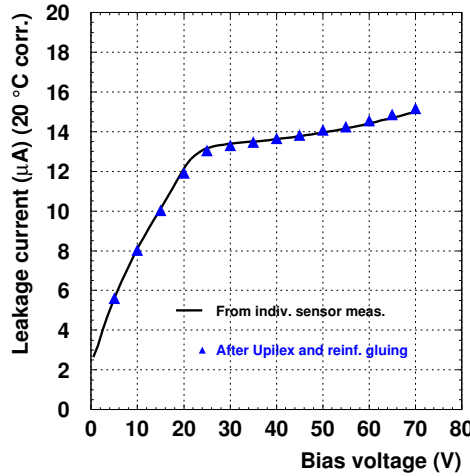


Figure 6.36: L12 GT 031 total current after Upilex and reinforcement gluing. The current is compatible with the sum of the individual sensor currents prior to assembly.

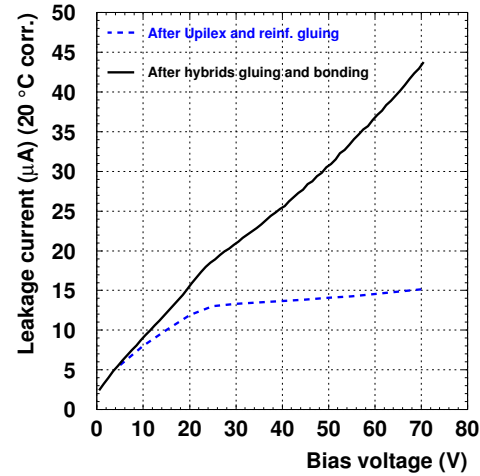


Figure 6.37: L12 GT 031 total current after partial bonding: p-strips of sensors 8 to 12 are not bonded. A damage is at the origin of the current increase.

It is now interesting to compare the strip current measurements with calibrations, as the ladder is equipped with hybrids.

6.7.3 Noise dependence on voltage

The ladder assembly gave us the occasion to study the noise properties of the ladder. Figure 6.41 describes the mean channel noise evolution, for both sides, with a bias voltage ranging from 5 to 70 V. Two configurations were tested: with 7 strips/channel and with 12 strips/channel. While the S-side noise remains rather stable, the K-side noise decreases drastically between 20 and 30 V: the depletion area reaches the sensors n-side, resulting in n-side strip insulation. This is in agreement with the depletion voltages determined for each sensor composing the ladder: the lowest voltage was 22 V, the largest 28 V. Once the bias voltage is over 30 V, the mean noise remains stable on the K-side. The results in figure 6.41 take into account all channels, including the noisy ones. Figure 6.42 describes the mean noise, excluding channels tagged 'noisy' during the calibration. The mean noise is more stable and lower than before, as expected. Nevertheless, it remains clear that the mean noise is larger with 12 strips/channel than for 7 strips/channel.

6.7.4 Leakage current effects

As the strip leakage current contributes to the ladder noise, it is interesting to examine the ladder strip currents and the corresponding channel noise. Thus the strip currents measured in the probe station were compared to the ladder calibration data obtained with the `calib`

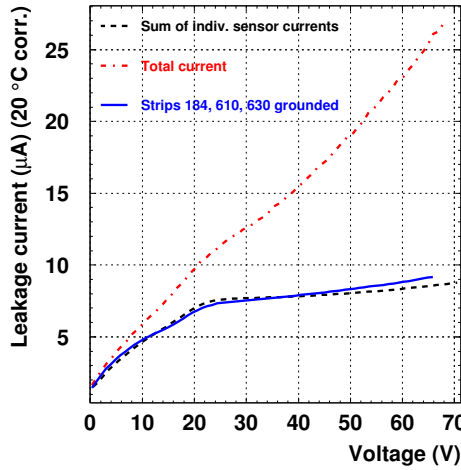


Figure 6.38: L12 GT 031 with 7 sensors biased. When the high current strips 184, 610 and 630 are grounded, the total ladder current becomes compatible with values prior to assembly.

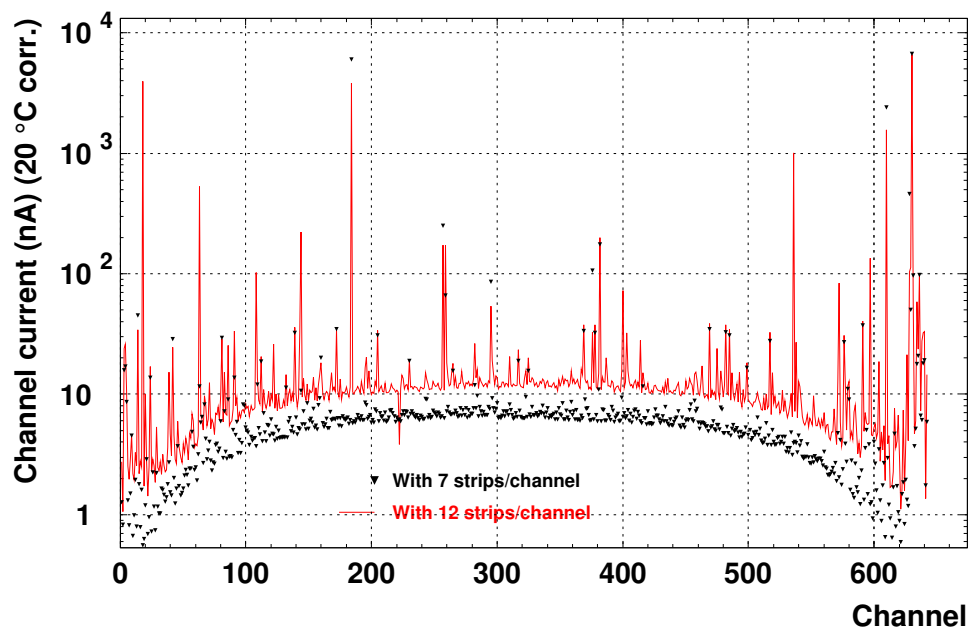
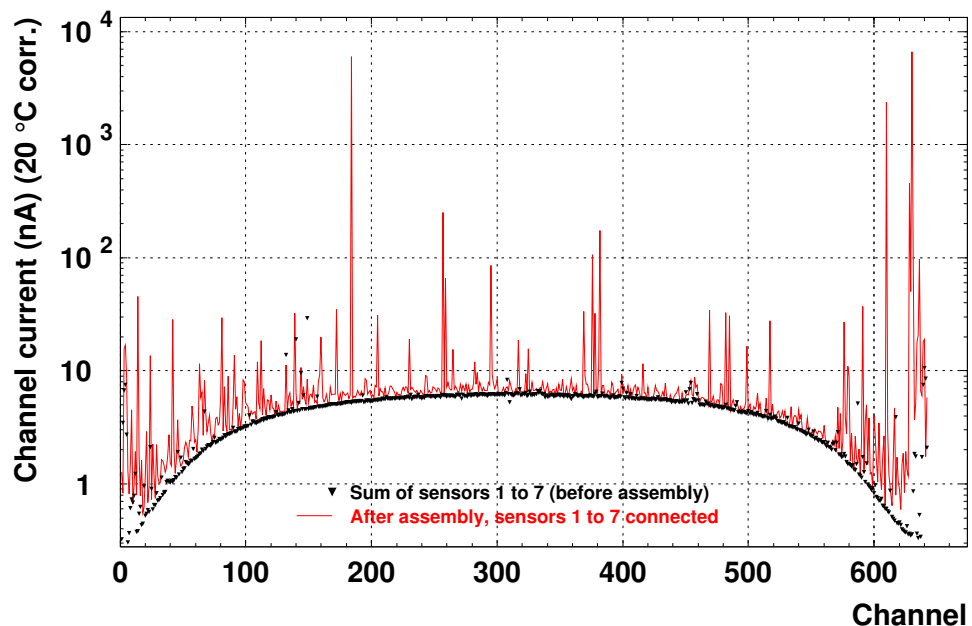
program.

A comparison between channel noise and corresponding channel current is shown in figure 6.43. Clearly, most of the noisy channels have a high leakage current. Two particular cases, though, present an interesting behaviour, as shown in figure 6.44. The central channel draws a current larger than $1 \mu\text{A}$ and is very noisy. Moreover this channel seems to perturb up to 8 neighbour channels, because of the coupling capacitance between the strips. We tested solutions to minimize the noise induce by a damaged central channel, to establish a repair strategy.

6.7.5 Repair by bond removal

The bond between the capacitor input and the Upilex strip of channel 17 was removed. A calibration showed that the neighbour channels were noisier than before (fig. 6.45 left). This can be understood if we consider a simplified schematics of the situation. The decoupling capacitor constitutes a low impedance connection to the hybrid local ground. This connection cut, the charges generated by the current fluctuation of the damaged strip are transmitted to the neighbour amplifiers, by way of the interstrip capacitances. This behaviour is thus understandable and expected. Still we observed some electronics malfunctions: the gain calibration of VA #1 was no more operative. Additionally, a test with a ^{90}Sr radioactive source showed that the gain of VA #1 was lower than for VAs #2 and #3. Thus a damage presumably due to static electricity discharge occurred during the bond removal. Other ways to disconnect bad channels were established in a probe station.

The first step was to reconnect, with probe needles, channel 17 to the capacitor (fig. 6.45 middle). The neighbour channels presented less noise than before the bond disconnection, also, channel 17 presented a low noise, despite the high strip current. This indicated that



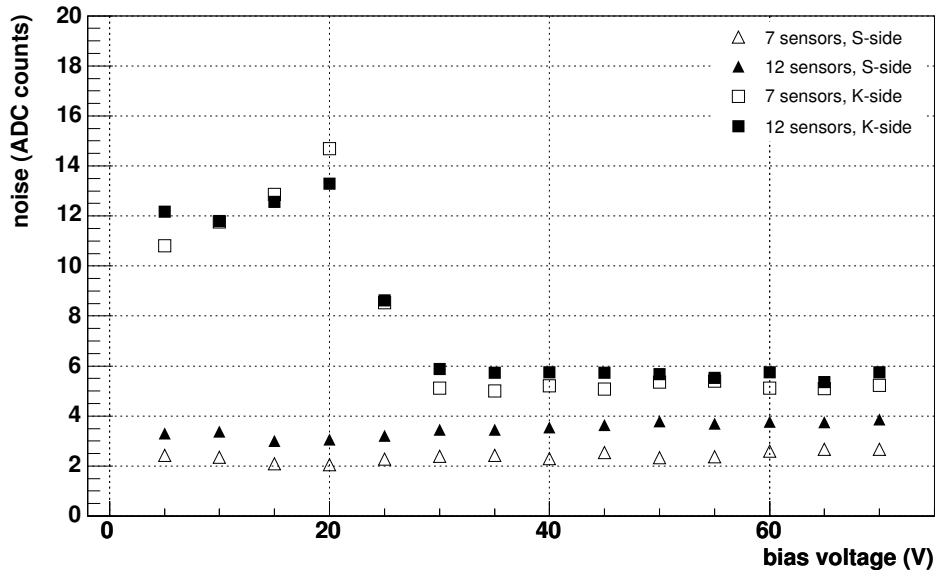


Figure 6.41: L12 GT 031 noise as a function of the bias voltage, for channels composed of 7 strips, and channels composed of 12 strips.

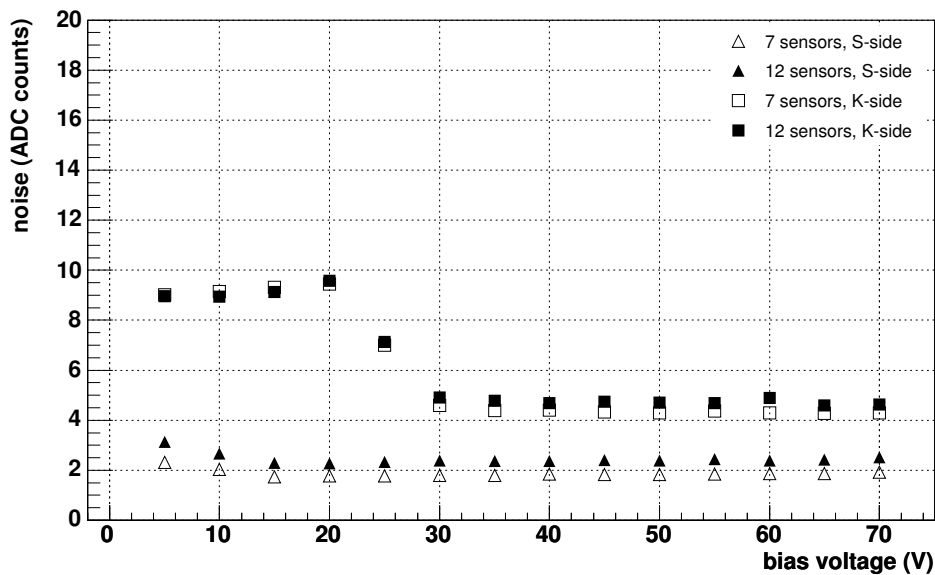


Figure 6.42: L12 GT 031 noise as a function of the bias voltage, for channels composed of 7 strips, and channels composed of 12 strips. Here the mean noise is computed excluded the high noise channels identified during the calibration.

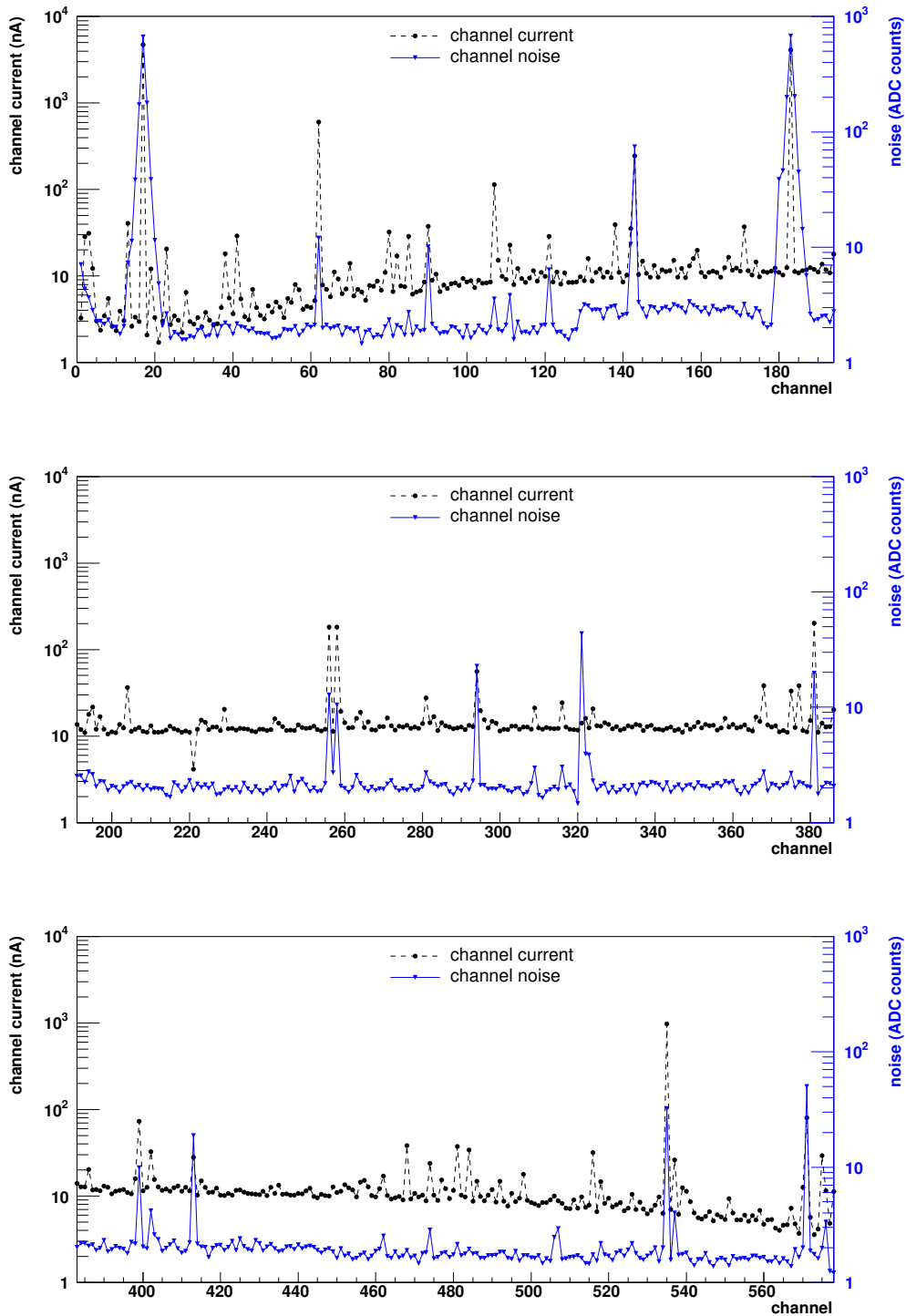


Figure 6.43: Comparison between the strip current with strip noise of ladder L12 GT 031.

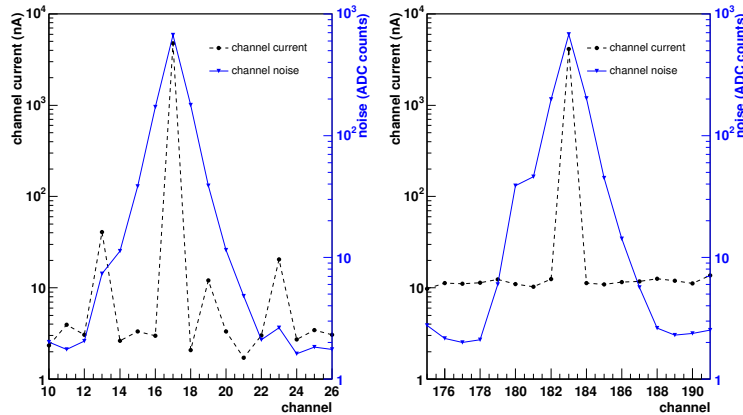


Figure 6.44: A high current strip (channel 17 on the left, channel 183 on the right) induces a cluster of noisy channels. The maximum noise channel corresponds to high current strip.

the preamplifier of channel 17 was damaged, and confirmed the gain decrease of VA #1.

The probe needles were used to connect channel 17 to the S-side bias line (fig. 6.45 right). In such a case, the noise decrease, compared to the previous situation. Connecting the noisy channel directly to the guard ring reduced the noise of neighbour channels. Of course, the comparison is biased due to the fact that the preamplifier gain performances are lower than before the bond cut. Hence a similar test was fulfilled on channel 183: in the probe station, the channel, still associated to the electronics, was connected with the S-bias line, the noise decreased up to 20% as shown in figure 6.46 (left). The bond between Upilex and capacitor was then removed: a noise increase is observed, as expected (fig. 6.46 center). Finally, probe needles connected channel 183 to the S-bias line: the noise decreased up to 7% (fig. 6.46 right). Note that channel 180 presents a different behaviour, and seems to be insensitive to the operations carried out on channel 183.

This way, a zero-impedance path to the bias is available, preferred to a connection via interstrip capacitance to the neighbour preamplifiers. Hence most of charges produced by the channel instability will be absorbed by the bias, and not the neighbour channels.

6.7.6 Remarks

The assembly of ladder L12 GT 031 allowed us to learn many aspects of the ladder assembly and ladder behaviour. First, following the discipline and procedure described in section 6.6.5, the ladder current after Upilex and reinforcement gluing was compatible with the expected values. We also acquired the confirmation that the microwire bonding is a source of damage. Finally, a solution to reduce the noise due to damaged strips is possible, nevertheless, a perfect control of static electricity discharge is mandatory, else the VAs may be damaged.

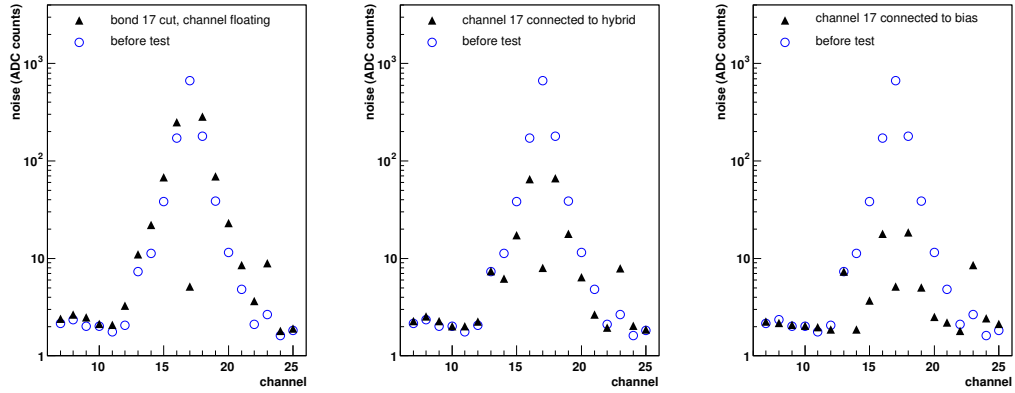


Figure 6.45: Bond 17 removal: the neighbour channels noise attenuated once the strip is connected to the bias (on the right). However, the center plot indicates that the VA gain has been reduced during the tests.

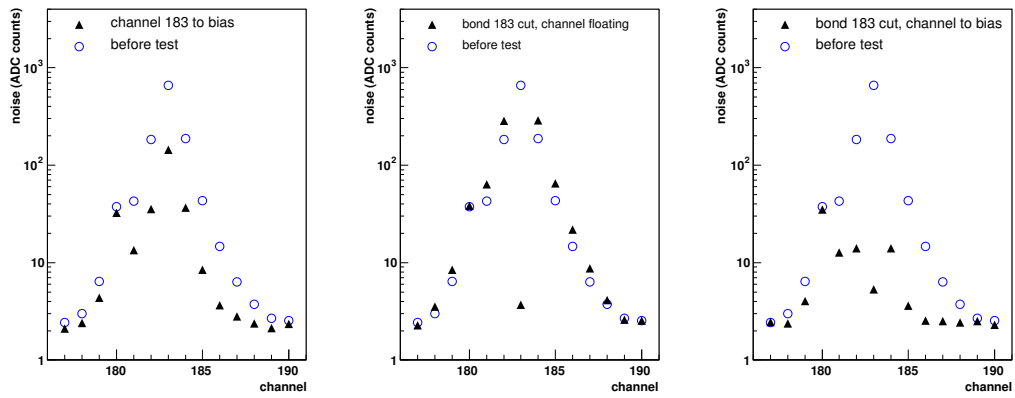


Figure 6.46: Bond 183 removal: on the left, channel is connected to bias, while still connected to the hybrid. The best neighbour channels noise reduction is achieved once the strip is connected to the bias, but disconnected from the hybrid (on the right). The channel left floating induces a noise increase.

6.8 Conclusions

The tests described in this chapter allowed us to better understand the factors which potentially alter the ladder quality during assembly, in particular the silicon surface abrasion due to dust particles. To minimize those risks, a more strict discipline was adopted in our clean room. Also, every sensor is individually examined right before assembly, and cleaned if necessary. Moreover, the jigs must be inspected and cleaned before every manipulation. Finally, a passivation on the silicon surface seems mandatory to reduce the abrasion damages. The reinforcement sanding was probably one of the sources of the AMS-01 quality decrease, and in AMS-02 this operation is done during the reinforcement production.

The assembly of a 12-sensors AMS-01 type ladder confirmed the efficiency of the reinforced clean room procedures, and allowed to understand the potential effects of wire bonding on the sensors.

Very high current strips, via the interstrip capacitance, induce noise on neighbour channels. This effect can be attenuated in connecting the high current strip to the bias line, while disconnecting it from the hybrid. This manipulation has to be done with care, though, in particular regarding the static electricity discharges.

Chapter 7

AMS-02 production

7.1 Introduction

After the assembly tests and procedure examinations described in last chapter, still in the recommissioning context, a pre-production started in Summer 2000. The procedures to harmonize the collaboration with our ETHZ colleagues at CERN were examined, and the real production started in January 2001.

Some aspects of the pre-production, then the production are discussed in the following sections. In particular, regarding the AMS-02 production,

7.2 Pre-production

The pre-production phase started in 2000. Five ladders composed of mechanical grade silicon sensors, i.e. detectors with final dimensions and metallization, but without implants, were assembled. These ladders allowed to:

- test the metrology programs;
- train using and optimizing the CAM/ALOT gluing machine;
- adjust the bonding machine parameters;
- define and test the phase 2 operations;
- test the shielding design and the shielding wrapping operations.

Each mechanical ladder had a different length: 9, 10, 11, 12 and 15 sensors.

Moreover, two electrical prototypes (2 and 12 sensors), equipped with preproduction sensors and hybrids (AMS-01 hybrid type with AMS-02 VA64_hdr9a) were assembled. The 12-sensor ladder was tested with a muon beam at CERN in September 2000 [23].

The metrology confirmed that the tools and silicon dicing allowed to achieve the desired assembly precision, with a residual rms smaller than $5 \mu\text{m}$. An interesting effect shown in figure 7.1 illustrates how ideally the alignment precision can be optimized: on the left, the

plot represents the residuals of a mechanical ladder which sensors originate from a common batch, and consequently were all cut with the same parameters. On the right are plotted the results for an AMS-02 ladder, which sensors are chosen to optimize the electrical properties, i.e. the sensors usually do not come from an unique batch, and are not cut in the same conditions. This is why the residual rms is larger than for the mechanical ladder.

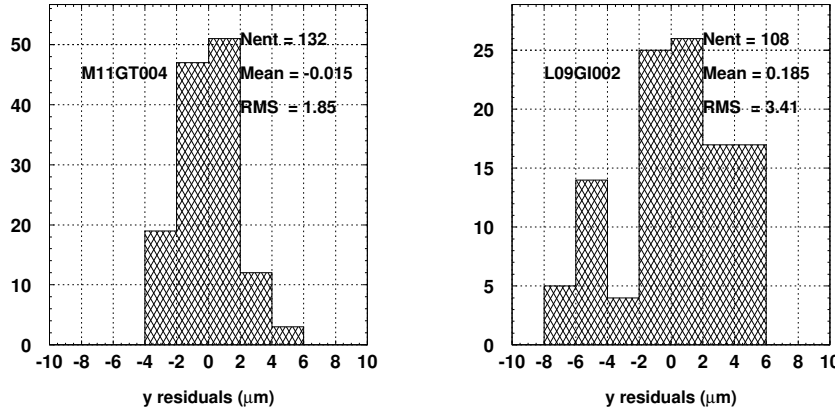


Figure 7.1: Metrology results of a mechanical ladder (left), and a production ladder (right). All the sensors composing the mechanical ladder were cut with the same cutting parameters, optimizing the residual rms. The sensors composing the production ladder come from various batches.

7.3 AMS-02 production

The ladder assembly started in Geneva in January 2001. Due to delays in the hybrid production, the first ladders were temporarily not equipped with front end electronics, although all the silicon bonding was done.

The Geneva assembly line produced 18 AMS-02 ladders, and refurbished 9 AMS-01 ladders as spares. A maximum production rate of 4 ladders/week was achieved. Due to delays on the silicon detectors procurement, Geneva finally could not produce the planned amount of 60 ladders, as the phase 2 production required the interruption of the phase 1 activities, in March 2003.

7.4 Extended electrical tests

The start of the phase 1 production allowed to perform particular electrical verifications. Thanks to these tests, some peculiarities observed in the early production found explanations, and helped diagnosing particular behaviours observed on few ladders during the production.

7.4.1 Low resistance RCAMS channels

Occasionally, ladder calibrations identify channels with an anomalously low raw noise (σ_0) value. As the raw noise is the rms of the channel raw ADC value, a low σ_0 indicates an excessively stable channel, meaning a preamplifier inefficiency, usually due to saturation. In such a case, the corresponding RCAMS channel is damaged (low resistance), and a direct measurement of the parallel resistance (R_p) value evidences this.

As an example, figure 7.2 compares, for ladder L09 GI 005 S-side, the channel raw noise and the corresponding capacitor parallel resistance: except for the first 64 channels (VA 1 was damaged), a clear correspondence between the low σ_0 channels and capacitors with low R_p exists. When the amplifier is saturated, its output is constant and thus insensitive to the silicon detector fluctuations. Therefore the common noise subtraction should not apply to the corresponding channel while the calibration program does: the channels with a low σ_0 are virtually noisy. Nevertheless, this behaviour is useful as it helps identifying those channels.

As a second check, once the defective hybrid of L09 GI 005 was removed, the strip currents were measured. If the silicon is at the origin of the noise, then the current is larger than expected. Figure 7.3 compares the ladder noise after repair with the channel currents and the expected channel current (the sum of the individual strip currents measured at the University of Perugia). Obviously, no correspondance exists between the strip current and the low σ_0 measurements of figure 7.2. No temperature correction have been applied: this is why we observe discrepancies between the current measurements. Nevertheless some small current peaks before and after assembly are comparable, as e.g. between channels 450 and 500. The number of high current channels has clearly increased after assembly, in particular, channel 509 draws a current above 10 μA . Some other peaks, with currents of the order of 10 nA are visible and correspond to a noise increase. Note that channel 509, due to its very high current, induces noise on neighbour channels (see section 6.7.4).

7.4.2 Bonding quality

The bonding quality is a key parameter, as non-optimum conditions may severely decrease the strip performance.

For instance, the bond quality of ladder L11 GI 007 was clearly lower than usual, and the number of noisy channels was abnormally high. A strip current measurement shows that at least five strips are seriously damaged, while some more present currents larger than before assembly (fig. 7.6). As no mechanical defect is observed (no scratch), the bonding is the source of those problems. The machine was serviced after the production of L11 GI 007.

Even with good parameters, an accident is possible: a strip damage due to bonding is shown in figure 7.4. This is the only one damaged strip, as current measurements confirm it: in figure 7.5 left, the damaged strip is disconnected and grounded. The total ladder current goes back to a normal value (2.9 μA at 80 V). Also, the isolated strip current is compared with the total current of corresponding channel: the damaged strip current is about 10^4 larger than the remaining strips composing the corresponding channel (figure 7.5, right).

Note that for a 11-sensor ladder, $11 \cdot 640 = 7040$ wire bonds are done on the S-side silicon,

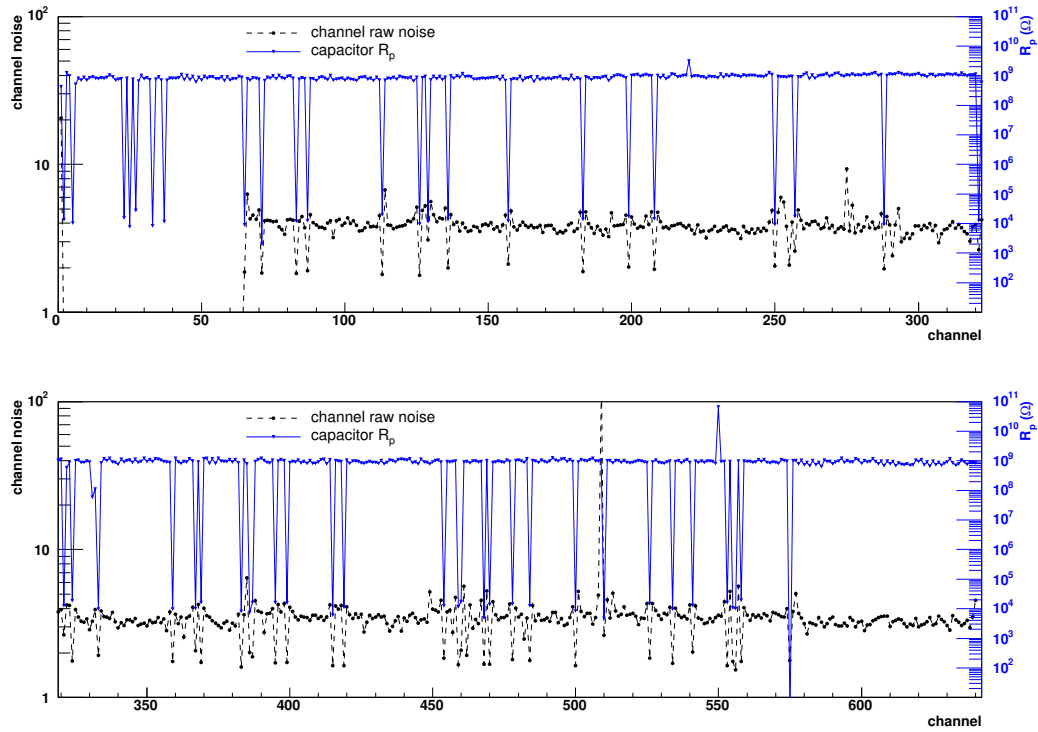


Figure 7.2: Ladder L09 GI 005: comparison between channel raw noise, and corresponding capacitor parallel resistance. Clearly, channels with low parallel resistance saturate the amplifier and induce a low raw noise. Note that VA 1 was damaged.

but actually, a wire bond connects two strips, i.e. there are $21 \cdot 640 = 13440$ possibilities to damage a silicon strip.

7.5 AMS-01 ladder refurbishment

Nine AMS-01 ladders were refurbished as spares. The refurbishment procedure is as follows:

1. A protective tape is deposited on the Upilex surfaces which are glued to the hybrids.
2. The hybrids are unglued from the Upilex cables, using a hot air welder.
3. The Upilex cables are shortened of 3 mm on the K-side, and 2 mm on the S-side.
4. AMS-02 hybrids are glued.
5. Additional bonding to increase the charge collection [23] is performed on the K-side (see appendix E.4).
6. The hybrids are bonded.

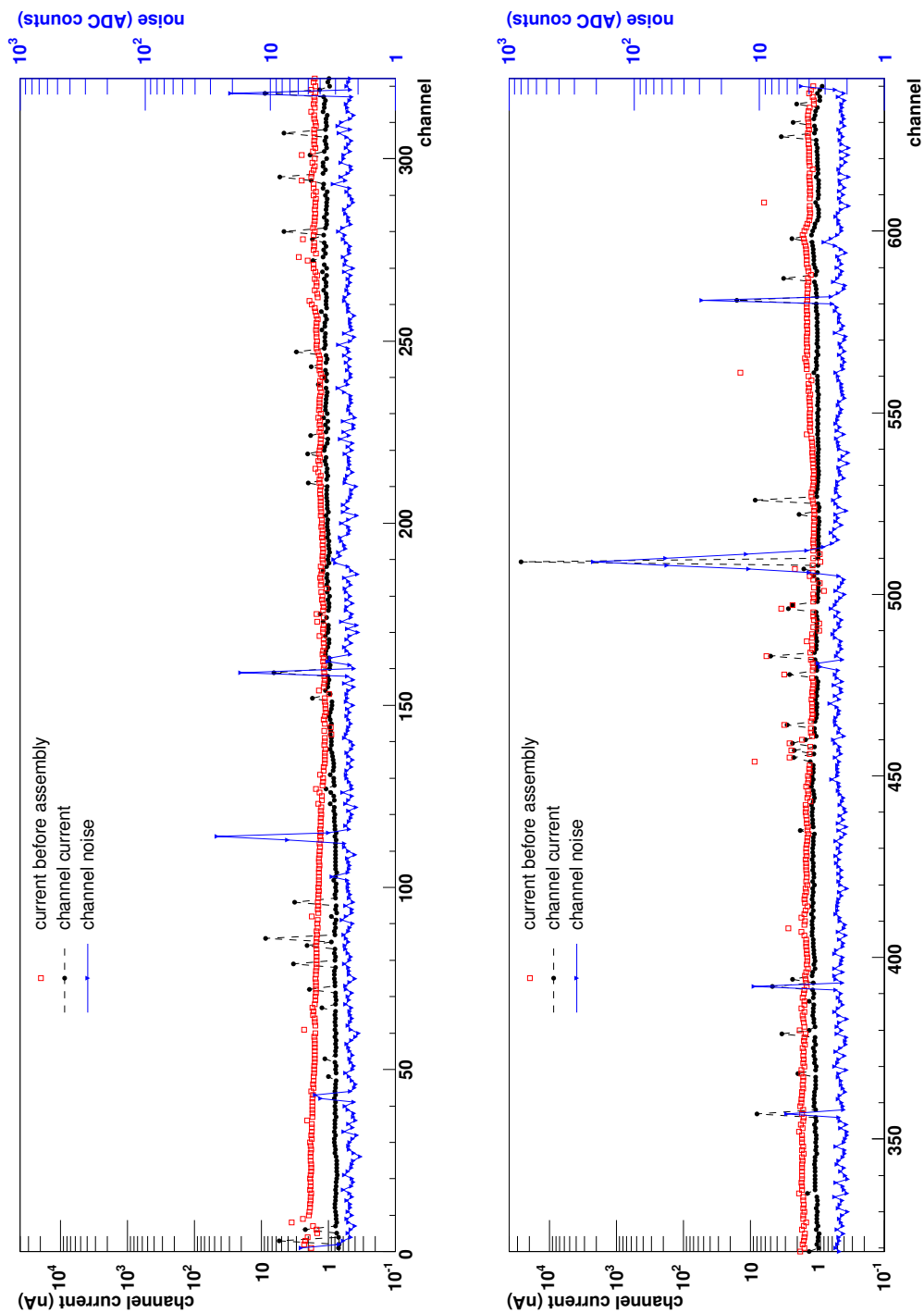


Figure 7.3: Ladder L 09 GI 005: comparison between channel noise after repair, strip current before assembly and strip current after assembly.

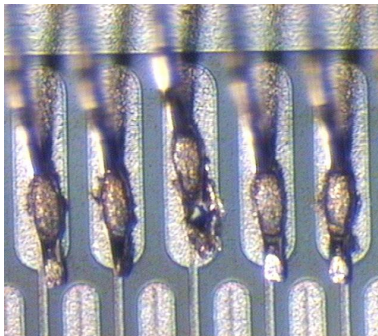


Figure 7.4: A strip damaged on ladder L11 GI 001. Only that strip produces the large ladder current of $21 \mu\text{A}$ at 80 V.

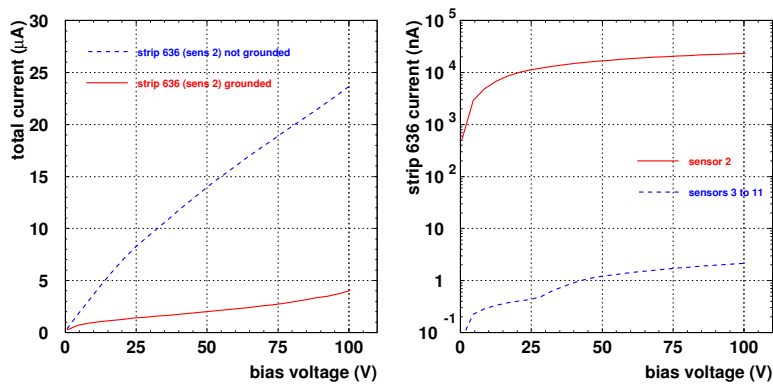


Figure 7.5: Ladder L11 GI 001: the electrical tests show that the damaged strip alone is responsible of the large current increase. On the left, the strip is grounded, and the remaining ladder current is measured to be $2.9 \mu\text{A}$ at 80 V. On the right, the strips normally daisy chained with strip 636 are measured: their total current is 10^4 smaller than strip 636 of sensor 2.

7.6 Silicon performances

As mentioned earlier, an important effort was produced to improve the silicon detector and the ladder qualities. The electrical tests reflect these improvements. Figures 7.7 and 7.8 show the channels noise, S- and K-side for the nine AMS-01 refurbished ladders. Figure 7.7 present the noise before refurbishment, with AMS-01 hybrids, figure 7.8 presents the noise distribution after the refurbishment, with AMS-02 hybrids. Although the mean noise on both sides did not increase, the rms of the noise distributions is reduced with the new hybrids.

Comparing figures 7.8 (AMS-01 silicon with AMS-02 hybrids) and 7.9 (AMS-02 ladders) show the influence of the silicon improvement between AMS-01 and AMS-02: as the front-end electronics is the same, the difference in the noise values originate from the silicon. The noise is obviously lower on both sides with AMS-02 silicon, and the rms of the noise distributions

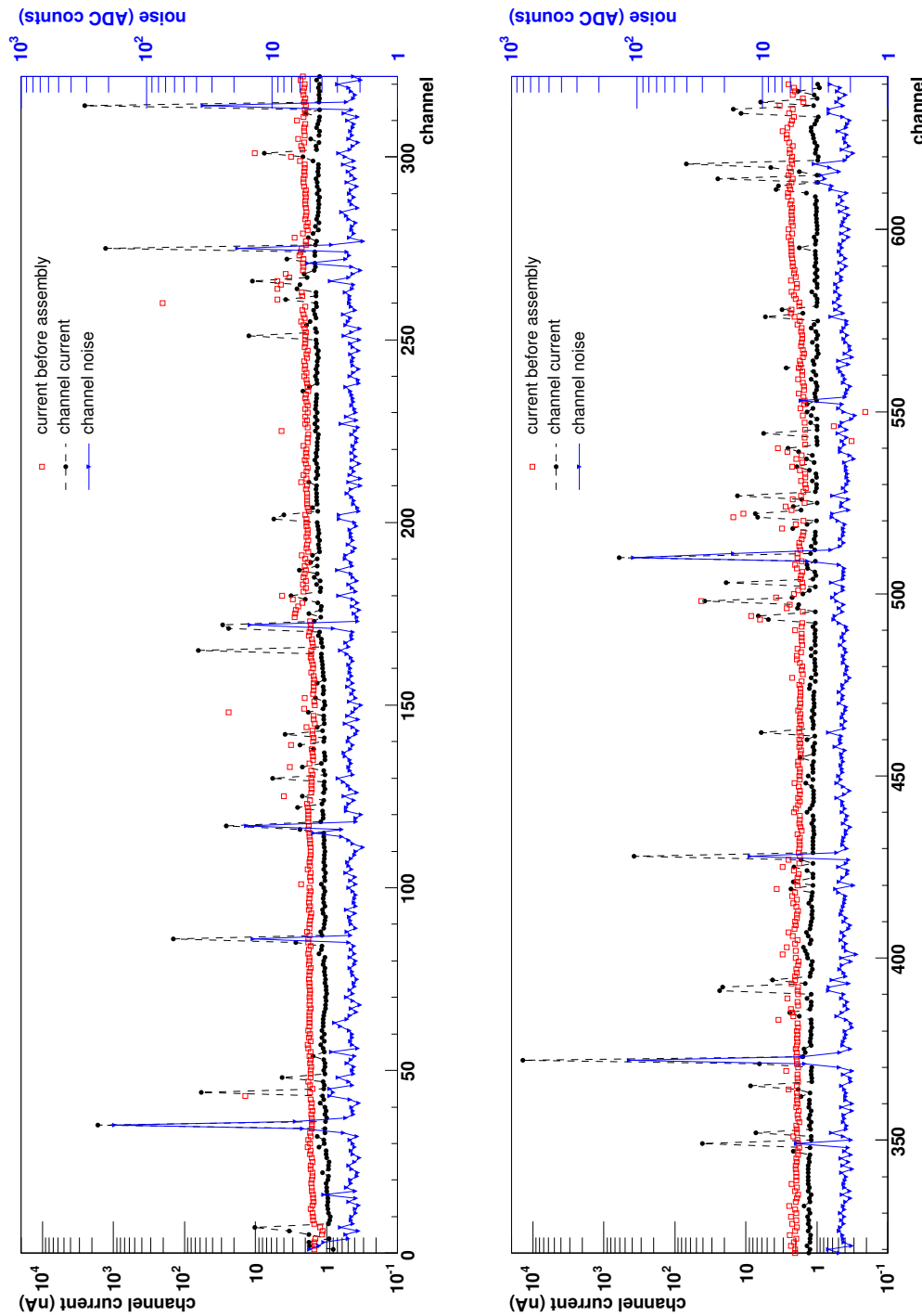


Figure 7.6: Ladder L11 GI 007 presents an abnormal large number of noisy channels, which correspond to high current strips. The strip currents before assembly do not reflect this feature. As no mechanical defect on the strips is observed we conclude that the bonding conditions are the source of the damages.

is smaller, too.

The S-side mean noise is larger with AMS-02 hybrids, evidence the improvements thanks to the new hybrids. Comparing the noise distribution for the refurbished AMS-01 ladders and the AMS-02 ladders show the improvement of the silicon sensors.

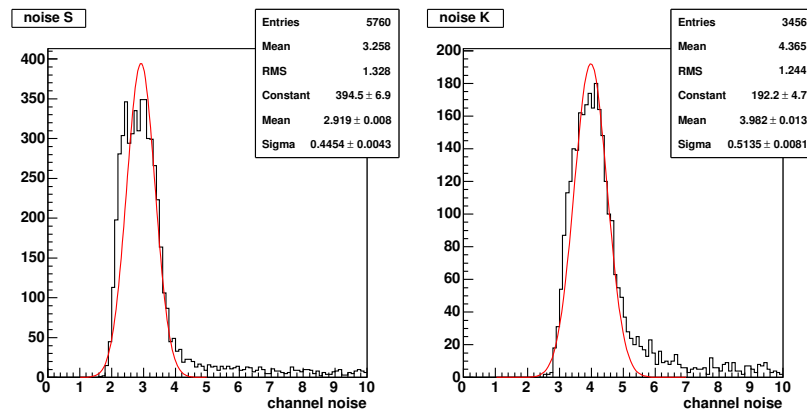


Figure 7.7: Noise performance of the S-side (left) and K-side (right) channels of nine AMS-01 ladders before refurbishment.

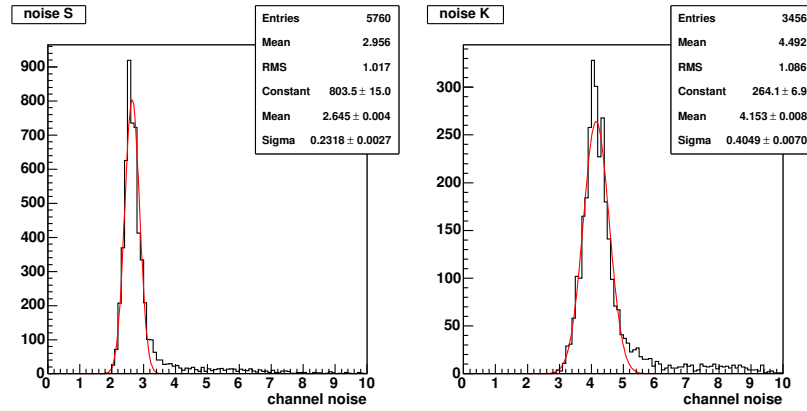


Figure 7.8: Noise performance of the S-side (left) and K-side (right) channels of the nine refurbished AMS-01 ladders.

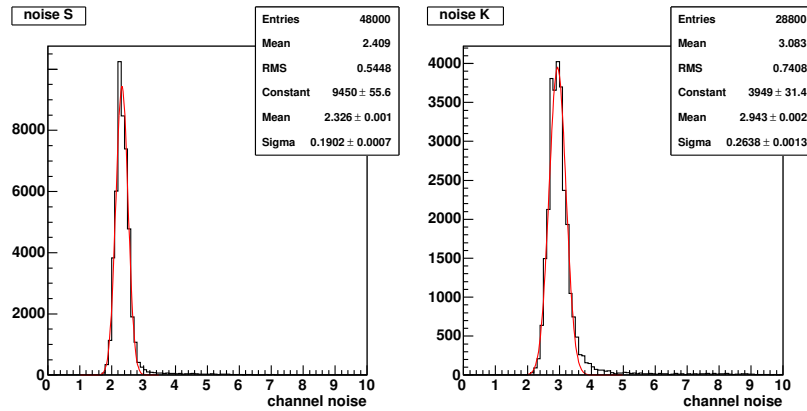


Figure 7.9: Noise performance of the S-side (left) and K-side (right) channels for 75 AMS-02 ladders.

Chapter 8

Beam test analysis

8.1 Introduction

To study the AMS-02 ladder performances with heavy ions, a 6-day beam test was scheduled for October 2002 at CERN, using the H8 beam line of the Super Proton Synchrotron (SPS). A fragmentation beam was produced with primary lead ions impinging on a beryllium target. The fragmentation beam had a momentum of $20 \frac{GeV}{c \cdot A}$, the ions were then selected depending on rigidity ($R = p/(Ze)$):

beam type	typical nuclei	R ($\frac{GV}{c \cdot Z}$)
$A/Z = 2$	^4He	40
$A/Z = 7/4$	^7Be	35
$A/Z = 3/2$	^3He	30

Table 8.1: Heavy ion beam types

Proton data were also collected, with a beam momentum ranging from 5 to 20 GeV/c.

The setup was operated with engineering models of the AMS-02 acquisition electronics, namely the TDR2 and the power supply boards.

8.2 Configuration

One power group, composed of a TBS (Tracker Bias Supply), a TPSFE (Tracker Power Supply Front End) and three TDR2 boards, all of the “engineering model” type, was available. Six ladders were operated, since a TDR2 board actually includes two TDRs. A light tight aluminium box ($200 \times 400 \times 860 \text{ mm}^3$) was assembled. The box was equipped with legs which allow a height correction up to 80 mm. A simple fixation system enabled to directly place the ladders in their transportation box. With such a system, a ladder can be quickly replaced. The plexiglas covers were removed at the level of the two last sensors, to minimize the material to be traversed by the beam.

A ladder support system used in a previous beam test in September 2000 was fixed to the aluminium box: it allowed to place a sixth ladder in a rotated position, as schematically shown in figure 8.1. The box dimensions constrain the ladder size to a maximum of 12 sensors.

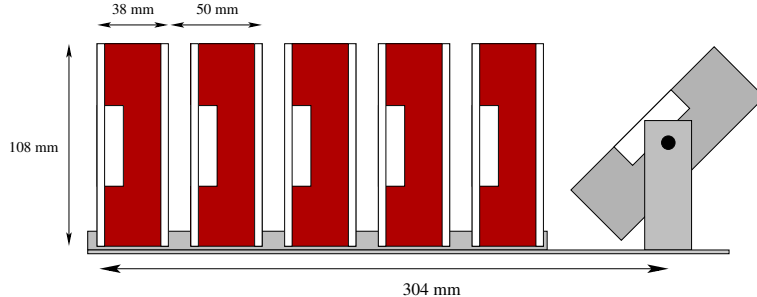


Figure 8.1: Ladder positions in the test box. Five ladders remain in their transportation box, thus making the manipulations easier.

This allows to limit the test box size, while keeping flexibility in the ladder selection (see table 4.1 on p.57). An unshielded ladder is easily stored in a transportation box, increasing the variety in the ladder choice. The test box can be set vertically: in such a configuration, with scintillators above and under the box, it is possible to detect cosmic rays.

The Tracker Data Reduction (TDR) boards control the ladder data acquisition: they pilot the hybrid readout sequence and digitize the analogue signals issued by each hybrid. Every TDR circuit is connected to one ladder and, after reset, calibrates the ladder to compute each channel pedestal, raw noise and noise. The delay between the trigger and hold signals is controlled by the user. The standard data acquisition consists in reading out the 1024 channels, subtracting the pedestal for each channel, computing and subtracting the common noise for each VA. Finally, a cluster identification is done. In real conditions, the communication bandwidth is limited to 2 Mbps and only the cluster information will be transmitted. Nevertheless the TDR can also transfer raw data alone or combined with the reduced data. This mode is used in debugging situations only. During beam tests, the mixed mode is preferred to evaluate the performance and reliability of the data reduction algorithm, provided sufficient data storage is available. In October 2002, only the raw mode was implemented during the three first days of operation.

The data acquired by the TDRs were transmitted to a PC-computer run under Linux, using the AMS Wire [60] protocol. AMS Wire is based on the SpaceWire [61] protocol, specifying full-duplex, point-to-point, serial data communication links. Space Wire is used in space applications, and allows transmission rates from 2 Mbps up to more than 100 Mbps.

Two other AMS sub-detector groups participated to the beam test: the RICH group, which was the main user, and the TOF group. A common trigger was set up and a common event number was available, to compare the beam test data. The main trigger was generated by the RICH scintillators, yet the tracker test box was also equipped with scintillators used to trigger the acquisition in case the RICH was not available. The tracker trigger signal was managed by an external board (the trigger board), connected to the PC with an AMS Wire

connection.

The trigger board associated to each event a `spill` bit to the PC, indicating when particles were extracted from the beam at trigger time, i.e. if the acquired event corresponded to beam particles or not. In the offspill period (i.e. no beam), a 100 Hz trigger signal was sent to the ladders, to make offline calibrations with the raw data. Moreover, the trigger board controlled the time difference from trigger to hold, which could be controlled from the acquisition software. The analysis described here focuses on the three first days of acquisition, where the set up was stable.

8.3 Selected ladders

Two low noise ladders per assembly line were requested, with properties as summarized in table 8.2.

Ladder	TDR	Ladder position in beam	Current (μA)	Mean noise (ADC counts)		Number of noisy channels	
				S	K	S	K
L12 AI 002	3up	6	2.5	2.2	2.7	3	4
L09 GI 003	3dn	5	2.7	2.6	3.3	6	8
L09 GI 011	4up	4	2.2	2.2	2.8	1	1
L07 PI 002	4dn	3	2.4	2.2	3.4	3	2
L07 PI 003	5up	2	74.4	2.3	3.4	1	6
L12 AI 001	5dn	1	3.0	2.2	2.9	2	2

Table 8.2: Properties of the ladders used during the 3 first days of the beam test. Channels are defined as noisy if $\sigma > 5$ on the S-side and $\sigma > 6$ on the K-side. 1 ADC count corresponds ~ 730 e.

As the serial numbers indicate (last three digits, see appendix G), the tested ladders can be considered as “preproduction” modules, although the assembly steps were considered as final. As a matter of fact, the beam test results revealed that the electronics performance was particular to each ladder, as listed in table 8.3. Five ladders chosen for the beam test presented peculiarities in the gain performances, some were due to low gain VA chips, others due to not final operational amplifier parameters which induce a lower amplification factor.

As a consequence, each ladder produces a signal with different characteristics. The problem related to low gain VA ladders was identified during the analysis, the corresponding hybrids were replaced later, when an identification procedure was established.

On ladder L09 GI 003, a bonding machine failure severely damaged two sensors, which were replaced before the beam test. Only L09 GI 003 is electrically representative of the final AMS-02 ladders. The performance observed during the test must thus be taken as a lower limit to the final performance.

Ladder	Property
L12 AI 002	not final operational amplifier resistors, S and K side
L09 GI 011	low gain VAs, s-side
L07 PI 002	not final operational amplifier resistors, K side
L07 PI 003	low gain VAs, s-side
L12 AI 001	not final operational amplifier resistors, S and K side

Table 8.3: Hybrid properties of the non-standard ladders.

8.4 Analysis

8.4.1 Alignment

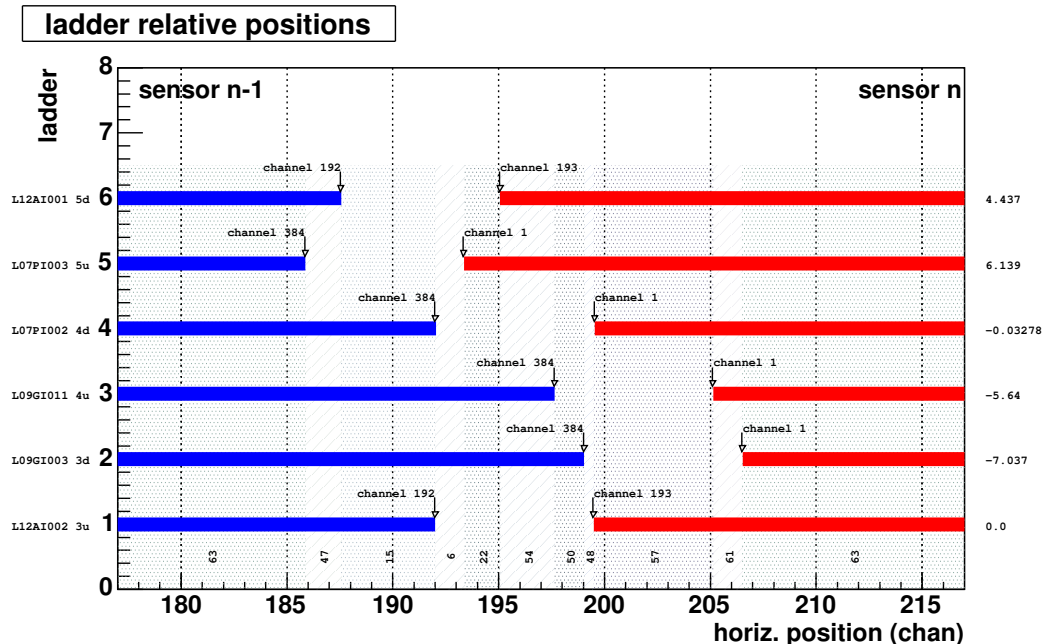


Figure 8.2: Relative longitudinal alignment of the ladders under test. The x axis is expressed in K-side channel units and is aligned with the channels of sensor $n - 1$ of ladder 1. The nominal gap distance corresponds to 7.5 channels. Note that due to the different ladder lengths, individual channel indices for sensors n and $n - 1$ are different for ladders 1 and 6.

The two last sensors of each ladder were exposed to the beam. Two of the six ladders have an even number of sensors. This has a non-negligible influence on the cluster localization. As noticed in section 4.5, the readout channels on the K-side are distributed over two sensors: channels 1 to 192 correspond to strips of sensors in odd position, channels 193 to 384 correspond to the even sensor strips. The beam test configuration imposes a conversion to combine the signals provided by the six ladders: the last sensor of ladders 1 and 6 is related to channels 193 to 384, while for the four remaining ladders the last sensor is related

to channels 1 to 192, as schematically shown in figure 8.2.

The beam cross section regularly changed during the test. In total, a relatively important surface of each sensors was exposed to beam as shown in figure 8.3.

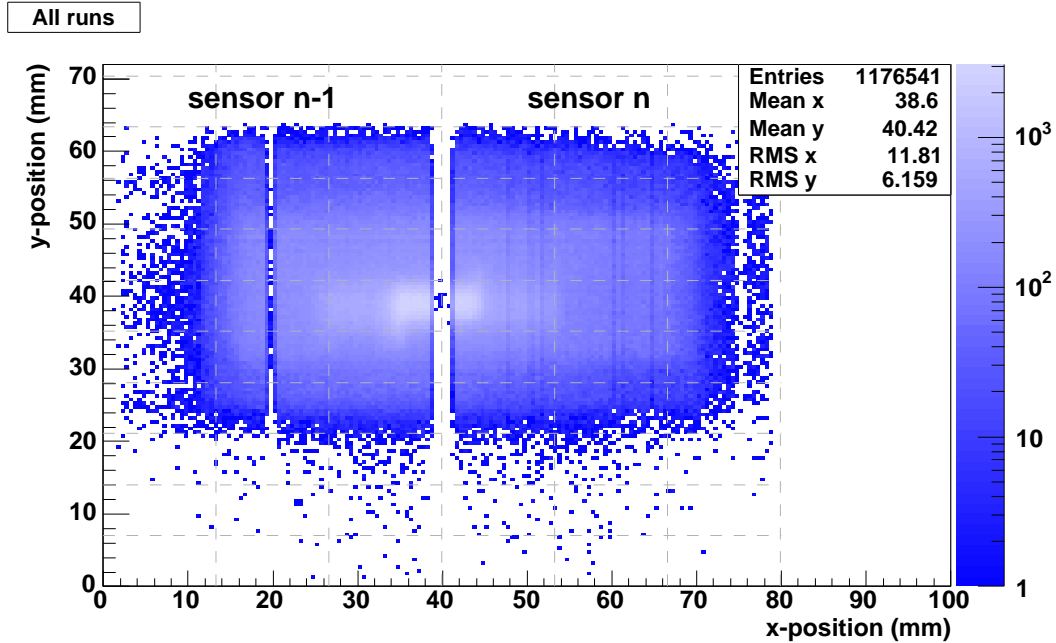


Figure 8.3: Beam profile on ladder 1, based on all nuclei runs used in this analysis. The dashed lines represent the VA separations.

8.4.2 Cluster identification

The analysis presented here is based on the raw data only, online data reduction is not used. The software was developed under C++, using the ROOT libraries. First, a data reduction algorithm was applied for each ladder, identifying the cluster locations with the following criteria (see section 3.11):

- A cluster is found at channel i if the residual is such that $r_i > 4.1 \cdot \sigma_i$;
- The cluster is limited by channels i_1 and i_2 such that $r_i > 1.5 \cdot \sigma_i$ for $i \in [i_1, i_2]$;
- The cluster integral, defined as:

$$I = \sum_{i_1}^{i_2} r_i \quad (8.1)$$

is larger than 7 ADC counts.

The following information is saved to disk:

- cluster first channel i_1 ,
- cluster length $\ell = i_2 - i_1 + 1$ (in channel units),

- cluster integral I (in ADC counts),
- cluster center of gravity in channel units, defined as:

$$cog = \frac{1}{I} \sum_{i_1}^{i_2} r_i \cdot i \quad (8.2)$$

- the location and value of the cluster maximum,
- the cluster signal over noise ratio.

8.4.3 Trigger to hold time

A particular time delay is necessary between the trigger and hold signals, equal to the VA shaping time. This shaping time depends on the preamplifier parameters (see section 3.12) and was set to be the same on the S- and K-side hybrids. During the AMS-02 hybrid development many tests, in particular with a single ladder cosmic ray test system [62], lead to the conclusion that the shaping time was close to 5 μs . The trigger to hold time chosen during the whole beam test was set to 4.5 μs , based on a cosmic ray measurement done the day before beam test start.

The first runs were used to measure the shaping time with an $A/Z = 2$ beam. A scan between 3.5 μs and 6.0 μs was done.

The integral distribution for each ladder side and for each run was then fitted with a Landau function. Figure 8.4 shows the most probable cluster integral value, for each ladder and side as a function of the trigger to hold time. On the S-side, the shaping time is lower than the expected 4.5 μs , while it is compatible with 4.5 μs on the K-side. This result was later confirmed with laser diode tests, showing that the S- and K-side signal properties are different [63]. As we will later see, this behaviour presents some advantages.

The conclusions based on the beam test data and the laser diode tests lead to the decision to set different trigger to hold times on the S- and K-side. In AMS-02, it will be 3 μs on the S-side and 4 μs on the K-side. These delays, controlled by the TDRs can be reprogrammed at any moment, except for the time difference, fixed by design to 1 μs .

8.4.4 Signal charge study

The aim of this study is to examine the signal produced by the passage of nuclei of various Z . The selected runs use the $A/Z = 2$, $A/Z = 3/2$, $A/Z = 7/4$ beam settings, with a total of 2'638'136 events. Single tracks of 6 ladders, on both S- and K-sides, were taken into account, thus reducing the event number to a total of 1'620'803. A refined procedure limited to VA 6 on ladders 1 to 5, and to VAs 6 and 7 on ladder 6, reduces the number of useful events to 1'017'861.

The raw track charge was computed as follows:

$$charge = \frac{1}{6} \sum_{l=1}^6 \sqrt{I_l} \quad (8.3)$$

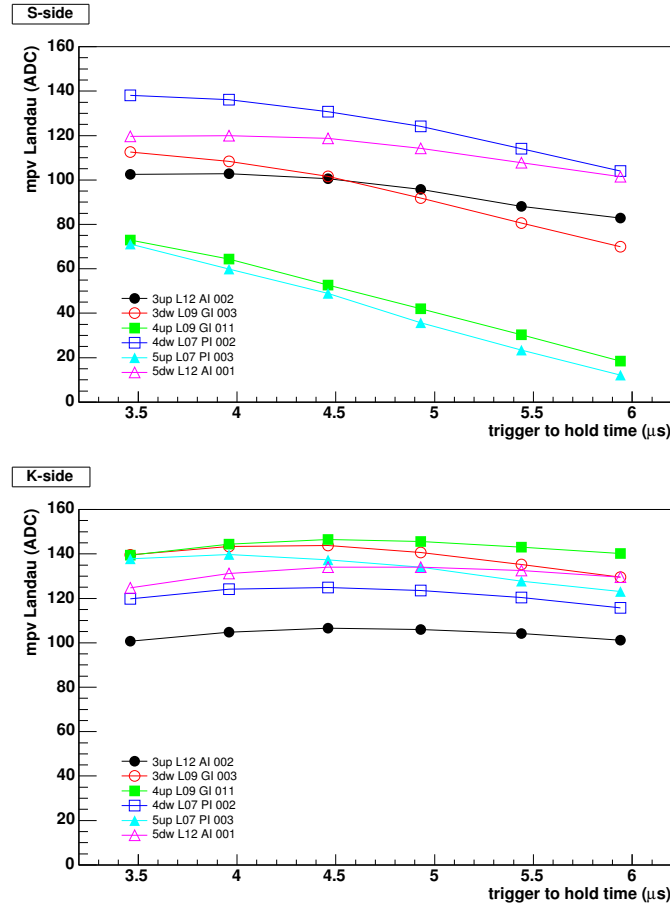


Figure 8.4: Most probable cluster integral value from a Landau fit, for each ladder and side, as a function of the trigger to hold time, for $A/Z = 2$ events. We observe that on the S-side the optimal shaping time is lower than the expected $4.5 \mu\text{s}$.

with l the ladder index. This charge estimation is plotted on fig. 8.5 for the S-side, and on fig. 8.6 for the K-side. Clearly, the measured charge behaviour is different on the S- and on the K-side. The element to which corresponds each peak has been indicated. Its identification was possible in combining both the S- and K- charges on a two-dimensional histogram (fig. 8.7).

On the S-side (fig. 8.5), a rather linear behaviour is observable for helium, lithium and beryllium, while the charges corresponding to boron, carbon, nitrogen, oxygen and fluorine are not separated. Starting with neon, a linear regime is re-established, up to titanium, above which no element separation is possible. On the K-side (fig. 8.6), peaks from helium to sodium are distinguishable and a linear relation between Z and the raw track charge estimation is clear from helium to neon. Above neon, elements are still observed as peaks in the distribution, but the separation between them is less clear. In particular, manganese, aluminium, argon and potassium are not clearly distinguished.

Interestingly enough, when one side is unable to separate two elements, the other side is:

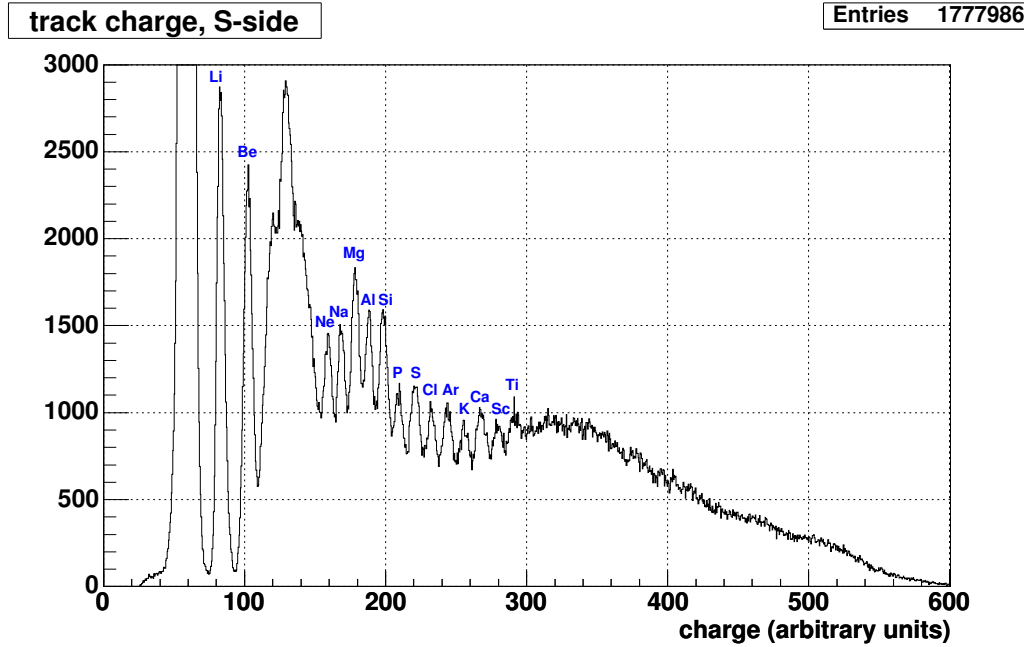


Figure 8.5: S-side track raw charge, in arbitrary units.

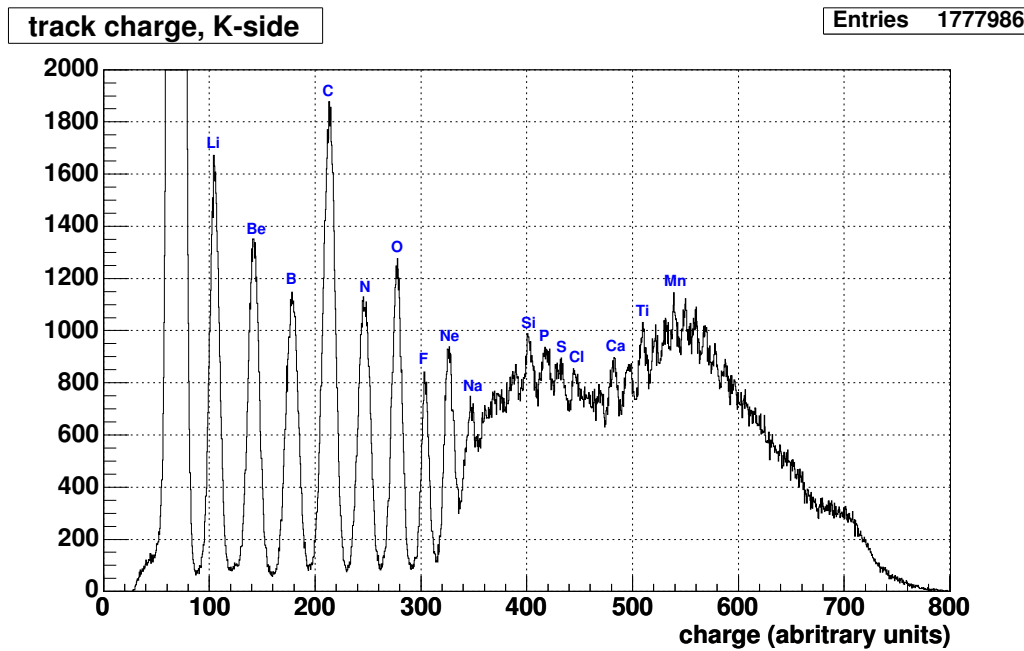


Figure 8.6: K-side track raw charge, in arbitrary units.

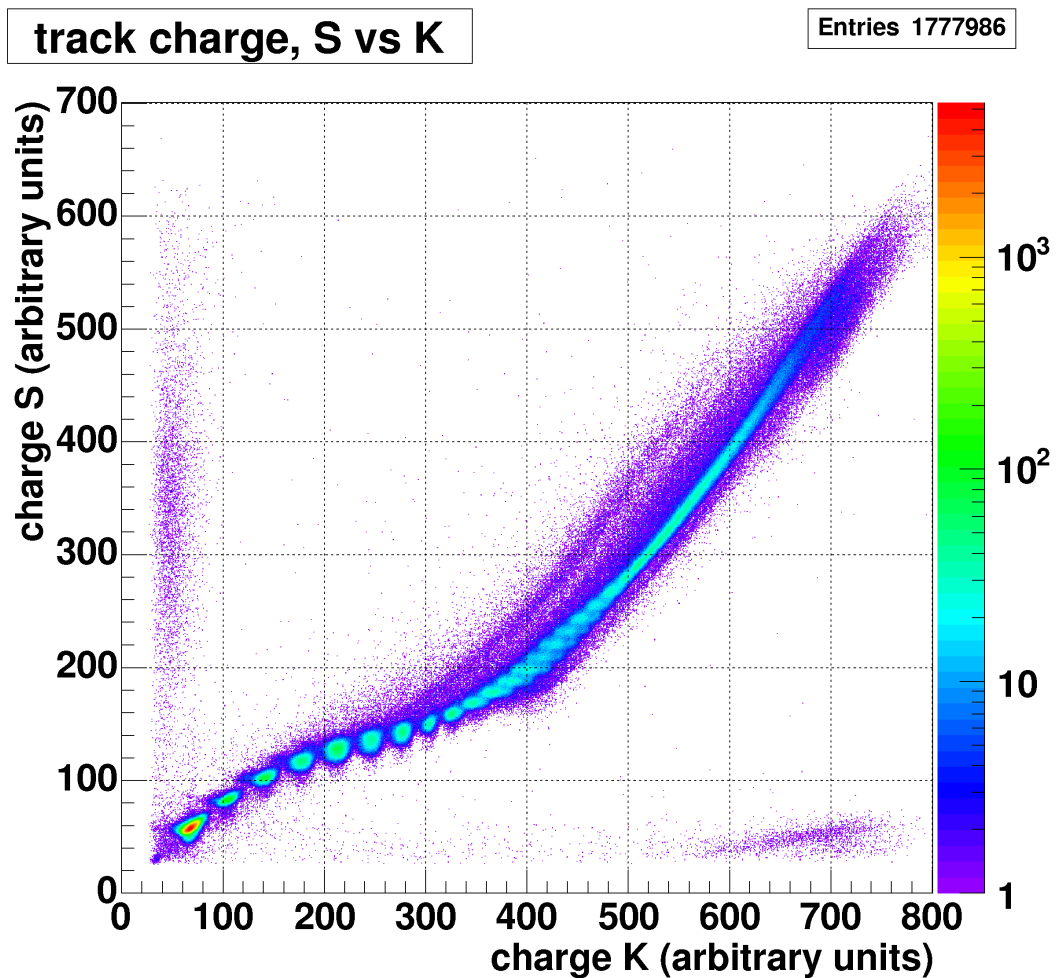


Figure 8.7: S-side track raw charge vs. K-side track raw charge estimations, in arbitrary units.

the K-side separates clearly B, C, N, O and F while the S-side does not. The S-side separates Mg, Al, Ar and K while the K-side does not.

The combination of both charge measurements is plotted in figure 8.7. Both regime changes are visible. The plot also explicits the difficulties to separate Mg from Al and Ar to K on the K-side charge histogram.

It has been observed that the signal cluster regularly presented a structure similar to the example shown in figure 8.8. This effect, not immediately taken into account, prevented the offline cluster finding program to work correctly, and these structures were separated into three clusters. The cluster finding procedure was then adapted to correctly analyse those events. A track containing at least one such cluster was then tagged as “type 2” track. As an example, figures 8.9 and 8.10 compare the raw charge distribution for all tracks and for the type 2 tracks. The presence of type 2 tracks is rather reduced on the K-side, but not on the S-side. In particular, starting from chlorine, the S-side tracks are exclusively of the type 2 family.

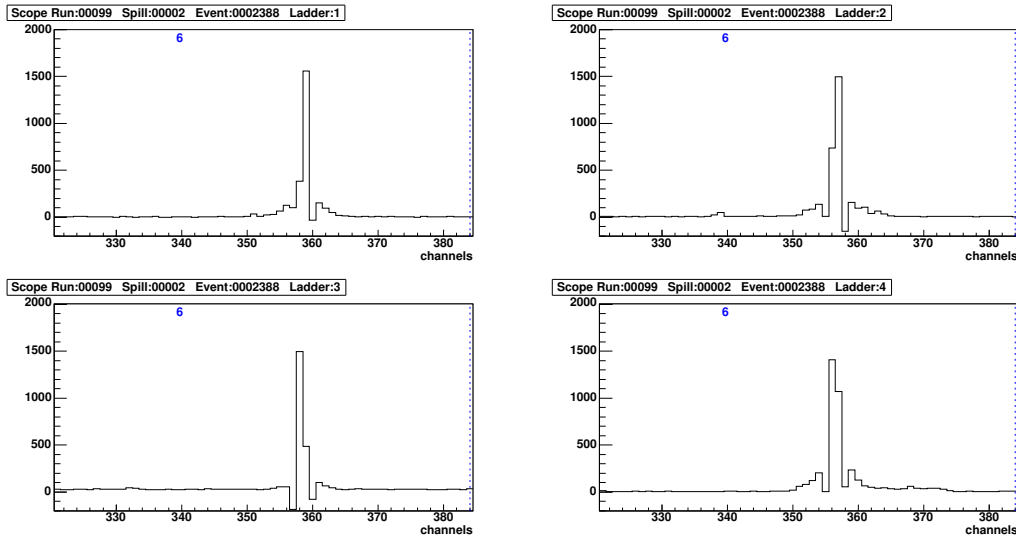


Figure 8.8: An example of an event with negative signal channels (type 2 clusters). Tracks with at least one such cluster are tagged as type 2 tracks.

It is also interesting to note that the proportion of type 2 tracks depends on the trigger to hold time, in particular on the S-side. As depicted in figure 8.11, the fraction of type 2 clusters increases on the S-side with the trigger to hold time. The S-side fraction equals the K-side fraction only with the lowest trigger to hold time.

The difference in raw charge distributions on S and K-sides is due to different gain behaviours on both sides. In consequence it is possible with one side to recover the weaknesses of the other side. The K-side distinguishes elements merged on the S-side, i.e. B, C , N, O and F. The S-side resolves a cluster of charges on the K-side starting from Mg up to K. In the next sections, we describe a method to calibrate the charge measurement and improve the element selection.

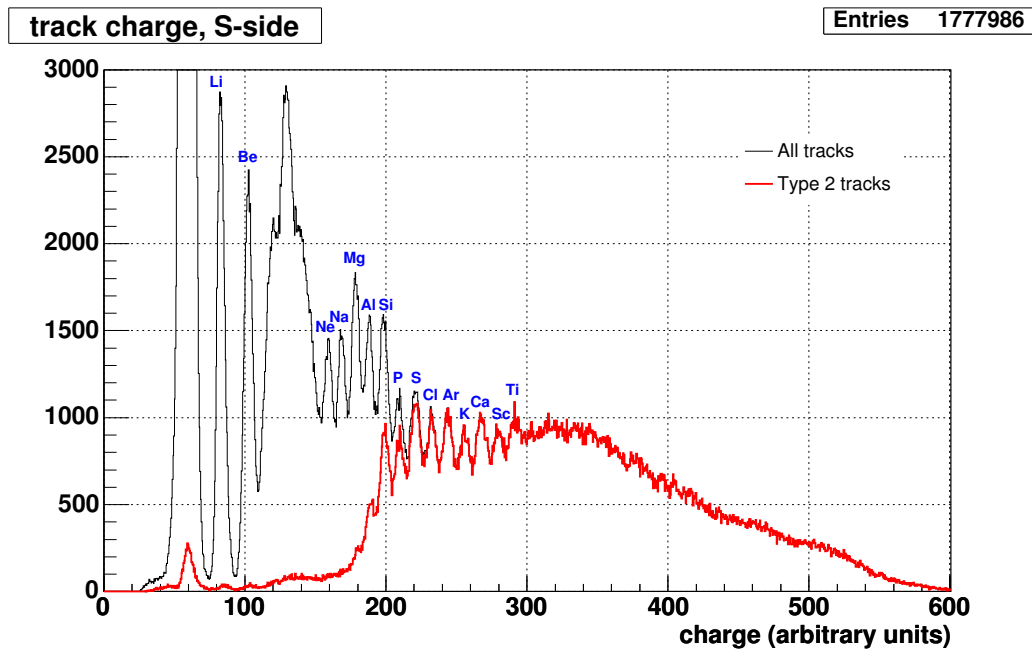


Figure 8.9: Contribution of the type 2 tracks on the S-side charge distribution.

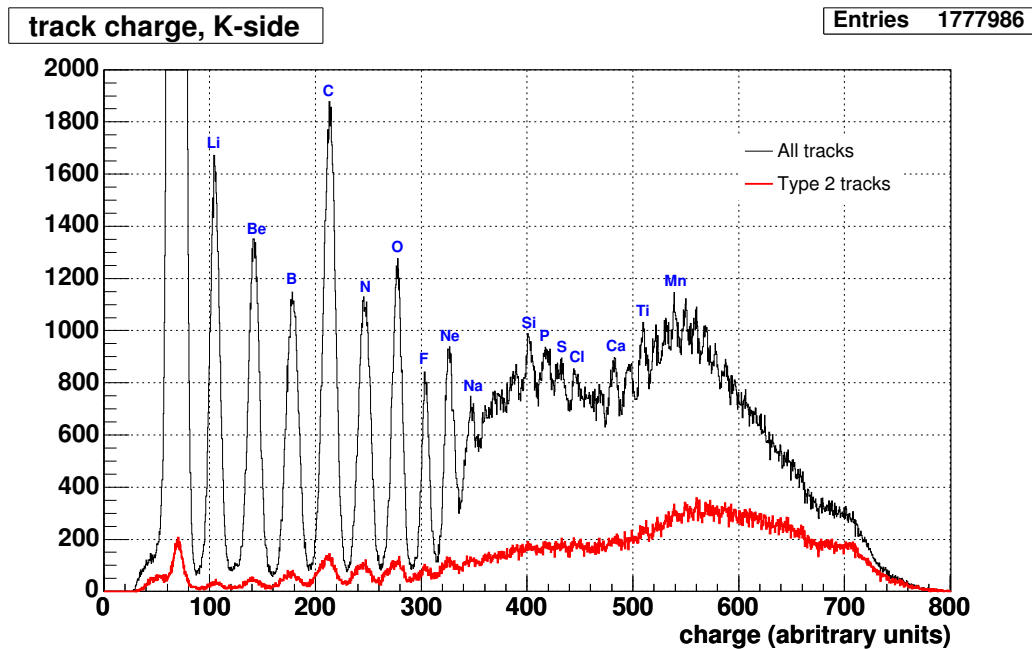


Figure 8.10: Contribution of the type 2 tracks on the K-side charge distribution.

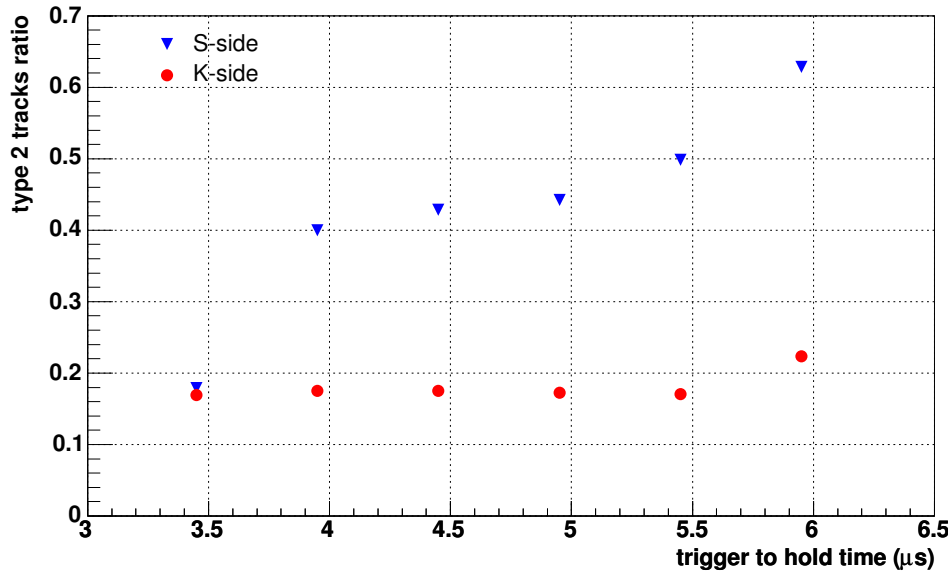


Figure 8.11: Fraction of type 2 tracks for six trigger to hold time settings. While the fraction remains stable on the K-side, it increases when the trigger to hold time moves away from the optimum VA shaping time.

8.4.5 Cluster integral corrections

Introduction

This section shows that the cluster integral depends on three different factors:

- the hybrid amplification;
- the charge of the crossing particle Z ;
- the cluster center of gravity.

The correction procedure described in following sections will be:

1. to determine, on a selected sample associated to a particular Z , the cluster integral dependence on the cluster center of gravity, using adequate interpolation functions.
2. to determine the maximum of the integral mean value for each Z , in order to define an interpolation function expressing Z^2 as a function of the cluster integral;
3. to use the selected center of gravity corrections on the cluster integral for a particular Z , then apply the integral to Z^2 correction.

Each correction function is calculated for a particular VA. On the S-side, a refined method has finally been chosen, but needs more statistics and can be only used for one VA.

Center of gravity dependence

As mentioned in section 8.3, each ladder presents particular gain properties. It is thus necessary to calibrate each ladder, to obtain a homogeneous response.

As observed in previous section, the charge comparison between both sides enables to disentangle easily the elements up to Ne, but a selection is still possible for larger Z . Thus elliptical domains from the 2-dimensional raw charge distribution on figure 8.7 were defined, to select a restricted sample of events describing each element signal. Subsequently, the cluster integral for each ladder was studied. For instance figures 8.12 to 8.15 show the integral for each ladder S-, respectively K-side, for the beryllium and oxygen ions.

In these four examples, the integral distribution clearly depends on the ladder properties and on the particle charge. The distributions also are different for the S- and K-sides. This is not surprising given the gain properties as well the charge histograms. Also, for some cases, the integral distribution presents a double-structure, clearly visible for beryllium on the K-side, but also oxygen on the S-side, as if the integral was actually composed of two or more distinct integral distributions. As the charge collection is dependent on the readout pitch, as well as on the implant pitch, the integral as a function of the cluster center of gravity was examined.

For each VA of each ladder, the cluster integral and center of gravity were stored in a 2-dimensional histogram. The center of gravity is expressed in channel units, i.e. an integral value corresponds to a readout strip. To optimally use the symmetry of the set-up, the center of gravity modulo 4 was examined, instead of the center of gravity alone. Figures 8.16 to 8.19 present the results for beryllium and oxygen, for each side, for a specific VA.

We observe a dependence of the cluster integral as a function of the center of gravity. Inspecting the profile histogram (figs. 8.22 and 8.23), we can compute a correction to the integral as a function of the center of gravity, with a periodicity of one readout channel. A refined method was examined for the S-side, for He, Be, B, C, N, O, F and Ne. Indeed, a profile histogram represents the mean of a slice of the 2-dimensional distribution. Nevertheless, it was observed that the integral distribution close to the readout strips was not symmetric, and was closer to a Landau distribution. To increase the fit quality of the cluster integral distribution in a slice, the cluster integral as a function of the center of gravity modulo 2 was examined. Depending on the cases, Landau or Gaussian fits were calculated:

- For ladder 6, all slices were fitted with a Landau function.
- For ladders 1 to 5, for He and Be, all slices were fitted with a Landau function.
- For ladders 1 to 5, for B, C, N, O, F and Ne, a Landau function was used, unless the center of gravity was in the [1.3, 1.7] and [2.3, 2.7] intervals (the region between readout strips), in which case, a Gaussian function was used.

The procedure listed above defines the integral values chosen to establish the relation between integral and center of gravity. It is now possible to inspect the relation between cluster integral and cluster center of gravity.

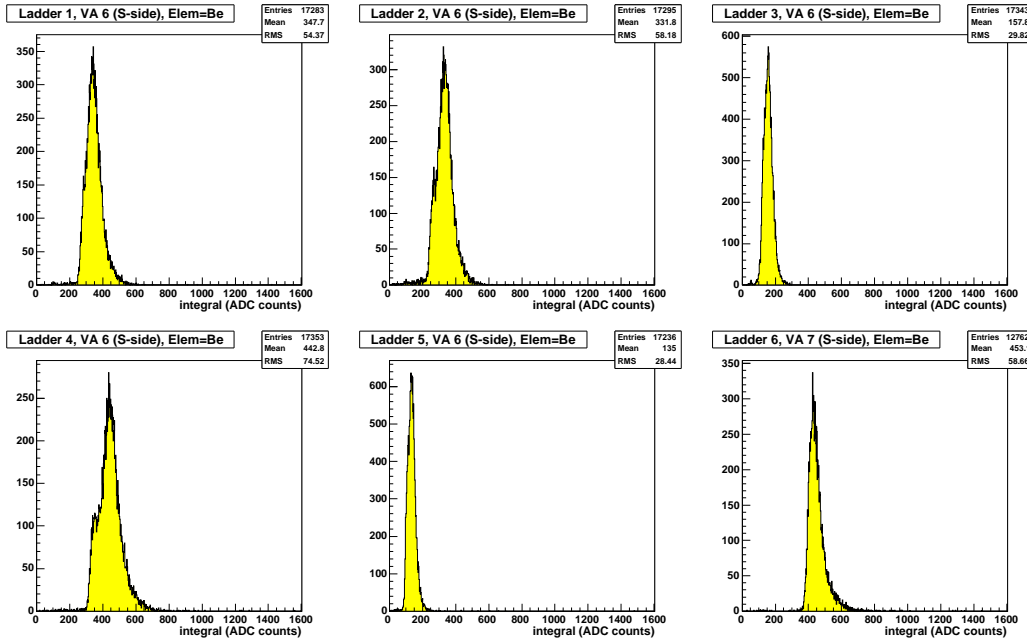


Figure 8.12: Cluster integral for a specific VA (S-side) of each ladder, for beryllium nuclei.

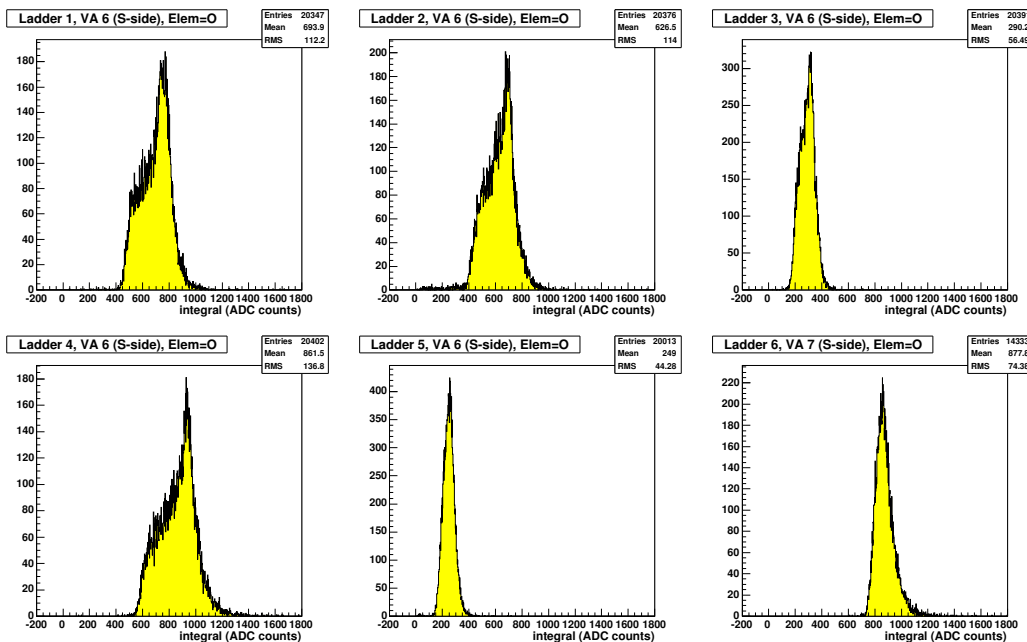


Figure 8.13: Cluster integral for a specific VA (S-side) of each ladder, for oxygen nuclei.

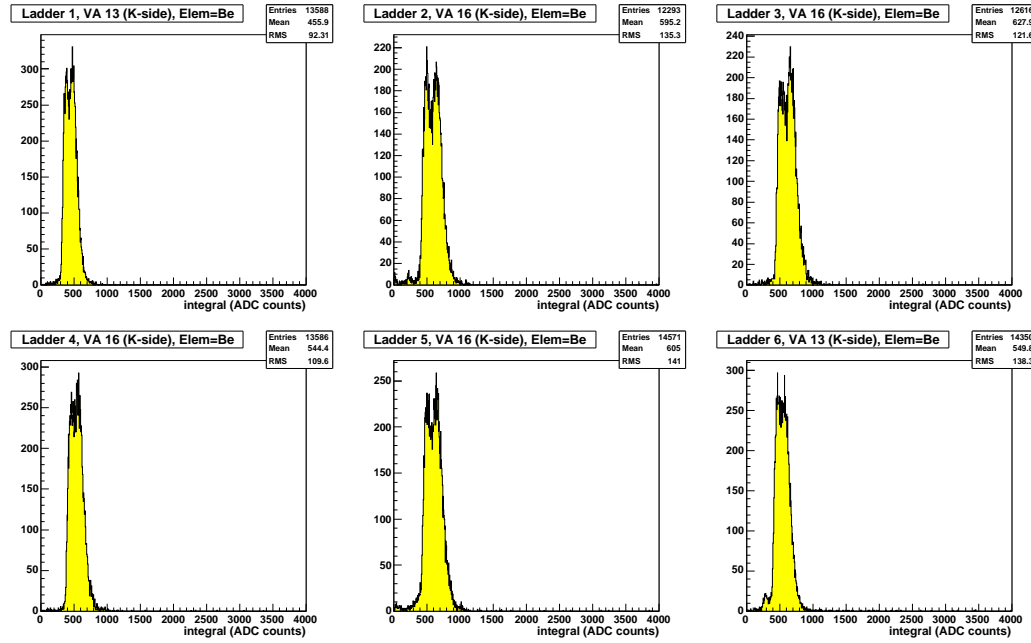


Figure 8.14: Cluster integral for a specific VA (K-side) of each ladder, for beryllium nuclei.

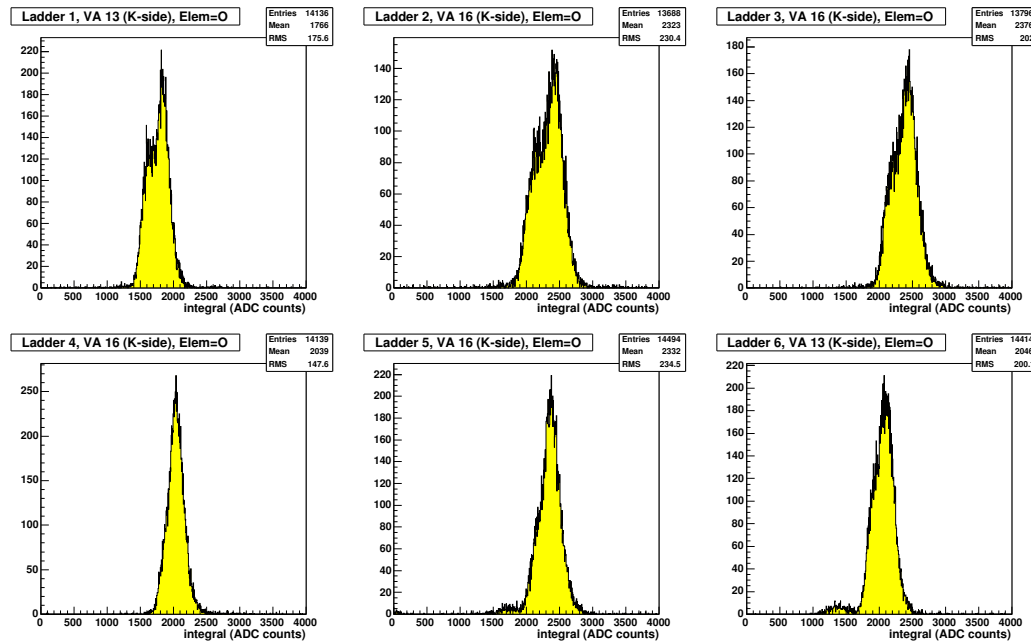


Figure 8.15: Cluster integral for a specific VA (K-side) of each ladder, for oxygen nuclei.

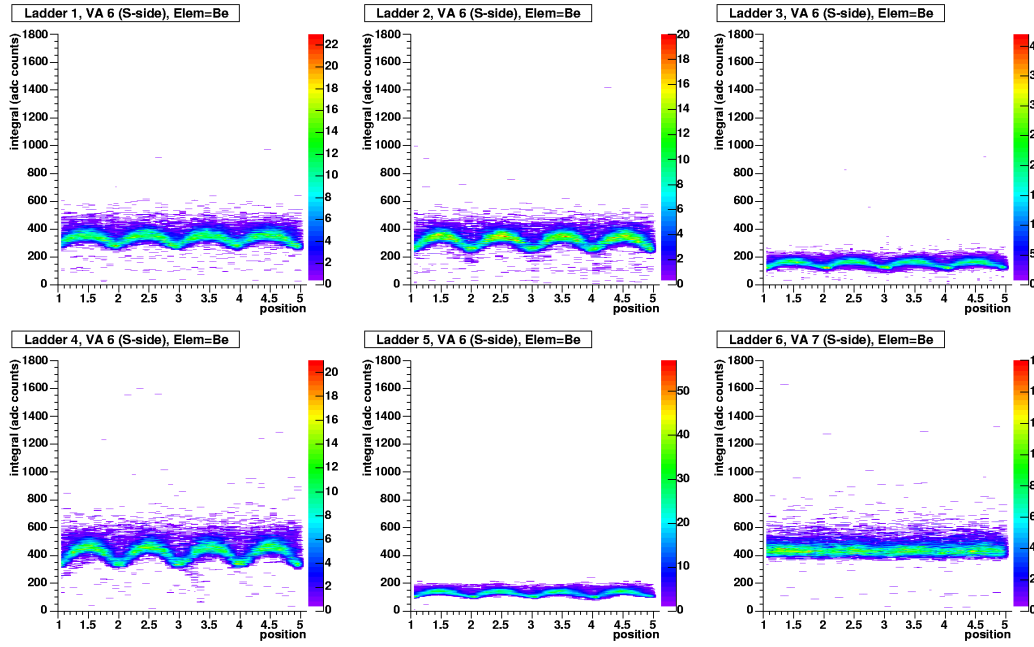


Figure 8.16: Cluster integral as a function of the cluster center of gravity, for beryllium events, on the VA6 (S-side).

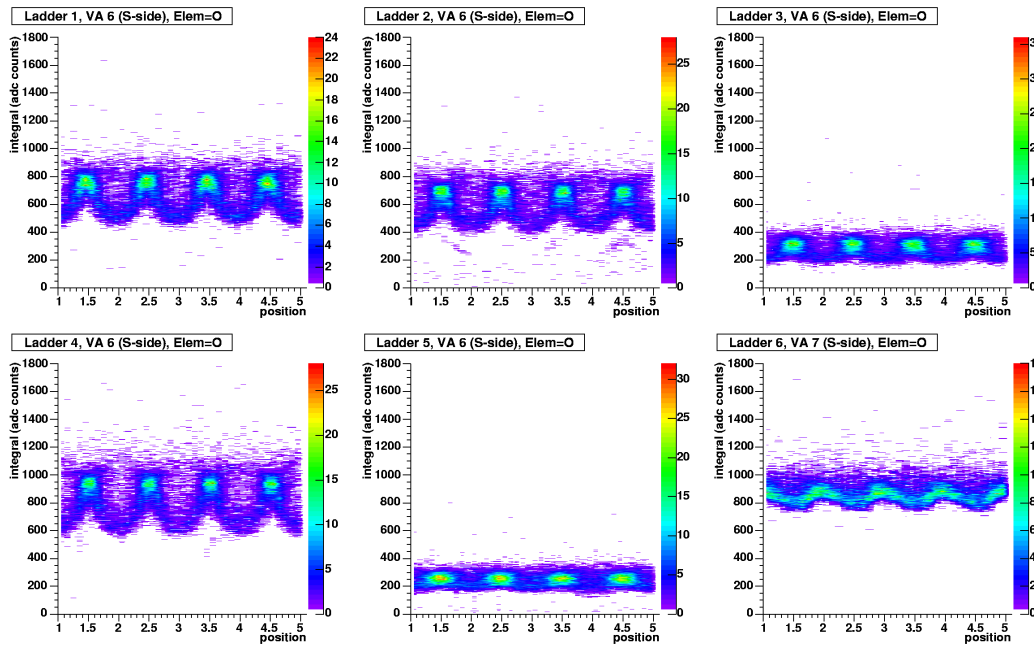


Figure 8.17: Cluster integral as a function of the cluster center of gravity, for oxygen events, on the VA6 (S-side).

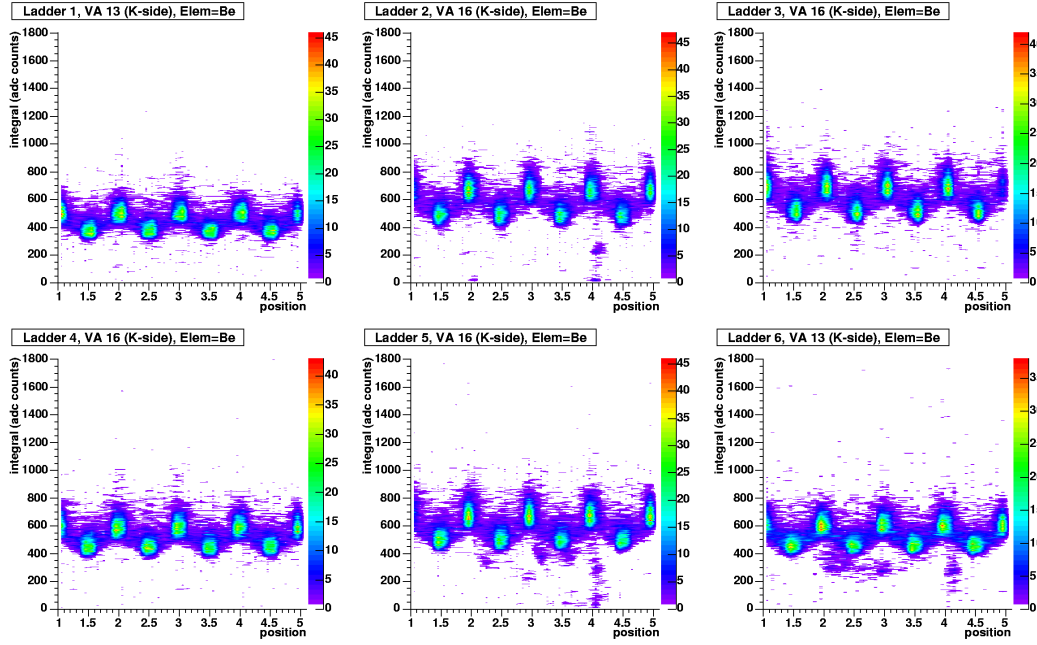


Figure 8.18: Cluster integral as a function of the cluster center of gravity, for beryllium events (K-side).

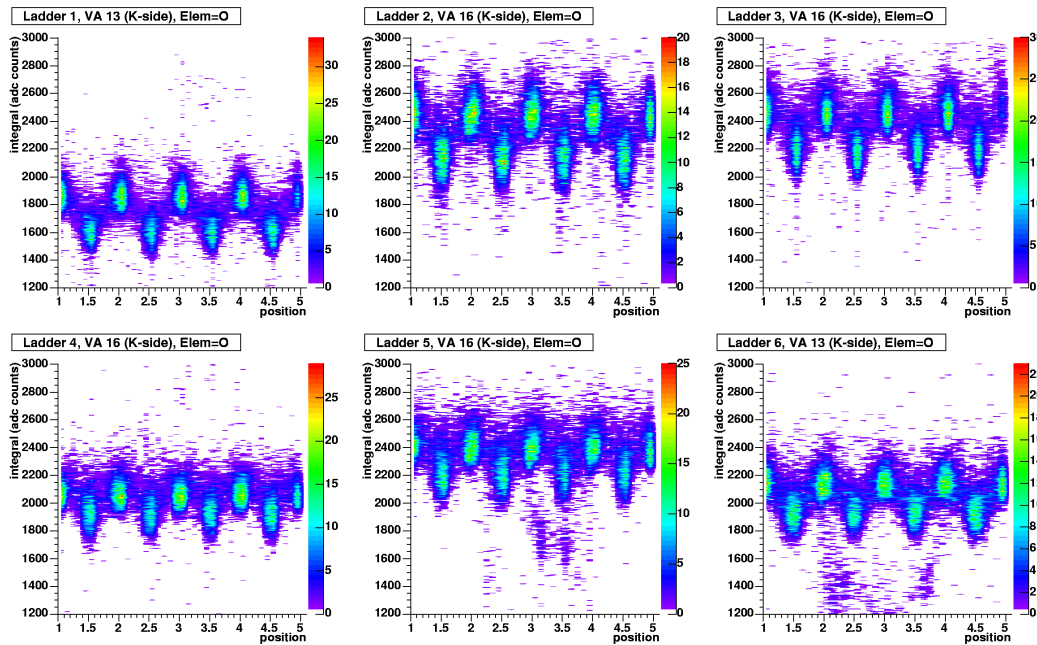


Figure 8.19: Cluster integral as a function of the cluster center of gravity, for oxygen events (K-side).

The results plotted in figures 8.20 and 8.21 represent the Gaussian mean or the Landau most probable value, depending on the cluster center of gravity. It appears that depending on Z and the ladder, the interpolating function must be adapted. Tables 8.4 and 8.5 describe the functions chosen for the S-side fits.

In particular, the position of the maximum cluster integral depends on Z and the ladder gain behaviour: the maximum, initially located at the intermediate positions, moves with higher Z to the readout strips.

Element	Fit function
He	$p_0 + p_1 \cdot \cos^{12}(\pi(x + p_2))$
Li, Be, Ti to Mn	$p_0 - p_1 \cdot \cos^4(\pi(x + p_2))$
B, C, N, O, F, Ne	$p_0 + p_1 \cdot (\sin(2\pi(x + p_2)) - 1)$
Fe to Ga	$p_0 - p_1 \cdot (1 + \cos(2\pi(x + p_2)))$
S to Sc	$p_0 - p_1 \cdot (1 - \cos(2\pi(x + p_2)))$
Na, ladders 3 and 5	$p_0 - p_1 \cdot (1 - \cos(2\pi(x + p_2)))$
Na, ladders 1, 2 and 4	p_0
Mg, ladders 2, 3 and 5	$p_0 - p_1 \cdot (1 - \cos(2\pi(x + p_2)))$
Mg, ladders 1 and 4	p_0
Al to P	$p_0 + p_1 \cdot (\cos^4(\pi(x + p_2)) - 1)$

Table 8.4: Fit functions used for the S-side ladders 1 to 5. The function depends on the chosen element.

Element	Fit function
He	$p_0 + p_1 \cdot (\sin^4(\pi(x + p_2)) - 1)$
Li, Be	p_0
B, C, N, O, F, Ne, Al to Ga	$p_0 + p_1 \cdot (\sin(2\pi(x + p_2)) - 1)$
Na, Mg	$p_0 + p_1 \cdot (\cos(2\pi(x + p_2)) - 1)$

Table 8.5: Fit function used to the S-side of ladder 6.

For the K-side, only one function was chosen:

$$p_0 + p_1 \cdot \cos^4(\pi(x + p_3)) + p_2 \cdot \cos(2\pi(x + p_3)) \quad (8.4)$$

It is particularly interesting to examine the evolution of the maximum integral value, chosen for normalization, with the atomic number.

Maximum mean of cluster integral relation with Z^2

Once the integral dependence on the center of gravity is determined, it is possible to deduce a relation between the interpolation function maximum and Z^2 , as show figures 8.24 and 8.25 for the S-side, and figures 8.26 and 8.27 for the K-side. These plots were in turn fitted with

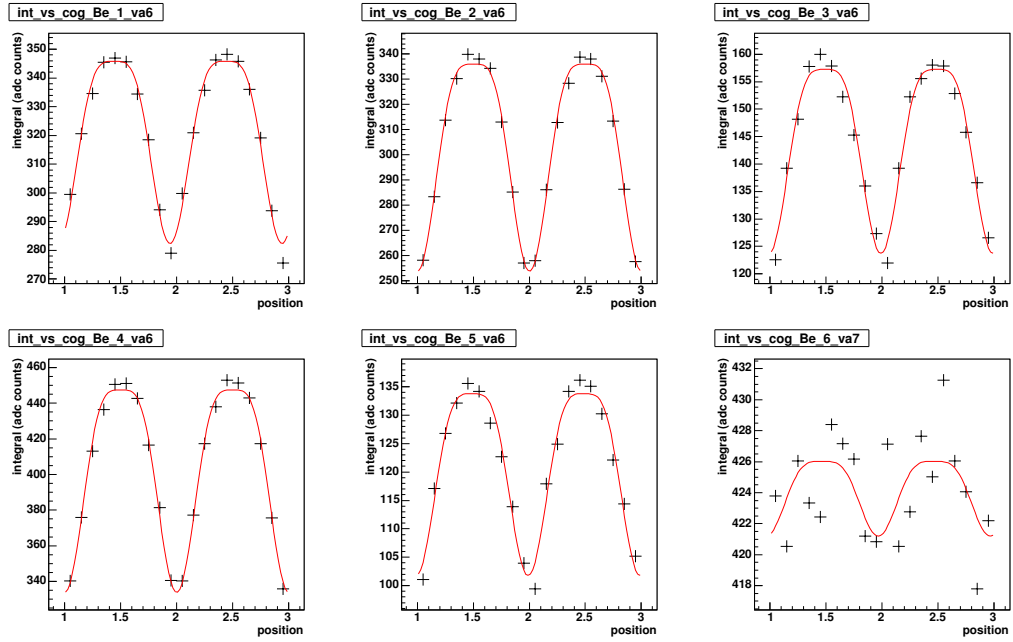


Figure 8.20: Fit on beryllium integral distribution, for one S-side VA. For positions close to the readout strips, a Landau fit is done. At intermediate positions, a Gaussian fit is done. For ladder 6, no dependence with the center of gravity is observed.

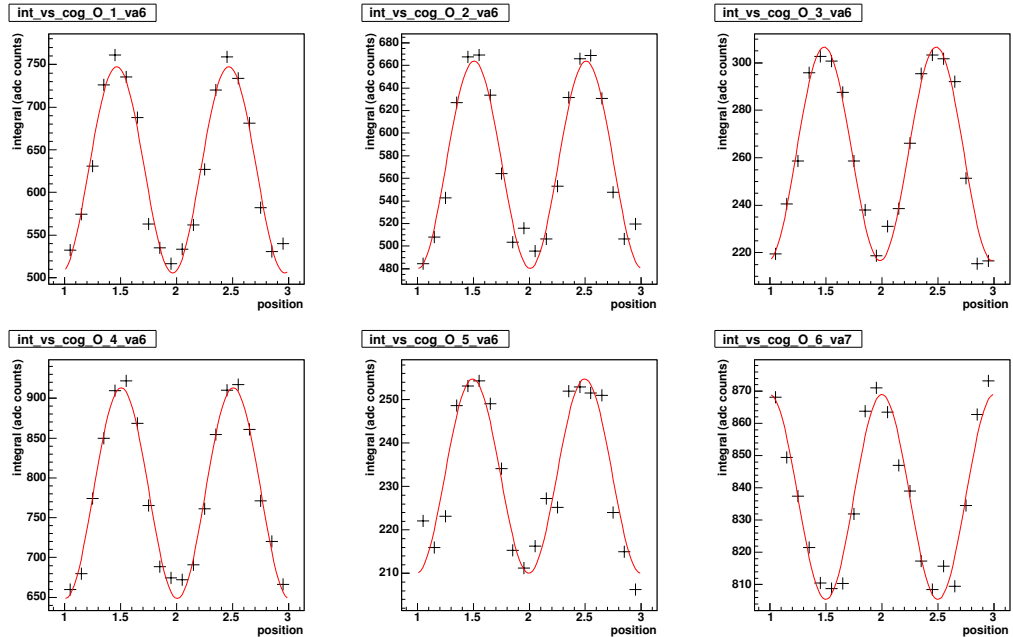


Figure 8.21: Fit on oxygen integral distribution, for one S-side VA. For positions close to the readout strips, a Landau fit is done. At intermediate positions, a Gaussian fit is done.

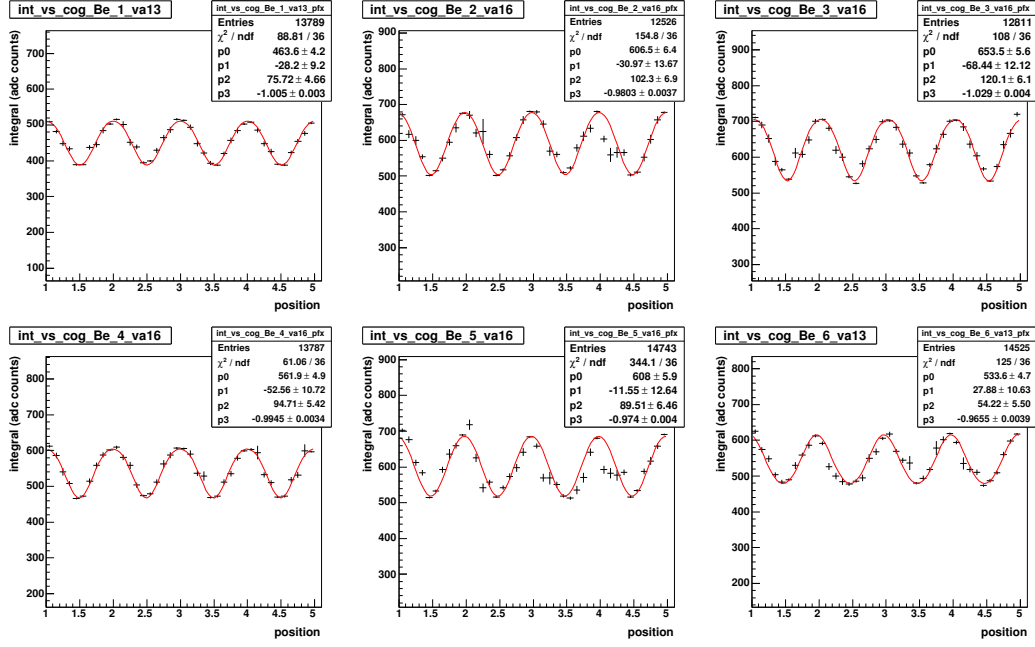


Figure 8.22: Fit on beryllium integral distribution, K-side, calculated with the profile histogram representing the integral vs. the center of gravity modulo 4.

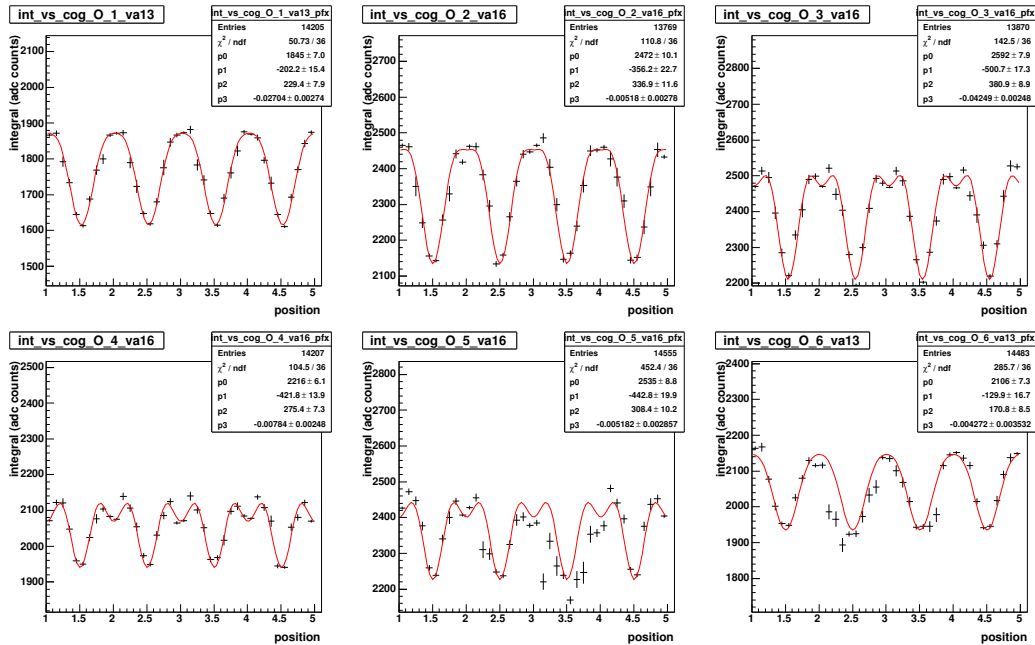


Figure 8.23: Fit on oxygen integral distribution, K-side, calculated with the profile histogram representing the integral vs. the center of gravity modulo 4.

polynomial functions. We note the different gain performances. On the S-side, the impacts of the low gain VAs of ladders 3 and 5 are clear. On the K-side, the hybrids with lower operational amplifier gain are clearly identifiable (ladders 1, 4 and 6). No more than four VAs on each side were calibrated, because of the lack of statistics on the remaining areas. The refined method reduced the examination location, on the S-side, to VA 6 for ladders 1 to 5, and to VA 6 and 7 for ladder 6.

The polynomial functions allowed to proceed to a first correction on the measured charge. At this step, no spatial correction is applied. The results, presented in figures 8.28 (S-side) and 8.29 (K-side) show a clear improvement, introducing a certain linearization. Figure 8.30 presents the two-dimensional plot of the charges. The next step will consist in introducing a center of gravity-dependent correction.

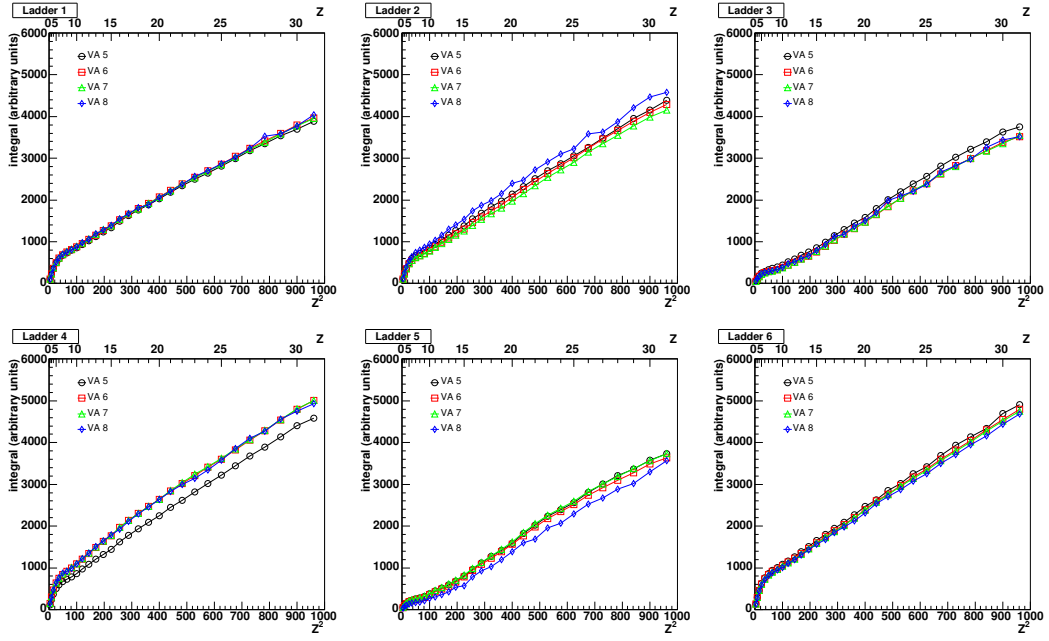


Figure 8.24: Mean cluster maximum integral as a function of Z^2 for S-side VAs.

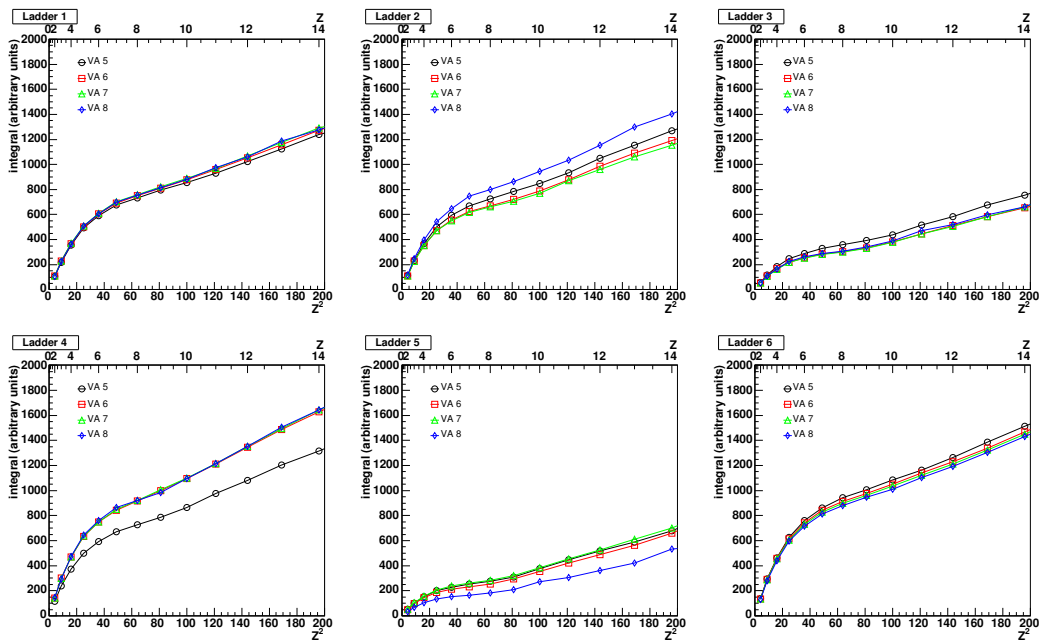
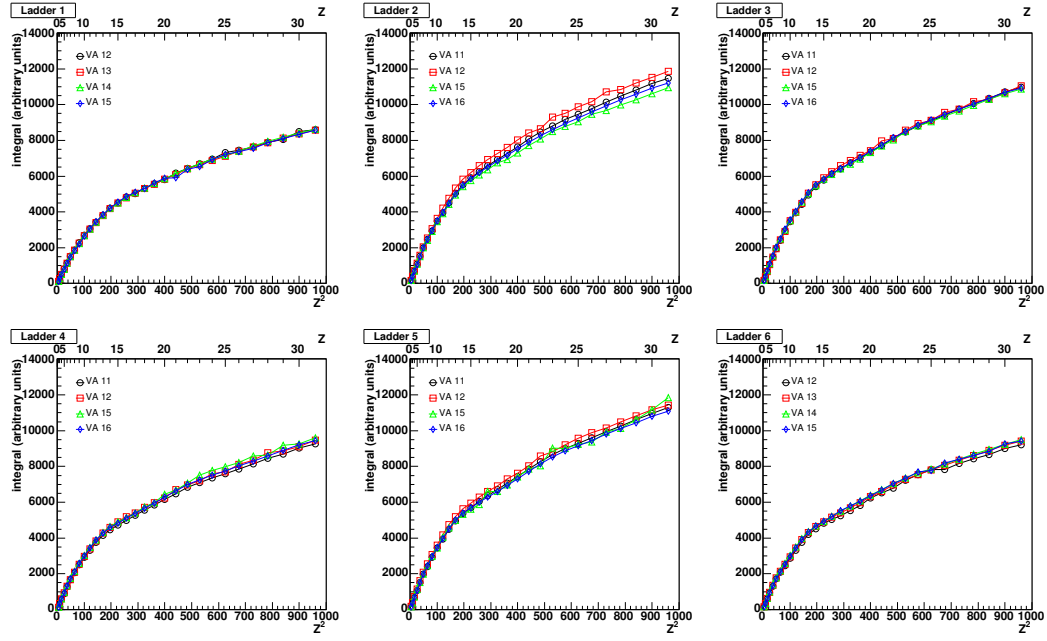
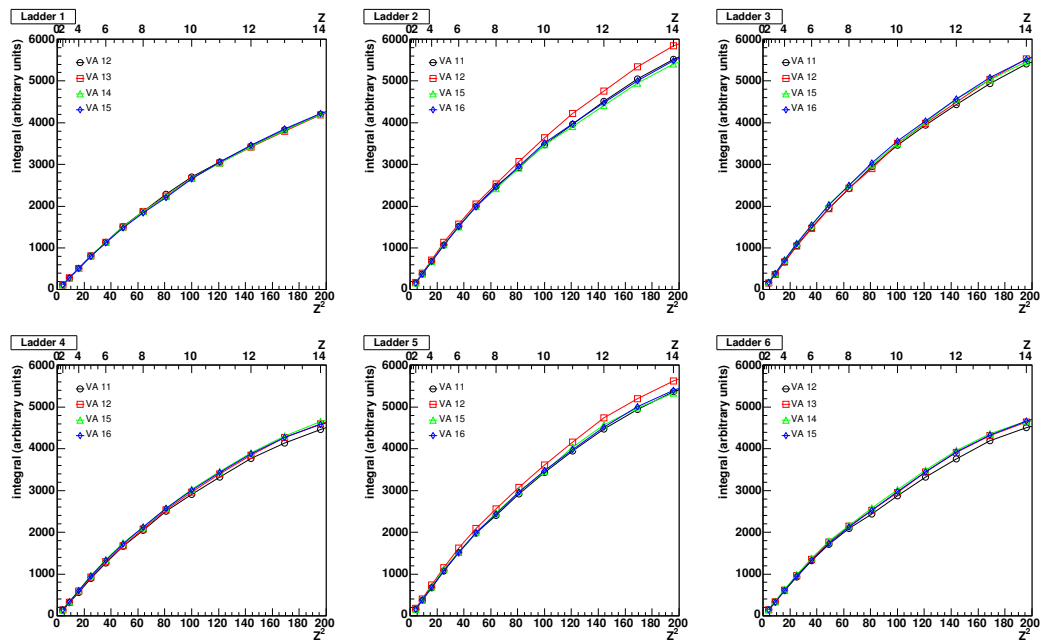


Figure 8.25: Mean cluster maximum integral as a function of Z^2 for S-side VAs (detail).

Figure 8.26: Mean cluster maximum integral as a function of Z^2 for K-side VAs.Figure 8.27: Mean cluster maximum integral as a function of Z^2 for K-side VAs (detail).

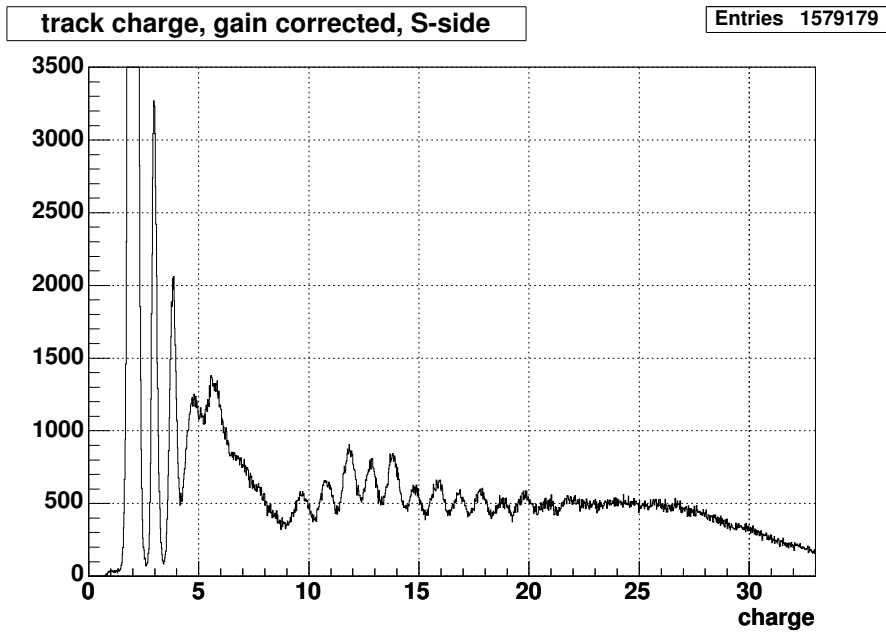


Figure 8.28: Gain correction, S-side. The cluster integrals are converted into corresponding Z^2 with a calibration function fitted on the plots presented in figure 8.24. No correction based on the cluster center of gravity is applied yet. All events, for 4 VAs on the S-side and 4 VAs on the K-side are taken into account.

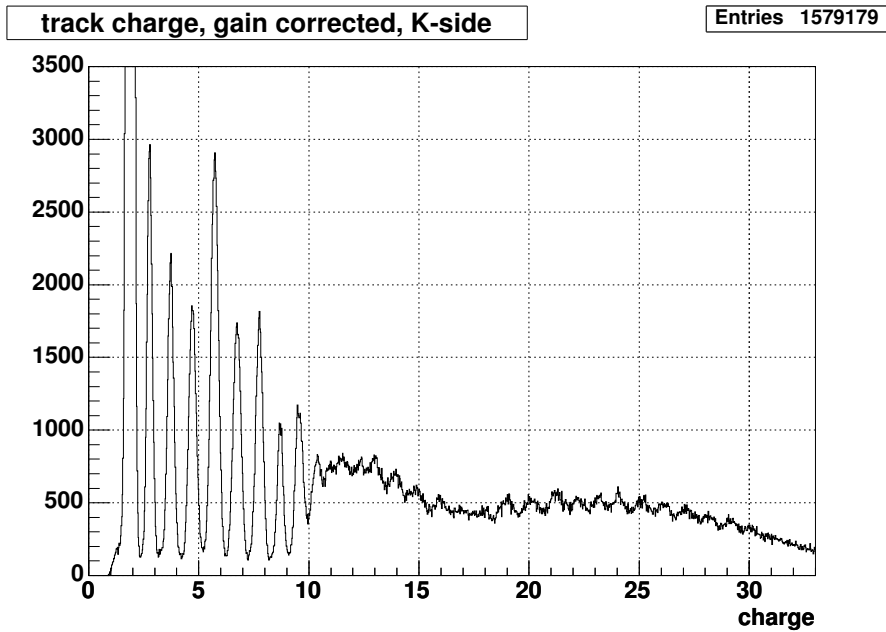


Figure 8.29: Gain correction, K-side. The cluster integrals are converted into corresponding Z^2 with a calibration function fitted on the plots presented in figure 8.26. No correction based on the cluster center of gravity is applied yet. All events, for 4 VAs on the S-side and 4 VAs on the K-side are taken into account.

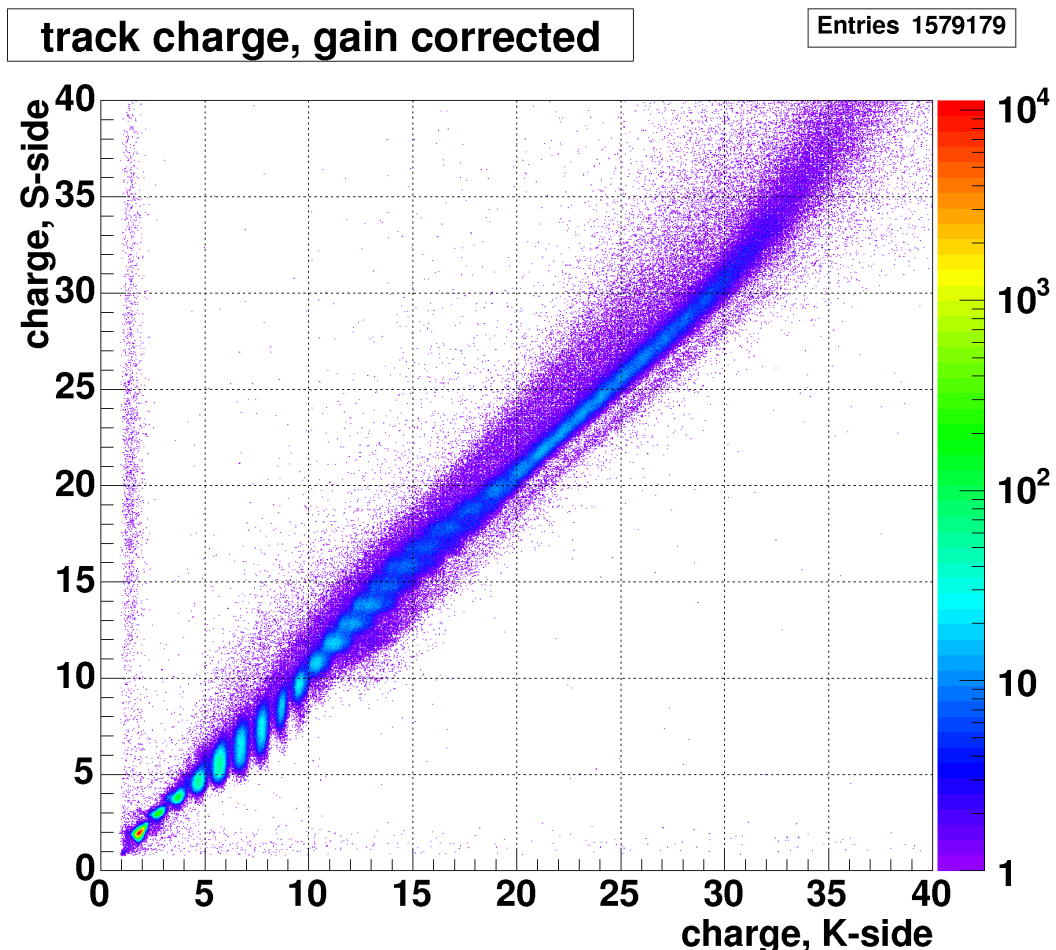


Figure 8.30: Gain correction, S-side vs K-side. The cluster integrals are converted into corresponding Z^2 with a calibration function fitted on the plots presented in figures 8.24 and 8.26. No correction based on the cluster center of gravity is applied yet. All events, for 4 VAs on the S-side and 4 VAs on the K-side are taken into account.

Distributions of corrected charges

Starting from the raw charge of the one track events, and applying the corrections according to a particular Z , the corrected charge distributions were examined. Actually three different charges were calculated:

$$c_0 = \frac{1}{6} \sum_{l=1}^6 \sqrt{I_l} \quad (8.5)$$

$$c_1 = \frac{1}{5} \left[\left(\sum_{l=1}^6 \sqrt{I_l} \right) - \max(\sqrt{I_l}) \right] \quad (8.6)$$

$$c_2 = \frac{1}{4} \left[\left(\sum_{l=1}^6 \sqrt{I_l} \right) - \max(\sqrt{I_l}) - \min(\sqrt{I_l}) \right] \quad (8.7)$$

(8.8)

l is the ladder index, c_1 and c_2 are two variants of the truncated mean of the charge, the principle being to suppress the tails of the distributions, to obtain a Gaussian-like distribution. Figures 8.31 and 8.32 show the three charge distributions for beryllium and oxygen, for each side. Every distribution is fitted with a Gaussian function, with parameters (see table 8.6) subsequently used for the element selection. The truncated charge c_1 presents the best compromise between fit quality and charge separation.

Element	S-side		K-side		Element	S-side		K-side	
	μ	σ	μ	σ		μ	σ	μ	σ
He	2.097	0.083	1.909	0.079	Mg	11.796	0.279	11.911	0.158
Li	2.989	0.098	2.863	0.095	Al	12.766	0.252	12.926	0.197
Be	3.965	0.111	3.871	0.110	Si	13.735	0.262	13.939	0.234
B	4.977	0.197	4.905	0.120	P	14.682	0.312	14.867	0.294
C	5.980	0.376	5.940	0.123	S	15.836	0.288	15.834	0.324
N	7.037	0.588	6.945	0.127	Cl	16.817	0.274	16.847	0.332
O	7.901	0.644	7.898	0.123	Ar	17.774	0.291	17.906	0.306
F	8.762	0.486	8.897	0.123	K	18.678	0.259	18.877	0.268
Ne	9.806	0.350	9.924	0.132	Ca	19.704	0.354	19.818	0.254
Na	10.806	0.305	10.890	0.140	Sc	20.765	0.391	20.811	0.271
					Ti	21.781	0.360	21.907	0.276

Table 8.6: Truncated charge c_1 fit parameters for elements from helium to titanium for both ladder sides.

Application of the corrections on the complete data set

All tools are now available to analyse all the data, with no pre-selected domain. The method used consists in testing an event with three subsequent possible values of Z and comparing them between the S- and K-sides. The best Z value is chosen using a test related to a likelihood ratio.

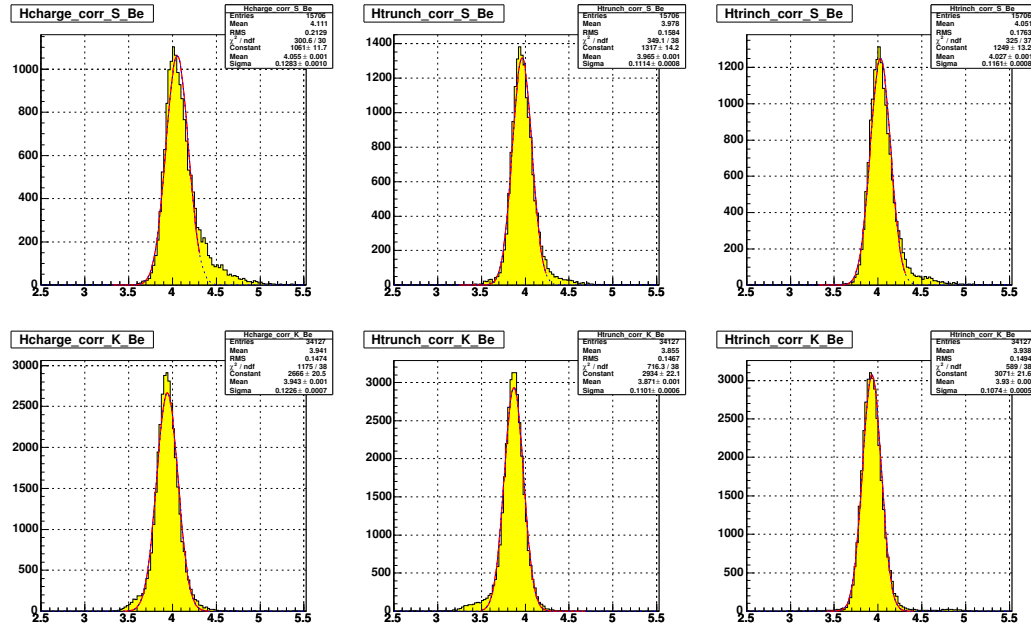


Figure 8.31: Charge, truncated charge 1 and truncated charge 2 distributions and Gaussian fits for beryllium.

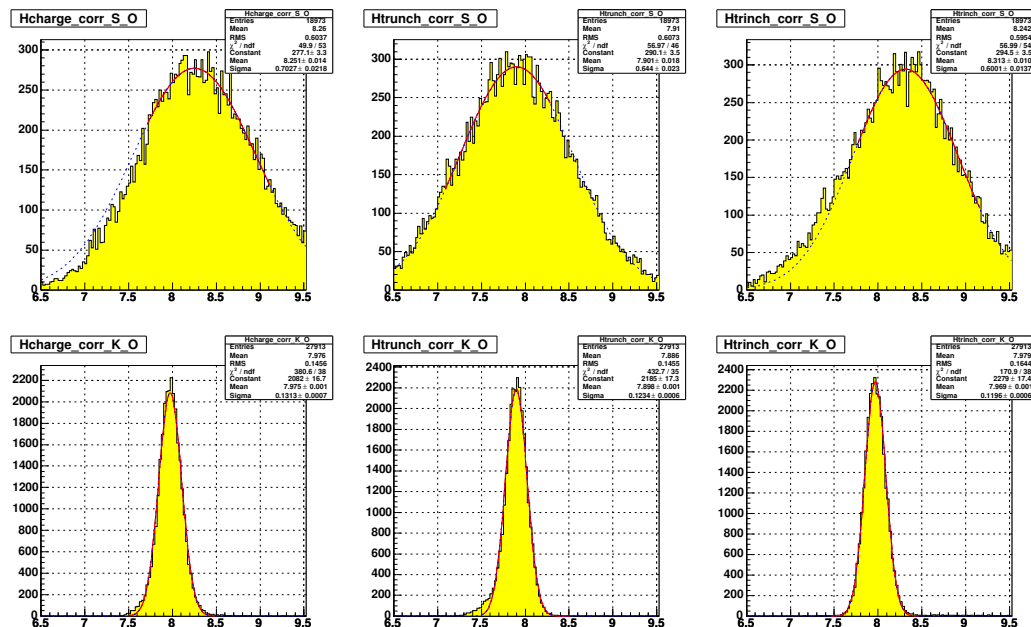


Figure 8.32: Charge, truncated charge 1 and truncated charge 2 distributions and Gaussian fits for oxygen.

The events are tagged with a given charge Z depending on the K-side raw charge if $Z < 11$ or $Z > 20$, else depending on the S-side raw charge. The raw charges are then corrected for $Z - 1$, Z and $Z + 1$, for both sides:

1. The cluster integral is corrected as a function of the cluster center of gravity.
2. The cluster corrected integral is converted into charge Z^2 using the gain calibration function.

The logarithm of the likelihood ratio for the three alternative charges is then computed, for both sides:

$$R_1^s = \ln \left(\frac{\mathcal{L}^s(Z)}{\mathcal{L}^s(Z-1)} \right) = \ln \left(\frac{\sigma_{Z-1}^s}{\sigma_Z^s} \right) - \frac{1}{2} \left[\left(\frac{c_Z^s - \mu_Z^s}{\sigma_Z^s} \right)^2 - \left(\frac{c_{Z-1}^s - \mu_{Z-1}^s}{\sigma_{Z-1}^s} \right)^2 \right] \quad (8.9)$$

$$R_2^s = \ln \left(\frac{\mathcal{L}^s(Z)}{\mathcal{L}^s(Z+1)} \right) = \ln \left(\frac{\sigma_{Z+1}^s}{\sigma_Z^s} \right) - \frac{1}{2} \left[\left(\frac{c_Z^s - \mu_Z^s}{\sigma_Z^s} \right)^2 - \left(\frac{c_{Z+1}^s - \mu_{Z+1}^s}{\sigma_{Z+1}^s} \right)^2 \right] \quad (8.10)$$

μ_Z^s , σ_Z^s correspond to the Gaussian fit parameters for charge Z on ladder side s , and c_Z^s corresponds to the track charge (or truncated charges), computed with corrections for element Z on ladder side s . The simplest cases examined by the program are:

$$\begin{aligned} R_i^s > 0 \quad \forall s, i &\Rightarrow Z \text{ accepted} \\ R_1^s > 0 \quad \forall s \text{ and } (R_2^S \leq 0 \text{ or } R_2^K \leq 0) &\Rightarrow Z-1 \text{ tested} \\ R_2^s > 0 \quad \forall s \text{ and } (R_1^S \leq 0 \text{ or } R_1^K \leq 0) &\Rightarrow Z+1 \text{ tested} \end{aligned}$$

The remaining cases are considered as special, and stored in a different histogram.

Figures 8.33 and 8.34 describe the charge distributions, after center of gravity and gain correction, for the S- and K-side respectively. We note that the improvement is poor on the S-side, in particular for the boron to fluorine range. This is explained by the fact that the VA gain performance do not allow to correctly separate the charges in that range, and that the center of gravity influences are hidden by the VA behaviour. On the other hand, an obvious improvement is observed on the K-side, in particular the charge separation between sodium and titanium. Clearly, the origin of the integral resolution loss on the K-side is mainly due to the center of gravity effect.

Figure 8.37 compares the correlation factors between S- and K-sides for the raw charge and for the corrected charge. A clear improvement is noted between sodium and calcium, again due to the K-side positive evolution. The RMS of the corrected charges on the S- and K-sides are compared in figure 8.38. Again, the effect the S-side VA gain non-linearity is observed.

8.5 Comments

Due to the VA non-linear response, the traversing particle charge can be measured up to $Z \leq 22$, using the information of six ladders. However, the AMS-02 tracker will be composed

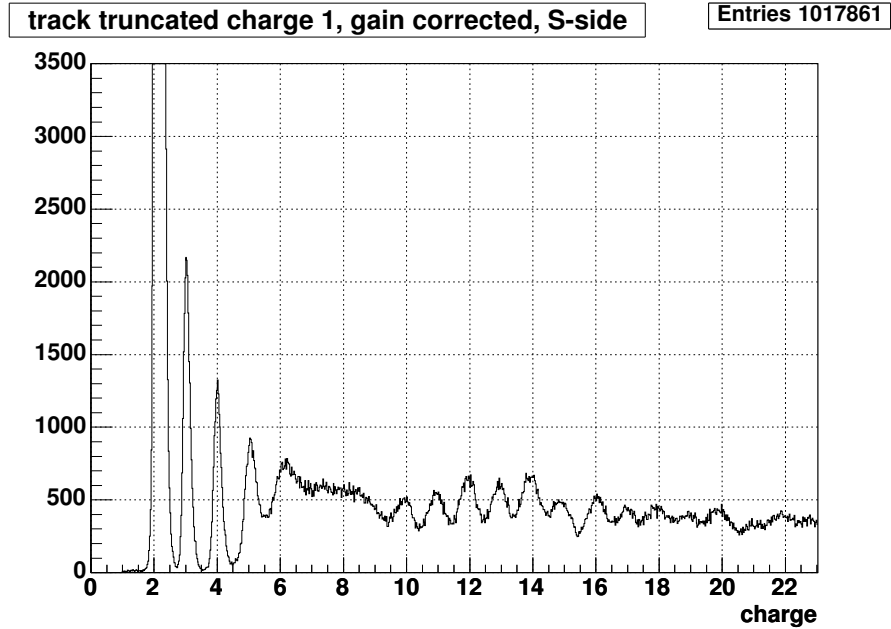


Figure 8.33: Final charge distribution, S-side. The cluster integrals have been corrected as a function of the center of gravity, then converted into standard charge, using a gain calibration function, based on a plot similar to fig. 8.24. In this case, a refined method (needing more statistics) was used, and only VA 6 (or VA 6 and VA 7 for ladder 6) could be calibrated.

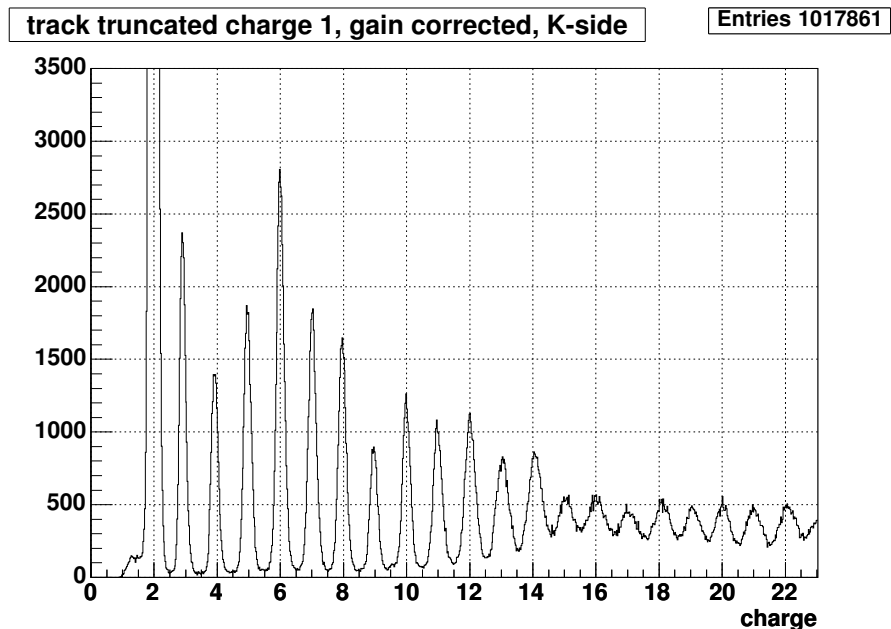


Figure 8.34: Final charge distribution, K-side. The cluster integrals have been corrected as a function of the center of gravity, then converted into standard charge, using a gain calibration function, based on data plotted in fig. 8.26.

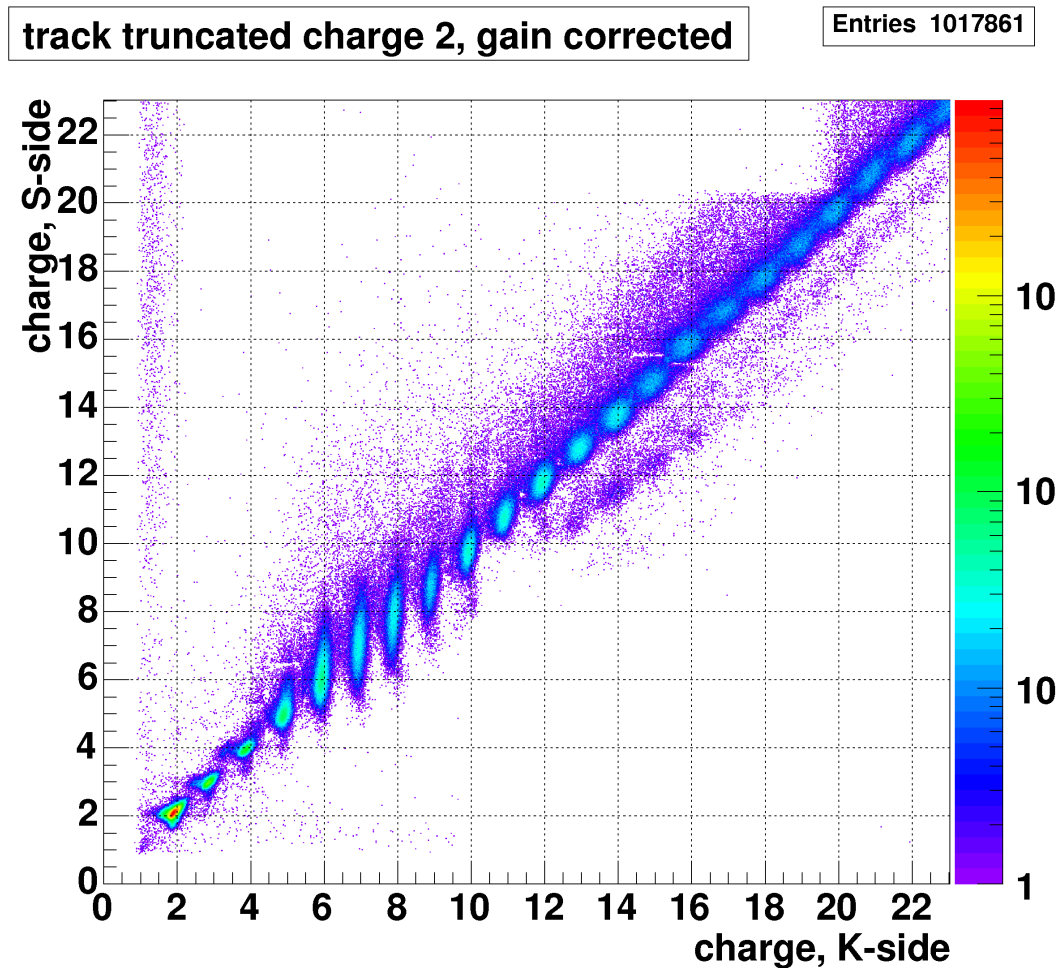


Figure 8.35: Final S charge vs. K charge plot. The cluster integrals have been corrected as a function of the center of gravity, then converted into standard charge.

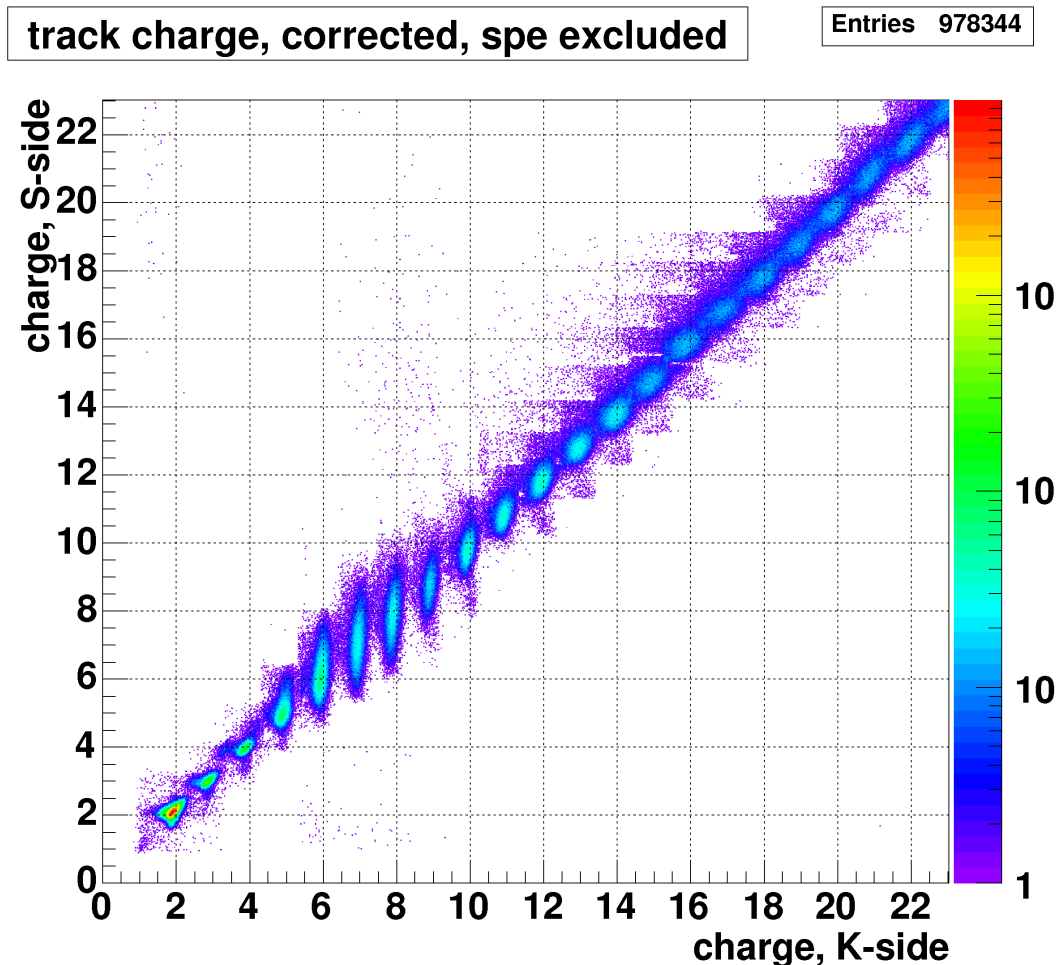


Figure 8.36: Final S charge vs. K charge plot. The cluster integrals have been corrected as a function of the center of gravity, then converted into standard charge. Events with worst agreement between S and K sides are here excluded.

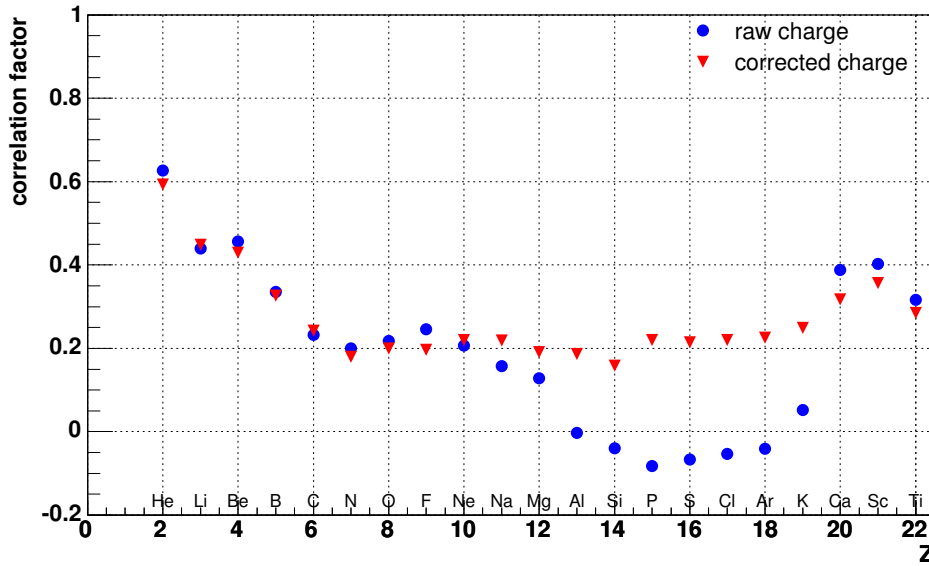


Figure 8.37: Correlation factors between the S- and K-side raw and corrected charges. A clear improvement is observed between sodium and calcium, due to the K-side evolution.

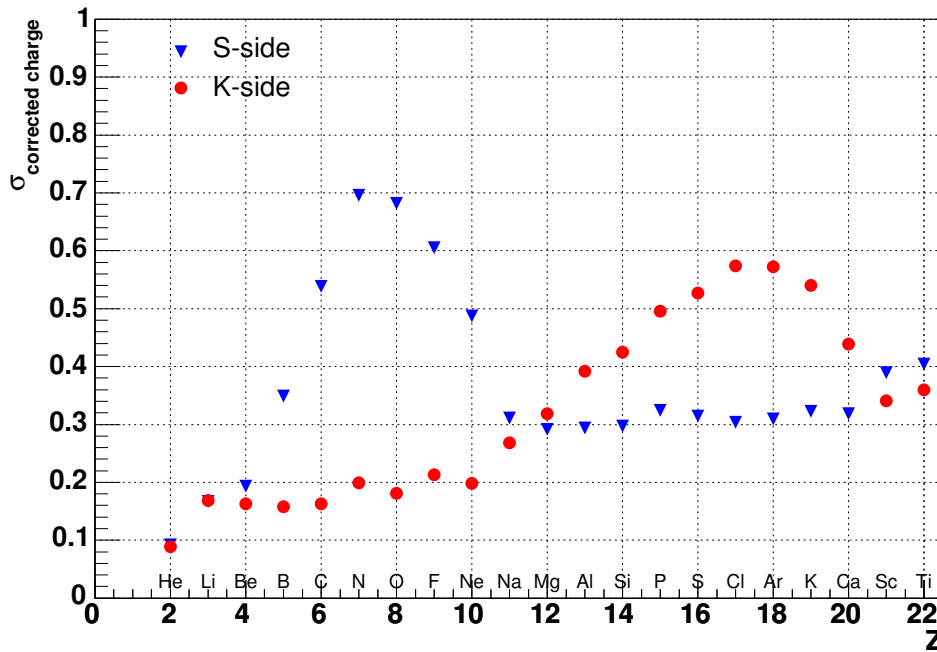


Figure 8.38: Rms of corrected charges, for the S- and K-sides. The effect of the S-side VA gain non-linearity is noted.

of eight layers of silicon detectors. As shown in figure 8.30, it could be possible to explore charges with $Z > 22$, but only the K-side seems to be efficient (compare figs. 8.28 and 8.29). To do a correct study for such charges, more statistics is necessary. Note also that the ladders tested in October 2002 presented various amplification performances which have been equalized since. Similar peculiarities were looked for and eliminated during the subsequent ladder production.

Further beam tests have been done using ladders presenting homogeneous gain properties. Also, the trigger to hold time has been adapted on the S-side, taking into account the measurements with $A/Z = 2$ beam and laser diode. The new trigger to hold times ($3 \mu\text{s}$ on the S-side, $4 \mu\text{s}$ on the K-side) improve the ladder performances for charges with $Z \geq 2$ while presenting unchanged characteristics for $Z = 1$ particles.

Unlike the real conditions AMS will be operated in, the particles during the beam test impinged all ladders but one at an angle of 90° . The cluster integral dependence with the center of gravity is large at a normal incidence, but is less important for the rotated ladder. This leads to the conclusion that the signal collected by the readout strips originates from two different phenomena, depending on the incidence angle: capacitive charge division with a 90° incidence, charge sharing for an inclined incidence.

If a particle crosses a detector between two readout strips, one expects to measure a lower cluster integral than if the particle crosses the detector close a readout strip: some charge is lost via the backplane capacitance. Nevertheless, we observed on the S-side, for $Z < 10$ the opposite phenomenon. A possible origin could be particular gain performances of the VAs on the S-side hybrids, and the fact that the trigger to hold time was different from the VA shaping time. A too large charge released on one single strip causes the preamplifier to saturate, while if a charge is spread between two channels, the total cluster saturation occurs at larger charge. This latter point should be checked with the beam tests conducted in October 2003 at CERN and November 2003 at GSI, Darmstadt.

The method described above presents one disadvantage, the necessity to a priori know the crossing particle charge, Z , as this value defines the specific correction to apply. This procedure introduce systematics which are still visible in the final result, presenting a bin structure (figs. 8.35 and 8.36).

To improve the cluster study, more parameters should be examined. The cluster length procures no indication on the number of strips dominating the cluster charge. It seems clear that for type 2 clusters, most of the charge is concentrated in 2-3 channels. This aspect could be examined further, if the new trigger to hold time setting on the S-side does not reduce the proportion of type 2 events.

Also, a Gaussian fit on the cluster pulse heights could be a supplemental parameter of interest, to compensate the negative ADC channels composing a type 2 cluster.

Finally, instead of using the cluster center of gravity information, one could do the study with a the real track coordinate, with the help of a telescope.

In the end, the center of gravity corrections are more important on the K-side than on the S-side: without such a correction, the data would be hardly useful on K. In addition, the large rms of the charge distribution on the S-side for elements from beryllium to neon is due

to the gain properties of the VAs.

No comparison with the RICH data was possible: the data used for the presented analysis correspond to a period during which the RICH was not operated in optimum conditions.

As noted in section 8.3, five ladders have low gain performance. Due to the lower gain, these ladders also presented lower noise values, this is why they were selected. This choice complicated the ladder comparison for this analysis, however it allowed to unveil unexpected anomalies. An adequate procedure was established to systematically examine the produced ladders.

Chapter 9

Conclusions

Silicon microstrip detectors are expensive and fragile. The procurement needs extensive testing, with a professional instrument test system. The assembly of silicon modules needs special equipment, tools and laboratories (clean rooms). A share between multiple assembly lines, some them of the industry, is more and more required.

However, due to their excellent spatial resolution, the silicon microstrip detectors are extensively used in particle physics experiments to reconstruct the particle tracks close to the interaction points.

The tests made at the University of Geneva on silicon sensors and modules confirmed the need of particularly stringent laboratory conditions, in particular in the quality control and the environment cleanliness. These tests allowed to better understand the calibration information relative to the silicon detector and readout electronics properties. Compared to AMS-01, the design of the AMS-02 sensors clearly improved the module properties, in terms of noise and leakage current.

A beam test made at CERN in October 2002 with a fragmentation beam showed that it is possible, with six ladders, to identify elements up to $Z = 22$, i.e. titanium.

Further analyses, in particular with the 2003 beam test data (six standard production ladders were tested, with an optimized trigger to hold time) confirm this conclusion. Moreover, a comparison with a RICH detector was possible, and a good agreement was observed.

The AMS-02 silicon tracker is composed of 8 silicon detector layers, totaling a surface of 6.39 m^2 . The silicon module quality will enable the tracker to provide tracks with normally 8 measurements of both the bending and non-bending coordinates. Compared to the beam test data, which used six ladders, the tracker performance will thus be further improved.

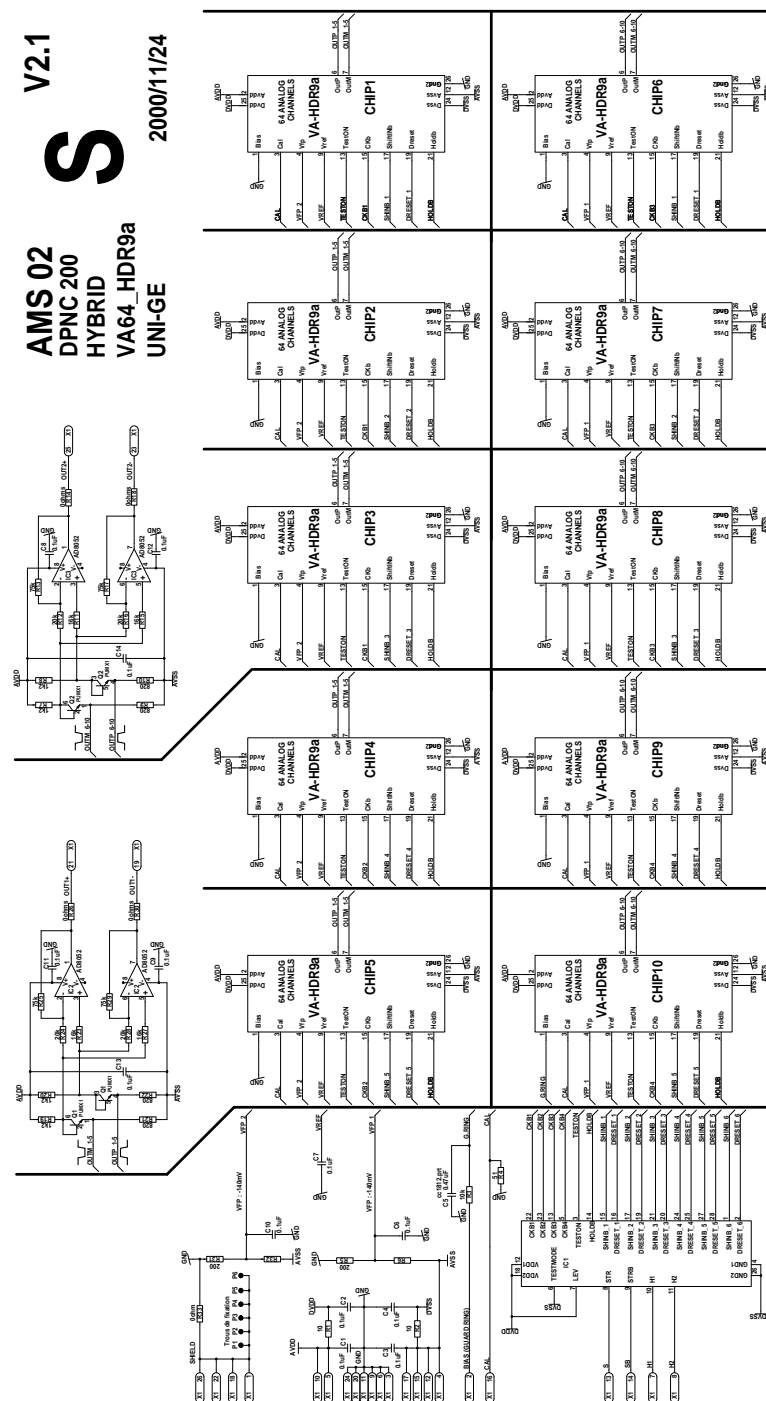
In winter 2004, the silicon modules and the plane integration will be completed. The tracker will then be assembled. The next step will be to integrate the tracker into the magnet, at CERN.

The various physics goals (study of antimatter, dark matter, high energy photons, cosmic ray composition), the technology and constraints applied on AMS make it an exceptional detector. The installation date is for now unknown, but the first data will be awaited with impatience, to explore this wide physics programme.

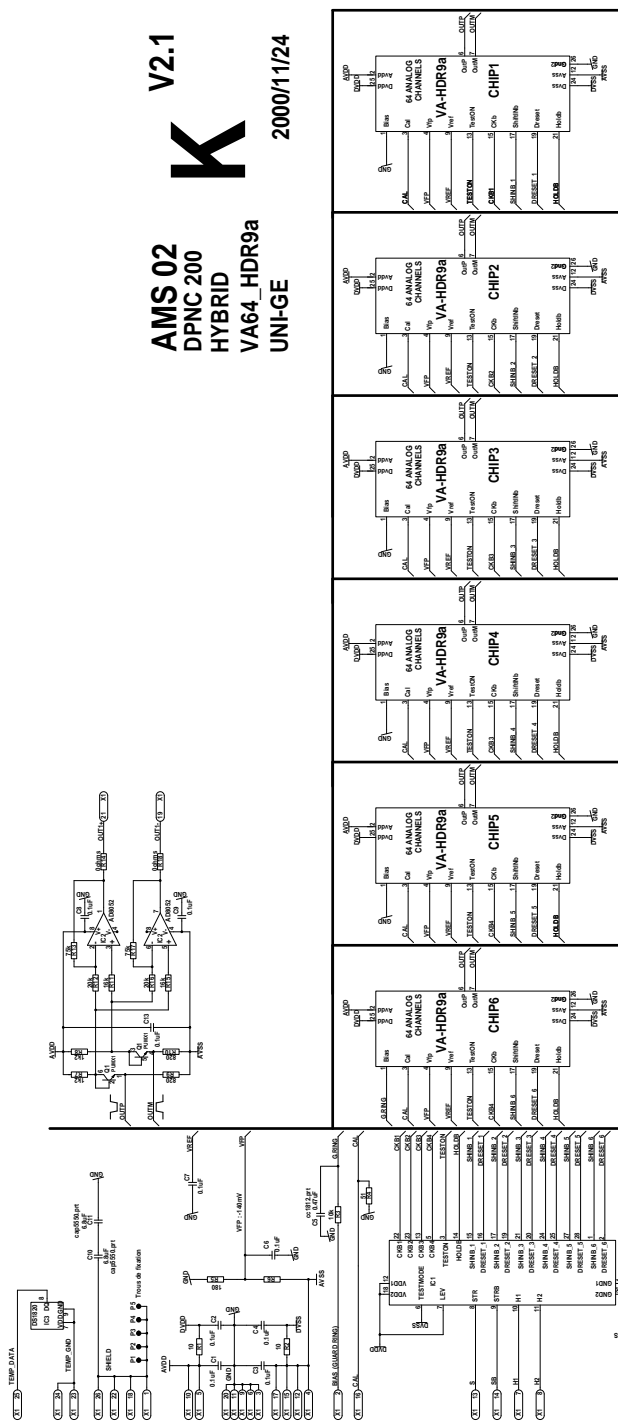
Appendix A

AMS-02 TFE hybrid schematics and designs

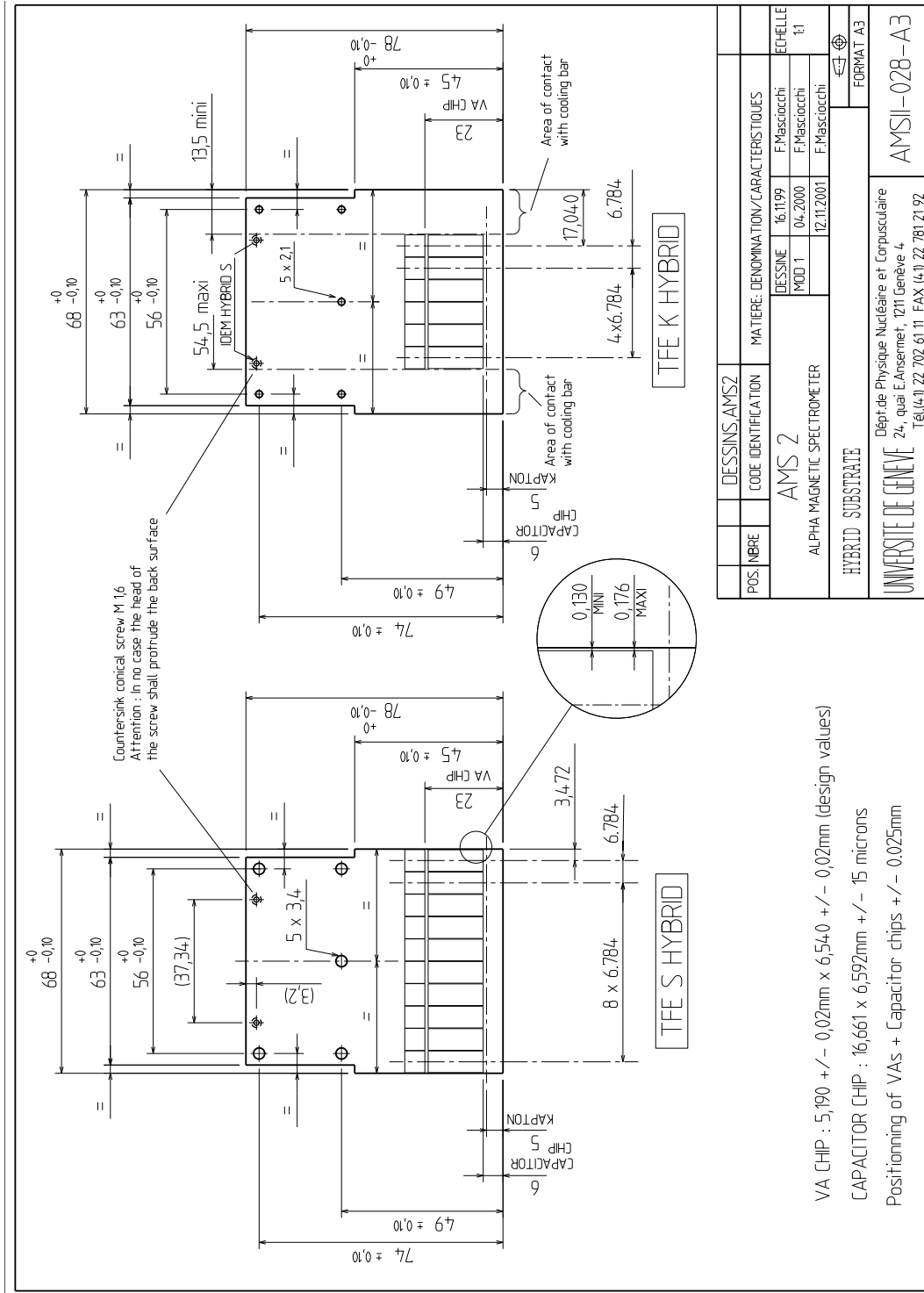
A.1 S-hybrid schematics



A.2 K-hybrid schematics



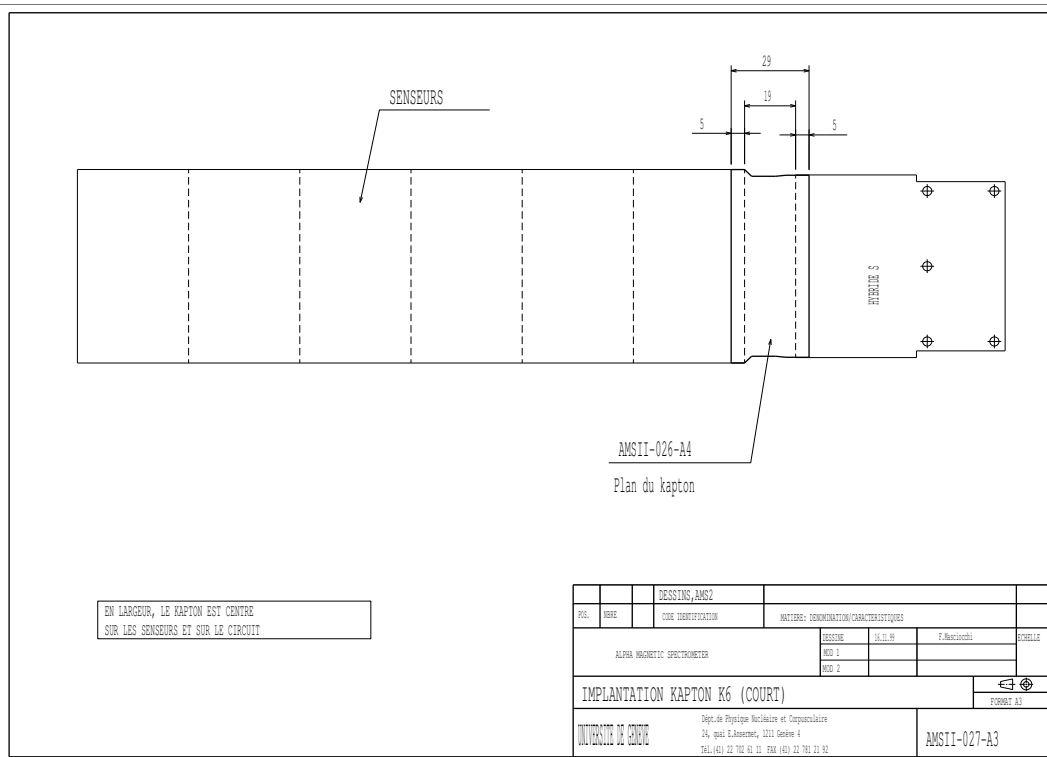
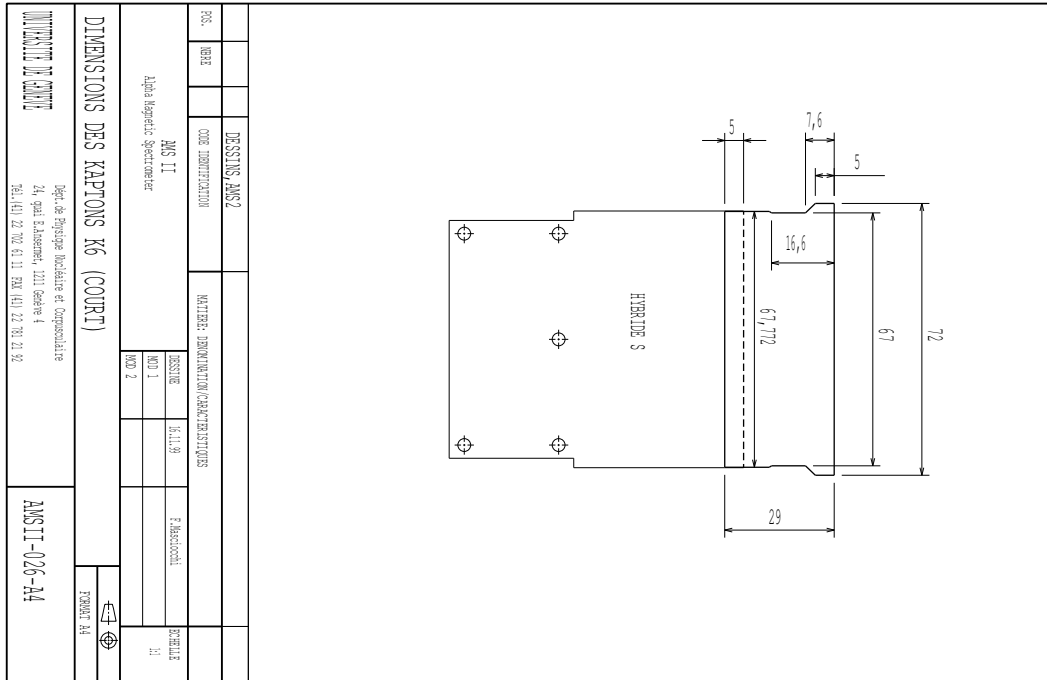
A.3 Mechanical designs



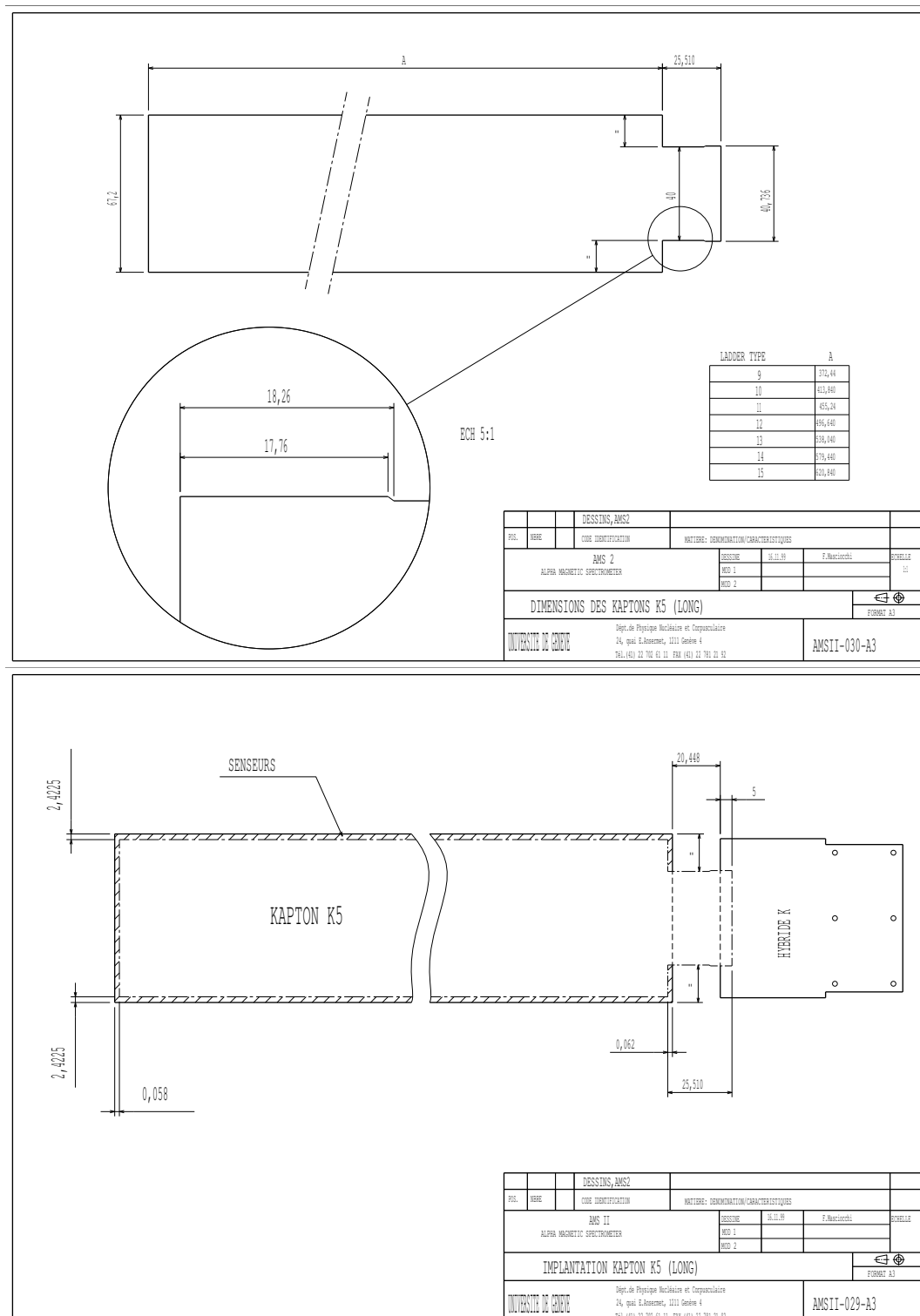
Appendix B

K6 and K5/7 Upilex dimensions and positions

B.1 K6 Upilex



B.2 K5/7 Upilex

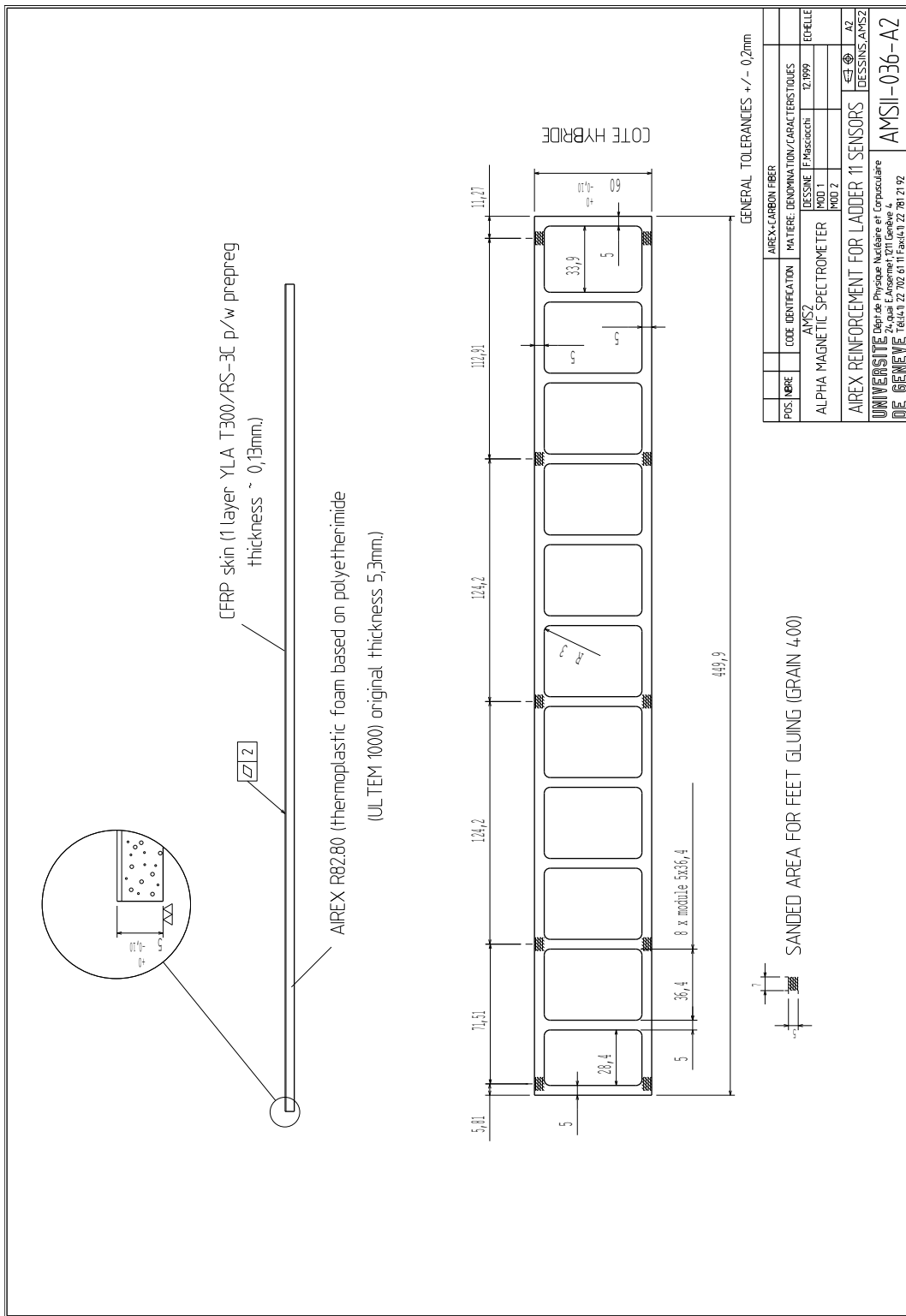


Appendix C

Reinforcement designs

On next page, the reinforcement of an 11-ladder is shown. The table below shows the parameters for all lengths. Distances between sanded area for feet gluing (from left to right, see figure next page):

ladder length	distance between area (mm)					
	1→2	2→3	3→4	4→5	5→6	6→7
7	71.51	124.2	71.51			
9	112.91	124.2	112.91			
10	71.51	124.2	124.2	71.51		
11	71.51	124.2	124.2	112.91		
12	112.91	124.2	124.2	112.91		
13	71.51	124.2	124.2	124.2	71.51	
14 O	71.51	124.2	124.2	124.2	112.91	
14 I	71.51	124.2	94.55	71.51	124.2	71.51
15	112.91	124.2	124.2	124.2	112.91	

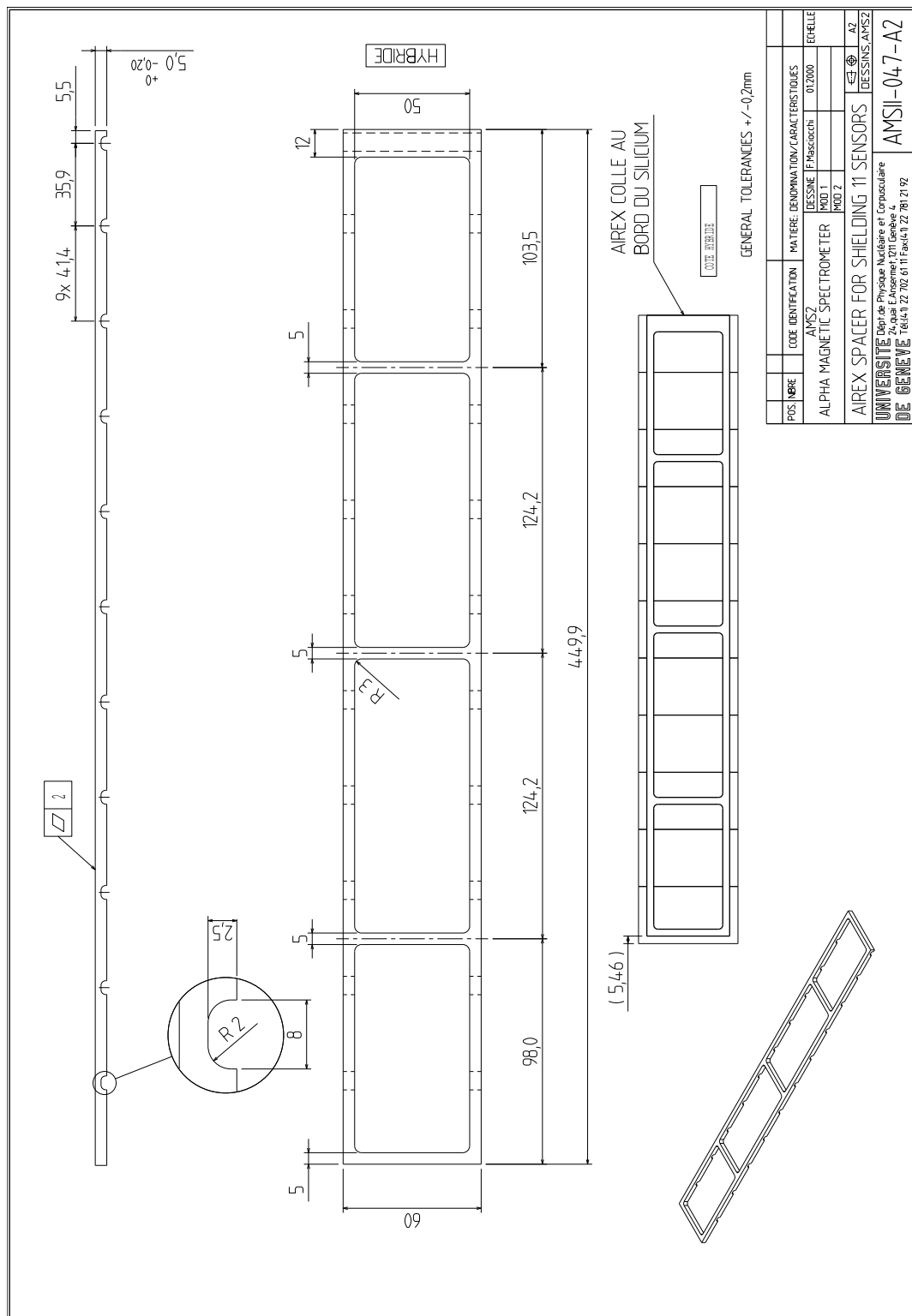


Appendix D

Spacer designs

On next page, the spacer of an 11-ladder is shown. The table below shows the parameters for all lengths. Intermediate dimensions (from left to right, see figure next page):

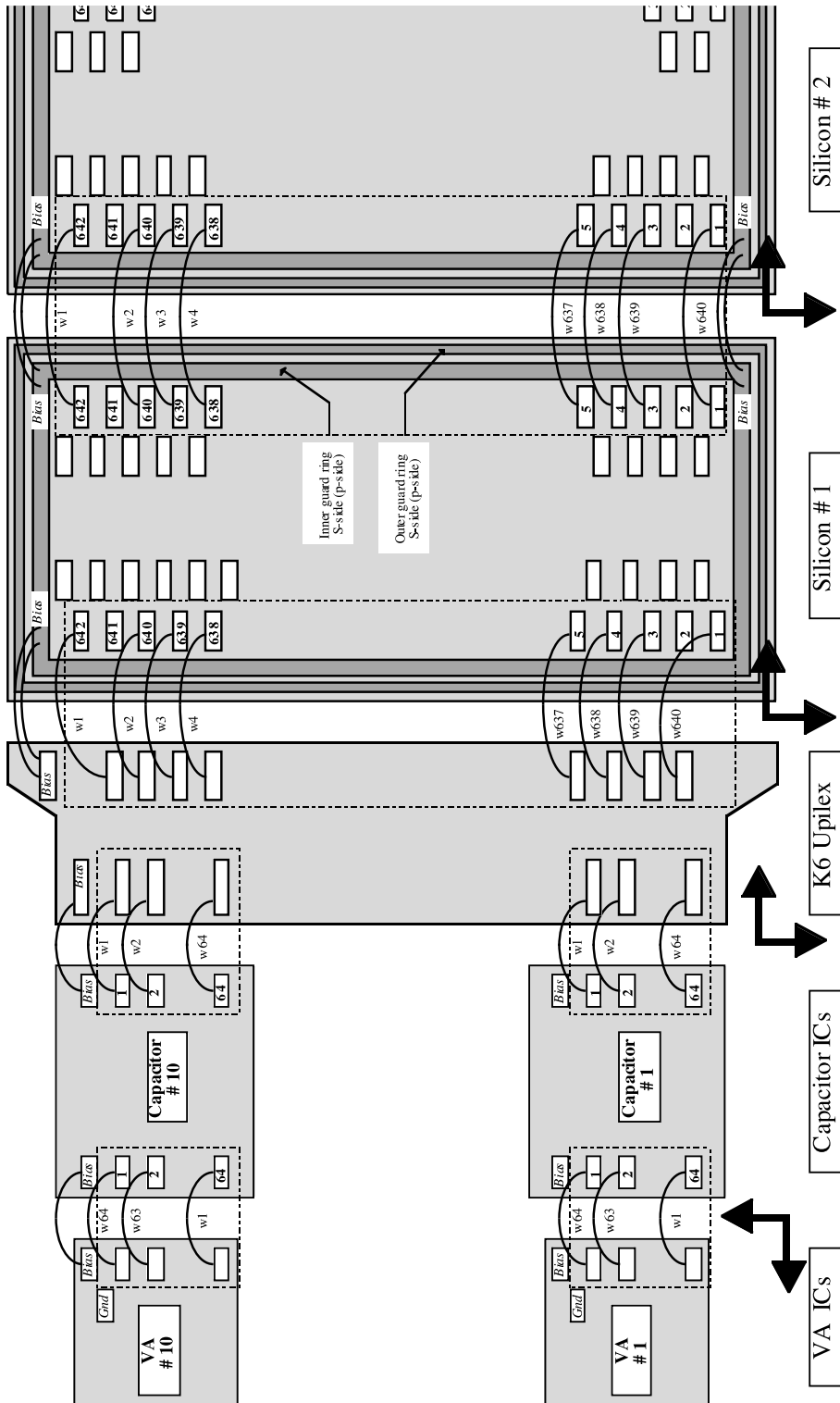
ladder length	distance between area (mm)				
	1→2	2→3	3→4	4→5	5→6
7	139.3	145			
9	139.4	124.2	103.5		
10	139.3	124.2	145		
11	98.0	124.2	124.2	103.5	
12	139.4	124.2	124.2	124.2	
13	139.3	124.2	124.2	145	
14	98.04	124.2	124.2	124.2	103.5
15	139.4	124.2	124.2	124.2	103.5



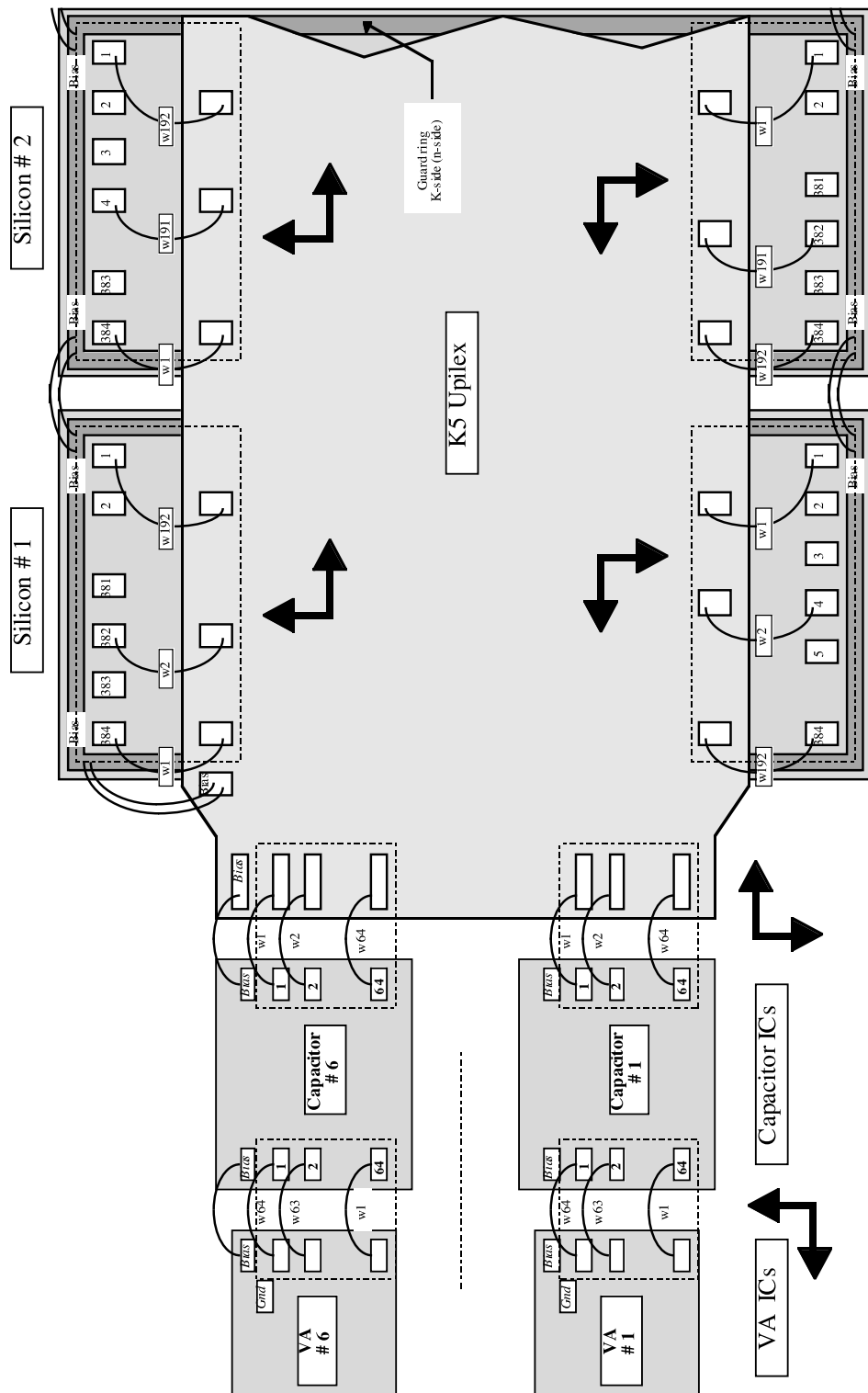
Appendix E

Ladder Bonding Schemes

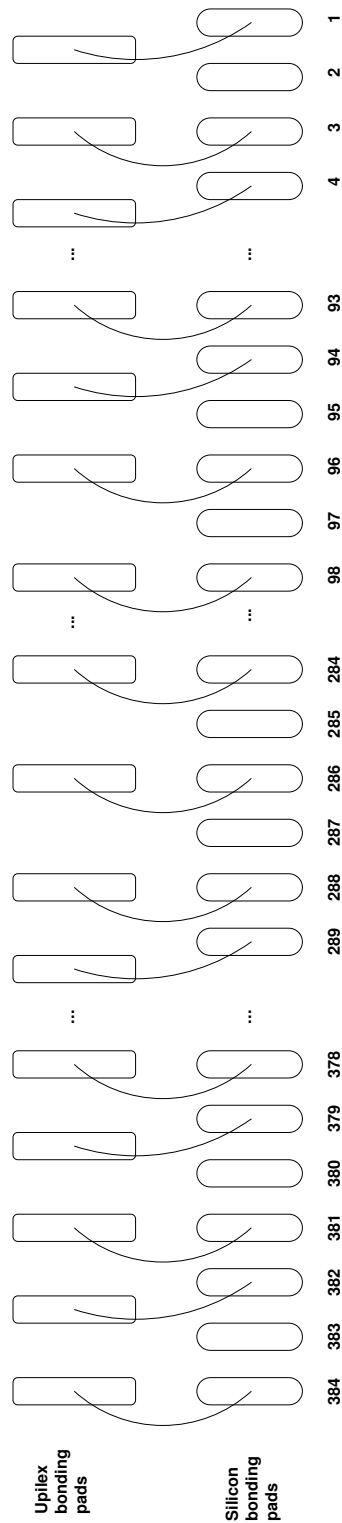
E.1 S-side bonding scheme



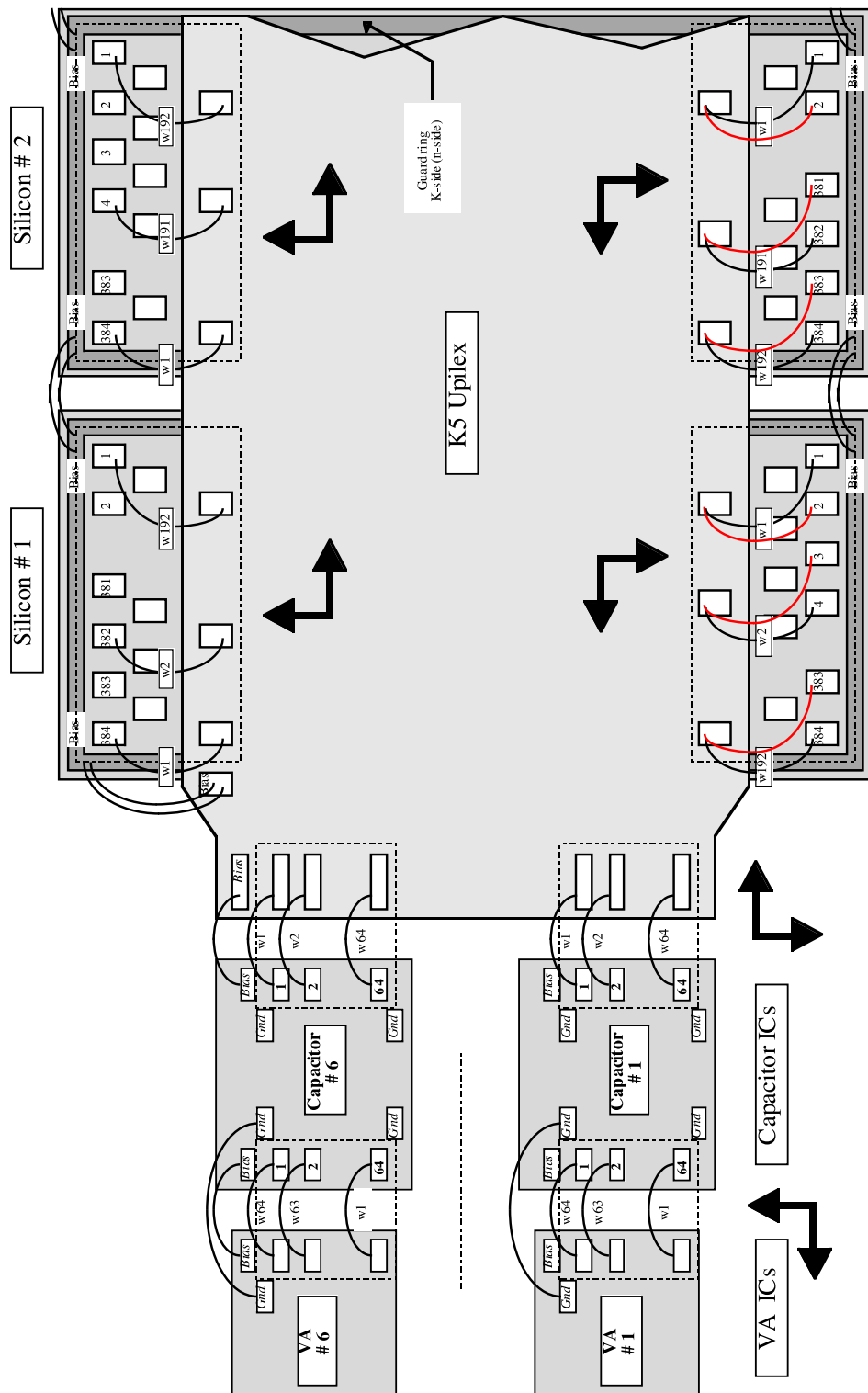
E.2 K-side bonding scheme



E.3 K7 bonding scheme



E.4 AMS-01 refurbished ladders K-side bonding scheme



Appendix F

Assembly phase 2

F.1 Hybrids preparation and feet gluing

AMS02 Ladder assembly phase 2 form (1/3)

Ladder:	Operators:	Date: ... / ... /200 ...	Time:
---------------	------------------	--------------------------	-------------

	Ok	Comment
1 Read carefully the ladder inspection form	<input type="checkbox"/>
2 Put ladder S-side up	<input type="checkbox"/>
3 If necessary, sharpen the hybrid angles (both sides)	<input type="checkbox"/>
4 If necessary, shorten K6 Upilex on the VA1 side	<input type="checkbox"/>
5 Clean the thread inside the columns	<input type="checkbox"/>
6 If necessary, add glue on the S-hybrid columns	<input type="checkbox"/>
7 If necessary, glue the S-connector screws	<input type="checkbox"/>
8 Put a drop of Araldite 2011 on bias line		
► between sensor 1 and K6 Upilex	<input type="checkbox"/>
► between K6 Upilex and capacitor	<input type="checkbox"/>
9 Wait 3 hours	<input type="checkbox"/>
10 Screw the K-side column	<input type="checkbox"/>
11 Put the protection tape into the box (bias side)	<input type="checkbox"/>
12 Slide the K-side box	<input type="checkbox"/>
13 Glue the S-side spacer on the S-hybrid	<input type="checkbox"/>
14 If necessary, dispense conformal coating on the S-hybrid	<input type="checkbox"/>
15 Wait 10 hours	<input type="checkbox"/>

AMS02 Ladder assembly phase 2 form (2/3)

	Ok	Comment
16 Remove the K-side box	<input type="checkbox"/>
17 Put ladder K-side up	<input type="checkbox"/>
18 If necessary, glue the K-connector screws	<input type="checkbox"/>
19 Put a drop of Araldite 2011 on bias line		
► between sensor 1 and K5 Upilex	<input type="checkbox"/>
► between K5 Upilex and capacitor	<input type="checkbox"/>
20 Wait 3 hours	<input type="checkbox"/>
21 Glue the K-side spacer on the K-hybrid	<input type="checkbox"/>
22 If necessary, dispence conformal coating on the K-hybrid	<input type="checkbox"/>
23 Wait 10 hours	<input type="checkbox"/>

AMS02 Ladder assembly phase 2 form (3/3)

	Ok	Comment
24 Turn the ladder to have S-side up	<input type="checkbox"/>
25 Dispense thermal conductive grease on K-hybrid	<input type="checkbox"/>
26 Screw the S-hybrid	<input type="checkbox"/>
27 Turn the ladder to have K-side up	<input type="checkbox"/>
28 Check the central column is screwed and has vibratite	<input type="checkbox"/>
29 Screw the central column (dinamometric screwdriver)	<input type="checkbox"/>
30 Turn the ladder to have S-side up	<input type="checkbox"/>
31 Dispense thermal conductive grease in the K-side box	<input type="checkbox"/>
32 Place the K-box	<input type="checkbox"/>
33 Put back the hybrids, and place the S-side box	<input type="checkbox"/>
34 Screw the hybrids (diagonal and central positions)	<input type="checkbox"/>
35 Turn the ladder to have K-side up	<input type="checkbox"/>
36 Screw the box (central hole)	<input type="checkbox"/>
DATE (when the feet were glued)	<input type="checkbox"/>
SERIAL NUMBER (jig used to glue the feet)	<input type="checkbox"/>
37 Check if the feet to be used are sanded	<input type="checkbox"/>

F.2 Airex spacer bonding

LADDER No : HYBRID BOX No :
SHIELD No : AIREX No ?

AMS2 Ladder shielding procedure

01/11/2002

-Ladder in transport box

A) Airex bonding

- Transfer the ladder from transport box to the spacer bonding jig
- According to ladder length, select an Airex spacer and the corresponding plexi guiding jig.
- Mount the Plexi jig to the spacer bonding jig.
- On a plate, prepare the 50mu film of Araldite 2011 (Thk controlled by 2 tapes of 50mu on the glas plate, equalize the layer.
- Place the spacer on the layer of Araldite, move slightly
- Remove carefully the Airex spacer, check the print on the glue layer to x-check Araldite is evenly distributed on the spacer.
- Turn the spacer, let the glue layer penetrate the cells of the Airex.
- Equalize again the glue layer on the glas plate
- Re-place the spacer on the layer of Araldite, move slightly
- Remove carefully the Airex spacer, check the print on the glue layer to x-check Araldite is evenly distributed on the spacer.
- Put the Airex spacer on the ladder, position is given by the Plexi jig – **(Attention ! spacer is not symmetric).**
- **Make sure the spacer is well positionned on the ladder.** Visa/date :
- Place the Plexi lid on top of the spacer.
- Add the brass loading blocks. (from 1 to 1.5 kg according to ladder length)
- **Protect the whole with a plastic foil.** Visa/date :
- **Let the Araldite cure at room temperature 8h.** Visa/date :
- Clean the glas plate.

F.3 Shielding wrapping

LADDER No : **HYBRID BOX No :**
SHIELD No : **AIREX No ?**

A) Shielding wrapping

- Prepare the wrapping table, remove all the pushers and clean.
- Position the shield on the table. Fix it with tape.
- **Add a protection tape on inner plane ladders.** **Visa/date :**
- Transfer carefully the ladder from the spacer bonding jig to the wrapping table
(Attention, the ladder feets have to pass through the holes in the shielding).
- **Fasten the ladder from underneath the table using M1.6 screws, every two rows**
(Attention not to overload the feets).
Visa/date :
- Mount the Pusher1
- Mount the Pusher 2, make sure the shielding is above the pusher.
- Using a soft wood blade, guide the shielding and move the pusher 1 towards the ladder.
- Move the pusher 1 to its final position and fasten the screws.
- Move the pusher 2 to its final position and fasten the screws.
- Lift the remaining shielding tongue and position the pusher 3.
- **Move the pusher 3 to its final position and fasten the screw.** **Visa/date :**
- Place the Alu pressing lid.
- **Make the solder junctions closing the shielding (tin-lead silver Sn62 type X39).** To do so it is necessary to displace slightly the alu lid longitudinally.
Visa/date :
- Transfer ladder to storage jig (ladder for inner plane on storage jig with hybrids at 90°, ladder for outer planes on storage jig with flat hybrids).
- **Solder the shield to reinforcement connexion.** **Visa/date :**
- **Electrical test.** **Visa/date :**
- **Mount and secure screws (A4 QUALITY) with Vibratite**
 - **1 x central screw M2 S side Torque 7.7cmN**
 - **1 x central screw M2 K side Torque 7.7cmN**
 - **4 x side screws M2 S side Torque 7.7cmN** **Visa/date :** ...
.....

Appendix G

Ladder naming scheme

The ladder name contains following information:

- ladder type $t = M$ (mechanical grade ladder), L (AMS-01 low voltage, AMS-02 standard ladder), H (AMS-01 high voltage ladder)
- ladder length $l = 7, 9, 10, 11, 12, 13, 14, 15$;
- assembly line $a = A$ (G&A), G (Geneva), P (Perugia), S (G&A supplemental production);
- destination layer in tracker p :

Ladder type	Layers	
	Inner	Outer
standard	I	O
alignment, lower	H	N
alignment, upper	J	P

the letter “T” is used to designate test ladders and cannot be used for AMS.

- assembly line serial number ser ;

The name is expressed as “ $tl\ ap\ ser$ ”, e.g. L09 GI 003 stands for “3rd ladder of the Geneva assembly line, to be installed on an inner layer, composed of 9 sensors”.

Bibliography

- [1] E. Hubble. A Relation between Distance and Radial Velocity among Extra-Galactic Nebulae. *Proc. Nat. Acad.*, 15:168–173, 1929.
- [2] A. A. Penzias and R. W. Wilson. A Measurement of excess Antenna Temperature at 4080 Mc/s. *Astrophys. J.*, 142:419–421, 1965.
- [3] J. C. Mather et al. Calibrator Design for the COBE far infraread absolute Spectrometer (FIRAS). *ApJ*, 512:511, 1999.
- [4] A. D. Sakharov. Violation of CP invariance, C asymmetry, and baryon asymmetry of the universe. *Sov. Phys. JETP Lett.*, 5:24–27, 1967.
- [5] V. Kuzmin et al. On anomalous electroweak baryon-number non-conservation in the early universe ? *Phys. Lett. B*, 155:36, 1985.
- [6] S. L. Glashow A. G. Cohen, A. De Rújula. A Matter-Antimatter Universe ? *Astroph. J.*, 495:539, 1998.
- [7] K. Hagiwara et al. 2002 Review of Particle Physics. *Phys. Rev. D*, 66:010001–1, 2002.
- [8] David Arnett. *Supernovae and Nucleosynthesis*. Princeton University Press, 1996.
- [9] Donald D. Clayton. *Principles of stellar Evolution and Nucleosynthesis*. The University of Chicago Press, 1983.
- [10] C. Anderson. The Positive Electron. *Phys. Rev.*, 43:491–494, 1933.
- [11] R. Battiston. Astro particle physics with AMS on the International Space Station. *J. Phys. G*, 29:891–902, 2002.
- [12] V. Choutko et al. Cosmic photon and positron spectra measurements modelling with AMS-02 detector at ISS. *Int. J. Mod. Phys. A*, 17:1817, 2002.
- [13] J. A. Simpson. Elemental and isotopic composition of the galactic cosmic rays. *Ann. Rev. Part. Sci.*, 33:323–381, 1983.
- [14] J. Casaus. Cosmic-ray Astrophysics with AMS-02. In *proceedings of 28th ICRC*, pages 2149–2152, 2003.

- [15] G. Lamanna. Astroparticle Physics with AMS-02. In *proceedings of 28th ICRC*, pages 1727–1730, 2003.
- [16] M. Pohl. Pulsars, Blazars and dark Matter with AMS. *Int. J. Mod. Phys. A*, 17:1809–1816, 2002.
- [17] M. Aguilar et al. The Alpha Magnetic Spectrometer (AMS) on the International Space Station: Part I - results from the test flight on the space shuttle. *Phys. Rept.*, 366:331–405, 2002.
- [18] J. Alcaraz et al. A silicon microstrip tracker in space: Experience with the AMS silicon tracker on STS-91. *Nouvo Cim.*, 112 A(11):1325–1343, 1999.
- [19] J. Alcaraz et al. Protons in near earth orbit. *Phys. Lett. B*, 472:215–226, 2000.
- [20] J. Alcaraz et al. Leptons in near earth orbit. *Phys. Lett. B*, 484:10–22, 2000.
- [21] J. Alcaraz et al. Cosmic protons. *Phys. Lett. B*, 490:27–35, 2000.
- [22] J. Alcaraz et al. Search for antihelium in cosmic rays. *Phys. Lett. B*, 461:387–396, 1999.
- [23] M. Cristinziani. *Search for Heavy Antimatter and Energetic Photons in Cosmic Rays with the AMS-01 Detector in Space*. PhD thesis, University of Geneva, Switzerland, 2002.
- [24] B. Blau et al. The superconducting magnet system of the alpha magnetic spectrometer AMS-02. *Nucl. Instr. and Meth. A*, 518:139–142, 2004.
- [25] B. Blau. The Superconducting Magnet of AMS-02. *Nucl. Physics B (Proc. Suppl.)*, 113:125–132, 2002.
- [26] S. Gentile J. Burger. The AMS-02 TRD for the International Space Station. In *28th ICRC proceedings*, pages 2161–2164, 2003.
- [27] S. Fopp. Entwicklung und Bau des Proportionalkammern für des Uebergangsstrahlungsdetektor des AMS02-Weltraumexperiments. Seminar at RWTH Aachen, 21.11.2003.
- [28] D. Casadei. The AMS-02 Time of Flight System. Final Design. In *proceedings of 28th ICRC*, pages 2169–2172, 2003.
- [29] D. Casadei et al. The AMS-02 Time of Flight System. *Nucl. Phys. B (Proc. Suppl.)*, 113:133–138, 2002.
- [30] M. Buénerd. The AMS-02 RICH Imager Prototype In-Beam Tests with 20 GeV/c per Nucleon Ions. In *proceedings of 28th ICRC*, pages 2157–2160, 2003.
- [31] J. Casaus. The AMS RICH detector. *Nucl. Physics B (Proc. Suppl.)*, 113:147–153, 2002.
- [32] S. Gentile. The Alpha Magnetic Spectrometer on the International Space Station. In *proceedings of 28th ICRC*, pages 2145–2148, 2003.

- [33] F. Cadoux et al. The AMS-02 electromagnetic calorimeter. *Nucl. Phys. B (Proc. Suppl.)*, 113:159–165, 2002.
- [34] E. Walker. Physique des Semiconducteurs. Course given at the University of Geneva, 1994.
- [35] A. Peisert. *Instrumentation in High Energy Physics*, ed. Fabio Sauli, chapter Silicon Microstrip Detectors. World Scientific, 1992.
- [36] G. Hall. Semiconductor Particle Tracking Detectors. *Rep. Prog. Phys.*, 57:481, 1994.
- [37] G. Batignani et al. Development and Performance of Double Sided Silicon Strip Detectors. *Nucl. Instr. and Meth. A*, 310:160–164, 1991.
- [38] M. Caria and E. Fiandrini. Characterization of Large Series of Double Sides Silicon Microstrip Detectors. INFN/AE-96/03.
- [39] A. Longoni et al. Instability of the Behaviour of High Resistivity Silicon Detectors due to the Presence of Oxide Charges. *Nucl. Instr. and Meth. A*, 288:35, 1990.
- [40] G. Batignani et al. Development of Double Side Readout Silicon Strip Detectors. *Nucl. Instr. and Meth. A*, 273:677, 1988.
- [41] P. Holl et al. The ALEPH Minivertex Detector. *Nucl. Instr. and Meth. A*, 257:587, 1987.
- [42] P. Holl et al. A Double-Sided Silicon Strip Detector with Capacitive Readout and a New Method of Integrated Bias Coupling. *IEEE Trans. Nucl. Sci.*, 36:251, 1989.
- [43] P.P. Allport et al. FOXFET biassed microstrip detectors. *Nucl. Instr. and Meth. A*, 310:155–159, 1991.
- [44] M. Krammer. Position reoslution and charge collection efficiency. *Nucl. Instr. and Meth. A*, 386:193–200, 1997.
- [45] M. Krammer and H. Pernegger. Signal collection and position reconstruction of silicon strip detectors with 200 μm readout pitch. *Nucl. Instr. and Meth. A*, 397:232–242, 1997.
- [46] U. Kötz et al. Silicon strip detectors with capacitive charge division. *Nucl. Instr. and Meth. A*, 235:481–487, 1985.
- [47] G. Barichello. Performance of long modules of silicon microstrip detectors. *Nucl. Instr. and Meth. A*, 413:17–30, 1998.
- [48] G. Ambrosi. The AMS Silicon Tracker readout system: design and performance. *Nucl. Instr. and Meth. A*, 435:215–223, 1999.
- [49] N. Dinu and E. Fiandrini. Electrical characterization of the large amount of silicon sensors for Alpha Magnetic Spectrometer (AMS) tracker. In *IMTC proceedings*, 2003.

- [50] M. Acciarri et al. The L3 silicon microvertex detector. *Nucl. Instr. and Meth. A*, 351:300–312, 1994.
- [51] Colibrys, Maladière 83, CH-2007 Neuchâtel.
- [52] A. Biland.
- [53] O. Toker et al. VIKING, a CMOS low noise monolithic 128 channel frontend for Si-strip detector readout. *Nucl. Instr. and Meth. A*, 340:575–579, 1994.
- [54] E. Nygård et al. CMOS low noise amplifier for microstrip readout Design and results. *Nucl. Instr. and Meth. A*, 301:506–516, 1991.
- [55] E. Beuville et al. AMPLEX, a low-noise, low power analog CMOS signal processor for multi-element silicon particle detectors. *Nucl. Instr. and Meth. A*, 288:157–167, 1990.
- [56] R. Ansari et al. Successful operation of a new Si-pad detector with ASIC readout at the CERN $\bar{p}p$ -collide. *Nucl. Instr. and Meth. A*, 288:240–244, 1990.
- [57] IDEas, <http://www.ideas.no>. *VAhdr9 V0.9 datasheet*.
- [58] M. Ribordy. *AMS-01: nouvelles limites à la présence de l'antihélium et contributions au détecteur de trajectoires*. PhD thesis, University of Geneva, Switzerland, 2000.
- [59] <http://root.cern.ch>.
- [60] Serial Communication Specification for AMS-02 Data Acquisition System. AMS Note DAQ-02.
- [61] <http://www.estec.esa.nl/tech/spacewire/>.
- [62] M. Cristinziani. Single Ladder Apparatus for Cosmics. AMS tracker meeting presentation (23.7.2002).
- [63] E. Cortina. AMS-02 Tracker: Shaping time determination. AMS internal note.